



**HAL**  
open science

# Fundamental flame characteristics and combustion chemistry for ammonia/methane blended fuels

Sophie Colson

► **To cite this version:**

Sophie Colson. Fundamental flame characteristics and combustion chemistry for ammonia/methane blended fuels. Thermics [physics.class-ph]. Université de Lyon; Tōhoku Daigaku (Sendai, Japon), 2020. English. NNT : 2020LYSEI103 . tel-03628358

**HAL Id: tel-03628358**

**<https://theses.hal.science/tel-03628358v1>**

Submitted on 2 Apr 2022

**HAL** is a multi-disciplinary open access archive for the deposit and dissemination of scientific research documents, whether they are published or not. The documents may come from teaching and research institutions in France or abroad, or from public or private research centers.

L'archive ouverte pluridisciplinaire **HAL**, est destinée au dépôt et à la diffusion de documents scientifiques de niveau recherche, publiés ou non, émanant des établissements d'enseignement et de recherche français ou étrangers, des laboratoires publics ou privés.



# INSA



TOHOKU  
UNIVERSITY

N° d'ordre NNT : 2020LYSEI103

## THESE de DOCTORAT DE L'UNIVERSITE DE LYON

opérée au sein de

**l'INSA de Lyon**

En cotutelle internationale avec

**l'université de Tohoku**

**Ecole Doctorale N° 162**

**MEGA (Mécanique, Energétique, Génie Civil, Acoustique)**

**Spécialité / discipline de doctorat :**

Thermique, Energétique

Soutenue publiquement le 13/11/2020, par :

**Sophie Colson**

---

# Fundamental flame characteristics and combustion chemistry for ammonia/methane blended fuels

---

Devant le jury composé de :

Baillot, Françoise	Professeur des universités, Université de Rouen	Rapporteure
Rousselle, Christine	Professeur des universités, Université d'Orleans	Rapporteure
Battin-Leclerc, Frédérique	Directrice de recherche, Université de Lorraine	Présidente
Escudie, Dany	Directrice de recherche, INSA de Lyon	Directrice de thèse
Kobayashi, Hideaki	Professeur des universités, Tohoku University	Directeur de thèse
Galizzi, Cédric	Maitre de conférences, INSA de Lyon	co-directeur de these



**Département FEDORA – INSA Lyon - Ecoles Doctorales – Quinquennal 2016-2020**

<b>SIGLE</b>	<b>ECOLE DOCTORALE</b>	<b>NOM ET COORDONNEES DU RESPONSABLE</b>
<b>CHIMIE</b>	<b>CHIMIE DE LYON</b> <a href="http://www.edchimie-lyon.fr">http://www.edchimie-lyon.fr</a> Sec. : Renée EL MELHEM Bât. Blaise PASCAL, 3e étage <a href="mailto:secretariat@edchimie-lyon.fr">secretariat@edchimie-lyon.fr</a> INSA : R. GOURDON	<b>M. Stéphane DANIELE</b> Institut de recherches sur la catalyse et l'environnement de Lyon IRCELYON-UMR 5256 Équipe CDFA 2 Avenue Albert EINSTEIN 69 626 Villeurbanne CEDEX <a href="mailto:directeur@edchimie-lyon.fr">directeur@edchimie-lyon.fr</a>
<b>E.E.A.</b>	<b>ÉLECTRONIQUE, ÉLECTROTECHNIQUE, AUTOMATIQUE</b> <a href="http://edeea.ec-lyon.fr">http://edeea.ec-lyon.fr</a> Sec. : M.C. HAVGOUDOUKIAN <a href="mailto:ecole-doctorale.eea@ec-lyon.fr">ecole-doctorale.eea@ec-lyon.fr</a>	<b>M. Gérard SCORLETTI</b> École Centrale de Lyon 36 Avenue Guy DE COLLONGUE 69 134 Écully Tél : 04.72.18.60.97 Fax 04.78.43.37.17 <a href="mailto:gerard.scorletti@ec-lyon.fr">gerard.scorletti@ec-lyon.fr</a>
<b>E2M2</b>	<b>ÉVOLUTION, ÉCOSYSTÈME, MICROBIOLOGIE, MODÉLISATION</b> <a href="http://e2m2.universite-lyon.fr">http://e2m2.universite-lyon.fr</a> Sec. : Sylvie ROBERJOT Bât. Atrium, UCB Lyon 1 Tél : 04.72.44.83.62 INSA : H. CHARLES <a href="mailto:secretariat.e2m2@univ-lyon1.fr">secretariat.e2m2@univ-lyon1.fr</a>	<b>M. Philippe NORMAND</b> UMR 5557 Lab. d'Ecologie Microbienne Université Claude Bernard Lyon 1 Bâtiment Mendel 43, boulevard du 11 Novembre 1918 69 622 Villeurbanne CEDEX <a href="mailto:philippe.normand@univ-lyon1.fr">philippe.normand@univ-lyon1.fr</a>
<b>EDISS</b>	<b>INTERDISCIPLINAIRE SCIENCES-SANTÉ</b> <a href="http://www.ediss-lyon.fr">http://www.ediss-lyon.fr</a> Sec. : Sylvie ROBERJOT Bât. Atrium, UCB Lyon 1 Tél : 04.72.44.83.62 INSA : M. LAGARDE <a href="mailto:secretariat.ediss@univ-lyon1.fr">secretariat.ediss@univ-lyon1.fr</a>	<b>Mme Sylvie RICARD-BLUM</b> Institut de Chimie et Biochimie Moléculaires et Supramoléculaires (ICBMS) - UMR 5246 CNRS - Université Lyon 1 Bâtiment Curien - 3ème étage Nord 43 Boulevard du 11 novembre 1918 69622 Villeurbanne Cedex Tel : +33(0)4 72 44 82 32 <a href="mailto:sylvie.ricard-blum@univ-lyon1.fr">sylvie.ricard-blum@univ-lyon1.fr</a>
<b>INFOMATHS</b>	<b>INFORMATIQUE ET MATHÉMATIQUES</b> <a href="http://edinfomaths.universite-lyon.fr">http://edinfomaths.universite-lyon.fr</a> Sec. : Renée EL MELHEM Bât. Blaise PASCAL, 3e étage Tél : 04.72.43.80.46 <a href="mailto:infomaths@univ-lyon1.fr">infomaths@univ-lyon1.fr</a>	<b>M. Hamamache KHEDDOUCI</b> Bât. Nautibus 43, Boulevard du 11 novembre 1918 69 622 Villeurbanne Cedex France Tel : 04.72.44.83.69 <a href="mailto:hamamache.kheddouci@univ-lyon1.fr">hamamache.kheddouci@univ-lyon1.fr</a>
<b>Matériaux</b>	<b>MATÉRIAUX DE LYON</b> <a href="http://ed34.universite-lyon.fr">http://ed34.universite-lyon.fr</a> Sec. : Stéphanie CAUVIN Tél : 04.72.43.71.70 Bât. Direction <a href="mailto:ed.materiaux@insa-lyon.fr">ed.materiaux@insa-lyon.fr</a>	<b>M. Jean-Yves BUFFIÈRE</b> INSA de Lyon MATEIS - Bât. Saint-Exupéry 7 Avenue Jean CAPELLE 69 621 Villeurbanne CEDEX Tél : 04.72.43.71.70 Fax : 04.72.43.85.28 <a href="mailto:jean-yves.buffiere@insa-lyon.fr">jean-yves.buffiere@insa-lyon.fr</a>
<b>MEGA</b>	<b>MÉCANIQUE, ÉNERGÉTIQUE, GÉNIE CIVIL, ACOUSTIQUE</b> <a href="http://edmega.universite-lyon.fr">http://edmega.universite-lyon.fr</a> Sec. : Stéphanie CAUVIN Tél : 04.72.43.71.70 Bât. Direction <a href="mailto:mega@insa-lyon.fr">mega@insa-lyon.fr</a>	<b>M. Jocelyn BONJOUR</b> INSA de Lyon Laboratoire CETHIL Bâtiment Sadi-Carnot 9, rue de la Physique 69 621 Villeurbanne CEDEX <a href="mailto:jocelyn.bonjour@insa-lyon.fr">jocelyn.bonjour@insa-lyon.fr</a>
<b>ScSo</b>	<b>ScSo*</b> <a href="http://ed483.univ-lyon2.fr">http://ed483.univ-lyon2.fr</a> Sec. : Véronique GUICHARD INSA : J.Y. TOUSSAINT Tél : 04.78.69.72.76 <a href="mailto:veronique.cervantes@univ-lyon2.fr">veronique.cervantes@univ-lyon2.fr</a>	<b>M. Christian MONTES</b> Université Lyon 2 86 Rue Pasteur 69 365 Lyon CEDEX 07 <a href="mailto:christian.montes@univ-lyon2.fr">christian.montes@univ-lyon2.fr</a>



# Fundamental Flame Characteristics and Combustion Chemistry for Ammonia/Methane Blended Fuels

Sophie Colson

## Résumé

Le réchauffement climatique provoqué par les émissions de  $\text{CO}_2$  est un danger majeur pour notre civilisation. Or, notre modèle de production est essentiellement basé sur l'utilisation de combustibles carbonés fossiles - charbon, pétrole, gaz - dont l'usage entraîne ces émissions. Une alternative à ce modèle serait d'augmenter l'utilisation de ressources renouvelables comme le solaire ou l'éolien pour la production d'énergie. Actuellement celles-ci ne couvrent cependant qu'une part marginale de la consommation d'énergie mondiale. Elles sont en effet connues pour leur intermittence et leur dispersion, entraînant des difficultés de stockage et de distribution de l'énergie produite.

Les combustibles non-carbonés ou neutres en carbone représentent dès lors une possibilité séduisante puisqu'ils permettraient le stockage des surplus ponctuels d'énergie de l'exploitation des renouvelables et garantiraient ainsi une distribution stable de l'énergie. De plus, certains de ces combustibles pourront être utilisés dans un futur proche dans les centrales à gaz existantes. Parmi ces combustibles, l'ammoniac est prometteur. En effet, c'est un combustible non-carboné qui peut être produit, en utilisant le surplus d'énergie des renouvelables, à partir d'eau et du nitrogène présent dans l'air, en combinant électrolyse de l'eau et procédé d'Haber Bosch. Il peut alors être stocké puis réutilisé plus tard lorsque les conditions sont moins favorables (nuit, hiver pour le solaire, absence de vent pour l'éolien...). L'énergie ainsi stockée peut être utilisée via des piles à combustible ou directement dans différents types de brûleurs.

Il reste néanmoins plusieurs défis à relever pour le déploiement à grande échelle de ce modèle. En particulier, la faible vitesse de la flamme d'ammoniac peut entraîner des problèmes pour sa stabilisation. Une solution consiste à mélanger l'ammoniac avec d'autres combustibles présentant une vitesse de flamme plus élevée. Parmi les candidats potentiels, le méthane a été sélectionné dans cette étude car les mélanges ammoniac/méthane peuvent être considérés comme un premier pas vers un modèle énergétique plus soutenable, et leur introduction dans les centrales à gaz existantes est possible à court terme. Mais la combustion de ces types de mélange, tout comme celle de l'ammoniac pur, reste encore assez peu étudiée.

Les problématiques des émissions de  $\text{NO}$  et de stabilisation des flammes doivent donc être considérées avec attention afin de permettre le développement de dispositifs de combustion appropriés. Une connaissance fondamentale plus complète de la combustion de ces mélanges est alors nécessaire. C'est l'objectif principal du travail présenté dans ce mémoire, qui, afin de compléter et enrichir les connaissances existantes, traite de l'étude de la chimie de la combustion et des propriétés fondamentales des flammes d'ammoniac/méthane et de leur stabilisation.

Dans un premier temps, dans le chapitre 2 de cette thèse, la chimie de combustion des flammes ammoniac/méthane ont été étudiées par simulation numérique. Les chemins réactionnels pour la combustion de ces mélanges ont été étudiés pour une large gamme de taux de concentration d'ammoniac dans le mélange de combustible,  $E$ . Il a été observé que les chemins réactionnels dans le cas de l'oxydation des deux fuels étaient toujours présents, mais avec certaines variations et interactions. Ces interactions sont plus importantes dans la gamme  $E = 0.15 - 0.30$  et contribuent à une formation plus importante de HCN et CN. Les émissions de NO atteignent une valeur maximale pour  $E = 0.6$ . La production de NO est dominée par la production via "Fuel-NO route". La production par les routes "thermal-NO" et "prompt-NO" est moins importante. Un changement dans la chimie de la réaction associée à l'abondance des radicaux NH a été observé et joue un rôle important dans la formation de NO. De plus, la structure des flammes de mélange ammoniac/méthane a été étudiée pour différentes configurations : flamme se propageant librement (freely propagating flame, FPF), flamme à contre-courant prémélangée (counterflow premixed twin flames, PCF) et flamme à contre-courant non-prémélangée (counterflow non-premixed flame, NCF). Cette étude de la structure de la flamme révèle l'importance des radicaux OH, H et O dans la chimie de combustion ainsi que celle de CH<sub>3</sub> et NH. L'analyse des réactions contribuant à la libération de chaleur dans la flamme a également été effectuée. Bien que la réaction  $\text{NH}_3 + \text{OH} = \text{NH}_2 + \text{H}_2\text{O}$  soit prédominante dans la combustion de l'ammoniac, son rôle demeure mineur dans le cas de la combustion de flammes ammoniac/méthane pour lesquelles les réactions de formation de CO<sub>2</sub> et CH<sub>2</sub>O sont dominantes et correspondent essentiellement aux chemins d'oxydation de la flamme de méthane. Le rôle de la diffusion des radicaux O, OH et H vers le front de flamme dans le cas des flammes de prémélange a aussi été considéré. Ceci a confirmé l'importance des radicaux OH dans la chimie de combustion de l'ammoniac. Pour les flammes ammoniac/méthane, l'importance relative de OH et H dépend de la valeur de  $E$ , OH acquérant une importance de plus en plus grande au fur et à mesure que l'ammoniac est introduit dans le mélange. Enfin, l'émission de NO (EINO) a été étudiée dans le cas des configurations FPF et PCF. Pour la configuration FPF, un temps de résidence court entraîne de plus larges valeurs de EINO pour les flammes d'ammoniac/méthane que pour celles de méthane pur. Cependant, pour des temps de résidence plus longs et dans les deux configurations (FPF et PCF), la valeur de EINO diminue quelle que soit la valeur de  $E$  considérée et passe au-dessous de celle du méthane. Pour un temps de résidence court, la valeur de EINO est plus petite pour la configuration à contre-courant (PCF) que pour la configuration de libre propagation, mais ces valeurs convergent pour des temps de résidence plus longs. Cette première étude a donc permis de clarifier les caractéristiques majeures de la chimie de combustion des flammes ammoniac/méthane, en particulier dans le cas de l'introduction de larges quantités d'ammoniac.

Dans un deuxième temps, correspondant au chapitre 3, l'étude se concentre sur les propriétés fondamentales des flammes de mélange ammoniac/méthane. Plus particulièrement, le taux d'étirement à l'extinction et les profils des espèces OH et NO dans la flamme ont été étudiés expérimentalement, en utilisant un brûleur à contre-courant. Le taux d'étirement à l'extinction a été obtenu pour les flammes non-prémélangée et prémélangée, sur une large gamme de taux d'ammoniac,  $E$ , et de richesses,  $\phi$ . Dans les deux configurations, un taux d'ammoniac élevé dans le mélange entraîne une diminution importante du taux d'étirement à l'extinction. Pour les flammes de prémélange, un maximum est atteint entre  $\phi = 0.9$  et  $\phi = 0.95$ . Cette position du maximum, pour les mélanges pauvres

d'ammoniac/méthane, peut être attribuée au nombre de Lewis qui est inférieur à l'unité. Les résultats expérimentaux ont ensuite été comparés aux résultats de simulations numériques en utilisant quatre mécanismes de cinétique chimique différents : GRI-Mech 3.0, le mécanisme de UCSD, et les mécanismes de Tian et Okafor. Pour les flammes non-prémélangées une bonne correspondance a été observée entre les résultats expérimentaux et les estimations obtenues par simulation numérique avec le mécanisme d'Okafor. Mais pour les flammes de prémélange, aucun des quatre mécanismes sélectionnés n'a pu reproduire la tendance expérimentale sur l'ensemble des conditions de mélange. Des écarts particulièrement importants entre expérience et simulation, et entre les résultats de simulation avec les différents mécanismes, ont été observés dans le cas des flammes pauvres. Ceux-ci sont encore plus prononcés dans le cas du méthane. Afin d'étudier plus en détail l'origine de ces écarts, une analyse de sensibilité, couplée à une analyse de l'évolution des chemins réactionnels pour les flammes à contre-courant et les mélanges pauvres, a été réalisées. Une comparaison avec d'autres mécanismes existants, possédant une chimie plus détaillée, montre que l'écart est fortement réduit si le mécanisme inclut un set de réactions d'oxydation du méthane suffisamment détaillé. L'analyse de sensibilité montre en effet que le taux d'étirement à l'extinction dépend de réactions apparaissant comme majeures dans l'étude des chemins réactionnels principaux ou encore l'analyse du taux de chaleur libérée, mais qu'il dépend également fortement des réactions qui a priori apparaissent comme mineures dans la chimie de réaction. Les profils des espèces OH et NO ont été obtenus expérimentalement sur le même brûleur contre-courant dans le cas des flammes de prémélange en utilisant la méthode PLIF. Une comparaison quantitative des FWHM des profils observés lors des expériences et simulations a été réalisée en s'appuyant sur les principes spectroscopiques de la technique PLIF. Par comparaison des résultats expérimentaux avec les résultats numériques, des conclusions similaires à celles obtenues pour le taux d'étirement à l'extinction ont été obtenues. Notamment, les quatre mécanismes sélectionnés tendent à être sur-réactifs avec une sur-estimation du taux d'étirement à l'extinction, ainsi que des largeurs de profil (FWHM) plus larges que l'observation expérimentale. De la même façon, de plus larges écarts ont pu être observés dans le cas des flammes pauvres, particulièrement pour le radical OH. Le taux d'étirement à l'extinction, propriété fondamentale de la flamme, ainsi que les profils des espèces OH et NO ont été observés expérimentalement dans cette étude. Leur comparaison avec les résultats de simulations pour les mécanismes réactionnels sélectionnés montre des écarts importants suivant les mélanges considérés, ainsi que des pistes de réflexion quant à leur amélioration.

Enfin, les effets de l'ajout d'ammoniac sur la stabilisation d'une flamme jet de méthane ont été étudiés dans le chapitre 4 via une approche expérimentale académique. Les caractéristiques d'une flamme jet non-prémélangée ammoniac/méthane, se développant dans un écoulement (coflow) d'air, ont été explorées ainsi que l'évolution des régimes de stabilisation de ces flammes, pour un taux croissant d'ammoniac dans le mélange de combustible. L'étude des phénomènes de suspension (liftoff) et de rattachement (re-attachment) a montré que l'ajout d'ammoniac entraîne une réduction importante du domaine de stabilisation et de la limite de suspension. Celle-ci peut être attribuée essentiellement à la combinaison d'effets thermique et chimique. La limite de rattachement, qui ne présente pas de dépendance avec la vitesse de coflow dans la gamme de vitesses considérée pour la flamme de méthane, devient dépendante de ce paramètre lors de l'ajout d'ammoniac. Pour de faibles vitesses de coflow, la limite de rattachement décroît graduellement quand  $E$  croît et lorsque la hauteur de stabilisation de la flamme

suspendue croit. Cependant, pour de plus grandes vitesses de coflow, une forte décroissance soudaine est observée. Cette décroissance soudaine correspond à la transition entre deux types de comportements de flammes suspendues dans la zone d'hystérésis de la cartographie de stabilisation. Le premier comportement correspond à la décroissance de la hauteur de stabilisation de la flamme suspendue quand la vitesse de jet est réduite ; la seconde correspond à une augmentation de la hauteur de suspension de la flamme suspendue quand la vitesse de jet est réduite. La transition entre ces deux types de comportement correspond aux effets couplés de la vitesse de coflow et de la concentration d'ammoniac sur la stabilisation de la flamme suspendue. Ce type de transition peut être généralisé pour d'autres types de combustibles, sous réserve d'avoir une flamme suspendue se stabilisant suffisamment haut dans le jet, correspondant à des cas de dilution importante ou encore des cas de grande vitesse de coflow. Enfin, les interactions entre les flammes attachées et le brûleur pour des vitesses inférieures à la vitesse de suspension (liftoff) ont été étudiées. L'évolution de la position du bout de flamme avec un taux croissant d'ammoniac montre que sa position est particulièrement affectée par les changements de propriétés de la flamme associés à l'ajout d'ammoniac, et plus particulièrement par les modifications de la fraction de mélange et de la vitesse locale de flamme. Ces variations induisent un décalage dans les régimes de stabilisation obtenus dans le cas de la flamme de méthane, relevant principalement des effets aérodynamiques et chimiques couplés au niveau de la lèvre du brûleur. Elles conduisent également à une évolution des interactions thermiques entre le bout de flamme et le brûleur soulignant toute l'importance des couplages aérothermochimiques en présence.

Cette étude a donc permis de clarifier différents aspects fondamentaux de la combustion des mélanges ammoniac/méthane en lien avec la chimie de combustion pour des mélanges à forte concentration d'ammoniac, la détermination de leurs propriétés fondamentales – taux d'étirement à l'extinction, profils OH et NO. Elle a apporté des éléments précis d'analyse et de comparaison de ces propriétés aux estimations obtenues à l'aide de simulations numériques avec quatre mécanismes réactionnels existants. De plus, l'étude fondamentale de l'influence de l'ajout d'ammoniac sur une flamme jet a été développé et approfondi. Ces différents aspects peuvent donc être utilisés comme outils, notamment dans les premières phases de dimensionnement et de conception de systèmes industriels. Ils peuvent également être utilisés comme un support à développer et à compléter pour la connaissance globale de la flamme, mais aussi afin d'améliorer et mettre à jour les modèles de chimie existants qui sont nécessaires à la réalisation de simulations dans des environnements complexes lors de la conception d'applications.

Comme perspective de ce travail, il apparaît que l'étude de profils d'autres radicaux dans la flamme pourrait être engagée. Combinée avec les résultats déjà acquis, elle fournirait un support solide pour le développement et la mise à jour des mécanismes réactionnels. Concernant l'étude fondamentale sur la stabilisation des flammes jet, il est envisagé une approche plus locale de la stabilisation, qui consoliderait les résultats obtenus concernant la chimie de réaction et les propriétés fondamentales de flamme. Ces différentes approches, ainsi combinées permettraient d'enrichir notre connaissance des flammes d'ammoniac/méthane et de contribuer au développement d'applications industrielles.

# Fundamental Flame Characteristics and Combustion Chemistry for Ammonia/Methane Blended Fuels

Sophie Colson

## Abstract

Global warming triggered by CO<sub>2</sub> production from human activities is a major threat to our civilization. Alternatives to our energy model based on fossil fuels are thus necessary. One solution is the exploitation of renewable resources. However, renewables still represent a marginal part of global energy production and are known for their intermittency and storage issues. Alternative carbon-free or carbon-neutral fuels are attractive as they allow the storage of the renewables production surplus, guarantee stable energy supply and can be quickly deployed in existing facilities. Among those alternatives, ammonia is considered as promising. Nonetheless, some challenges remain for its large-scale deployment such as ammonia low burning velocity triggering stabilization issues. One solution is to mix ammonia with other fuels having a higher burning velocity. Among the potential candidates, methane was selected in this study because ammonia/methane mixtures can be considered as the first step toward a greener model of energy production. Their study is thus the purpose of the present work.

The combustion of ammonia/methane blends is still poorly known, especially for blends with a large ammonia content. Thus, ammonia/methane flames were first investigated through numerical simulations, from the viewpoint of combustion chemistry. The reaction path of those blends was investigated over a wide range of mixing ratio,  $E$ . It could be observed that both fuel oxidation paths were conserved, but that interaction sub-paths appeared depending on  $E$ . Those interactions were larger in the range of  $E = 0.15 - 0.30$ , contributing to larger HCN and CN production. The NO emission peaked at  $E = 0.6$ . Fuel-NO route dominated the production of NO and thermal-NO and prompt-NO were less important. A switch in the chemistry associated with the abundance of NH radicals was shown to be of importance in NO formation. Besides, the flame structure was considered for different configurations: the freely propagating flame (FPF), the counterflow premixed twin flames (PCF) and the counterflow non-premixed flame (NCF). These studies revealed the importance of OH, H and O in the chemistry as well as CH<sub>3</sub> and NH. Analysis of the reactions contributing to the heat release in flames was also performed. Even though  $\text{NH}_3 + \text{OH} = \text{NH}_2 + \text{H}_2\text{O}$  was key to ammonia combustion, its role remains minor compared with CO<sub>2</sub> and CH<sub>2</sub>O formation steps for blend flames. The role of O, OH and H radicals back diffusion in the premixed flames was investigated and confirmed the importance OH radicals in ammonia chemistry. For ammonia/methane flames, the relative importance of OH and H depended on  $E$ . Finally, the emission index of NO (EINO) was considered in FPF and PCF. For FPF, short residence time led to higher EINO in the ammonia/methane flame case than in the methane flame case. However, for longer residence time, EINO of the mixtures decreased to lower values than the methane one. Also, for short residence time, EINO was smaller in the PCF than FPF, but their value converged for longer residence time.

Then, extinction stretch rates and OH and NO profiles were investigated experimentally using counterflow flame configurations. Extinction stretch rate was obtained for both premixed and non-premixed flames over a wide range of  $E$  and equivalence ratios,  $\phi$ . In both premixed and non-premixed flames, large  $E$  led to a drastic decrease in the extinction stretch rate. For premixed flames, the maximum extinction stretch rate was observed between  $\phi = 0.9$  and  $\phi = 0.95$  and was attributed to the Lewis number effect. The experimental results were then compared to numerical simulation results using four selected detailed chemistries: GRI-Mech 3.0, UCSD mechanism, Tian's and Okafor's mechanisms. Whereas for non-premixed flames a good fit could be observed between experiment and simulation, no satisfactory fit could be seen in the premixed flame case. Large discrepancies between experiment and numerical simulation were observed for lean flames and were more pronounced for the methane flame case. Combining sensitivity analysis and comparisons with other kinetics revealed that discrepancies might result from a lack in the methane oxidation chemistry of the selected chemistries and should be further investigated in future studies. OH and NO profiles were obtained experimentally for counterflow premixed twin flames using PLIF measurements. Quantitative comparison of the experimental FWHM of the profiles to simulations was performed based on spectroscopic principles for PLIF applied in the present case. From comparison with numerical simulations, similar conclusions to the extinction behaviors could be drawn for lean mixtures, for which large discrepancies were observed. A general over-reactivity by mechanisms in the OH and NO production was observed and should be considered for mechanisms improvement.

Finally, the effects of ammonia addition on a methane jet flame were investigated from a fundamental point of view. A non-premixed ammonia/methane jet in an air coflow was employed and the stabilization regimes of those flames were first investigated with increasing  $E$ . Determination of the liftoff and re-attachment limits of the flames showed that larger  $E$  led to a large decrease in the liftoff limit attributed essentially to combined thermal and chemical effects. The re-attachment limit was found to be dependent on the air coflow velocity. For low air coflow velocities, the re-attachment limit decreased gradually with  $E$  as the lifted flame height increased. However, for larger air coflow velocities, a sudden drop was observed. This drop corresponds to the transition between two different lifted flame behaviors in the hysteresis region of the flame stabilization map. The first one corresponds to the decrease in lifted flame height as the jet velocity is decreased, the second one to an increase in the lifted flame height with a decrease in the jet velocity. The transition between these two behaviors corresponds to the combined effects of air coflow velocity and  $E$ . This could be generalized for all types of fuels, provided that lifted flames are sufficiently high, corresponding to large dilution cases or large coflow velocities. Finally, attached flames interactions with the burner up to the liftoff limit were further studied. Evolution of the flame position with  $E$  shown that the attached flame tip position was highly affected by the change in the flame properties through the change in the stoichiometric mixture fraction and local flame speed. These changes induced a shift in the previously determined attached flame stabilization regimes due to coupled chemical and aerodynamical effects in the wake of the burner lip. This impacted in turn the thermal interactions between the flame base and the burner, showing the key role of the aero-chemical coupling in presence.

# Content

<b>Résumé</b> .....	<b>i</b>
<b>Abstract</b> .....	<b>v</b>
<b>Content</b> .....	<b>vii</b>
<b>List of figures and tables</b> .....	<b>xi</b>
<b>Chapter 1 Introduction</b> .....	<b>1</b>
1. Background.....	1
1.1. The role of combustion in our societies.....	1
1.2. Green ammonia model and ammonia combustion .....	7
2. Previous studies on ammonia/methane combustion .....	14
2.1. Study on the ammonia and ammonia/methane flames chemistry.....	14
2.2. Experimental studies of ammonia/methane flame characteristics .....	16
2.3. Ammonia flame stabilization.....	19
3. Objective and scope of the present study.....	20
3.1. Fundamental study on ammonia/methane flame chemistry.....	21
3.2. Fundamental study on ammonia/methane flame stabilization.....	22
4. Structure of the thesis .....	23
<b>Chapter 2 Chemistry of ammonia/methane flames</b> .....	<b>24</b>
1. Introduction .....	24
2. Ammonia/methane flames chemistry .....	26
2.1. Reaction path analysis .....	26
2.2. Emissions characteristics.....	33
2.3. Flame structure .....	36
2.4. Heat release in the flames .....	46

3. Effect of diffusion of OH, H and O radicals in the flames .....	51
3.1. Objectives and methodology .....	51
3.2. Comparison of methane, ammonia and hydrogen .....	53
3.3. The case of ammonia/methane flames.....	57
4. NO emission index for ammonia/methane premixed flames and effect of flame stretch.....	59
4.1. Method and objectives.....	59
4.2. Definition of the flame front and beginning of consumption of fuel.....	59
4.3. Residence time definition .....	60
4.4. EINO in ammonia flame case.....	63
4.5. EINO in methane flame case .....	64
4.6. EINO in the case of ammonia/methane flames .....	65
5. Conclusions .....	68
<b>Appendix .....</b>	<b>71</b>
2A. Detailed reaction path with Okafor's mechanism.....	71
2B. Reaction path using other chemistries .....	76
<b>Chapter 3 Assessment of detailed chemistry models for ammonia/methane flames by comparison with experiments using counterflow configuration.....</b>	<b>86</b>
1. Introduction .....	86
1.1. Objective of the chapter.....	86
1.2. Overview of existing mechanisms and selection of four kinetics for ammonia/methane flames .....	87
1.3. Counterflow flame experimental setup.....	91
1.4. 1D modeling and its limits.....	92
1.5. Velocity profiles considerations for modeling.....	98
2. Experimental analysis of the extinction stretch rate of counterflow premixed twin flames .	109
2.1. Conditions of study.....	109
2.2. Experimental results and comparisons with numerical simulations .....	109
2.3. Further discussion on lean flames.....	112

3. Experimental analysis of the extinction stretch rate of counterflow non-premixed flame ...	115
3.1. Conditions of study.....	115
3.2. Experimental results and comparisons with numerical simulations.....	116
4. Evaluation of the chemistry based on OH and NO distributions in the flame using OH and NO-PLIF .....	119
4.1. Objective and investigated conditions .....	119
4.2. Experimental setup and method.....	121
4.3. Quantitative evaluation based on the FWHM of OH and NO-PLIF measurements.....	123
5. Conclusions .....	130
<b>Appendix .....</b>	<b>133</b>
3A. 1D modeling of counterflow flames.....	133
3B. Details of PIV measurements .....	136
3C. Reaction path for lean methane counterflow premixed twin flames .....	141
3D. Experimental OH and NO FWHM results .....	143
<b>Chapter 4 Fundamental characteristics of ammonia/methane-air non-premixed jet flames .....</b>	<b>144</b>
1. Introduction .....	144
1.1. Stabilization issues.....	144
1.2. Introduction on non-premixed jet flames.....	145
1.3. Objective of this chapter .....	149
1.4. Experimental setup .....	150
2. Effects of ammonia addition on the stabilization regimes of methane non-premixed jet flames.....	155
2.1. Previous works on the effects on the stabilization regimes of the air coflow velocity and dilution of the fuel jet.....	155
2.2. Experiment on ammonia/methane jet flames.....	158
3. Evolution of the stabilization process of the attached flame .....	177
3.1. The case of methane jet flame .....	177

3.2. Effect of ammonia addition .....	179
4. Conclusions .....	192
<b>Appendix .....</b>	<b>195</b>
4A. Attached flame tip position measurements.....	195
4B. Temperature mapping.....	197
<b>Chapter 5 Conclusion .....</b>	<b>199</b>
1. Ammonia/methane combustion chemistry .....	199
2. Fundamental flame characteristics and chemistry validation using counterflow flames.....	201
3. Stabilization mechanisms of ammonia/methane non-premixed jet flames.....	202
4. Perspectives of research in future .....	204
<b>References .....</b>	<b>206</b>
<b>Acknowledgments .....</b>	<b>220</b>
<b>List of publications.....</b>	<b>222</b>

# List of figures and tables

## Chapter 1

Fig. 1.1. Shares of total primary energy supply (TPES) in 1971 and 2016; from IEA [1].....	1
Fig. 1.2. (a) World total final consumption (TFC) by region; (b) Energy consumption per sector in OECD countries between 1971 and 2016; from IEA [1]. .....	2
Fig. 1.3. Location of proved fossil fuel reserves in 2015 from ourworldindata.org [19]. .....	6
Fig. 1.4. Share of electricity production by type of energy resource; from IEA [17]. .....	7
Fig. 1.5. Ammonia production plant design from CEP magazine [20]. .....	8
Fig. 1.6. Green ammonia society model.....	10
Fig. 1.7. X-15 Rocket powered aircraft; Picture from NASA website [41]. .....	11
Table 1.1. Ammonia exposure level and its danger by Valera-Medina et al. [32].....	9
Table 1.2. AEGL classification for ammonia exposure depending on the level of concentration and duration of exposure from the NIH [33]. .....	9
Table 1.3. Characteristics of ammonia, methane and hydrogen fuels [43]. .....	12

## Chapter 2

Fig. 2.1. Methane oxidation path for the stoichiometric condition at atmospheric pressure.....	27
Fig. 2.2. Ammonia oxidation path for the stoichiometric condition at atmospheric pressure.....	28
Fig. 2.3. Ammonia oxidation branch in the ammonia/methane reaction path for small $E$ . .....	29
Fig. 2.4. Evolution of NH consumption rate with increasing $E$ for FPF: (a) in terms of mole/cm <sup>3</sup> s; (b) in terms of percent of total NH consumption. ....	29
Fig. 2.5. NH distribution for $E = 0, 0.15$ and $0.30$ in relation with the reaction path evolution for FPF. ....	30
Fig. 2.6. Interactions between methane and ammonia oxidation path in ammonia/methane/air flame at $E = 0.3$ and for FPF. C-N species are represented in purple while carbon species are represented in blue and nitrogen species in orange.....	31
Fig. 2.7. Evolution burnt gas emissions for FPF with $E$ : (a) H <sub>2</sub> , NO, CO <sub>2</sub> and CO; (b) N <sub>2</sub> O, NO <sub>2</sub> , and NH <sub>3</sub> ; (c) NH <sub>3</sub> and CH <sub>4</sub> ; (d) HCN and CN. ....	34

Fig. 2.8. Formation and consumption of NO for FPF with $E$ : (a) NO formation routes; (b) NO consumption route. ....	35
Fig. 2.9. Formation (black arrows) and consumption (grey arrows) path for NO.....	35
Fig. 2.10. Flame structure for FPF, at $\phi = 1.0$ : (a) methane/air flame; (b) ammonia/air flame.....	37
Fig. 2.11. Methane and ammonia flames main intermediate species for FPF at $\phi = 1.0$ : methane/air premixed flame (a) H, OH, O, HO <sub>2</sub> , and H <sub>2</sub> O <sub>2</sub> , (b) CH <sub>3</sub> , CH <sub>2</sub> O, and HCO, (c) CO and CO <sub>2</sub> ; ammonia/air premixed flame (d) H, OH, O, HO <sub>2</sub> , and H <sub>2</sub> O <sub>2</sub> , (e) NH <sub>2</sub> , NH and HNO, (f) NO, NO <sub>2</sub> and N <sub>2</sub> O. ....	37
Fig. 2.12. Rate of production of radicals for FPF: (a) methane/air premixed flame; (c) ammonia/air premixed flame.....	38
Fig. 2.13. Global structure of a premixed ammonia/methane flame using the 1D freely propagating flame model (FPF), with $E = 0.2$ and $\phi = 1.0$ . ....	39
Fig. 2.14. Net reaction rates of the main contributor to N <sub>2</sub> consumption for $E = 0.2$ and FPF. ....	40
Fig. 2.15. 1D freely propagating flame (FPF) structure for $E = 0.2$ : (a) OH, H, O; (b) HO <sub>2</sub> , H <sub>2</sub> O <sub>2</sub> ; (c) CH <sub>3</sub> , CH <sub>2</sub> O, CH <sub>2</sub> , HCO; (d) HCO, CH <sub>2</sub> *, CH and C; (e) NH <sub>2</sub> , NH, HNO and NO, NO <sub>2</sub> and N <sub>2</sub> O; (f) HCN and CN. ....	41
Fig. 2.16. Global structure of a counterflow premixed twin flames (PCF) for $E = 0.2$ , $\phi = 1.0$ and a stretch rate of 300 s <sup>-1</sup> (40% of extinction stretch rate value, the stagnation plane at $x = 0.136$ cm is not represented in the present graph). ....	42
Fig. 2.17. Counterflow premixed twin flame (PCF) detailed structure for $E = 0.2$ , $\phi = 1.0$ and stretch rate of 300 s <sup>-1</sup> : (a) OH, H, O; (b) HO <sub>2</sub> , H <sub>2</sub> O <sub>2</sub> ; (c) CH <sub>3</sub> , CH <sub>2</sub> O, CH <sub>2</sub> , HCO; (d) HCO, CH <sub>2</sub> *, CH and C; (e) NH <sub>2</sub> , NH, HNO, NO, NO <sub>2</sub> and N <sub>2</sub> O; (f) HCN and CN. ....	43
Fig. 2.18. Global structure of a counterflow non-premixed flame (NCF) for $E = 0.2$ , with a stretch rate of 60 s <sup>-1</sup> .....	44
Fig. 2.19. Heat released profile in a counterflow flame for $E = 0.2$ and a stretch rate of 60 s <sup>-1</sup> : (a) non-premixed (NCF); (b) premixed (PCF) for $\phi = 1.0$ .....	44
Fig. 2.20. Counterflow non-premixed flame structure (NCF) for $E = 0.2$ and a stretch rate of 60 s <sup>-1</sup> : (a) OH, H, O; (b) HO <sub>2</sub> , H <sub>2</sub> O <sub>2</sub> ; (c) CH <sub>3</sub> , CH <sub>2</sub> O, CH <sub>2</sub> , HCO; (d) HCO, CH <sub>2</sub> * CH and C; (e) NH <sub>2</sub> , NH, HNO, NO, NO <sub>2</sub> and N <sub>2</sub> O; (f) HCN and CN. ....	45
Fig. 2.21. CH <sub>4</sub> /air premixed flame (FPF) reaction path at $\phi = 1.0$ : rate of reaction in black; main contributors to heat release in the flame in gray. ....	46
Fig. 2.22. Structures of CH <sub>4</sub> /air and NH <sub>3</sub> /air flames premixed flames in relation with heat release profiles for FPF: HRR of (a) CH <sub>4</sub> case, (d) NH <sub>3</sub> case; RoR of (b) CH <sub>4</sub> case, (e) NH <sub>3</sub> case; RoP of main intermediates in (c) CH <sub>4</sub> case, (f) NH <sub>3</sub> case.....	47
Fig. 2.23. NH <sub>3</sub> flame reaction path for FPF, $\phi = 1.0$ : rate of reaction in black; main contributors to heat released in the flame in gray. ....	48

Fig. 2.24. The heat release evolution with increasing $E$ for FPF at $\phi = 1.0$ : (a) repartition by subsets of reaction. C: carbon subset, C-N: carbon-nitrogen interaction subset, H <sub>2</sub> -O <sub>2</sub> : H <sub>2</sub> -O <sub>2</sub> subset, N: nitrogen subset. (b) C-N subset only. ....	50
Fig. 2.25. Effect of enhanced radical diffusion on the laminar burning velocity of 1D freely propagating flames (FPF) at $\phi = 1.0$ : (a) H <sub>2</sub> /air flame; (b) CH <sub>4</sub> /air flame; (c) NH <sub>3</sub> /air flame. $\square$ , $\circ$ , $\Delta$ represents OH, H and O, respectively. ....	54
Fig. 2.26. Effect of enhanced diffusion on the extinction stretch rate of counterflow premixed twin flames (PCF) for $\phi = 1.0$ : (a) NH <sub>3</sub> /air flame; (b) CH <sub>4</sub> /air flame. ....	56
Fig. 2.27. Rate of production of O, OH, H in counterflow premixed twin flames structure (PCF), for a stretch rate of 40 s <sup>-1</sup> : (a) ammonia/air flame and (b) methane/air flame. ....	56
Fig. 2.28. Effect of the enhanced diffusion of radicals on the laminar burning velocity of ammonia/methane flame (FPF). Mixture of $E = 0.30$ and $\phi = 1.0$ . $\square$ , $\circ$ , $\Delta$ represents OH, H and O, respectively. ....	57
Fig. 2.29. Rate of Production (RoP) of H, OH, and H in an ammonia/methane/air 1D freely propagation flame (FPF) of at $E = 0.3$ . ....	58
Fig. 2.30. NH <sub>3</sub> mole fraction profile for a 1D freely propagating flame (FPF). The crosses represent the value of NH <sub>3</sub> mole fraction when the temperature is 1% of the temperature rise in green, 0.1% of the temperature rise in red, or 0.01% of the temperature rise in blue. ....	60
Fig. 2.31. Validation of density definition of residence time for 1D freely propagating flame (FPF). ....	61
Fig. 2.32. Evolution of $\tau$ depending on the integrated distance: (a) FPF; (b) PCFF. ....	62
Fig. 2.33. Evolution of $\tau$ : $L = 5$ cm, grey; $L = 2$ cm, orange; $L = 1.5$ cm, blue; $L = 1$ cm, yellow. ....	62
Fig. 2.34. EINO of FPF and PCF depending on the residence time. FPF is in orange, other curves correspond to PCF results with various $L$ . Numerical error (flames too close to the burner) are kept in (a) and removed in (b). ....	64
Fig. 2.35. EINO for methane FPF (orange) and PCF with $L = 10$ mm (grey) and 100 mm (blue). ....	64
Fig. 2.36. EINO in freely propagating flame (FPF) for ammonia/methane mixtures at stoichiometry. ....	66
Fig. 2.37. EINO in PCF for ammonia/methane mixtures at stoichiometry. ....	66
Fig. 2.38. EINO of PCF in plain lines and symbols, and FPF in dashed lines, for fuel mixing ratio $E = 0, 0.3, \text{ and } 1$ . The dashed red rectangle corresponds to the region shown in Fig. 2.37. ....	67

Table 2.1. Summary of the simulation study in this chapter. ....	25
Table 2.2. Equivalence between $E$ and $X_{\text{NH}_3}$ .....	26
Table 2.3. Reaction path summary by main sub-paths for FPF. ....	32
Table 2.4. Chart of the detailed reactions with a large contribution to heat release in the $\text{CH}_4/\text{air}$ premixed flame (FPF). ....	46
Table 2.5. Chart of the detailed reactions with a large contribution to the heat released in $\text{NH}_3$ flame for FPF, $\phi = 1.0$ . ....	48
Table 2.6. Chart of the detailed reactions with a large contribution to the heat released in $\text{NH}_3/\text{CH}_4/\text{air}$ flame for FPF, $E = 0.2$ and $\phi = 1.0$ . ....	50
Table 2A. 1. Detailed reaction path with Okafor's mechanism. ....	71
Table 2A. 2. Reaction path with Tian's mechanism .....	76
Table 2A. 3. Reaction path with GRI-Mech 3.0. ....	80
Table 2A. 4. Reaction path with UCSD mechanism .....	83

## Chapter 3

Fig. 3.1. Representation of the counterflow burners: (a) premixed twin flames configuration; (b) non-premixed flame configuration. ....	91
Fig. 3.2. Flame direct picture, $E = 0.15$ : (a) twin premixed flame configuration; (b) non-premixed flame configuration. ....	92
Fig. 3.3. Schematics of PIV measurement experimental setup. ....	100
Fig. 3.4. Methane counterflow non-premixed flame in equal velocity (EV) conditions, $U = 210$ mm/s: Velocity mapping; Axial velocity profile from experiment and simulations with conditions (A), (B) and (C). ....	101
Fig. 3.5. Methane counterflow non-premixed flame in equal momentum boundary condition for $U_{\text{air}} = 210$ mm/s and $U_{\text{CH}_4} = 290$ mm/s. Velocity mapping; Axial velocity profile from experiment and simulations with conditions (A), (B) and (C). ....	102
Fig. 3.6. Relations between bulk velocity and the one measured using PIV at the burner outlet: (a) equal velocity (EV) condition; (b) and the equal momentum (EM) condition. ....	103
Fig. 3.7. Schematics of the observations on velocity profiles at the burner outlets: (a) equal velocity condition; (b) equal momentum condition. ....	104

Fig. 3.8. Axial velocity profile at the air outlet ( $\square$ ) and fuel outlet ( $\circ$ ): (a) equal velocity (EV) with $U = 210$ mm/s; (b) equal momentum (EM) conditions with $U_{air} = 210$ mm/s and $U_{CH_4} = 290$ mm/s.....	104
Fig. 3.9. Comparison of $g_z$ as a function of $g_n$ in the present study to previous experiments results by Kobayashi and Kitano [138].....	107
Fig. 3.10. Velocity profiles for methane/air counterflow premixed twin flames: (a) $\phi = 0.8$ and $U = 210.6$ cm/s; (b) $\phi = 1.2$ and $U = 96.9$ cm/s. $\times$ represent the PIV experimental results, the plain lines are the simulations results. ....	108
Fig. 3.11. Extinction stretch rate of ammonia/methane/air counterflow premixed twin flames for several $E$ and $\phi$ . ....	110
Fig. 3.12. Extinction stretch rate of ammonia/methane/air premixed twin flames with ammonia mixing ratio, $E$ : (a) $\phi = 0.7$ ; (b) $\phi = 0.9$ ; (c) $\phi = 1.2$ .....	111
Fig. 3.13. Experimental and numerical results of the extinction stretch rate at $\phi = 0.7$ with $E$ , for comparison with AramcoMech 2.0 and Okafor's mechanism after modification in this study. ....	113
Fig. 3.14. The sensitivity of extinction stretch rate for methane/air lean flame. ....	115
Fig. 3.15. Extinction stretch rate of ammonia counterflow non-premixed flames. Oxidizer: air enriched with $O_2$ , $N_2/O_2$ between 0.75/0.25 and 0.70/0.30.....	117
Fig. 3.16. Extinction stretch rate of methane/ammonia counterflow non-premixed flame. Oxidizer: air. ....	118
Fig. 3.17. Example of OH and NO-PLIF profiles for counterflow premixed twin flames at $E = 1$ and $\phi = 1.2$ . ....	119
Fig. 3.18. Schematics of the region of study for OH and NO-PLIF profiles.....	121
Fig. 3.19. Schematics of the PLIF experimental setup. ....	122
Fig. 3.20. Example of OH-PLIF image: $E = 0.15$ , $\phi = 0.8$ , $U = 196.1$ cm/s. The dashed line is the burner axis, the square represents the region between the burners. ....	123
Fig. 3.21. Fluorescence intensity evolution with laser beam energy: (a) OH; (b) NO. ....	124
Fig. 3.22. Boltzmann fraction for the $P_1(7.5)$ , $P_1(8.5)$ , $P_1(9.5)$ , $P_1(10.5)$ , $Q_{12}(22.5)$ , $P_2(22.5)$ transition lines.....	126
Fig. 3.23. Comparison of the experimental and numerical FWHM: (a) OH; (b) NO. ....	128
Fig. 3.24. Determination coefficient by equivalence ratio. ....	128

Fig. 3A. 1. Radial velocity as a function of $r$ , for various $z$ position, from PIV measurement on an ammonia/air counterflow premixed twin flames. ....	133
Fig. 3B.1. Schematics of the seeding system. ....	136
Fig. 3B.2. Axial velocity profile of a methane counterflow premixed twin flames at $\phi = 1.0$ and $g_z = 490 \text{ s}^{-1}$ : PIV experiment in blue crosses; fitting curves in black dashed line. ....	137
Fig. 3B.3. Comparison of experimental and numerical results for a methane/air counterflow premixed twin flames: (a) $\phi = 0.8$ and $U = 210.4 \text{ cm/s}$ (b) $\phi = 1.2$ and $U = 97.1 \text{ cm/s}$ . ....	138
Fig. 3B.4. Experimental velocity profile between the burner and the stagnation plane and region identified for modeling validation. ....	139
Fig. 3B.5. Simulated $z_{min}$ as a function of the experimental one. ....	140
Table 3.1. Extinction stretch rate obtained for the methane-air counterflow non-premixed flame in different configurations. Measurement using Eq. ( 3.5 ).....	97
Table 3.2. Geometric configurations selected in this study.....	99
Table 3.3. Relations $U_{z0} - U$ , $g_{r0} - U$ and $g_z - g_n$ , with $U$ in cm/s for ammonia/methane/air flames.....	107
Table 3.4. Lewis number of ammonia and methane mixtures calculated following work by Fairbanks and Wilke [47] and transport and thermal data from Okafor et al. [10].....	110
Table 3.5. Cases studied for OH and NO profiles. ....	120
Table 3C.1. Reaction path coefficients for lean methane premixed flames with Okafor's mechanism. ....	141
Table 3C.2. Reaction path coefficients for lean methane premixed flames with Tian's mechanism. ....	142
Table 3C.3. Reaction path coefficients comparison for Tian's and Okafor's mechanisms.....	142
Table 3D.1. Experimental OH and NO FWHM results. ....	143

# Chapter 4

Fig. 4.1. Representation of a non-premixed fuel-air jet flame structure at a fixed height above the burner. ....	146
Fig. 4.2. Flame shape evolution with the jet velocity. ....	147
Fig. 4.3. Ammonia/methane non-premixed jet flame in the present configuration: (a) attached flame before liftoff, (b) lifted flame after liftoff. ....	148
Fig. 4.4. Experimental setup. ....	150
Fig. 4.5. Lifted flame height, $H_L$ , and jet breakpoint height, $H_T$ , on a shadowgraph image. ....	152
Fig. 4.6. Burner end and thermocouple positions. ....	154
Fig. 4.7. Stabilization map as a function of the air coflow velocity and for different lip thickness, $\delta$ , from Takahashi and Schmolli [169]: circles $\delta = 0.2$ mm; squares $\delta = 1.2$ mm; diamonds $\delta = 2.4$ mm. ....	156
Fig. 4.8. Liftoff limit $(Q_d/Q_{ox})_{\text{lift}}$ and $(Q_d/Q_f)_{\text{lift}}$ as a function of the fuel jet Pelet number, $Pe_f$ , from the work by Marin [191]. ....	157
Fig. 4.9. Evolution of the stabilization regimes with $E$ for $U_{co} = 0.026$ m/s. ....	159
Fig. 4.10. Self-similar relation at liftoff from the work by Marin [191] for inert gases, and ammonia from the present study. The dashed line represents the laminar-to-turbulent transition in a pipe flow. ....	160
Fig. 4.11. Evolution of $C_L$ and $C_A$ with $E$ for $U_{co} = 0.026$ m/s. ....	161
Fig. 4.12. Evolution of the liftoff re-attachment with $U_{co}$ for $E = 0, 0.1, 0.15, 0.2$ and $0.25$ . The dashed line represents the laminar-to-turbulent transition in pipe flow. ....	162
Fig. 4.13. Hysteresis region for ammonia addition at $U_{co} = 0.2$ m/s. The dashed line indicates the laminar-to-turbulent transition in pipe flow ( $Re_J = 2300$ ). ....	163
Fig. 4.14. Evolution of the hysteresis region with $E$ for $U_{co} = 0.026, 0.1, 0.2, 0.3$ m/s. ....	164
Fig. 4.15. Variation of $H_T/D_i$ with $Re_J$ for $E = 0$ and $E = 0.2$ . The dashed line corresponds to the pipe flow transition at $Re_J = 2300$ . ....	167
Fig. 4.16. Evolution of $H_T/D_i$ and $H_L/D_i$ with $E$ and $Re_J$ for $U_{co} = 0.026$ m/s. ....	167
Fig. 4.17. Schematics of flame re-attachment. ....	168
Fig. 4.18. Evolution of $H_T/D_i$ for $U_{co} = 0.026$ m/s and $0.2$ m/s with $Re_J$ . Subscripts 1 and 2 correspond to the change in the decreasing slope observed for $U_{co} = 0.026$ m/s and $U_{co} = 0.2$ m/s, respectively. ....	169

Fig. 4.19. Evolution of lift height with $Re_J$ for $U_{co} = 0.026$ m/s, 0.1 m/s and 0.2 m/s: (a) $E = 0$ ; (b) $E = 0.1$ ; (c) $E = 0.20$ and (d) $E = 0.25$ .....	170
Fig. 4.20. Schematics of the re-attachment behaviors A and B and the re-attachment drop (RD). .....	172
Fig. 4.21. Behavior B from shadowgraph images: (a) $Re_J = 1067$ ; (b) $Re_J = 2339$ ; (c) $Re_J = 2657$ . ....	173
Fig. 4.22. Schematic diagram of the direct re-attachment A ( $H_L < H_{Tc}$ ). ....	174
Fig. 4.23. Schematic diagram of the re-attachment B after lifted flame height increases ( $H_L > H_{Tc}$ ). ....	175
Fig. 4.24. Definition of $H_a$ and $R_a$ from CH* chemiluminescence image. Original image on the left, deconvoluted one on the right. The red contour represents the threshold value for detection.....	177
Fig. 4.25. Evolution of $H_a$ and $R_a$ with $Re_J$ : (a) $E = 0$ ; (b) $E = 0.1$ ; (c) $E = 0.2$ ; (d) $E = 0.3$ . ....	180
Fig. 4.26. Evolution of flame tip position with the momentum ratio, $MR$ , and the ammonia mixing ratio, $E$ : (a) $R_a$ ; (b) $H_a$ . ....	181
Fig. 4.27. Variation of $R_a$ and $H_a$ relatively to methane flame case with ammonia mixing ratio, $E$ .....	182
Fig. 4.28. Schematic diagram of the change in flame positioning explaining the shift observed in the flame extremum position. ....	183
Fig. 4.29. Evolution of flame position ( $R_a$ , $H_a$ ) for jet velocity up to lift and $E = 0$ (squares), $E = 0.1$ (diamonds), $E = 0.2$ (triangles), $E = 0.3$ (circles). The positions just before liftoff are colored in black.....	184
Fig. 4.30. Burner lip temperature, $T_{lip}$ , and conductive heat flux to the burner, $Q$ , for methane flame. Plain line represents $T_{lip}$ results from Lamige work [117], plain squares represent $T_{lip}$ in the present study and empty squares represent $Q$ in the present study. ....	185
Fig. 4.31. Evolution of $T_{lip}$ (plain symbol) and $Q$ (empty symbol) with $Re_\delta$ for $E = 0$ (squares), $E = 0.1$ (diamonds), $E = 0.2$ (triangles) and $E = 0.3$ circles. Regimes Ia and b, II and III obtained for methane flames are represented with dashed lines.....	186
Fig. 4.32. Burner lip temperature, $T_{lip}$ , with $Re_\delta$ for $E = 0$ (squares), $E = 0.1$ (diamonds), $E = 0.2$ (triangles), $E = 0.3$ (circles). The dashed line represents the transition between regimes Ia and Ib. ....	187
Fig. 4.33. Variation of flame adiabatic temperature and burner lip temperature with $E$ . ....	188
Fig. 4.34. The relative importance of $d_a$ on $T_{lip}$ depending on the aerodynamic regime: (a) regime I; (b) regimes II and III for $E = 0$ (blue squares), $E = 0.1$ (orange diamonds), $E = 0.2$ (grey triangles) and $E = 0.3$ (yellow circles).....	189

Fig. 4.35. Variation of $T_{lip}$ (full symbol) and $d_a$ (empty symbol) with $Re_f$ : blue squares, $E = 0$ ; orange diamonds, $E = 0.1$ ; grey triangles, $E = 0.2$ ; yellow circles, $E = 0.3$ .....	189
Fig. 4.36. Normalized temperature contours in the 4 different regimes. The red dashed line represents the maximum temperature position for $z = 2$ mm and $E = 0$ , the blue dashed line represents the edges of the contour at 25% for $z = 2$ and 8 mm and $E = 0$ .....	191
Fig. 4A.1. Representation of steps 7 and 8. Dark squares represent pixel values under 45% threshold for Step 7, 40% threshold for Step 8. ....	196
Fig. 4B.1. Photo of a complete flame crossing.....	197
Table 4.1. Coefficients for the self-similar relation $(Q_d/Q_f)_{lif} = (\delta \cdot Pe_f^2 + \lambda \cdot Pe_f - \psi \cdot \Delta Pe_{ox} + \kappa) \cdot K_{df}$ from the work by Marin [191]. ....	157
Table 4.2. Evolution of the critical air coflow velocity $U_{co,c}$ for various $E$ . ....	165
Table 4.3. Thermal and diffusion properties of ammonia/methane mixtures at 298 K and 1 atm. ....	166
Table 4.4. Observations on lifted flame evolution within the hysteresis region.....	176
Table 4.5. Evolution of $Z_{st}$ and $S_{L0}$ with ammonia mixing ratio, $E$ . ....	181
Table 4A. 1. Acquisition parameters. ....	195



# Chapter 1

## Introduction

### 1. Background

#### 1.1. The role of combustion in our societies

##### 1.1.1. Energy consumption growth, fossil fuel depletion and global warming.

Since the beginning of industrialization, the development of human societies has been increasingly relying on the exploitation of fossil fuel resources for energy production. Around 80% of our global energy production today is still relying on fossil fuels [1] as presented in Fig. 1.1. In the meantime, even though the current state of the global fossil fuel reserves and how long they can last is still subject to debate [2], there is a consensus on their finite amount. Moreover, the extensive use of fossil fuels has led to a tremendous amount of CO<sub>2</sub> production, which combined with other human activities (other emissions but also deforestation), led to the situation of global warming as we know it today.

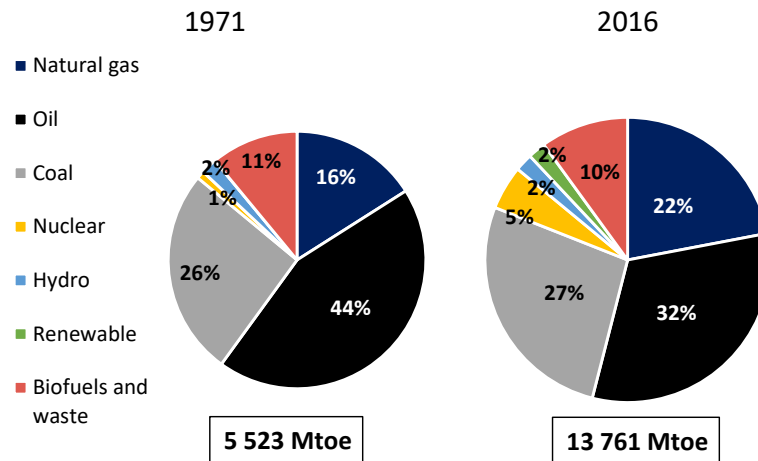


Fig. 1.1. Shares of total primary energy supply (TPES) in 1971 and 2016; from IEA [1].

The unsustainability of this situation is a social and political concern and a challenge for scientific communities: carbon storage [3,4], carbon emission mitigation [5], fossil fuels alternatives [6,7], energy mix [8,9], social and geopolitical consequences of global warming [10,11] or global warming prevention policies [12] became a vital subject of research.

Global energy demand has been rising since the eighteenth century. This increase, initially fostered by the development of the industry in Europe and North America, was later supported by the more widespread access to electricity among the population in these regions. The generalization of mechanization in the industry and the large-scale deployment of new technologies kept supporting this increase. More recently, with the expansion of access to these technologies to a growing number of consumers in different regions of the Earth, the global energy consumption exploded as presented in Fig. 1.2.

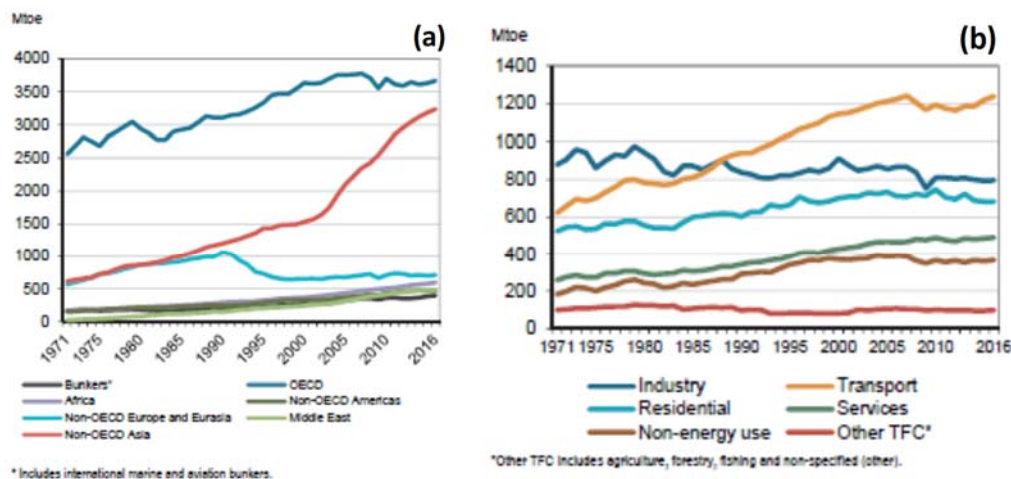


Fig. 1.2. (a) World total final consumption (TFC) by region; (b) Energy consumption per sector in OECD countries between 1971 and 2016; from IEA [1].

The energy consumption repartition on the globe is unequal. The increase in demand is principally supported by the consumption of OECD countries (Europe, Turkey, Israel, Japan, Australia, United States, Canada, Mexico and Chile) and Asian non-OECD countries (mainly China and India), with a sharp increase observed since the 2000s. The energy consumption of Middle Eastern, South American and African countries presents a quick rise, approaching the consumption from non-OECD Europe and Eurasia countries. But it remains yet minor compared to that of the OECD and Asian non-OECD countries.

Energy consumption by sector also differs depending on the regions considered. In the OECD countries, the industry is a significant pole of consumption, even if on the decline. Transportation became the first energy-consuming sector since the 1990s, followed by the industry and the residential use of energy (heating, electricity). On a global scale, the industry remains nonetheless the first energy-consuming sector, followed by the transportation sector and the residential utilization.

Whereas our global consumption of energy resources is fast (it has been multiplied by 2.25 in less than 30 years [1]), oil, gas and coal are produced from the degradation of organic material which lasts thousands of years. The smaller the reserves of fossil fuels become, the more expensive these resources are and the harder it is to predict their availability. Indeed, resources exploitations that were not economically viable in the past, and thus not accounted, might become profitable with the increase in the price of the resource. An exact date of the complete depletion of fossil fuel reserves might be complicated to assess, but most of the studies give 50 years of exploitation for oil and gas and around 100 years for coal [2]. These durations are questionable and might seem short but are nothing compared to the effects of global warming which are related to the use of these fossil fuels.

The greenhouse effect and global warming are not new concepts. The greenhouse effect theory was discussed in the nineteenth century. This effect explains that greenhouse gases in the Earth atmosphere, absorbing and emitting in the thermal infra-red, are responsible for warming up the temperature of the surface of the Earth (compared with a planet where those gases are absent). Thanks to the greenhouse effect, the surface of the Earth is liveable, with a mean temperature close to 15 °C. In 1896, Arrhenius identified CO<sub>2</sub> as a greenhouse gas (GHG) and showed that the concentration of CO<sub>2</sub> in the earth's atmosphere and its variations, were responsible for the variation of temperature of the Earth's surface [13].

However, global warming triggered by human activity was not considered seriously before the 1960s – 1970s. Its widespread recognition in scientific communities and by the population, the economic and political spheres was more gradual. Global warming affects both the environment and the populations. Temperature changes in the atmosphere and the oceans are affecting wildlife and ecosystems [14]. Large precipitations causing floods, as well as drought and extreme heatwaves in some regions are becoming more common and will occur more frequently as the global temperature keeps increasing [15]. This will impact our societies on various levels, with new issues appearing in food production [11] as well as health [10]. The sea-level rise is also another issue which will affect many cities. Those climate changes are, in turn, causing population migration, which might affect local economics and create geopolitical tensions.

One first step in human-driven global warming prevention was taken in Kyoto, with the ratification of the Kyoto Protocol in 1997. More recently, with the 2015 Paris Agreement, 196 states agreed to

actively reduce their greenhouse gas emissions to limit the global temperature rise below 2C above the pre-industrial level. These global policies are triggering local initiatives for emission mitigations, as each signing country pledged to follow a roadmap with specific targets for global warming mitigation. Those incentives are also fostering research activities in the energy field, especially research on low-carbon alternatives, research on energy efficiency improvement, renewable energy, power storage, etc. [16]

### *1.1.2. Energy production in the world*

Energy resources can be divided into two categories: fossil and non-fossil. From Fig. 1.1, it can be observed that most of the energy production is based on fossil fuels. These fossil fuels are primarily oil, coal and natural gas. Energy production from these resources is based on combustion and is a source of greenhouse gases (GHG) emissions.

Non-fossil resources are including nuclear energy, biofuels and waste as well as other renewable energies such as hydro-energy, solar, or wind energy. These alternatives to fossil fuels present attractive characteristics for global warming mitigation as they generate lower or no carbon emissions. They remain nonetheless challenging as briefly explained in the following.

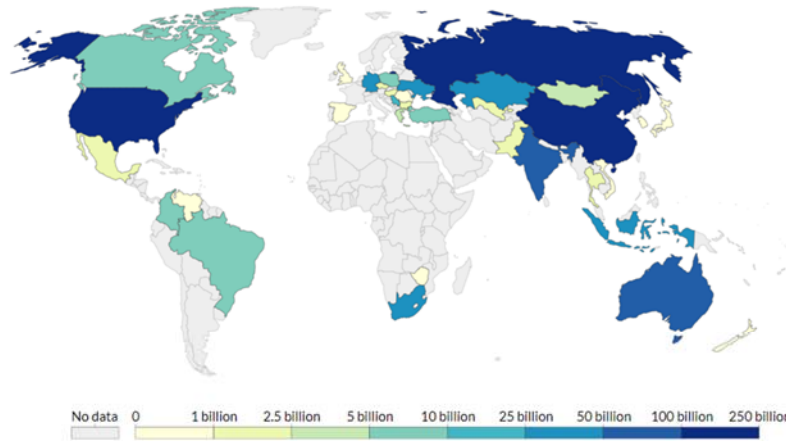
Nuclear energy is a carbon-free, stable source of energy. However, the management and the safety of nuclear plants and nuclear waste management are obvious issues with no definitive solutions. Biofuels or waste valorization are seducing alternatives as they are renewable (from the degradation of plants or waste). Even though their combustion tends to lower emissions, their consumption generates GHG. Moreover, the diversity of their composition is challenging for large-scale utilization. Their production from plants, might compete with food production and have a dramatic social and environmental impact. Hydro-energy has been used for centuries and holds an important part in the energy mix of some countries. For example, the hydro-energy accounts for up to 90% of Norway's energy mix. However, the viability of this resource depends on countries, with large disparities between the northern and southern regions. Solar and wind energy are promising resources, as they might be exploited anywhere in theory. Their efficiency, however, varies a lot depending on exploitation areas. Some regions offer low sunlight or short sunlight durations depending on seasons in the case of solar energy. For wind energy, there are restrictions to some regions where winds are frequent, but not too intense for wind

turbines. Even though they account for a marginal part of the global energy production, with 2% of the global energy TPES in 2016, their share has been growing swiftly since the 2000s especially for solar. They are already an important part of the energy mix for some countries, where policies have facilitated their development. It is the case in Europe where wind energy represents more than 10% of the electricity production in Spain, Germany and the UK [17], and solar energy more than 5% in Italy and Germany; but also in Japan where almost 5% of the domestic electricity production is from solar energy. The main challenge for solar and wind energy remains their intermittency and storage [18].

Renewable energy also possesses the advantage of allowing for local production of energy, limiting its importation and the resulting dependence on supplier countries. Indeed, most of the fossil energy resources of the globe are shared between less than 10 countries as presented in Fig. 1.3. Coal production is dominated by China (for more than 40%); Oil production is shared for more than 50% between Russia, the USA, Saudi Arabia and the OECD countries; Natural gas by Qatar, Iran, Russia and the USA for around 50% [1].

### Coal Proved Reserves, 2015

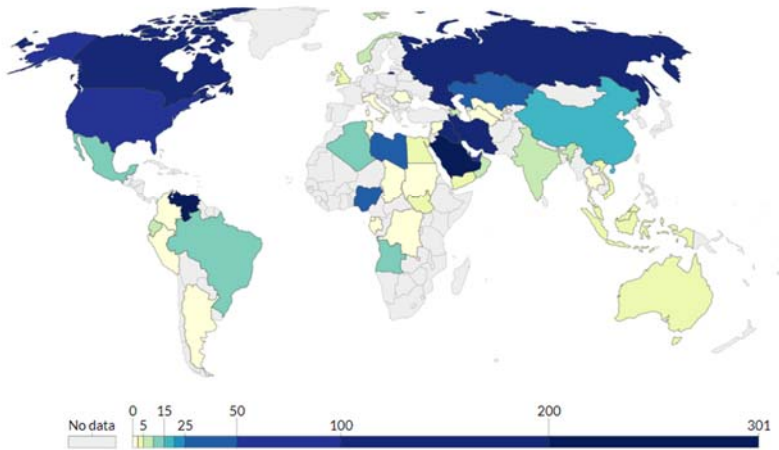
Total proved coal reserves, measured in tonnes. Proved reserves is generally taken to be those quantities that geological and engineering information indicates with reasonable certainty can be recovered in the future from known reservoirs under existing economic and operating conditions.



Source: BP Statistical Review

### Oil Proved Reserves, 2015

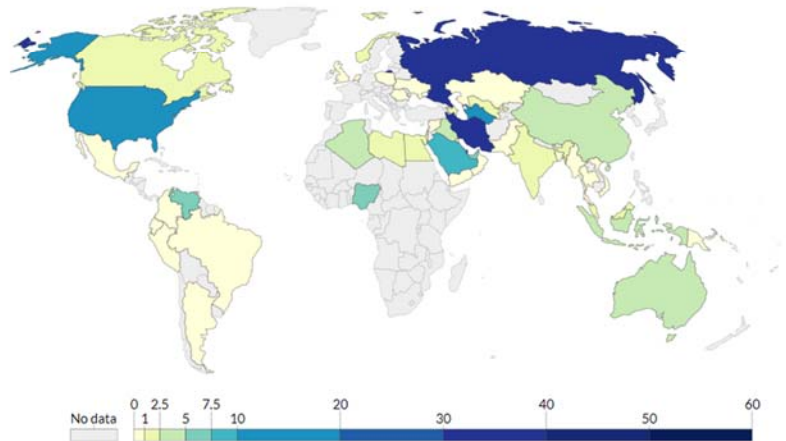
Total proved oil reserves, measured in thousand million barrels. Proved reserves is generally taken to be those quantities that geological and engineering information indicates with reasonable certainty can be recovered in the future from known reservoirs under existing economic and operating conditions.



Source: BP Statistical Review

### Natural Gas Proved Reserves, 2015

Total proved gas reserves, measured in trillion cubic metres. Proved reserves is generally taken to be those quantities that geological and engineering information indicates with reasonable certainty can be recovered in the future from known reservoirs under existing economic and operating conditions.



Source: BP Statistical Review



Fig. 1.3. Location of proved fossil fuel reserves in 2015 from ourworldindata.org [19].

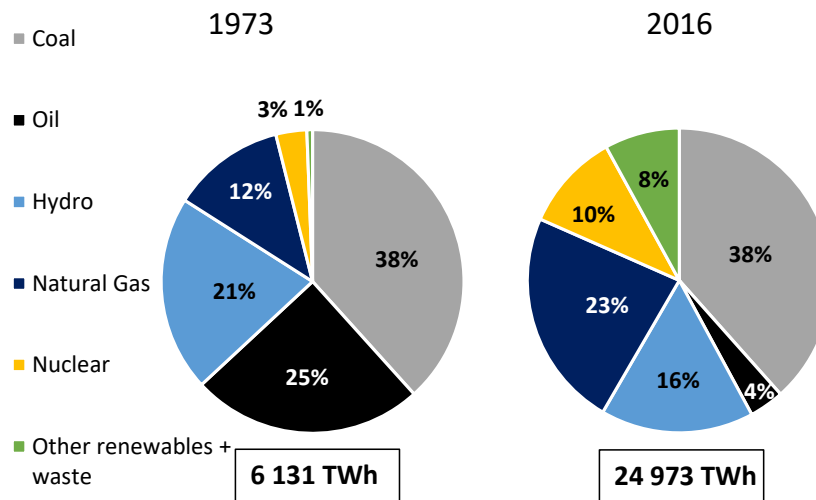


Fig. 1.4. Share of electricity production by type of energy resource; from IEA [17].

Renewable energy is still a minor part of our energy production as introduced in Fig. 1.4. The transition to an all-renewable energy model of society is not achievable in the short term, whereas the environmental emergency is already affecting the living conditions of some communities. To achieve the targets established in the Kyoto and Paris agreements, the transition to a realistic low carbon society model is to be favored. It requires a larger deployment of renewable energy in the coming decades, with adapted technologies of storage and transport, as well as the improvement of the current combustion systems for emission mitigation, combined with carbon capture and storage systems. The use of alternative fuels, such as ammonia, readily usable in existing combustion systems, allowing immediate reduction of our GHG emissions should be investigated.

## 1.2. The green ammonia model and ammonia direct combustion

### 1.2.1. Production process and distribution of ammonia

Ammonia has been employed extensively in the agricultural industry for over 100 years. Ammonia-based fertilizers use is widespread and supports the food supply for an ever-increasing global population. Most of the ammonia is currently produced by the Haber-Bosch process. It was developed at the beginning of the twentieth century by Fritz Haber and Carl Bosch. The process converts hydrogen ( $H_2$ ) and nitrogen ( $N_2$ ) to ammonia ( $NH_3$ ) in high-pressure reactors, with several layers of catalysts constituted of iron oxides with other minor elements such as Ca, Al, K, or Si. Most of the hydrogen used in this process is currently obtained from methane ( $CH_4$ ). Separation of carbon and hydrogen atoms is achieved by steam reforming at high-pressure and high-temperature with a nickel catalyst. The nitrogen

(N<sub>2</sub>) necessary for the Haber-Bosch process is obtained from the air cryogenic separation process. The industrial process is described in Fig. 1.5.

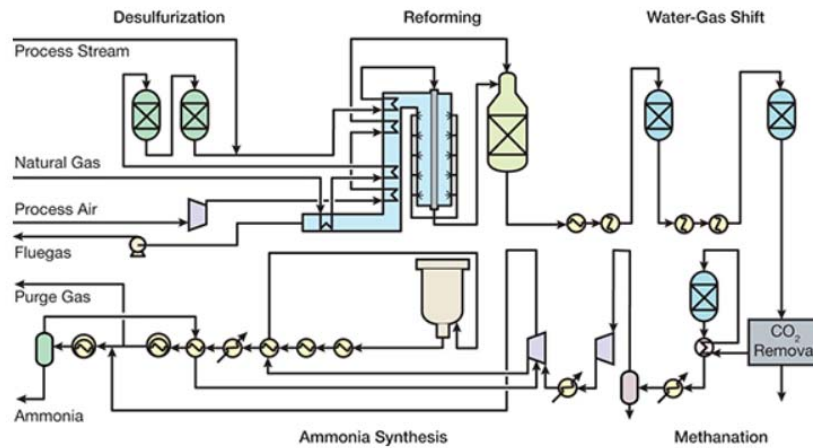


Fig. 1.5. Ammonia production plant design from CEP magazine [20].

Production of ammonia was estimated to contribute to up to 1% of the global GHG emission in 2010 [21,22]. To mitigate those emissions, CO<sub>2</sub> capture from the steam reforming process in ammonia plants can be examined [23,24]. Other production methods are also investigated to reduce the environmental impact of ammonia production. Most of them involve the use of the Haber-Bosch process, with hydrogen produced from water electrolysis, with electricity supplied from diverse resources [22,24–27]: biomass and waste, nuclear energy, hydro-energy, or other renewables such as wind and solar energy. Costs and efficiency of such plants exhibit promising perspectives of development [28,29]. With the growing interest in the use of ammonia as an energy carrier, new methods for ammonia clean production have been reported. Catalyst-free plasma-based processes [30], as well as Samarium-Water Ammonia Production (SWAP) [31], give encouraging costs and efficiency results.

Thanks to its extensive use as a fertilizer, ammonia distribution network (transportation and storage) is broad and well-controlled. Ammonia transportation has been handled for decades, transported by train, boat, or truck. Pipelines also exist in some countries and storage infrastructures are widespread all over the globe. Ammonia is stored in conditions close to that of propane. Indeed, liquid ammonia is obtained at -33 °C at atmospheric pressure or 9.9 atm at 25 °C. The required infrastructures are thus affordable and the maintenance costs reasonable.

Ammonia is a toxic gas. It is also corrosive and dangerous to the health and the environment if not handled with care. It is a colorless gas with a pungent characteristic smell, even at low concentrations level for which its inhalation is not dangerous for health. Ammonia density is lighter than air which leads to prompt dispersion of the gas in case of an accident. Its auto-ignition temperature is high (650 °C), with explosivity range in 16% - 25% in volume in the air. The safety management system for handling ammonia and the related regulations are well established in many countries. The levels of ammonia concentration representing a danger for the health are presented in Table 1.1 and Table 1.2

Table 1.1. Ammonia exposure level and its danger by Valera-Medina et al. [32]

Ammonia concentration in the air	Observations
From 20 - 50 ppm	Detectable smell
From de 50 – 100 ppm	No permanent effect on health, even for a long time exposure
From de 400 – 700 ppm	Eyes, ears, nose and throat irritation. No permanent effect on short-time exposure. Danger for long exposure.
From de 2000 – 3000 ppm	Danger. Less than half an hour of exposure is lethal.
From de 5000 – 10000 ppm	edema, suffocation

Table 1.2. AEGL classification for ammonia exposure depending on the level of concentration and duration of exposure from the NIH [33].

Acute Exposure Guideline Levels	10 min	30 min	4h	8h
AEGL 1: No problem	30 ppm	30ppm	30ppm	30ppm
AEGL 2: Medium irritation (eyes and throat, coughing)	220 ppm	160ppm	110ppm	110pm
AEGL 3: Lethal	1600ppm	1100ppm	550ppm	390ppm

### 1.2.2. Green ammonia: a clean vector of energy

Ammonia can be produced from renewable resources, as introduced in the previous section. When the electricity is not absorbable by the grid, the surplus of electricity can be employed to produce H<sub>2</sub> by water electrolysis and then NH<sub>3</sub> by Haber-Bosh process or directly for NH<sub>3</sub> production, using specific fuel-cells. The NH<sub>3</sub> produced is then stored or transported close to the consumer. It can later be converted back to H<sub>2</sub> and used for electricity production using fuel-cells or in carbon-free combustion systems

such as gas-turbine or engines. Ammonia can also be directly exploited without any conversion as a fuel for combustion. This conversion scheme represented in Fig. 1.6, using ammonia as a clean vector of energy, is also referred to as the green-ammonia model for society [34,35].

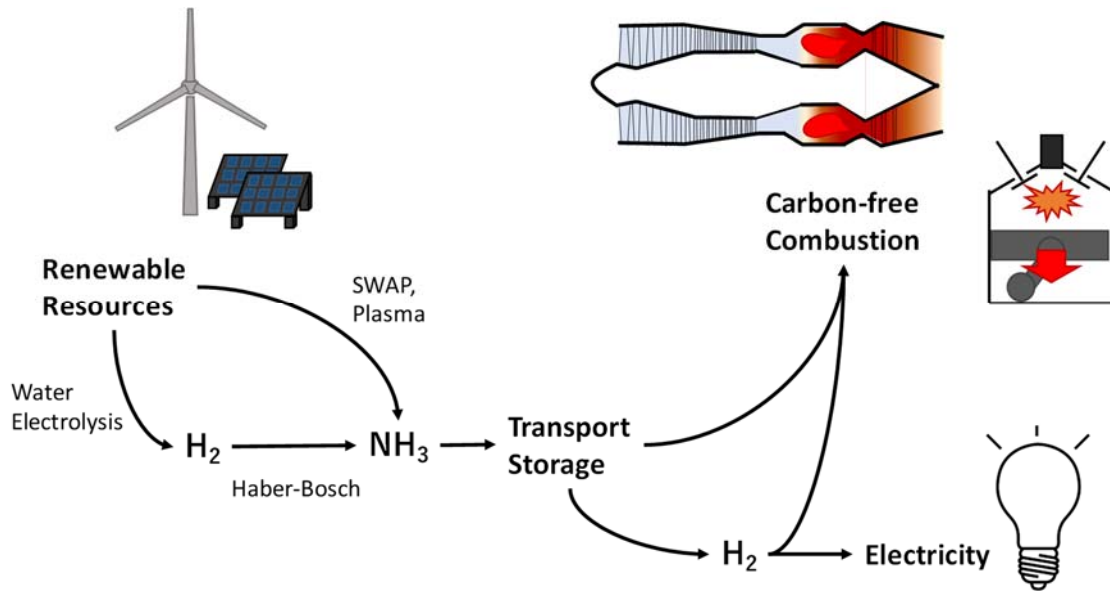


Fig. 1.6. Green ammonia society model.

Renewable resources still represent a minor share of the TPES (2016: 4% including hydro energy, 14% including biofuels and waste), but their broad deployment is on-going. The use of solar panels, for example, have been rising since the 2000s, especially in Europe and China [17,36]. With their development, their cost has also been decreasing. Even if 100% green-ammonia is still not possible today, a soft transition from our hydrocarbon model to a greener model is possible due to the multiple ways to produce ammonia: from brown-ammonia (hydrocarbon-based) to blue-ammonia (biomass combined with  $CO_2$  capture) toward green-ammonia.

The commercial viability of such a model has been discussed as well as its environmental benefit [22,26,28,32,35,37–39]. The development of the production of ammonia at a lower cost, as well as the development of its use as an energy medium, also provides new perspectives for isolated regions. The energy supply of those places which now relies on importations of hydrocarbons might be produced locally in the future by the mean of renewable resources as the technologies price down. The development of the production of ammonia from renewable resources might also ease the local

production of ammonia as a fertilizer in regions that currently rely on importation. This would lead to greater autonomy in these regions for food production.

### 1.2.3. Ammonia as a fuel

Ammonia production was primarily driven by fertilizer production in the past. The recent outbreaks in the use of ammonia as a clean energy carrier also triggered the study of its use as a fuel. However, the use of ammonia as a fuel is not recent and was considered during World War II. In 1940, Belgium, facing penury due to the war, developed hybrid engines coal gas/ammonia for buses to ensure public transportation [40]. Ammonia was later utilized as a fuel in the 1960s in a joint research program between NASA and the Air Force. The rocket engine was powered by anhydrous ammonia and liquid oxygen. Ammonia/gasoline vehicles were later developed in the 2000s. However, the efficiency of those technologies remained low, restraining their development to small scale or prototype stages.



Fig. 1.7. X-15 Rocket powered aircraft; Picture from NASA website [41].

The renew in the study of ammonia as a fuel, since the 2000s, comes from the fact that ammonia is carbon-free fuel. With environmental targets and regulations on carbon emission stricter, the research for carbon-free alternatives has been growing. The combustion of hydrogen, ammonia, or their mixture with hydrocarbons is now examined for carbon emissions reduction.

A comparison of ammonia, hydrogen and methane (as a reference for natural gas) fuel characteristics and combustion characteristics in the air is presented in Table 1.3. It can be observed from the two first lines of this table that ammonia is a convenient fuel for transport and storage as mentioned earlier. And

though being a toxic and corrosive gas, ammonia storage is well handled, whereas hydrogen storage is still challenging [42].

Table 1.3. Characteristics of ammonia, methane and hydrogen fuels [43].

	Ammonia NH <sub>3</sub>	Methane CH <sub>4</sub>	Hydrogen H <sub>2</sub>
Boiling Temperature (at 1 atm) [°C]	-33.4	-161	-253
Condensation pressure (at 25 °C) [atm]	9.90	N/A	N/A
Lower heating value, LHV [MJ/kg]	18.6	50	120
Flammability limit [equivalence ratio $\phi$ ]	0.63 – 1.4	0.5 – 1.7	0.1 – 7.1
Adiabatic flame temperature [°C]	1800	1950	2110
Maximum laminar burning velocity [m/s] ( $\phi$ close to 1)	0.07	0.37	2.91
Minimum auto-ignition temperature [°C]	650	630	520

However, ammonia has a low burning intensity when compared to methane or hydrogen: it has a small lower heating value (LHV), a narrow flammability range, a low adiabatic flame temperature, a low laminar burning velocity and a low auto-ignition temperature. Those characteristics, interesting when considering safety problems, are challenging when considering the design of combustion systems, especially regarding flame stabilization issues.

Moreover, though being carbon-free, the production of various pollutants may arise from the use of ammonia as a fuel. Nitrogen oxides, particularly nitric oxide, NO and nitrogen dioxide NO<sub>2</sub>, as well as nitrous oxide, N<sub>2</sub>O, should be carefully monitored. Indeed, NO and NO<sub>2</sub> are known to be an environmental threat, as they contribute to acid rains and ozone depletion. They are also considered to be harmful to health, especially respiratory functions. N<sub>2</sub>O is a GHG and its large production would further contribute to global warming. Production of nitrogen oxides is thus another challenge when considering ammonia combustion.

Overcome those two main challenges, stabilization issue and NO<sub>x</sub> emissions is a key for the large-scale deployment of ammonia as a carbon-free fuel in the industry.

In most of the combustion studies, ammonia is considered only as an additive for the study of fuel NO<sub>x</sub> formation-consumption process in conventional fuels [44–52], or selective catalytic reduction of NO<sub>x</sub>. Fewer studies concern ammonia as a fuel [53–62] or co-firing fuel [63–70]. Nonetheless, recent

advances [60,61,71] show that despite its low burning intensity, ammonia can be burnt in gas-turbines for power generation, showing promising perspectives.

Preheating, gas recirculation or co-firing represent different strategies to investigate for enhancement of the burning intensity. Co-firing, with hydrogen (fully carbon-free strategy) or various hydrocarbons (CO<sub>2</sub> mitigation), has attracted attention as it allows for the quick deployment of ammonia in existing structures. The issue of NO<sub>x</sub> emissions should be carefully investigated, but it was shown that it can be partially handled by the careful design of burners and selective catalytic systems for the burnt gases [61,72]. The study of ammonia as fuel is thus of interest for developing new efficient and reliable designs, answering to the different challenges observed for ammonia combustion in industrial burners.

Furthermore, ammonia co-firing being of practical interest in the short-term CO<sub>2</sub> emission mitigation strategies in the industry, their study is necessary. These studies should cover a broad range of combustion aspects going from general combustion characteristics, such as ignition delay time or laminar burning velocity, as well as flame structure, flame chemistry or formation paths of pollutants and more practical aspects such as flame stabilization.

## 2. Previous studies on ammonia/methane combustion

The present study focuses on the hydrocarbon-ammonia co-firing strategy, as a means for CO<sub>2</sub> mitigation. Before further developing the objective of this work in Section 3, the present achievements in the research on ammonia hydrocarbon blends combustion are reviewed in the present section. More specifically and in relation to the two main challenges associated with ammonia combustion which are stabilization and emissions as developed in Section 1.2.3, three main axes are developed here: ammonia/methane blend chemistry, experimental determination of ammonia blend fuels combustion characteristics and ammonia blend fuels stabilization. Indeed, fundamental knowledge of chemistry is necessary for understanding how NO is formed in a flame. Fundamental flames characteristics such as the laminar burning velocity or the ignition delay time are also essential for the design of combustion applications. Besides, they represent a way, through comparisons of numerical simulations and experiments to confront and validate existing chemistry. Finally, the stabilization issue being a major concern for ammonia flame, considering ammonia blend fuel flame stabilization is crucial.

### 2.1. Study on the ammonia and ammonia/methane flames chemistry

The issue of NO emissions, and more generally NO<sub>x</sub>, have been the subject of several studies in combustion to determine how they are produced. One of the approaches consists in looking at the detailed chemistry of the flame to identify the reactions responsible for NO production. Hydrocarbons being widely used in industrial applications, nitro-methane chemistry has been intensively investigated in the literature. The review study of Miller and Bowman [44] details the nitrogen reactions at stake in combustion processes. This work focuses on hydrocarbon combustion and how nitrogen species interact with hydrocarbons. NO formation is well described with a developed section for each mechanism of formation: thermal, prompt, or fuel. Since then, a large number of studies have been performed to develop a more comprehensive knowledge of the nitrogen chemistry in combustion. Aiming primarily at NO<sub>x</sub> emission reduction from conventional fuel combustion, most of these studies deal with the interactions between the carbon and nitrogen species during combustion. Tremendous effort has been done to update this chemistry, the related reaction constants as well as the thermochemistry of the

associated species. These studies include the experimental and ab-initio determination of reaction constants, but also the comparison of experimental results and simulations with updated reactions sets. Though not being exhaustive, some contributions, because of their interest in the scope of the present study, should be cited.

Successive studies by the department of chemical engineering of the technical university of Denmark [47–49,54,69,73–76] have been investigating the nitrogen chemistry since the 2000s. These works are fundamental studies on some subsets of reactions, updates and development of a mechanism for ammonia/methane oxy-fuel combustion. In addition, experimental validations on a large set of species profile in a well-controlled environment were performed. Work on high-pressure ammonia oxidation and NO<sub>x</sub> formation in methane flame were also considered. Tian's mechanism [69], developed by the group on these studies, was validated in those conditions but tended to underpredict the reactivity of ammonia/methane mixtures in different configurations [63,77]. A recent update of the review by Miller and Bowman was subsequently proposed by Glaborg et al. [78]. Formation mechanisms of NO, including thermal, prompt, N<sub>2</sub>O and N<sub>2</sub>H, HCN, HNCO and ammonia oxidation routes are examined, as well as the SNCR reduction and reburning route are detailed, providing a solid ground for the discussion proposed in the present study.

Extensive work from the combustion physics group of Lund University [50,57,79–84] has been performed for the development of the detailed kinetics for combustion. High-quality diagnostics studies on nitrogen radicals (NH, NH<sub>2</sub>) and NO distributions in ammonia-air and ammonia-doped methane flames allowed for the development of the nitrogen chemistry, with subsequent mechanisms developed.

Work by Lamoureux et al. [52] provided a detailed experimental study for methane flames doped with NO and NH<sub>3</sub>, combined with reaction path analysis and sensitivity analysis for those flames. Experimental profiles were including main reactant and product species, essential radicals, O, H, OH, CH<sub>3</sub>, CH<sub>2</sub> and several nitrogen species including NO, NH<sub>3</sub>, HCN. Experiments were performed under low pressure (similarly to work by Tian et al. [69]) and ammonia and NO were introduced in trace quantities, in the scope of the mitigation of NO<sub>x</sub> emissions in the case of biomass applications. A comparison of the experimental results with simulations using different available mechanisms in the literature showed general agreements except for HCN. Discussion on this discrepancy based on the difference in the HCN production routes (NO reburning and NH<sub>3</sub> oxidation) was done and suggests

further study is necessary. The importance of the  $\text{CH}_i$  radicals was also highlighted and disparities with modeling observed.

Other experimental works aiming at the validation/improvement of nitrogen subset in kinetics were proposed by various groups. Texas A&M University [85,86] observed the ignition for nitromethane and ammonia in a broad range of pressure and temperature, with a significant contribution to mechanisms improvement. Groups from Tohoku University produced a broad range of experimental results, from laminar burning velocity in an atmospheric and high-pressure environment and various fuel mixtures ( $\text{CH}_4/\text{H}_2/\text{NH}_3$ ), ignition characteristics in microflow reactor and proposed a detailed and reduced mechanism for ammonia/methane flames [62–65,77,87–89] and discussion on kinetics available in the literature.

In a more extensive approach, for a broader range of hydrocarbons, the NUI Galway and its partners [80,90–95] work on the development of a reliable kinetics, thermal and transport data for combustion of hydrocarbons, including nitrogen combustion chemistry. Similar efforts have been provided by the University of California San Diego combustion group [96,97] with mechanisms updates for hydrocarbons combustion and by the CRECK modeling group of Politecnico de Milano [98].

However, the development of those kinetics models and the mechanisms of the formation of NO proposed in these studies were essentially based on the investigation of hydrocarbons with nitrogen compounds only added as a trace. In the context of the development of ammonia/methane cofiring application, with ammonia added in large amounts, those models remain to be confirmed. Thus, the formation mechanisms of NO should be carefully investigated as well as and specificities of those flames from the viewpoint of the chemistry.

## 2.2. Experimental studies of ammonia/methane flame characteristics

The study of flames fundamental characteristics is of particular interest for the development of combustion systems. Hydrocarbon fuels, and particularly methane, have been extensively studied in the past. Though the properties and characteristics of those flames are well mastered, the mixture of these fuels with other fuels or diluents remains merely investigated. The study of flames characteristics also allows for the validation of the detailed kinetics used for the modelization of complex combustion environments. The main features of the chemistry of hydrocarbon fuels with the introduction of nitrogen

compounds are globally understood. Nonetheless, the quantitative prediction of the combustion process requires validation of those mechanisms on a large range of flame characteristics and conditions.

In the case of methane/ammonia mixtures, the number of studies of flame fundamental characteristics remains scarce. Most of them concern a limited range of mixing ratios and specific flame configuration. Studies for ammonia and its blends under high-temperature or high-pressure conditions are particularly scarce [64,76,86–89,99,100]. Disparities in the flame characteristics selected can also be observed. Most of the efforts focused on the laminar burning velocity of those flames. Laminar burning velocity, reflecting the propagation properties of flame, is of importance for the good understanding of flame and particularly when considering stabilization issues for example. As a fundamental in combustion, laminar burning velocity and its adequate experimental observation, as well as its comparison with kinetics, have been the subject of several studies and is well mastered in the community. Experimental observation of this flame parameter for ammonia and its blends has been performed by several groups, using spherically propagating flame in a closed vessel [53,63–65,87,88,100] or heat-flux burner [101]. Though several issues specifically related to the use of ammonia have been suggested, such as buoyancy or closed vessel wall interaction with gaseous ammonia, the agreement between the experimental results observed is good overall, but discrepancy with the prediction of this characteristic by different mechanisms is often large as presented on the Fig. 8 of a work by Okafor et al. [63], requiring further work on the kinetics.

Other flame characteristics have attracted less attention though being of fundamental interest for prediction improvement. Work on ignition delay time, essential for the validation of chemistries, have been performed by Mathieu and Petersen [86] under high-pressure condition, between 1 and 30 atm, for ammonia flames, but the studies on this parameter remain scarce. Extinction stretch rate is of use when considering flame-flow interaction. Local flame extinction in highly turbulent flow observed in furnaces is a critical issue as it affects flame stability, combustion efficiency and emissions. The good prediction of this phenomenon is essential to develop efficient applications. However, the discrepancy between the mechanisms was observed to be larger for the extinction stretch rate than for the laminar burning velocity, showing that mechanisms that give close estimates of laminar burning velocity, tend to diverge in their estimates of extinction stretch rate [43]. From simulations results, it could be seen that flame temperature, close to extinction, might decrease between 100 K and 200 K, depending on flame cases, compared with the flame temperature considered in the freely propagating case. The flame thickness and flame structure

are also affected. Thus, the predominance of the reactions at stakes changes due to these variations, revealing some differences in the kinetic scheme. This parameter should thus be accordingly carefully investigated.

Species distributions across the flame front are also of particular interest for mechanism validation. Indeed, comparison of these experimental profiles in well-controlled burners with their predictions is a critical tool to validate the reaction sets associated with the formation of this specific species, as well as allows for the identification of lack in the chemistry or improvement to bring. Those experimental measurements are though challenging and require a careful investigation of the flame environment, including velocity flow field considerations as well as temperature measurements in most of the cases. Some of them being intrusive, their impact in the experimentally observed result can undermine proper comparison with numerical prediction. Laser-induced fluorescence (LIF) was used in several works on nitromethane flames and combined with temperature measurements allowed for a quantitative comparison of the experimental and numerical profiles of OH, NH, NH<sub>2</sub> and NO [50,57,82,102] as already mentioned in the previous section. Sampling, directly in the flame or in the exhausted gases, is another method for species prediction validation. This strategy, adopted in a large number of study allows for the observation of an extensive set of species, including C<sub>2</sub> hydrocarbons, CH<sub>i</sub> species, H, OH or O radicals, as well as some nitrogen and CN species, depending on the sampling analysis strategy adopted [49,50,52,54,62,76,77,103–105].

However, these studies focus on a limited range of conditions, including low-pressure conditions, small concentrations of ammonia, or other nitrogen compounds. Thus, species profile for methane/ammonia flame at atmospheric pressure and over a wide range of mixing conditions is required. Determination of other fundamental flame characteristics, such as the extinction stretch rate is also required. Validation of the existing kinetics on those criteria should also be considered for improving the quantitative prediction of these quantities. Such validation indeed contributes to better prediction of the flame behavior in a more complex environment, such as furnaces or gas-turbines using 3D modeling with the validated kinetics, leading to the development of better design or strategies for industrial applications.

## 2.3. Ammonia flame stabilization

Due to its low laminar burning velocity, ammonia flame stabilization is a major concern in the development of ammonia fuel combustion systems. The early study by Verkamp et al. [106] compared the stability limit of ammonia to methane flames, showing substantially higher energy for ignition, narrower flammability range, larger quenching distances, as well as a smaller flame stabilization domain.

Nonetheless, several strategies can be applied to tackle the ammonia flame stabilization issues. Among them are pre-heating, fuel-mixing, or oxygen enrichment, all of them aiming at a higher flame laminar burning velocity to ease flame stabilization. Such strategies have been investigated through the measurement of the laminar burning velocity variations in those conditions [53,63–65,87,88,100].

Premixed ammonia flame stabilization on a flame holder was also investigated by Rohde et al [107]. In their study, the flame could not be stabilized on the flame holder without the addition of oxygen injection through the holder. The gradual addition of oxygen led to a greater blowoff limit and enhanced stabilization, showing the interest of the oxygen-enrichment strategy.

The use of swirl burners is known to improve flame stabilization [108] as this configuration introduces recirculation structures and promote fast-mixing and is frequently considered in gas turbines design. Ammonia/air premixed swirling flames were investigated by Hayakawa et. al. [109]. In such configuration, the recirculation structures generated by the swirling flow driving the mixing of some of the burnt gases with the fresh ones were considered for explaining the flame stabilization [110]. The flame stabilization was consequently greatly influenced by the modification of injection angles or liner geometry as they change the swirling flow structure [43,61,109].

The adoption of both fuel mixing strategy and swirling burner were also investigated for ammonia/hydrogen mixtures [111–113], as well as ammonia/methane mixture [114–116]. Those demonstrations are encouraging, but the fundamentals of the ammonia stabilization process remain poorly investigated. Clarification of the stabilization process for ammonia flames, as well as the impacts of ammonia gradual introduction in blend fuel configurations, is thus necessary.

### 3. Objective and scope of the present study

The subject of the present study concerns the elucidation of fundamental combustion characteristics of ammonia blended fuels flames for the development and the optimization of gas turbine and industrial furnaces. The fuel mixture considered in this study is the methane/ammonia mixture. This choice corresponds to the need for CO<sub>2</sub> mitigation strategy applicable in the short-term and aims at the development of ammonia co-firing technologies, by the gradual introduction of ammonia in existing facilities working on natural gas [35].

When considering the expansion of the use of ammonia in industrial combustors, two main issues, mentioned in Section 1.2.3, are the flame stabilization, related to the low reactivity of ammonia, and the emissions of pollutants, particularly NO<sub>x</sub>, appearing in larger quantity due to the introduction of ammonia. The problematic can thus be re-written as follows:

- How to stabilize ammonia blend fuels' flames in industrial combustors.
- How to reduce NO<sub>x</sub> emissions while keeping combustion efficiency.

To answer these questions, the fundamental combustion characteristics of ammonia/methane blends need to be investigated. Knowledge of the chemistry of these blended fuels is necessary to understand how and in which conditions NO<sub>x</sub> are formed, to later quantify, monitor and mitigate those emissions. Flame stabilization and flame interaction with its environment (wall, flow) should also be discussed: what type of interactions exist between the flow and the flame, between the walls and the flame? How does this impact the flame stability and NO<sub>x</sub> emissions? How does the introduction of ammonia in a methane flame change those interactions?

To answer those questions, the present work was divided into the two main thematic focuses developed in the following. The research was performed under the co-supervision of two teams, using the facilities of the two laboratories in Tohoku University and INSA de Lyon involved in international collaboration. The study of the fundamental characteristics of the flame and flame chemistry was performed in the Institute of Fluid Sciences (Tohoku University), whereas stabilization issues were investigated in the CETHIL (INSA de Lyon). This choice has been driven by the previous activities of each laboratory using the expertise of the Japanese partner lab on flame properties investigation and

ammonia combustion, and the one of the French partner laboratory regarding stabilization issues and interaction of the flame with its environment. The specific objectives of the two main thematic focuses investigated are detailed in Sections 3.1 and 3.2.

### 3.1. Fundamental study on ammonia/methane flame chemistry.

The first objective is to understand the chemistry of the ammonia/methane flames and the NO<sub>x</sub> production/consumption in a basic flame configuration, the counterflow flame configuration. Chemistry validation on 1D flames, ammonia/methane flame structure and stretch effect on NO<sub>x</sub> production/consumption processes were reviewed. These studies are prerequisites for the later use of chemistries in 3D simulations and the improvement of concrete applications.

Knowledge of ammonia/methane chemistry can be found in the literature. However, those studies have been performed in a specific range of conditions. Most of these studies were limited to the addition of a small amount of ammonia, or limited stoichiometry or pressure range. There is thus a need for the consolidation of the existing knowledge of chemistry for a wider range of usage. The present study is limited to atmospheric case, but a wide range of fuel mixing ratio and stoichiometry was considered.

Detailed reaction mechanisms should be investigated on simple flame cases, where the uncertainties in the modeling can be limited to the knowledge of chemistry. The NO<sub>x</sub> production/consumption mechanisms should be studied and confirmed in this configuration before moving to a more complex environment. The configuration selected in this study is the counterflow flame configuration. This configuration is well documented in the literature and allows for the experimental observation of flames which are close to 1D and can be modeled relatively easily.

A preliminary and general study on the ammonia/methane flame chemistry has been performed. It aims at identifying the main reaction paths, the expected evolution of flame structure and NO<sub>x</sub> production with the large addition of ammonia to methane flame. This first analysis allows for the global understanding of the flame chemistry and provides key trends and general knowledge necessary for understanding the physics of phenomenon observed in concrete applications. The specificities of ammonia/methane flames are here highlighted.

This first analysis is followed by an evaluation of different detailed chemistries available in the literature. This second approach aims at providing a set of reliable experimental data and discriminating

mechanisms on their ability to reproduce them. The target is to contribute to the development of reliable kinetics which is necessary to industrials for quantitative simulations of complex combustion applications. The evaluation is based on the quantitative measurement of extinction stretch rate and its comparison with the simulated one using existing mechanisms; and the observation of the OH and NO profiles obtained from PLIF measurements.

### 3.2. Fundamental study on ammonia/methane flame stabilization

The stabilization phenomenon is crucial in all industrial applications. The present study aims at understanding the mechanisms at stakes and how they evolve when introducing ammonia compared with the well-studied case of methane flame. This was investigated using a non-premixed jet burner configuration.

In this simple configuration, it is possible to understand how the flame interacts with the burner and see the influence of thermal, chemical and aerodynamics parameters on flame position and stability. A detailed study of a pure methane flame on the same burner has been performed in the past by the same team [117–119] and used as a reference in the present work. The chemical parameter was specifically investigated, through the introduction of ammonia in the fuel jet.

The effects of the introduction of ammonia on the stabilization regimes were first investigated. For that purpose, the effects of ammonia addition on the liftoff and re-attachment limits of a non-premixed methane jet flame in an air coflow were observed. This study was further expanded to the study of the lifted flames within the hysteresis region, to explain the re-attachment limit evolution with ammonia addition. The coupled aerodynamics and chemical effect were shown to be dominant.

Then, the evolution of the interactions between an attached flame and the burner when adding ammonia up to liftoff was investigated. To do so, the evolution of the attached flame was scrutinized, observing the evolution of the flame position in the attached flame combustion regimes, as well as the flame and burner temperature evolution. The interactions occurring at the wake of the burner lip, and the changes brought by ammonia addition, could thus be highlighted.

## 4. Structure of the thesis

This thesis is constituted of 5 chapters, focusing each on the content introduced as follows:

Chapter 1 presents the background and objective of the present work. It includes a summary of the previous works in the present field and highlights how the present work integrates into this larger framework.

Chapter 2 focuses on the ammonia/methane flame chemistry. A general overview of the main reactions paths, flame structures, pollutant emissions, heat release, effects of radicals diffusion and NO<sub>x</sub> formation is done using 1D simulations with the premixed freely propagating model and the counterflow premixed and non-premixed flames models.

Chapter 3 corresponds to the experimental determination of fundamental flame properties in the counterflow flame burner configuration. The extinction stretch rate of both premixed and non-premixed flames was investigated, as well as the distribution of the OH and NO species in the case of the premixed twin flames, from PLIF measurements. The experimental results are then compared to simulation ones for the evaluation of four detailed kinetics selected from the literature.

Chapter 4 details the effect of the introduction of ammonia in a methane non-premixed jet flame in an air coflow. The evolution of the stabilization domain, particularly the liftoff and reattachment limits, was observed experimentally and introduced in this chapter. The evolution of the lifted flame within the hysteresis domain was subject to detailed attention, as well as the attached flame stabilization mechanisms evolution up to the transition to liftoff.

Finally, Chapter 5 concludes this thesis, summarizing the main results obtained in this work and the potential perspectives for further developments.

# Chapter 2

## Chemistry of ammonia/methane flames

### 1. Introduction

Combustion phenomenon corresponds to the combination of several mechanisms, including fluid dynamics, thermodynamics as well as chemistry or transport phenomena, all interacting with each other. Understanding these mechanisms and how they interact with each other is fundamental for the development of efficient applications. The chemistry of ammonia/methane flame is investigated in this chapter and has for objective to clarify the main features of the chemistry of those flames still merely investigated at present. The knowledge of chemistry is essential for understanding pollutant formation from the combustion process, but also the evolution of flame fundamental characteristics related to the reaction time, or the heat release in the flame. These can be associated with flame properties such as developed in Chapter 3 of this thesis, and later, on stabilization of the flame which can be related to the variation of those properties as will be further discussed in Chapter 4.

Nitro-methane chemistry has been intensively investigated in the literature since the review study of Miller and Bowman [44], as detailed in Chapter 1. The aim of this chapter, based on the work previously mentioned, is to provide information on the chemistry of ammonia/methane flames and highlight their specificities. Thus, the cases where ammonia is introduced in large quantities in the fuel mixture were examined, but a complete review of the nitrogen chemistry is not the purpose of this work.

The details of the ammonia/methane flames reaction path, flame structure, the heat released in the flame, and pollutant emissions are presented in Section 2 of this chapter, which gives a broad overview of the chemistry of those flames. Specificities of both ammonia and methane flame chemistries are included in this section before moving to their mixtures. The study of the premixed flame structure revealed some major differences in the ammonia and methane flames structures and reaction paths, particularly regarding the consumption of the essential H, OH and O radicals in the flame. This difference in the role of radicals was thus further investigated in Section 3, where the effect on flame properties of the back-diffusion of these radicals is examined for ammonia, methane, and their mixture as well as for the simple case of hydrogen which is used here as a reference for comparison. Finally, and

in complement to the general study on the flame chemistry, the case of the NO<sub>x</sub> emission being of particular interest when considering ammonia/methane combustion, it will be further detailed in Section 4. This later section introduces the relationship between NO production and residence time, introducing the emission index of NO (EINO) in the simulations for both freely propagating flames and counterflow flames.

To investigate the flame chemistry, simulations were performed using the Chemkin-Pro software, using 1D freely propagating flame modeling (FPF), as well as the counterflow flame modeling for both counterflow premixed twin flames (PCF) and counterflow non-premixed flames (NCF). A summary of the conditions investigated in this chapter is introduced in Table 2.1

Table 2.1. Summary of the simulation study in this chapter.

Subject investigated	Section	Freely propagating flame (FPF)	Premixed counterflow twin flames (PCF)	Non-premixed counterflow flame (NCF)
Reaction Path	2.1	O	X	X
Emissions characteristics	2.2	O	X	X
Flame structure	2.3	O	O	O
Heat release	2.4	O	X	X
Radical diffusion role	3	O	O	X
NO emission (EINO)	4	O	O	X

The reaction path analysis and the pollutant emissions were analyzed using the freely propagating flame model (FPF). The flame structure was observed for freely propagating and counterflow flames (FPF, PCF and NCF), to understand the specificities of each configuration. Heat release in the flame was then studied for FPF and related to the flame structure studied. The role of radical back-diffusion was then associated with the observations on the premixed flame structure and was thus performed for FPF and PCF only. Finally, the NO emission index study was limited to premixed flames (FPF and Premixed CFF). All simulations are done for stoichiometric mixtures under atmospheric pressure.

The quantity of ammonia used in the mixture is evaluated based on lower heat value of both fuels and follows the definition given in [43,63,88] and written as follows:

$$E = \frac{X_{\text{NH}_3} \text{LHV}_{\text{NH}_3}}{X_{\text{NH}_3} \text{LHV}_{\text{NH}_3} + X_{\text{CH}_4} \text{LHV}_{\text{CH}_4}} \quad (2.1)$$

where  $X_i$ , is the mole fraction of the specie  $i$ , and  $LHV_i$ , the lower heat value of the specie  $i$ . The choice of this definition of mixing rather than the simple mole fraction mixing ratio is arbitrary and related to conventions used for gas turbine applications. The equivalence between the two quantities is recalled in Table 2.2.

Table 2.2. Equivalence between  $E$  and  $X_{\text{NH}_3}$ 

$E$	$X_{\text{NH}_3}$
0	0
0.05	0.118
0.10	0.220
0.15	0.309
0.20	0.388
0.30	0.520
0.60	0.792
1	1

## 2. Ammonia/methane flame chemistry

### 2.1. Reaction path analysis

In the present study, the ammonia/methane flame chemistry was first investigated using the 1D freely propagating flame (FPF) model from the Chemkin-Pro package [120]. Flame simulation results are used to investigate the oxidation reaction path occurring during the combustion for a gradually increasing ammonia mixing ratio,  $E$ .

Effects of ammonia introduction on the reaction path, flame structure, and on the production of pollutants such as  $\text{NO}_x$ , but also  $\text{CO}_2$  and  $\text{CO}$  are investigated. The mechanism chosen for this study is Okafor's mechanism [63]. It includes 356 reactions and 59 species and has been validated on laminar burning velocity for ammonia/methane mixtures with a large content of ammonia. The evolution of the reaction path with ammonia addition being the purpose of this preliminary study, the detailed comparison of the reaction path using different mechanisms was not presented in this section. However, similar observations were done for Tian's mechanism [121], GRI-Mech 3.0 mechanism [122], and the UCSD mechanism [96]. The differences between the different mechanisms occur in the minor sub-paths, and the ammonia oxidation path depending on the presence or absence of the  $\text{N}_2\text{H}_2$  specie in the chemical mechanism. In the case of Tian's and Okafor's mechanisms,  $\text{N}_2\text{H}_2$  being included, the oxidation path includes the  $\text{N}_2\text{H}_2 \rightarrow \text{N}_2\text{H} \rightarrow \text{N}_2$  branch. For the UCSD mechanism and GRI-Mech 3.0, the  $\text{NH}_3$  oxidation is slightly different, with  $\text{N}_2\text{H}$  obtained directly from  $\text{NH} + \text{NH}_2$ , and reduced directly as in

the work by Miller and Bowmann [44]. The interactions between methane and ammonia oxidation branches are essentially similar for all the mechanisms investigated. However, depending on the presence of  $\text{H}_2\text{CN}$  in the mechanism and the reaction associated, these interactions involved the  $\text{CH}_i$  and  $\text{HCCO}$  in slightly different ratio. These interactions are fully described later in the present section. The full tables are available in Appendix 2A for each of these mechanisms and comparison between mechanism is not further detailed in the present section.

Both methane and ammonia oxidation pathways have been already produced elsewhere in the literature [44] but are introduced in Figs. 2.1 and 2.2 as support for the discussion. The reaction paths were obtained by calculation of the integral reaction rate of each of the 356 reactions in the mechanism on the complete calculation domain (from preheating to burn gas region). This integration aims at distinguishing the reactions which are predominant in the whole flame region. The slowest reaction (production of less than 1% of any reactant) are excluded from the analysis. The other reactions were gathered in sub-paths to create the reaction path. Full data are available in tables in Appendix 2A, and the summarized results, for the main sub-paths, are shown in Table 2.3. The reaction path coefficients in Tables 2.3a, b and c are the ones normalized by the ammonia and methane first oxidation step, to be able to compare directly each sub-path with each other. The coefficients in the tables thus correspond to the  $I_j$  values defined as in Eq. ( 2.2 ), with  $j$  corresponding to each subpath considered, and  $i$  to each reaction in the subpath  $j$ :

$$I_j = \frac{\sum_{i \in j} k_i}{\sum_{i \in \text{NH}_3 \rightarrow \text{NH}_2, \text{CH}_4 \rightarrow \text{CH}_3} k_i} \quad (2.2)$$

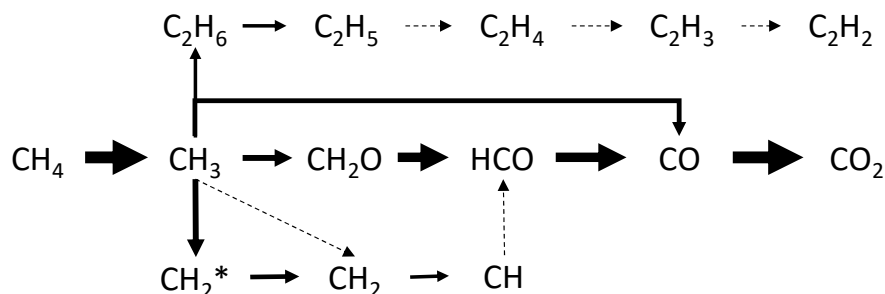


Fig. 2.1. Methane oxidation path for the stoichiometric condition at atmospheric pressure.

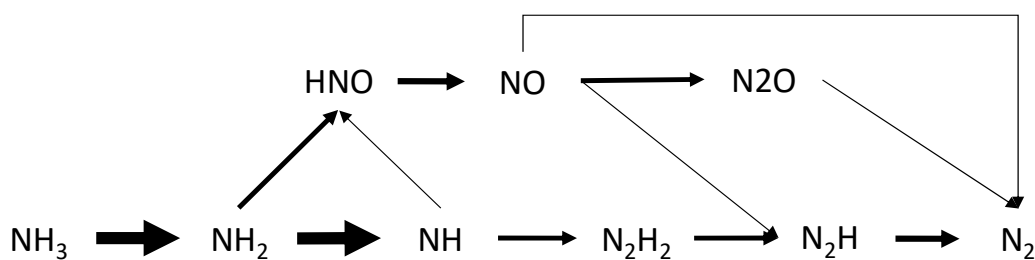


Fig. 2.2. Ammonia oxidation path for the stoichiometric condition at atmospheric pressure.

The analysis shows the two main oxidation paths of methane and ammonia remains essentially unchanged, as presented in Fig. 2.1 and Fig. 2.2. Interactions between those oxidations path and changes in the two oxidation paths are presented in Table 2.3 and detailed in the following.

- Methane oxidation branch

First, on the methane oxidation branch, presented in Table 2.3a, it can be observed that the first oxidation step  $\text{CH}_4 \Rightarrow \text{CH}_3$  remains the fastest path in the mechanism up to large values of  $E$ . Indeed, at  $E = 0.30$ , while the mole fraction of  $\text{NH}_3$  in fuel is slightly superior to the one of  $\text{CH}_4$ , this path remains the fastest one. The branching in  $\text{CH}_3$  also shows some changes, with reaction from  $\text{CH}_3$  to  $\text{CH}_2^*$  and  $\text{CH}_3\text{O}$  becoming relatively faster when the amount of ammonia is increasing in the fuel mixture.  $\text{CH}_2^*$  is then reacting with nitrogen species creating interactions with the  $\text{NH}_3$  oxidation branch, while  $\text{CH}_3\text{O}$  is reduced to  $\text{CH}_2\text{O}$ , at a speed which is comparable to the direct reaction  $\text{CH}_3 \Rightarrow \text{CH}_2\text{O}$ .

- Ammonia oxidation branch

Changes in the case of the  $\text{NH}_3$  oxidation path are more pronounced. In the case of small amounts of ammonia introduced in the fuel mixture ( $E < 0.05$ ), the mechanism slightly differs from pure ammonia case as in Fig. 2.2.  $\text{NH}_3$  is first reduced through  $\text{NH}_2$  and  $\text{NH}$ , as in Fig. 2.2, but the  $\text{N}_2\text{H}_2$ -  $\text{N}_2\text{H}$  sub-path is neglectable. Remaining  $\text{NH}_2$  radicals react with  $\text{O}$  radical to form  $\text{HNO}$  which is converted then in  $\text{NO}$ . Few  $\text{N}_2\text{H}_2$  is produced from  $\text{NH}$ , which is essentially either transformed in  $\text{N}$  and then  $\text{NO}$  or directly in  $\text{NO}$ .  $\text{NO}$  is then directly reduced to  $\text{N}_2$ , the  $\text{N}_2\text{O}$  branch being relatively slow. The ammonia oxidation branch for those conditions is represented in Fig. 2.3. These observations are consistent with all the previous studies with ammonia introduced as a trace in a methane flame [52] and the  $\text{NO}_x$  formation from  $\text{NH}_3$  oxidation as described in [44,78].

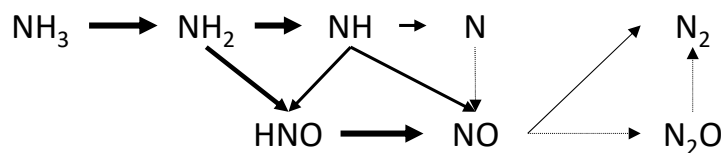


Fig. 2.3. Ammonia oxidation branch in the ammonia/methane reaction path for small  $E$ .

When the  $\text{NH}_3$  amount is increased in the mixture ( $E > 0.05$ ), the NH consumption branching switches from the NO and N-NO branch to the  $\text{N}_2\text{H}_2$  branch which represents an important production path of  $\text{N}_2$  in pure ammonia case [69]. This switch can be seen when looking at the NH consumption paths as described in Fig. 2.4. It can be observed that the  $\text{NH} \Rightarrow \text{NO}$  and  $\text{NH} \Rightarrow \text{NO}$  represent large consumption sub-paths for all the mixing cases. However, for  $E > 0.05$ , this share in consumption decreases as seen in Fig. 2.4b. Simultaneously to this change, the branches of  $\text{N}_2\text{O}$  formation and reduction to  $\text{N}_2$  becomes also faster.

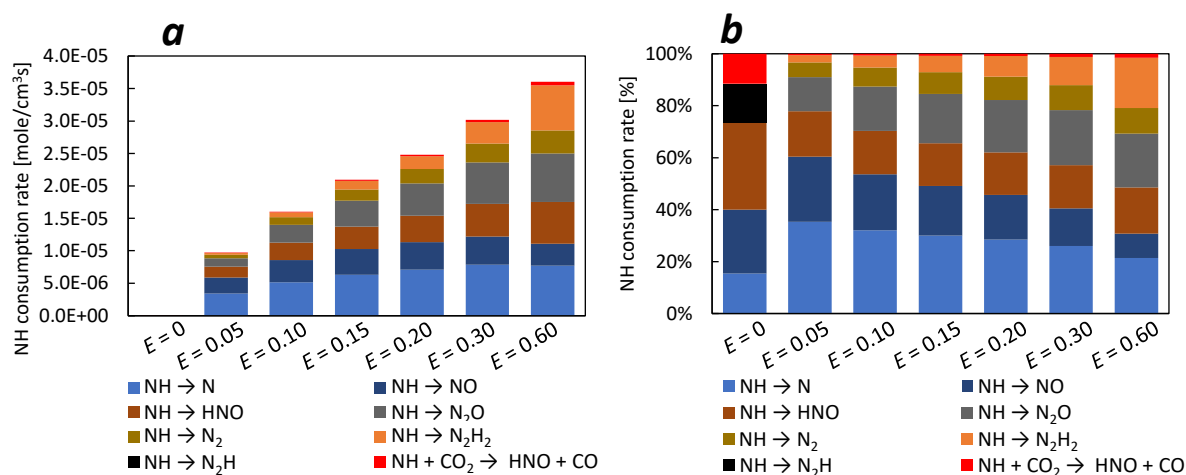


Fig. 2.4. Evolution of NH consumption rate with increasing  $E$  for FPF: (a) in terms of mole/cm<sup>3</sup>·s; (b) in terms of percent of total NH consumption.

NH is thus an essential radical for the ammonia/methane flame chemistry. It is consumed through several sub-path in the flame, and competition in its consumption leads to an evolution of the reaction path of the ammonia/methane flame. Major NH consumption routes presented in Fig. 2.4 are summarized here. First, it is consumed through N production, with reaction  $\text{NH} + (\text{H}, \text{OH}) = \text{N} + (\text{H}_2, \text{H}_2\text{O})$ ; but also for NO direct production through reaction  $\text{NH} + (\text{O}, \text{O}_2) = \text{NO} + (\text{H}, \text{OH})$ ; and HNO production, with reactions  $\text{NH} + (\text{OH}, \text{O}_2, \text{CO}_2) = \text{HNO} + (\text{H}, \text{O}, \text{CO})$ . As ammonia is introduced in the mixture, more OH will react with  $\text{NH}_3$  to give  $\text{NH}_2$  and then NH. The larger pool of NH and  $\text{NH}_2$  can

explain why the  $\text{NH} \Rightarrow \text{N}_2\text{H}_2$  sub-path becomes faster (through reaction  $\text{NH} + \text{NH}_2 = \text{N}_2\text{H}_2 + \text{H}$ ) and gradually competes for the  $\text{NH} \Rightarrow \text{N}$ ,  $\text{NO}$  branch. The  $\text{N}_2\text{H}_2$  production becomes then a major consumption path through reaction  $\text{NH} + \text{NH}_2 = \text{N}_2\text{H}_2 + \text{H}$ .  $\text{NH}$  also appears in  $\text{NO}$  reduction path through reactions  $\text{NO} + \text{NH} = \text{N}_2\text{O} + \text{H}$ , and  $\text{NO} + (\text{N}, \text{NH}, \text{NH}_2) = \text{N}_2 + (\text{O}, \text{OH}, \text{H}_2\text{O})$ .

The availability and distribution of the  $\text{NH}$  radical in the flame thus play an important role in the change observed in the reaction path. The detailed flame structure will be investigated in later Section 2.3, but the evolution of the distribution of  $\text{NH}$  for methane and ammonia/methane mixture represented in Fig. 2.5 to highlight the change observed in the reaction path and described here. Indeed, as ammonia is introduced, it can be observed that the  $\text{NH}$  production region gradually moves from a downstream production in the hot burnt gases to a production upstream of the reaction zone, as observed from the evolution of  $\text{NH}$  distribution in Fig. 2.5. Indeed, for methane flames, the hot burnt gas region is where  $\text{N}_2$  reacts to form  $\text{N}_2\text{O}$ ,  $\text{N}_2\text{H}$  or  $\text{N}$  later reacting to form  $\text{NH}$ . When introducing ammonia,  $\text{NH}$  is formed essentially from  $\text{NH}_2$ , by reaction with  $\text{O}$ ,  $\text{OH}$  and  $\text{H}$  radicals, explaining this change.

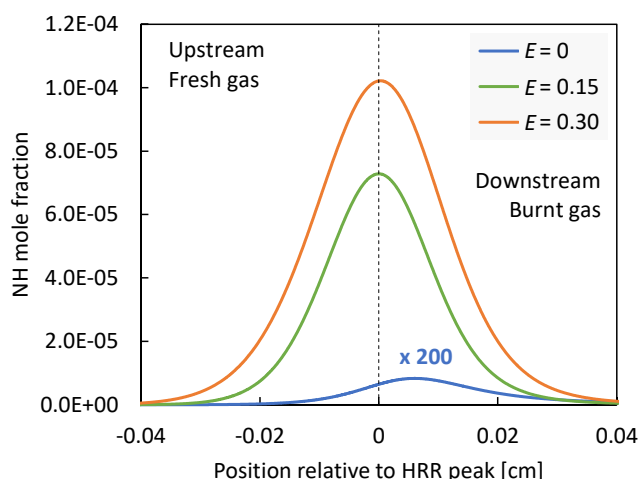


Fig. 2.5.  $\text{NH}$  distribution for  $E = 0, 0.15$  and  $0.30$  in relation with the reaction path evolution for FPF.

- C – N interactions

Interactions between carbon and nitrogen species in ammonia/methane flames are also of interest in the case of the use of blend fuels. Indeed, cyanide compounds,  $\text{CN}$ , resulting from these interactions are, for example, toxic for most of them and dangerous for both human health and the environment. The reactions leading to their formation and their interactions with the two fuels oxidation branch described in Figs. 2.1 and 2.2 are briefly introduced in the following.

The main interactions between the methane oxidation branch and the ammonia one are shown in Fig. 2.6. The carbon compound is essentially brought from the reactions of  $\text{CH}_i$  species. These species are minor species when considering the oxidation of methane but have been revealed to play a significant role when considering cyanide formation [52]. Another source of C for the interactions with nitrogen species is HCCO, produced from the  $\text{C}_2\text{H}_x$  branch of methane oxidation. In stoichiometric conditions, this path is neglectable but might become more important for rich flames or at higher pressure where the recombination of  $\text{CH}_3$  to  $\text{C}_2\text{H}_6$  is more pronounced [89]. The  $\text{CH}_i$  and HCCO react with the NO formed in the reacting and burnt gas regions to give cyanide compounds:  $\text{H}_2\text{CN}$  (amidogen methylene), HCN (hydrogen cyanide), HNCO (isocyanic acid), HCNO (fulminic acid).

The fastest interaction path involves the reaction of  $\text{CH}_2$  with NO to give HNCO, which is later reacting to form CO and NH. The second fastest reaction involves CH and NO reaction to give HCN, NCO, and then CO. Other slower interactions concern the conversion of HCCO in HCNO and HNCO by reaction with NO and the reaction of  $\text{CH}_3$  with N and NO radical to give  $\text{H}_2\text{CN}$  and later HCN.

On the overall, those interactions tend to consume the NO present in the flame and the burnt gases for the formation of intermediates C-N species, later consumed to give NH,  $\text{NH}_2$ , and  $\text{N}_2\text{O}$ . The carbon species involved are for most of them converted to CO, then reacting to form  $\text{CO}_2$ . Finally, even if traces of HCN and CN can be found in the burnt gases as observed in Fig. 2.7, they remain by far neglectable when compared with the  $\text{NO}_x$  emissions of such flames.

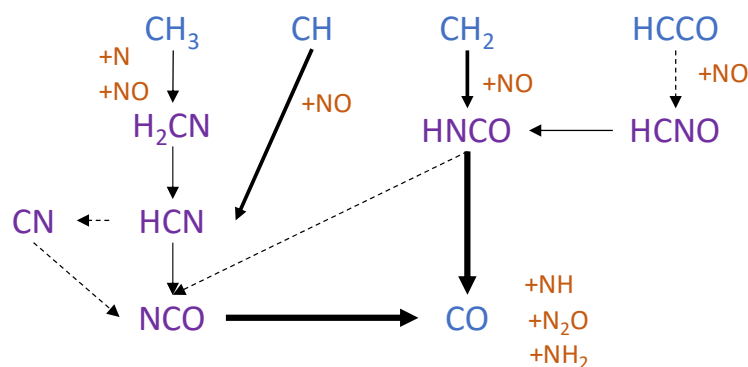


Fig. 2.6. Interactions between methane and ammonia oxidation path in ammonia/methane/air flame at  $E = 0.3$  and for FPF. C-N species are represented in purple while carbon species are represented in blue and nitrogen species in orange.

Table 2.3. Reaction path summary by main sub-paths for FPF.

## a) Methane oxidation path coefficients.

Sub-path $j$	$E = 0$	$E = 0.05$	$E = 0.10$	$E = 0.15$	$E = 0.20$	$E = 0.30$	$E = 0.60$
$\text{CH}_4 \Rightarrow \text{CH}_3$	1	0.8953	0.8010	0.7149	0.6373	0.5017	0.2157
$\text{CO} \Rightarrow \text{CO}_2$	0.7454	0.6672	0.6002	0.5381	0.4818	0.3843	0.1720
$\text{HCO} \Rightarrow \text{CO}$	0.4393	0.3966	0.3597	0.3255	0.2940	0.2376	0.1104
$\text{CH}_2\text{O} \Rightarrow \text{HCO}$	0.4400	0.3897	0.3487	0.3122	0.2798	0.2238	0.1044
$\text{CH}_3 \Rightarrow \text{CH}_2\text{O}$	0.2720	0.2329	0.2015	0.1739	0.1501	0.1111	0.0409
$\text{CH}_3 \Rightarrow \text{CH}_2^*$	0.2400	0.2184	0.1973	0.1773	0.1588	0.1257	0.0533
$\text{CH}_3 \Rightarrow \text{CO}$	0.1737	0.1478	0.1271	0.1091	0.0936	0.0683	0.0237
$\text{CH}_2^* \Rightarrow \text{CH}_2$	0.1182	0.1065	0.0952	0.0847	0.0750	0.0578	0.0223
$\text{CH}_2 \Rightarrow \text{CH}$	0.0874	0.0765	0.0672	0.0590	0.0515	0.0382	0.0124
$\text{CH}_3 \Rightarrow \text{CH}_3\text{O}$	0.0762	0.0669	0.0615	0.0571	0.0533	0.0469	0.0302
$\text{CH}_3\text{O} \Rightarrow \text{CH}_2\text{O}$	0.0674	0.0627	0.0596	0.0567	0.0540	0.0489	0.0328
$\text{C}_2\text{H}_6 \Rightarrow \text{C}_2\text{H}_5$	0.0617	0.0595	0.0540	0.0482	0.0426	0.0323	0.0108
$\text{CH}_3 \Rightarrow \text{C}_2\text{H}_6$	0.0608	0.0588	0.0535	0.0478	0.0423	0.0322	0.0108

## b) Ammonia oxidation path coefficients.

Sub-path $j$	$E = 0$	$E = 0.05$	$E = 0.10$	$E = 0.15$	$E = 0.20$	$E = 0.30$	$E = 0.60$
$\text{NH}_3 \Rightarrow \text{NH}_2$	0	0.1047	0.1990	0.2851	0.3627	0.4983	0.7843
$\text{NH}_2 \Rightarrow \text{NH}$	0	0.0598	0.1108	0.1574	0.1998	0.2742	0.4298
$\text{HNO} \Rightarrow \text{NO}$	0.0002	0.0508	0.0869	0.1157	0.1387	0.1730	0.2157
$\text{NH}_2 \Rightarrow \text{HNO}$	0	0.0386	0.0661	0.0871	0.1029	0.1237	0.1353
$\text{NO} \Rightarrow \text{NO}_2$	0.0002	0.0263	0.0318	0.0329	0.0321	0.0288	0.0183
$\text{NO}_2 \Rightarrow \text{NO}$	0.0002	0.0259	0.0313	0.0322	0.0314	0.0281	0.0176
$\text{NH} \Rightarrow \text{N}$	0.0001	0.0235	0.0378	0.0489	0.0578	0.0706	0.0871
$\text{NO} \Rightarrow \text{N}_2$	-0.0014	0.0189	0.0385	0.0552	0.0689	0.0892	0.1146
$\text{NH} \Rightarrow \text{NO}$	0.0001	0.0167	0.0254	0.0311	0.0349	0.0391	0.0385
$\text{NH} \Rightarrow \text{HNO}$	0.0002	0.0120	0.0204	0.0281	0.0351	0.0484	0.0791
$\text{N} \Rightarrow \text{NO}$	0.0013	0.0115	0.0154	0.0184	0.0210	0.0253	0.0336
$\text{NO} \Rightarrow \text{N}_2\text{O}$	-0.0001	0.0088	0.0200	0.0309	0.0409	0.0575	0.0847
$\text{N}_2\text{O} \Rightarrow \text{N}_2$	-0.0002	0.0085	0.0191	0.0292	0.0381	0.0524	0.0702
$\text{N}_2\text{H} \Rightarrow \text{N}_2$	-0.0004	0.0061	0.0166	0.0284	0.0409	0.0665	0.1385
$\text{NO} \Rightarrow \text{N}_2\text{H}$	-0.0001	0.0046	0.0115	0.0187	0.0256	0.0382	0.0624
$\text{NH} \Rightarrow \text{N}_2\text{H}_2$	0	0.0018	0.0055	0.0103	0.0160	0.0296	0.0789
$\text{N}_2\text{H}_2 \Rightarrow \text{N}_2\text{H}$	0	0.0018	0.0052	0.0099	0.0154	0.0284	0.0761

c) Main interactions path coefficients.

Sub-path $j$	$E = 0$	$E = 0.05$	$E = 0.10$	$E = 0.15$	$E = 0.20$	$E = 0.30$	$E = 0.60$
<b>NCO <math>\Rightarrow</math> CO</b>	0.0001	0.0066	0.0083	0.0088	0.0087	0.0075	0.0032
<b>HNCO <math>\Rightarrow</math> CO</b>	0	0.0057	0.0075	0.0083	0.0085	0.0079	0.0038
<b>CH<sub>2</sub> <math>\Rightarrow</math> HNCO</b>	0	0.0048	0.0063	0.0068	0.0068	0.0061	0.0027
<b>HCN <math>\Rightarrow</math> NCO</b>	0.0001	0.0043	0.0055	0.0059	0.0059	0.0053	0.0025
<b>CH<sub>3</sub> <math>\Rightarrow</math> H<sub>2</sub>CN</b>	0	0.0033	0.0044	0.0049	0.0052	0.0050	0.0031
<b>H<sub>2</sub>CN <math>\Rightarrow</math> HCN</b>	0	0.0033	0.0044	0.0049	0.0052	0.0050	0.0031
<b>CH <math>\Rightarrow</math> HCN</b>	0	0.0023	0.0028	0.0029	0.0027	0.0021	0.0006
<b>HCN <math>\Rightarrow</math> CN</b>	0	0.0019	0.0025	0.0028	0.0028	0.0027	0.0014
<b>CN <math>\Rightarrow</math> NCO</b>	0	0.0017	0.0022	0.0025	0.0025	0.0024	0.0013
<b>HCNO <math>\Rightarrow</math> HNCO</b>	0	0.0017	0.0023	0.0025	0.0026	0.0024	0.0010
<b>HNCO <math>\Rightarrow</math> NCO</b>	0	0.0013	0.0017	0.0018	0.0018	0.0016	0.0007
<b>HCCO <math>\Rightarrow</math> HCNO</b>	0	0.0012	0.0017	0.0020	0.0021	0.0021	0.0010
<b>CH<sub>3</sub> <math>\Rightarrow</math> HCN</b>	0	0.0012	0.0016	0.0019	0.0020	0.0021	0.0013

## 2.2. Emission characteristics

The evolution of the burnt gas emissions depending on the ammonia content is introduced in Fig. 2.7. The figure presents the amounts of CO, CO<sub>2</sub>, NO, NO<sub>2</sub>, N<sub>2</sub>O, NH<sub>3</sub>, CH<sub>4</sub>, H<sub>2</sub>, HCN and CN in the burnt gases, from the simulations using 1D freely propagating flame model (FPF). Values were taken in the hot burnt gas region, 9.9 cm downstream of the heat release peak. Those species are the primary pollutants obtained by the combustion of methane and ammonia.

From Figs. 2.7c and d, it can first be observed that unburnt NH<sub>3</sub> and CH<sub>4</sub> are by far neglectable when compared to CO, CO<sub>2</sub>, and NO<sub>x</sub> species. Similarly, HCN and CN remain sufficiently small to be neglected. Indeed, Fig. 2.7c shows that mixtures of  $E = 0.6$  present a larger amount of unburnt ammonia than  $E = 1$ , showing that interactions between the fuels affect the burning efficiency. The order of the fraction of unburnt ammonia is however of the order of a few ppbv. The peak of unburnt methane is observed in the  $E = 0.2$  region, then decreasing, but its order is however much smaller than unburnt ammonia and can be considered neglectable. From Fig. 2.7d, it can be observed that the HCN and CN species concentration are of the order of the ppt and peak at  $E = 0.2$  and  $E = 0.1$  respectively, the region of  $E$  for which interactions have been observed to be the more important in the reaction path analysis. They remain though neglectable, especially when compared to NO<sub>x</sub> or unburnt ammonia.

The evolution of the main product species is now described. A non-linear reduction in the amount of CO and CO<sub>2</sub> with  $E$  could be observed in Fig. 2.7a. They are still not halved for  $E = 0.3$ , corresponding to more than 50% ammonia in terms of mole fraction in the fuel mixture. CO<sub>2</sub> amount decreases slowly with  $E$ , and CO remains almost constant and up to  $E = 0.20$ . A larger decrease is then observed for larger  $E$ , between 0.2 and 0.3. NO amount first increases with  $E$  and then decrease between  $E = 0.3$  and  $E = 1$ . The same trend is observed for H<sub>2</sub> in the burnt gases, which is present in non-neglectable quantities. The NO<sub>2</sub> and N<sub>2</sub>O emission, presented in Fig. 2.7b also presents a non-linear trend: the NO<sub>2</sub> production peaks at  $E = 0.15$  before decreasing gradually and N<sub>2</sub>O slightly later between  $E = 0.2$  and  $E = 0.3$ .

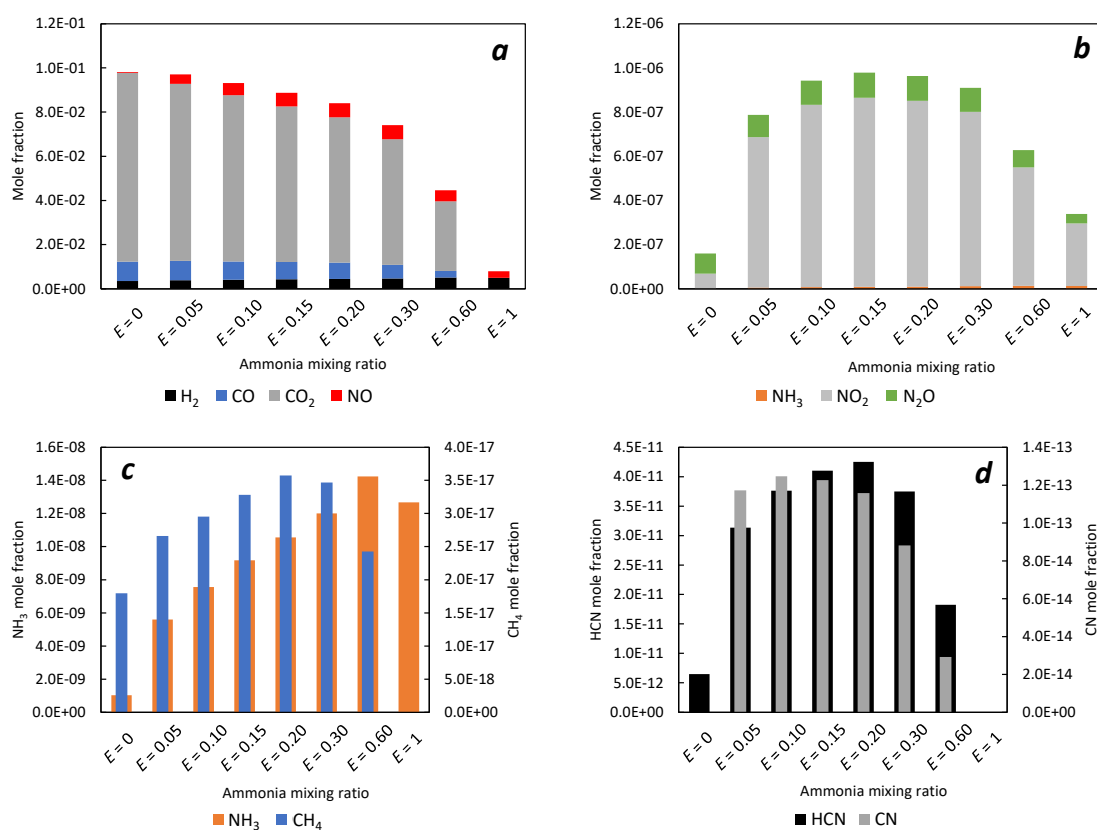


Fig. 2.7. Evolution burnt gas emissions for FPF with  $E$ : (a) H<sub>2</sub>, NO, CO<sub>2</sub> and CO; (b) N<sub>2</sub>O, NO<sub>2</sub>, and NH<sub>3</sub>; (c) NH<sub>3</sub> and CH<sub>4</sub>; (d) HCN and CN.

The trend observed in the NO emissions, peaking close to  $E = 0.30$ , is further analyzed by drawing parallels with the reaction path. For that purpose, Fig. 2.8 presents the details of formation and consumption rates for NO and the different routes are illustrated in Fig. 2.9. The gradual introduction of ammonia leads to larger production from the fuel-NO route, characterized by the greater rate of

production of NO from HNO, as observed in Fig. 2.8a. Both Figs. 2.8a and b also highlight this trend, with the  $\text{NO} \Rightarrow \text{HNO}$  contribution to NO reduction decreasing and the  $\text{NO} \Rightarrow \text{N}_2\text{O}$  and  $\text{NO} \Rightarrow \text{N}_2\text{H}$  reduction increasing. The peak in NO emission follows the peak observed in the formation rate. The increase is essentially due to the  $\text{HNO} \Rightarrow \text{NO}$  fuel route, which becomes larger with greater ammonia and thus NH and  $\text{NH}_2$  radicals. The decrease after  $E = 0.30$ , corresponds to the decrease in the  $\text{NH} \Rightarrow \text{NO}$  and  $\text{NO}_2 \Rightarrow \text{NO}$  production route, and a constant NO consumption rate as the increase in the  $\text{NO} \Rightarrow \text{N}_2\text{H}$  and  $\text{NO} \Rightarrow \text{N}_2\text{O}$  routes, promoted by greater  $\text{NH}_i$  concentration, compensate for the decrease in the  $\text{NO} \Rightarrow \text{NO}_2$  route and CN interaction route, leading to an overall decrease in NO emissions. The decrease in those two NO consumption routes can be associated with the greater competition for OH radical in the  $\text{NO} \Rightarrow \text{NO}_2$ , and  $\text{CH}_i$  radical in the CN interaction route. The first one might reasonably be attributed to the larger consumption of OH through the reaction  $\text{NH}_3 + \text{OH} = \text{NH}_2 + \text{H}_2\text{O}$ , while the second one is associated with the reduction of  $\text{CH}_4$  concentration in the fuel mixture.

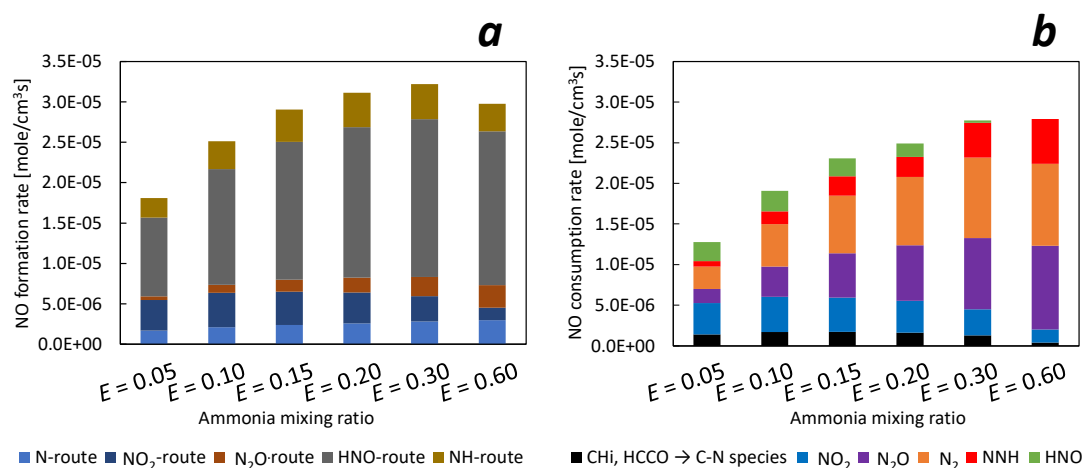


Fig. 2.8. Formation and consumption of NO for FPF with  $E$ : (a) NO formation routes; (b) NO consumption route.

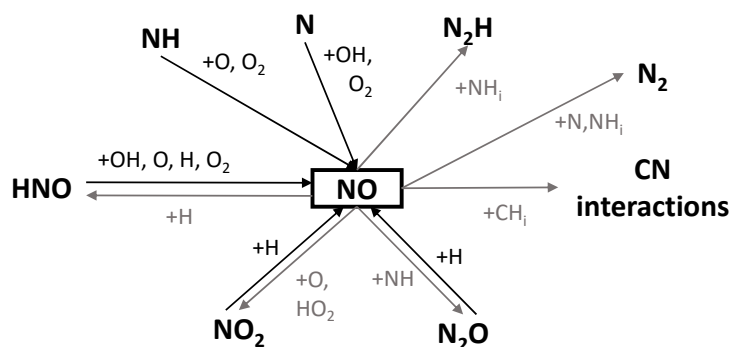


Fig. 2.9. Formation (black arrows) and consumption (grey arrows) path for NO.

## 2.3. Flame structure

The use of global reaction path analysis, though showing the principal reactions at stake, is not sufficient to describe the complete dynamics of the combustion reaction. The detailed flame structure was thus examined to get a deeper understanding of flame chemistry and highlight the specificities of the flame. Several flame configurations can be considered in industrial applications. In most of the cases, high-pressure, turbulent, partially premixed flames will be observed. Kinetics of those flames cannot be apprehended directly, but they can be locally associated with more simple flames. In this study, and as a first approach, simple stationary 1D flames were considered. The specificities of ammonia/methane flame are first highlighted using the 1D Freely propagating flame configuration (FPF). Then, the effect of the stretch on the premixed flame structure is studied using the counterflow premixed twin flame configuration (PCF). Finally, the non-premixed counterflow flame structure (NCF) is presented.

### 2.3.1. Structure of the 1D freely propagating flame

As a first approach, the 1D freely propagating flame structure of an ammonia/methane premixed flame is introduced. First, to clarify the differences between the two fuels, the flame structure of the methane and ammonia are introduced and compared. Then, ammonia/methane flame structure is presented.

Figure 2.10 represents the evolution of the main reactants and products for both ammonia/air and methane/air premixed flames at stoichiometry. As discussed in previous Sections 2.1 and 2.2, the combustion of methane will mainly lead to the production of  $H_2O$  and  $CO_2$ .  $CO$  and  $H_2$  also appear as intermediates of combustion as seen in Fig. 2.10a, but their amount remains small. In methane/air premixed flame, the  $NO$  formed is mainly produced through the thermal  $NO$  mechanism. However, the total amount of  $NO$  remains much smaller than the  $CO$  emissions, and thus not represented in Fig. 2.10a. In the ammonia/air premixed flame case, the overall structure remains similar, with the gradual decrease of the reactant before the flame front, and the apparition of the products afterward, as described in Sections 2.1 and 2.2. One of the main differences observable in the flame structure in Fig. 2.10b is the slower temperature gradient and the larger preheating zone thickness which is characteristic of ammonia flames.

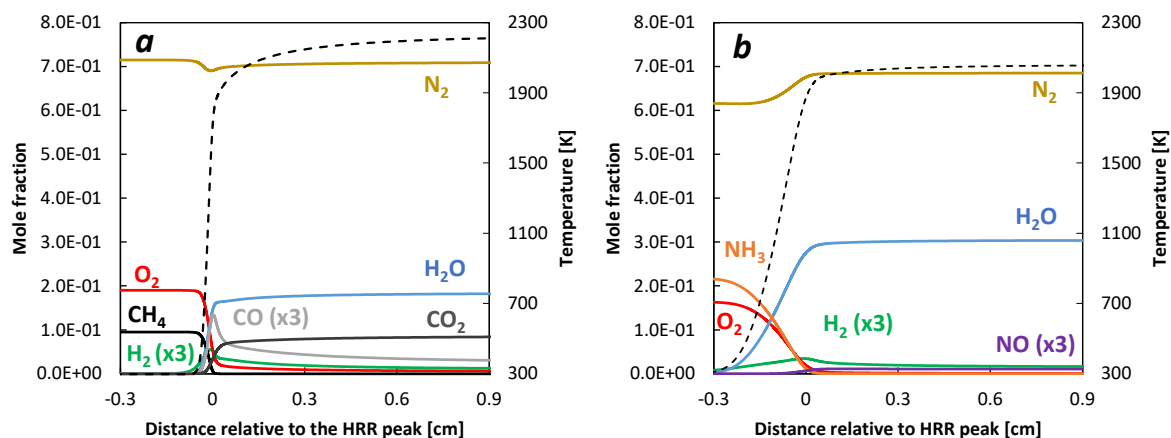


Fig. 2.10. Flame structure for FPF, at  $\phi = 1.0$ : (a) methane/air flame; (b) ammonia/air flame.

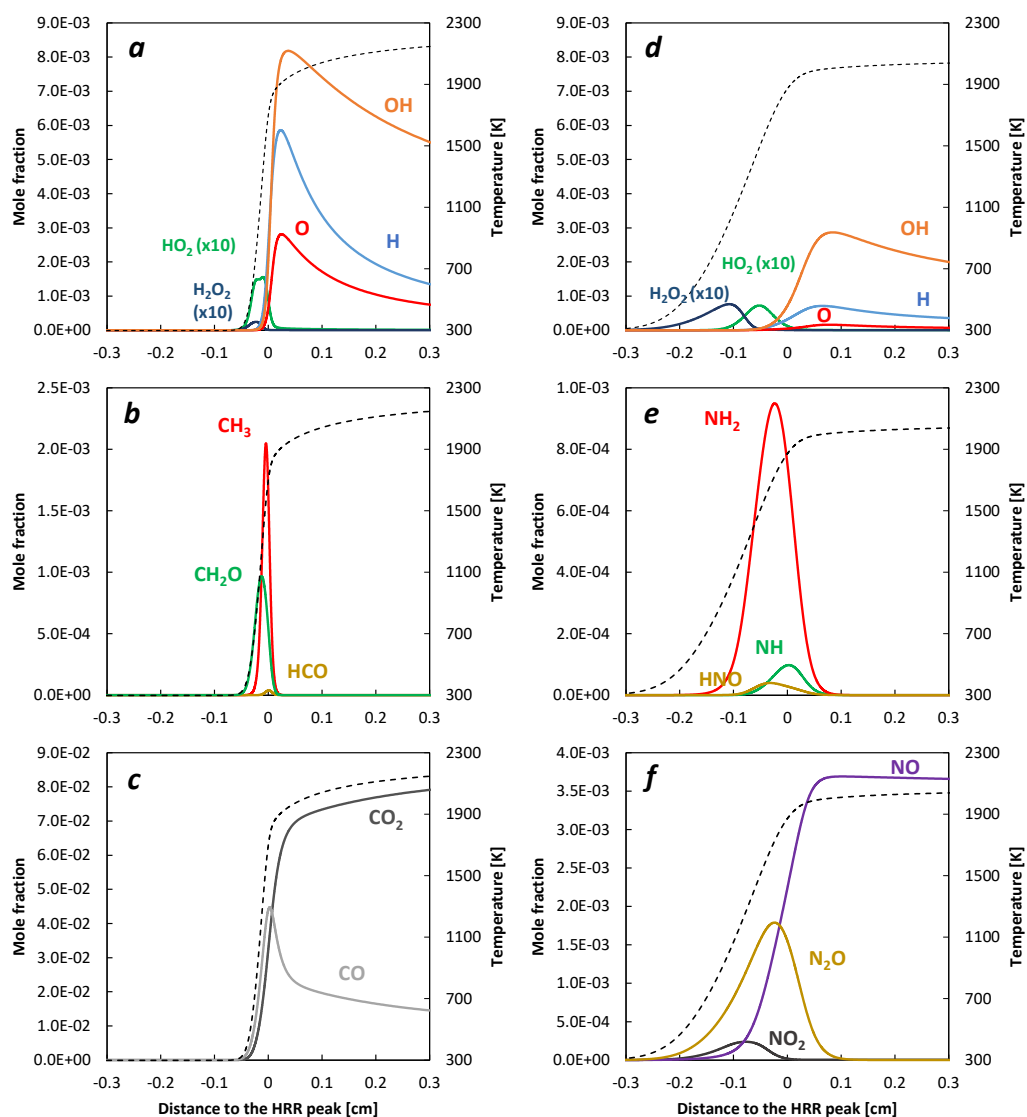


Fig. 2.11. Methane and ammonia flames main intermediate species for FPF at  $\phi = 1.0$ : methane/air premixed flame (a) H, OH, O, HO<sub>2</sub>, and H<sub>2</sub>O<sub>2</sub>, (b) CH<sub>3</sub>, CH<sub>2</sub>O, and HCO, (c) CO and CO<sub>2</sub>; ammonia/air premixed flame (d) H, OH, O, HO<sub>2</sub>, and H<sub>2</sub>O<sub>2</sub>, (e) NH<sub>2</sub>, NH and HNO, (f) NO, NO<sub>2</sub> and N<sub>2</sub>O.

Similarities between methane and ammonia flame structure can also be observed in Fig. 2.11 featuring the flame's main intermediates reactants. For both flames, the radical pool of OH, O, and H, necessary for the first dissociation reactions in both ammonia and methane reaction path are present in the hot burnt gas region as seen in Figs. 2.11a and d. Their back-diffusion toward the fresh mixture is thus necessary for the reactions with CH<sub>4</sub> and NH<sub>3</sub>. This is illustrated in Fig. 2.12, where the rate of production of CH<sub>3</sub>, NH<sub>2</sub>, OH, H, and O are represented. The maximum production rate of CH<sub>3</sub> corresponds to the maximum consumption of H, OH, and O radicals in the methane flame, while the one of NH<sub>2</sub> corresponds to the maximum consumption of OH, H, and O. Another characteristic feature of ammonia flame is observable from Fig. 2.12, which is the relative order of the production and consumption rates of those radicals. Whereas in methane flame, H is dominant, OH is more important in ammonia flames. This can also be observed by looking at the first dissociation reaction of CH<sub>4</sub> and NH<sub>3</sub> in the reaction path. Whereas for methane, production of CH<sub>3</sub> through CH<sub>4</sub> + H = CH<sub>3</sub> + H<sub>2</sub> and CH<sub>4</sub> + OH = CH<sub>3</sub> + H<sub>2</sub>O are relatively equilibrated (40% and 37%), in the case of ammonia, more than 80% of the NH<sub>2</sub> is produced through the reaction NH<sub>3</sub> + OH = NH<sub>2</sub> + H<sub>2</sub>O.

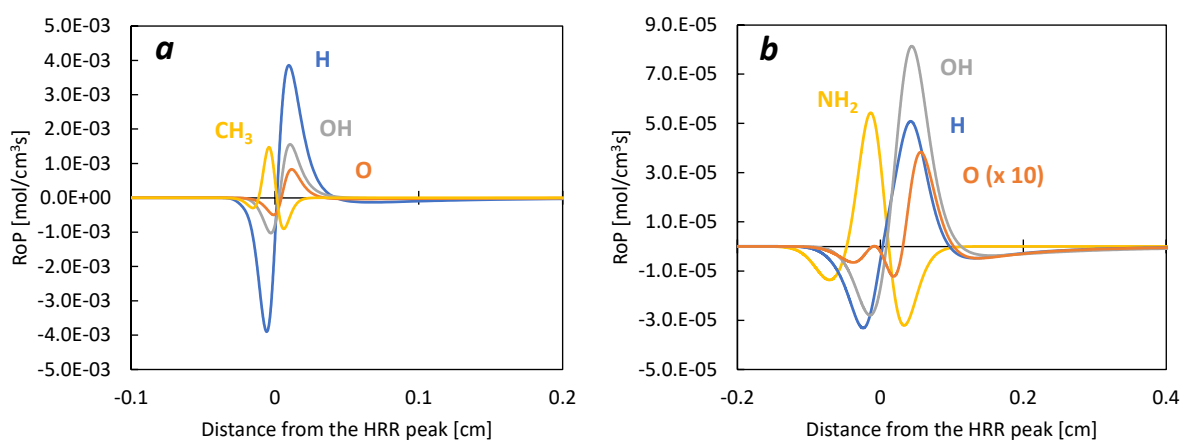


Fig. 2.12. Rate of production of radicals for FPF: (a) methane/air premixed flame; (c) ammonia/air premixed flame.

Furthermore, comparing Figs. 2.11a and d, it can be observed that the quantity of those OH, O, and H radicals are divided by more than a factor 2 in ammonia case compared to the methane case. It is also interesting to notice that, even though similar to what is observed in methane flame, the mole fraction of HO<sub>2</sub> and H<sub>2</sub>O<sub>2</sub> intermediates, characteristic of low-temperature environment, decreases in ammonia case too, their proportion relative to the other OH, H and O radicals is larger than in the methane case.

After the first dissociation step,  $\text{CH}_3$  and  $\text{NH}_2$  intermediates appear in the flame as presented in Figs. 2.11b and e, both slightly before the heat release peaks. In the case of methane,  $\text{CH}_3$  mainly decomposes into  $\text{CH}_2\text{O}$ , also slightly before the main heat release peaks, while for ammonia,  $\text{NH}_2$  is mainly converted into  $\text{NH}$ . Those intermediate will later react as shown in the reaction paths in Figs. 2.1 and 2.2, giving mainly  $\text{HCO}$  and  $\text{HNO}$ . Finally, Figs. 2.11c and d present the main products,  $\text{CO}$  and  $\text{CO}_2$  in methane case, and  $\text{NO}$ ,  $\text{NO}_2$  and  $\text{N}_2\text{O}$  in ammonia case. The production of  $\text{NO}$  in the ammonia flame is comparable to the production of  $\text{CO}$  in methane flame, with the apparition of a maximum just after the heat release peak, and a gradual decay in the burnt gas region.  $\text{N}_2\text{O}$  and  $\text{NO}_2$  apparent to intermediate species and are only present as a trace in the burnt gas region as developed in Section 2.2.

Methane/air and ammonia/air premixed flame structure specificities being clarified, the case of the ammonia/methane premixed flame will be developed in the following.

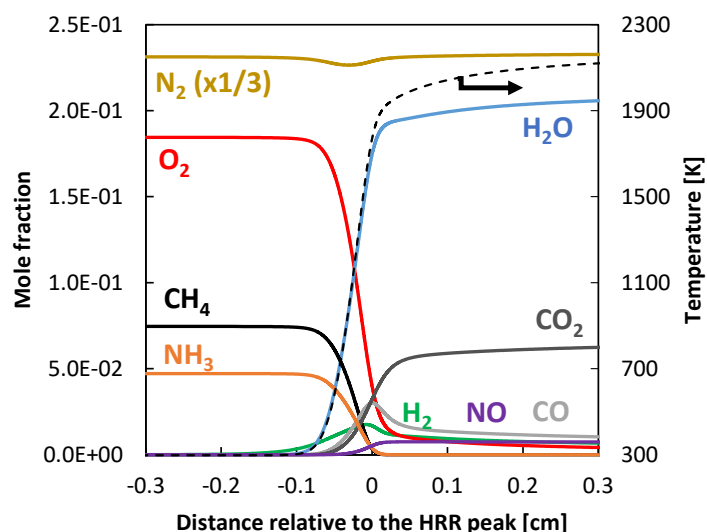


Fig. 2.13. Global structure of a premixed ammonia/methane flame using the 1D freely propagating flame model (FPF), with  $E = 0.2$  and  $\phi = 1.0$ .

Fig. 2.13 shows the flame structure for an ammonia mixing ratio  $E = 0.2$ , and an equivalence ratio  $\phi = 1.0$ . Most of the  $\text{CH}_4$  molecules are converted into  $\text{CO}_2$ , and to a lower extent in  $\text{CO}$ , intermediate in the production of  $\text{CO}_2$ . It can be noted that  $\text{CO}$  appears in the burnt gases in an amount comparable to the  $\text{NO}$  produced.  $\text{NH}_3$  is converted mostly into  $\text{N}_2$ , but also in  $\text{NO}_x$ .  $\text{NO}_x$  observed are largely dominated by  $\text{NO}$ .  $\text{NO}$  can be produced through several mechanisms in ammonia/methane flame: prompt, thermal and fuel  $\text{NO}$ . To evaluate prompt and thermal mechanisms, the  $\text{N}_2$  consumption rates

are observed. From the reaction path analysis, most of the consumption of  $N_2$  is done by reaction with CH radicals, as can be seen in Fig. 2.14. This occurs where CH radicals are present in sufficient quantity and at sufficiently high temperatures. This  $N_2$  contributes to the production of HCN and HCNN. The former is then consumed as presented in Fig. 2.6, leading to CO and NH,  $NH_2$ , and  $N_2O$ ; and the latter is directly consumed to produce  $N_2$  and HCO. Overall, this consumption of  $N_2$  has a negligible impact on the NO production: thermal and prompt NO formation is much smaller than  $NH_3$ -fuel NO. It is also worth noticing that  $H_2$  is produced in great quantity and is present in the burnt gases in a non-neglectable amount.

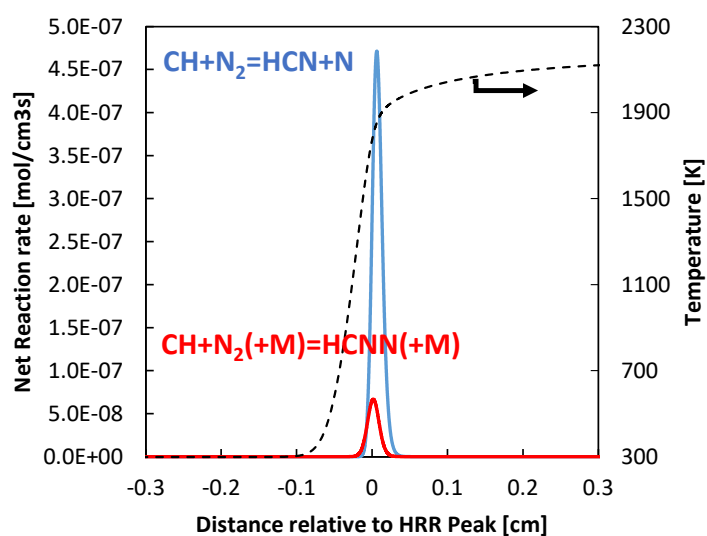


Fig. 2.14. Net reaction rates of the main contributor to  $N_2$  consumption for  $E = 0.2$  and FPF.

The details of the flame structure are displayed in Fig. 2.15, showing the main intermediates of reactions. The first two graphs Figs. 2.15a and b show the reactants from the  $H_2$ - $O_2$  kinetics. No significant changes can be observed when these distributions are compared to those of methane flames in Fig. 2.11a. OH, H and O are produced downstream of the reaction zone, in the high-temperature region, while  $HO_2$  and  $H_2O_2$  remain minor constituents appearing in the low-temperature region, upstream of the reaction zone. Moreover, it was found that the rate of production and consumption of H and OH radicals are gradually switching with an increase of  $E$ . Whereas H radical production and consumption is a key to methane flame chemistry, the weight of H radical in the ammonia/methane flame chemistry is gradually reduced to the benefit of OH radicals, which are fundamental in ammonia combustion chemistry.

The Figs. 2.15c and d compare the methane oxidation main intermediates for the case  $E = 0.2$ . The details of methane oxidation have been discussed widely [44,123] and are not the purpose of this work. One of the differences relative to pure methane flame is the relative abundance of HCO and  $\text{CH}_2$ . Whereas they are present in almost equal amounts in methane/air premixed flame, in the present ammonia mixing ratio ( $E = 0.2$ ), HCO abundance is the half of the  $\text{CH}_2$  one. Many parameters might influence this, including competition reactions due to  $\text{NH}_3$  addition, acting as a chemical sink for O, H, and particularly OH, as well as interaction reactions involving the  $\text{CH}_3$  specie.

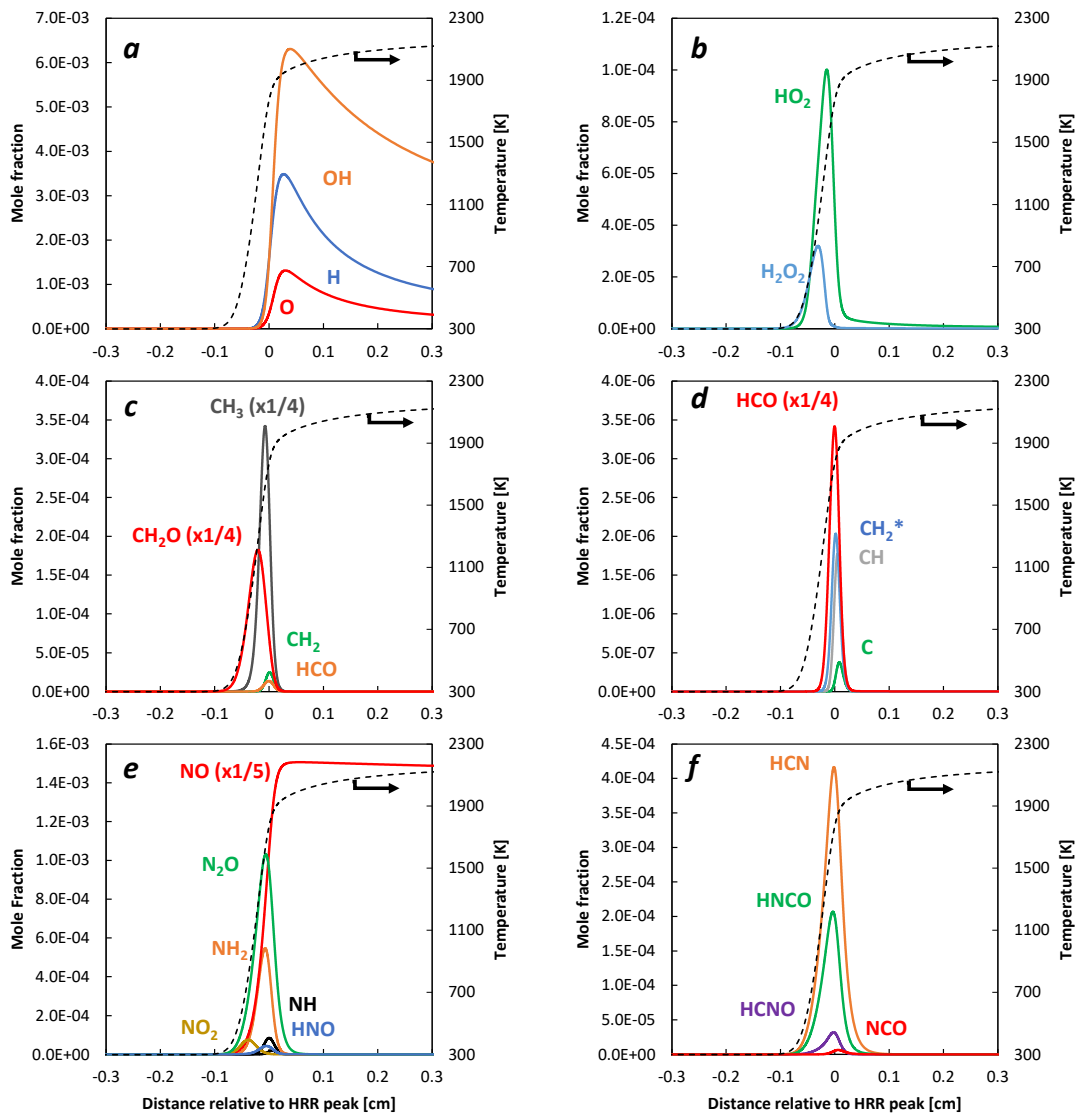


Fig. 2.15. 1D freely propagating flame (FPF) structure for  $E = 0.2$ : (a) OH, H, O; (b)  $\text{HO}_2$ ,  $\text{H}_2\text{O}_2$ ; (c)  $\text{CH}_3$ ,  $\text{CH}_2\text{O}$ ,  $\text{CH}_2$ , HCO; (d) HCO,  $\text{CH}_2^*$ , CH and C; (e)  $\text{NH}_2$ , NH, HNO and NO,  $\text{NO}_2$  and  $\text{N}_2\text{O}$ ; (f) HCN and CN.

From Fig. 2.15e, the evolution of the main intermediates of the  $\text{NH}_3$  oxidation branch throughout the flame can be observed. Comparing these distributions with the one of pure ammonia flame in Figs. 2.11e and f, it could be observed that the  $\text{NH}_3$  conversion into  $\text{NO}$  and  $\text{NO}_2$  is higher in the case of the present  $E = 0.2$  ammonia/methane mixture than in the case of pure ammonia. Indeed, a higher rate of  $\text{NO}$  formation was observed for this mixing ratio  $E$ , than for  $E = 1$ , as developed in Fig. 2.8 of Section 2.2. The more abundant cyanides species are presented in Fig. 2.15f. They are products of the C-N interaction determined in the reaction path analysis and are consistent in terms of abundance to the relative speed of production/consumption presented in Fig. 2.8.

### 2.3.2. Structure of counterflow premixed twin flames

Counterflow premixed twin flames (PCF) have a similar structure to that of freely propagating flames (FPF), as shown in Figs 2.8 and 2.9. A higher stretch rate leads to a decrease in the flame temperature and in a reduction of the reaction zone (the flame thickness is decreased at higher stretch rates, and distance full scale on the figures is thus divided by 2).

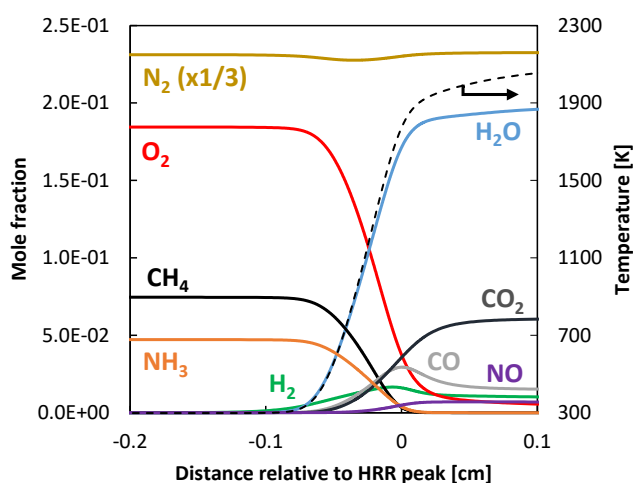


Fig. 2.16. Global structure of a counterflow premixed twin flames (PCF) for  $E = 0.2$ ,  $\phi = 1.0$  and a stretch rate of  $300 \text{ s}^{-1}$  (40% of extinction stretch rate value, the stagnation plane at  $x = 0.136 \text{ cm}$  is not represented in the present graph).

The comparison of the flame structure of the freely propagating flame (FPF) and the counterflow premixed twin flames (PCF) in Figs. 2.7 and 2.9, reveals that the maximum concentration of the species with a peak in the burnt gas region tends to decrease with higher stretch rate. This is the case for  $\text{OH}$ ,  $\text{H}$ ,

O, and NO species.  $\text{NH}_2$  maximum value is also slightly reduced. These decreases are related to the shorter residence time in the counterflow flame than in the freely propagating case. The stretch rate affects the structure of the flame differently depending on the species. Kinetics thus also evolves due to the shorter residence time which is in turn affecting the overall kinetics and the distributions in the flame.

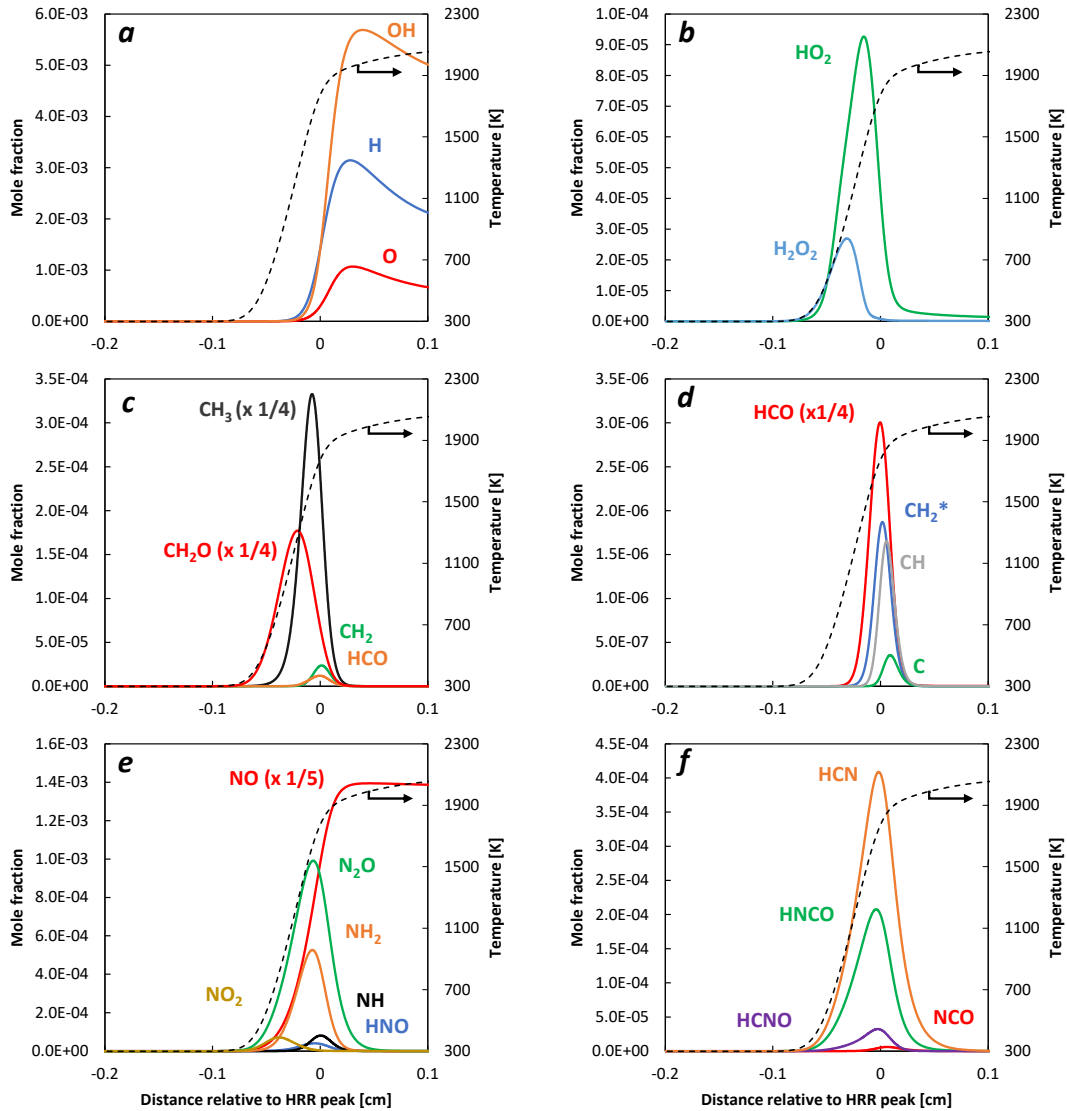


Fig. 2.17. Counterflow premixed twin flame (PCF) detailed structure for  $E = 0.2$ ,  $\phi = 1.0$  and stretch rate of  $300 \text{ s}^{-1}$ : (a) OH, H, O; (b)  $\text{HO}_2$ ,  $\text{H}_2\text{O}_2$ ; (c)  $\text{CH}_3$ ,  $\text{CH}_2\text{O}$ ,  $\text{CH}_2$ ,  $\text{HCO}$ ; (d)  $\text{HCO}$ ,  $\text{CH}_2^*$ , CH and C; (e)  $\text{NH}_2$ , NH, HNO, NO,  $\text{NO}_2$  and  $\text{N}_2\text{O}$ ; (f) HCN and CN.

### 2.3.3. Structure of a counterflow non-premixed flame

The non-premixed flame has a quite different structure than the premixed flame due to the different repartition of reactants distributions. In this study, the non-premixed counterflow flame (NCF) was

considered. The flame can be split into fuel and oxidizer regions. In Figs. 2.10, 2.11 and 2.12, and going from the fuel side to the oxidizer side, the fuels gradual decomposition can be observed: from  $\text{CH}_4$  to  $\text{CH}_3$ ,  $\text{CH}_2\text{O}$ ,  $\text{HCO}$ ,  $\text{CO}$ , and  $\text{CO}_2$  and from  $\text{NH}_3$  to  $\text{NH}_2$ ,  $\text{NH}$ ,  $\text{HNO}$ ,  $\text{NO}$ ,  $\text{NO}_2$ ,  $\text{N}_2$ . Peaks of  $\text{CO}_2$ ,  $\text{NO}$ , and  $\text{H}_2\text{O}$  distributions correspond with the main heat released and the temperature peak.  $\text{H}_2$  peaks on the fuel side, close to the  $\text{CO}$  peak. Likewise, on the oxidizer side,  $\text{O}_2$  is decomposed, and  $\text{H}_2\text{O}_2$  and  $\text{HO}_2$  are formed in the lower temperature regions and  $\text{OH}$ ,  $\text{H}$ , and  $\text{O}$  in the higher temperature region.

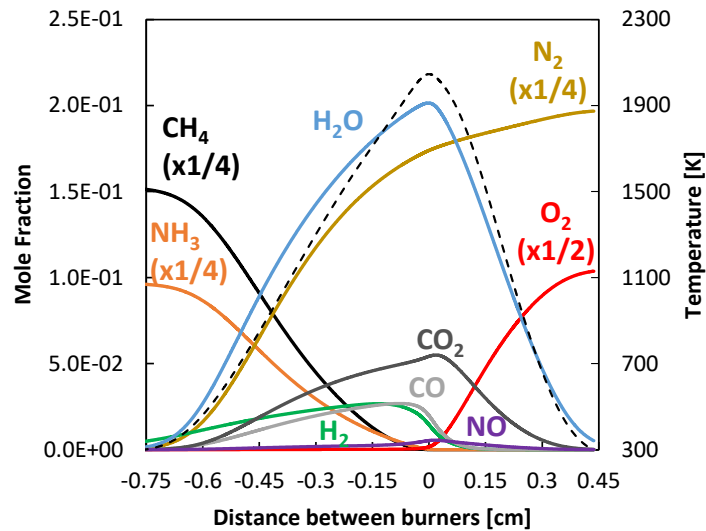


Fig. 2.18. Global structure of a counterflow non-premixed flame (NCF) for  $E = 0.2$ , with a stretch rate of  $60 \text{ s}^{-1}$ .

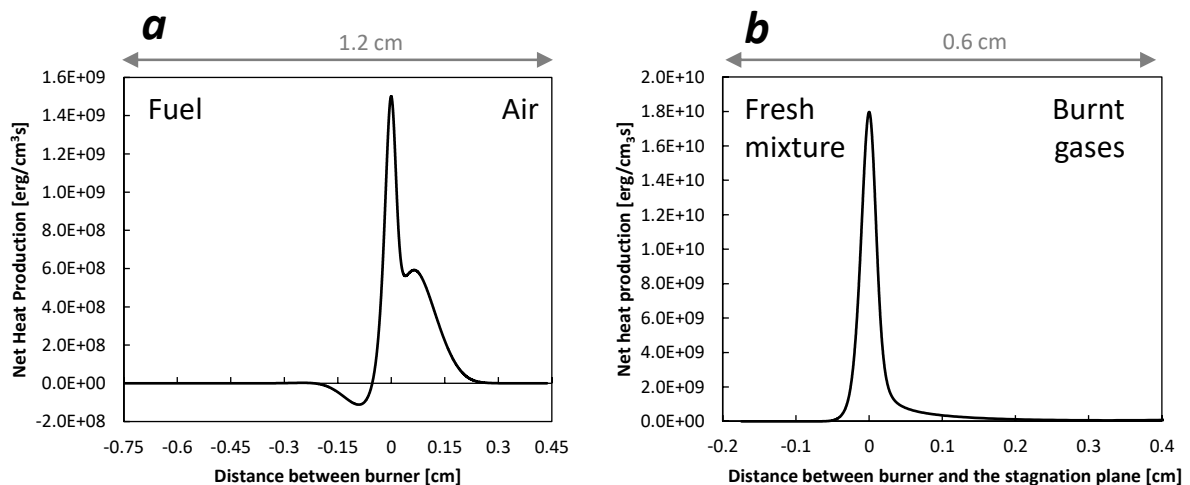


Fig. 2.19. Heat released profile in a counterflow flame for  $E = 0.2$  and a stretch rate of  $60 \text{ s}^{-1}$ : (a) non-premixed (NCF); (b) premixed (PCF) for  $\phi = 1.0$ .

The heat released profiles display some specificities when compared to premixed flame cases as introduced in Fig. 2.19. It is characterized by an endothermic region where  $\text{CH}_3$ ,  $\text{CH}_2$ ,  $\text{NH}_2$ ,  $\text{NH}$  are formed, and two exothermic peaks, the first one corresponding to  $\text{H}_2\text{O}$  and  $\text{CO}_2$  formation region, and the second in the oxidizer region. The  $\text{NO}$  concentration is peaking simultaneously to the largest heat release peak but its distribution is broad and covers both fuel and oxidizer regions, leading to the production of  $\text{N}_2\text{O}$  (by reaction with  $\text{NH}$  essentially) on the fuel side and  $\text{NO}_2$  (by reaction with  $\text{O}$ ,  $\text{OH}$ ,  $\text{HO}_2$  and  $\text{O}_2$ ) on the oxidizer side. The C-N species, formed essentially from  $\text{CH}_i$  and  $\text{NO}$  as presented in Fig. 2.6, appear in the fuel side of the flame, close to those species.

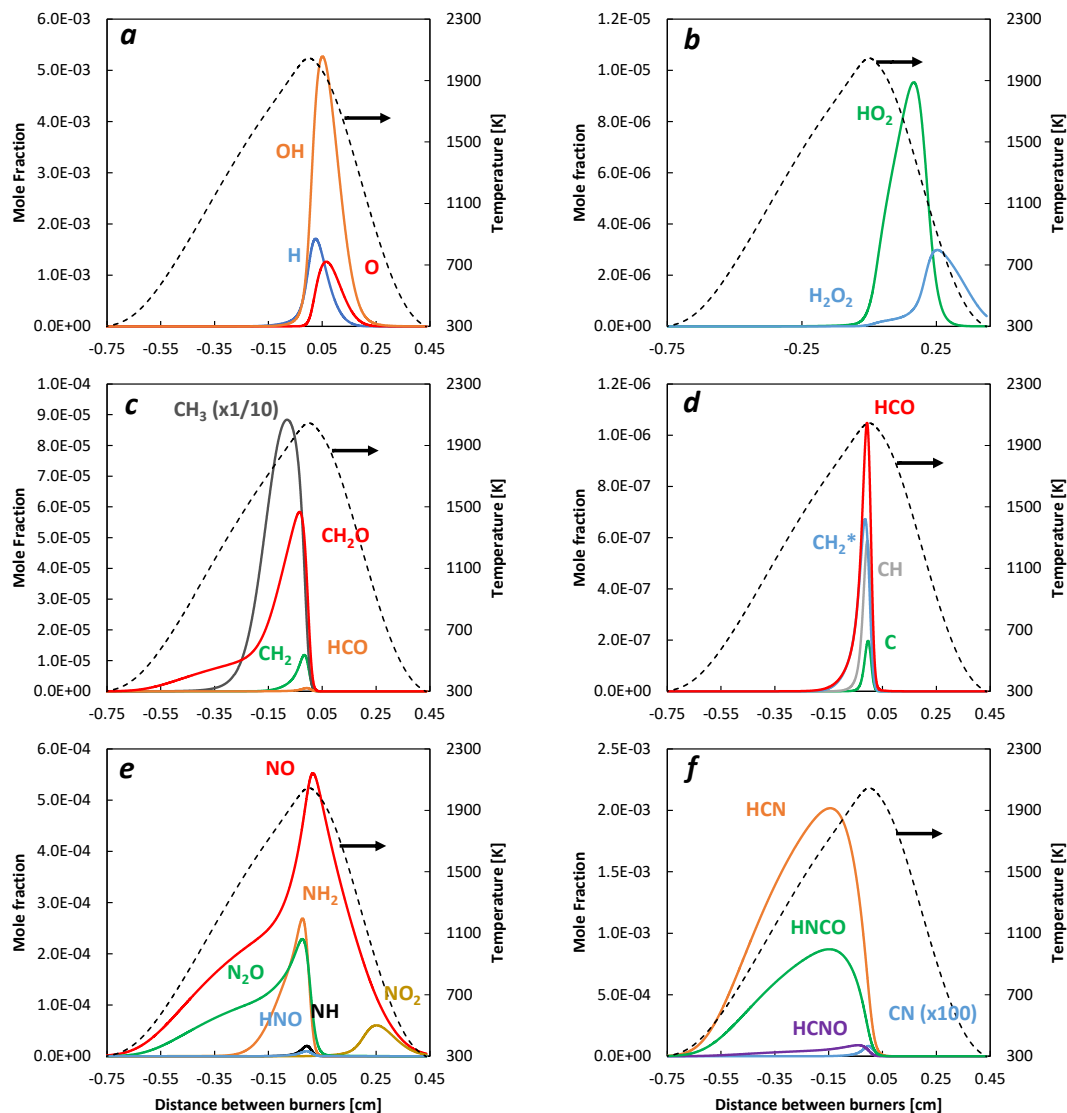


Fig. 2.20. Counterflow non-premixed flame structure (NCF) for  $E = 0.2$  and a stretch rate of  $60 \text{ s}^{-1}$ :  
 (a)  $\text{OH}$ ,  $\text{H}$ ,  $\text{O}$ ; (b)  $\text{HO}_2$ ,  $\text{H}_2\text{O}_2$ ; (c)  $\text{CH}_3$ ,  $\text{CH}_2\text{O}$ ,  $\text{CH}_2$ ,  $\text{HCO}$ ; (d)  $\text{HCO}$ ,  $\text{CH}_2^*$ ,  $\text{CH}$  and  $\text{C}$ ; (e)  $\text{NH}_2$ ,  $\text{NH}$ ,  
 $\text{HNO}$ ,  $\text{NO}$ ,  $\text{NO}_2$  and  $\text{N}_2\text{O}$ ; (f)  $\text{HCN}$  and  $\text{CN}$ .

## 2.4. Heat release in the flames

The analysis of heat release in the flame has been performed to identify the main reactions at the origin of the heat released in the flame. The identification of these reactions, in addition to the flame structure study, gives a complete overview of the flame. The methane and ammonia flames are investigated first before focusing on the ammonia/methane flames. The study is based on numerical simulation using the 1D freely propagating flame model (FPF), in the stoichiometric condition.

In the case of CH<sub>4</sub> flame, most of the heat is released through elementary reactions  $O + CH_3 = H + CH_2O$ ,  $OH + CO = H + CO_2$ ,  $H + CH_3 + M = CH_4 + M$ ,  $O + CH_3 \Rightarrow H + H_2 + CO$  and  $OH + H_2 = H + H_2O$  as presented in Table 2.4, where HRR denotes the mean heat released rate by reactions. Contributions of each elementary reaction are represented in Fig. 2.21 which shows the CH<sub>4</sub> oxidation reaction previously introduced.

Table 2.4. Chart of the detailed reactions with a large contribution to heat release in the CH<sub>4</sub>/air premixed flame (FPF).

Reaction	Mean HRR [J/cm <sup>3</sup> s]	Percentage of net heat released [%]
$H + O_2 \rightleftharpoons O + OH$	-1.490	-13.09
$O + CH_3 \rightleftharpoons H + CH_2O$	1.318	11.58
$OH + CO \rightleftharpoons H + CO_2$	1.144	10.05
$H + CH_3 + M \rightleftharpoons CH_4 + M$	1.037	9.11
$O + CH_3 \Rightarrow H + H_2 + CO$	0.865	7.60
$OH + H_2 \rightleftharpoons H + H_2O$	0.820	7.20
$H + OH + M \rightleftharpoons H_2O + M$	0.742	6.52
$OH + HO_2 \rightleftharpoons O_2 + H_2O$	0.702	6.17
$H + O_2 + H_2O \rightleftharpoons HO_2 + H_2O$	0.619	5.44
$OH + CH_4 \rightleftharpoons CH_3 + H_2O$	0.475	4.17

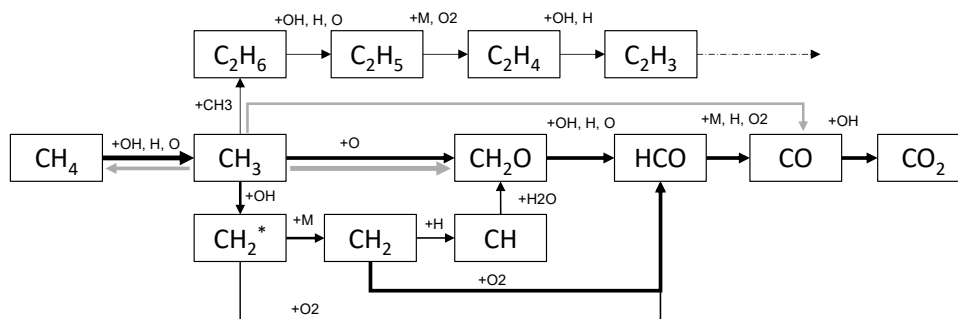


Fig. 2.21. CH<sub>4</sub>/air premixed flame (FPF) reaction path at  $\phi = 1.0$ : rate of reaction in black; main contributors to heat release in the flame in gray.

Figure 2.22 shows the flame structures of the  $\text{NH}_3$  flame and the  $\text{CH}_4$  flames, in relation with the heat-releasing reactions profiles. HRR stands for heat release rate, RoR for the rates of reaction and RoP for the rates of production of the main intermediate species. In  $\text{CH}_4$  flames, the main reactions contributing to heat release are related to  $\text{CH}_3$  consumption.  $\text{CH}_3$  radicals are essential in  $\text{CH}_4$  flame. They are formed in the upstream part of the flame region owing to the two fast reactions  $\text{H} + \text{CH}_4 = \text{CH}_3 + \text{H}_2$  and  $\text{OH} + \text{CH}_4 = \text{CH}_3 + \text{H}_2\text{O}$  with a low contribution to heat release (around 4%), as represented in Fig. 2.22a.  $\text{CH}_3$  is then consumed mainly through  $\text{O} + \text{CH}_3 = \text{H} + \text{CH}_2\text{O}$ ,  $\text{OH} + \text{CO} = \text{H} + \text{CO}_2$ ,  $\text{H} + \text{CH}_3 + \text{M} = \text{CH}_4 + \text{M}$ ,  $\text{O} + \text{CH}_3 \Rightarrow \text{H} + \text{H}_2 + \text{CO}$  and heat is released. A pool of radicals, mainly  $\text{H}$ ,  $\text{O}$  and  $\text{OH}$ , is then formed in the downstream part of the flame region, as shown in Figs. 2.22b and c. They thus back-diffuse upstream to fuel the elementary reactions previously stated as developed in Section 2.3.1.

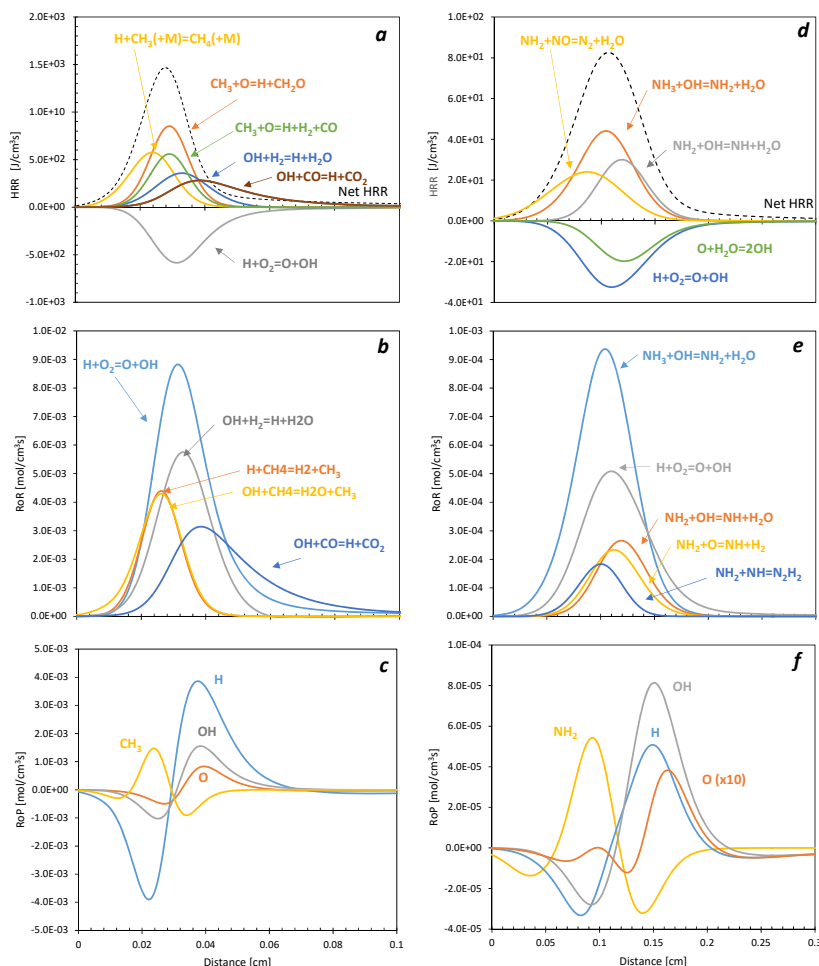


Fig. 2.22. Structures of  $\text{CH}_4/\text{air}$  and  $\text{NH}_3/\text{air}$  flames premixed flames in relation with heat release profiles for FPF: HRR of (a)  $\text{CH}_4$  case, (d)  $\text{NH}_3$  case; RoR of (b)  $\text{CH}_4$  case, (e)  $\text{NH}_3$  case; RoP of main intermediates in (c)  $\text{CH}_4$  case, (f)  $\text{NH}_3$  case.

In the case of  $\text{NH}_3$  flame, the main contributors to heat release are  $\text{NH}_3 + \text{OH} \rightleftharpoons \text{NH}_2 + \text{H}_2\text{O}$ ,  $\text{NH}_2 + \text{OH} = \text{NH} + \text{H}_2\text{O}$ , and  $\text{NH}_2 + \text{NO} = \text{N}_2 + \text{H}_2\text{O}$ , as summarized in Figs. 2.22d, e, f and Table 2. 5, and the reaction  $\text{NH}_3 + \text{OH} \rightleftharpoons \text{NH}_2 + \text{H}_2\text{O}$  is dominant. Similar to the  $\text{CH}_4$  flame case, those reactions are symbolized with grey arrows in the reaction path in Fig. 2.23. In the  $\text{NH}_3$  flame case, the flame structure is focussed on the consumption/production of the  $\text{NH}_2$  intermediate. More than 80% of  $\text{NH}_2$  is produced from reaction  $\text{NH}_3 + \text{OH} = \text{NH}_2 + \text{H}_2\text{O}$ .  $\text{NH}_2$  is then mainly consumed downstream of the flame region to produce  $\text{NH}$  and other intermediates leading to  $\text{N}_2$  formation. A pool of radicals is also produced downstream of the reaction zone. As mentioned already in Section 2.3,  $\text{OH}$  and  $\text{H}$  production rates proportions are reversed compared to the case of  $\text{CH}_4$  flame, Figs. 2.22c and f.  $\text{OH}$  is also of importance in the heat release process as it appears in 2 of the 3 main reactions contributing to the heat release previously mentioned, which is one of the specific features of  $\text{NH}_3$  combustion chemistry.

Table 2. 5. Chart of the detailed reactions with a large contribution to the heat released in  $\text{NH}_3$  flame for FPF,  $\phi = 1.0$ .

Reaction	Mean HRR [ $\text{J}/\text{cm}^3\text{s}$ ]	Percentage of net heat release [%]
$\text{NH}_3 + \text{OH} \rightleftharpoons \text{NH}_2 + \text{H}_2\text{O}$	0.296	14.11
$\text{H} + \text{O}_2 \rightleftharpoons \text{O} + \text{OH}$	-0.259	-12.34
$\text{NH}_2 + \text{NO} \rightleftharpoons \text{N}_2 + \text{H}_2\text{O}$	0.202	9.63
$\text{NH}_2 + \text{OH} \rightleftharpoons \text{NH} + \text{H}_2\text{O}$	0.176	8.37
$\text{OH} + \text{H} + \text{M} \rightleftharpoons \text{H}_2\text{O} + \text{M}$	0.163	7.78
$2\text{OH} \rightleftharpoons \text{O} + \text{H}_2\text{O}$	-0.146	-6.94
$\text{HNO} + \text{OH} \rightleftharpoons \text{NO} + \text{H}_2\text{O}$	0.138	6.57
$\text{OH} + \text{H}_2 \rightleftharpoons \text{H} + \text{H}_2\text{O}$	0.134	6.38
$\text{NH} + \text{NO} \rightleftharpoons \text{N}_2\text{O} + \text{H}$	0.131	6.25
$\text{N}_2\text{O} + \text{H} \rightleftharpoons \text{N}_2 + \text{OH}$	0.129	6.15

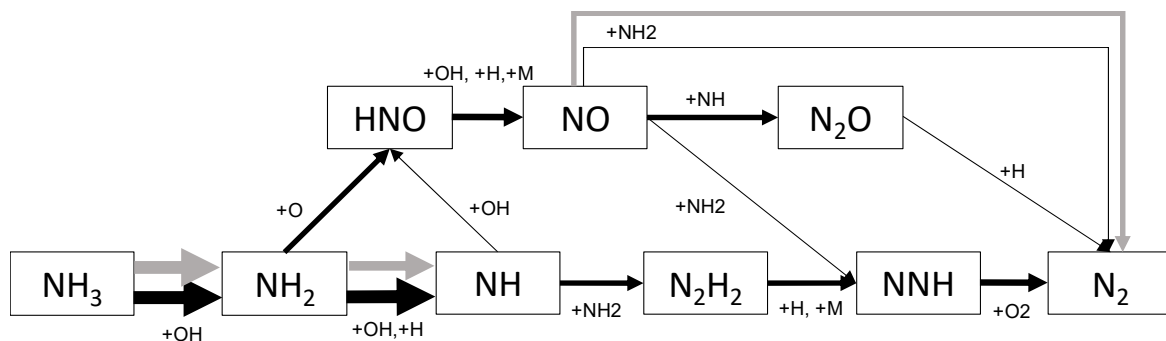


Fig. 2.23.  $\text{NH}_3$  flame reaction path for FPF,  $\phi = 1.0$ : rate of reaction in black; main contributors to the heat released in the flame in gray.

Following the study of both methane and ammonia flames, the cases of the gradual introduction of ammonia in a methane flame are considered in the following.

To identify major changes in the heat production in the flame, the production of heat per reaction was integrated over the whole flame and gathered per subset of reactions: carbon subset, nitrogen subset, H<sub>2</sub>-O<sub>2</sub> subset, and carbon-nitrogen species and represented in Fig. 2.24a.

The heat produced in the flame is gradually decreased as ammonia is introduced in the mixture. For methane or low ammonia content flames, the heat is essentially produced from reactions related to carbon species as seen in Fig. 2.24. H<sub>2</sub>-O<sub>2</sub> subset and nitrogen subset of reaction represent only a minor contribution to heat for those flames. Heat production is thus essentially driven by reaction  $O + CH_3 = H + CH_2O$ ,  $OH + CO = H + CO_2$ , and  $H + CH_3 (+M) = CH_4 (+M)$ , like in the methane flame case.

For methane/ammonia flames, with a fuel mixing ratio  $E = 0.2$ , most of the heat produced in the flame corresponds to  $OH + H_2 = H + H_2O$  with close to 8% of the heat production; followed by  $OH + CO = H + CO_2$ ,  $O + CH_3 = H + CH_2O$  and  $H + CH_3 (+M) = CH_4 (+M)$  representing together 21% of the heat produced; and  $HNO + H = H_2 + NO$ , the only reaction of nitrogen subset in the top 10 reactions, with close to 5% of the heat production. The main contributor to heat release in pure ammonia flame,  $NH_3 + OH = NH_2 + H_2O$ , remains minor even at  $E = 0.2$ , representing only less than 3% of heat production. A chart of the main heat release contributor is included in Table 2.6.

When ammonia is introduced up to  $E = 0.30$ , heat release by hydrocarbon species is already reduced by half, corresponding to the methane mole fraction decrease in the fuel mixture ( $E = 0.30 \Leftrightarrow X_{CH_4} = 0.48$ ), and is comparable to the one from nitrogen subset of reaction, with  $HNO + H = H_2 + NO$  remaining predominant in the subset.

Carbon-nitrogen interactions are neglectable for all the cases investigated. Nonetheless, their contribution peaks around  $E = 0.1$ ,  $E = 0.15$ , showing greater interactions between the two fuels oxidation paths, corresponding to the C-N subset, for this range of  $E$ .

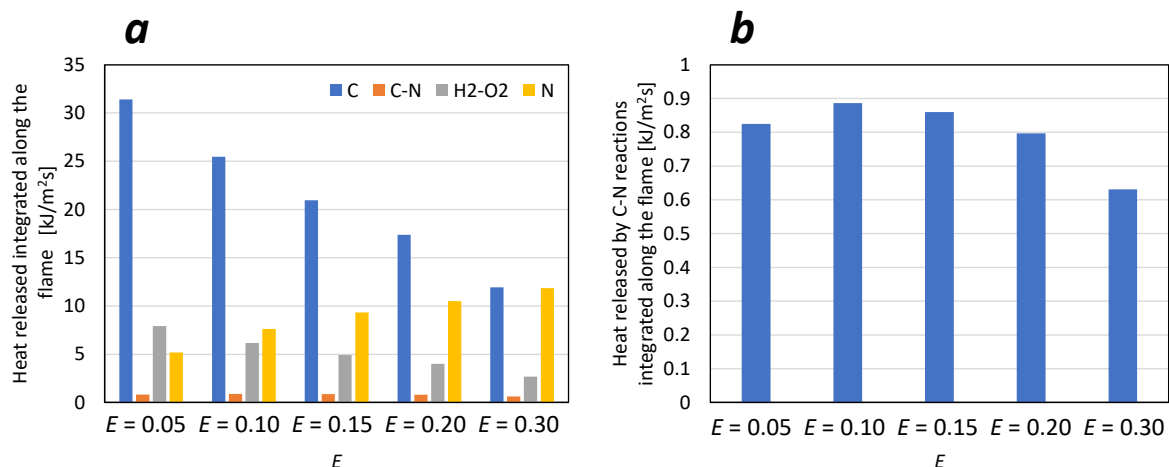


Fig. 2.24. The heat release evolution with increasing  $E$  for FPF at  $\phi = 1.0$ : (a) repartition by subsets of reaction. C: carbon subset, C-N: carbon-nitrogen interaction subset, H<sub>2</sub>-O<sub>2</sub>: H<sub>2</sub>-O<sub>2</sub> subset, N: nitrogen subset. (b) C-N subset only.

Table 2.6. Chart of the detailed reactions with a large contribution to the heat released in NH<sub>3</sub>/CH<sub>4</sub>/air flame for FPF,  $E = 0.2$  and  $\phi = 1.0$ .

Reaction	Mean HRR [ $\text{J}/\text{cm}^3\text{s}$ ]	Percentage of net heat release [%]
$\text{H} + \text{O}_2 = \text{O} + \text{OH}$	-0.430	-13.16
$\text{OH} + \text{H}_2 = \text{H} + \text{H}_2\text{O}$	0.266	8.13
$\text{OH} + \text{CO} = \text{H} + \text{CO}_2$	0.254	7.78
$\text{O} + \text{CH}_3 = \text{H} + \text{CH}_2\text{O}$	0.244	7.47
$\text{H} + \text{CH}_3 (+\text{M}) = \text{CH}_4 (+\text{M})$	0.198	6.05
$\text{HNO} + \text{H} = \text{H}_2 + \text{NO}$	0.172	5.26
$\text{H} + \text{OH} + \text{M} = \text{H}_2\text{O} + \text{M}$	0.164	5.03
$\text{O} + \text{CH}_3 = \text{H} + \text{H}_2 + \text{CO}$	0.160	4.91
$2\text{OH} = \text{O} + \text{H}_2\text{O}$	-0.143	-4.38
$\text{OH} + \text{HO}_2 = \text{O}_2 + \text{H}_2\text{O}$	0.140	4.30
$\text{H} + \text{O}_2 + \text{H}_2\text{O} = \text{HO}_2 + \text{H}_2\text{O}$	0.115	3.51
$\text{OH} + \text{CH}_4 = \text{CH}_3 + \text{H}_2\text{O}$	0.112	3.44
$2\text{CH}_3 (+\text{M}) = \text{C}_2\text{H}_6 (+\text{M})$	0.098	3.00
$\text{OH} + \text{CH}_2\text{O} = \text{HCO} + \text{H}_2\text{O}$	0.084	2.59
$\text{NH}_3 + \text{OH} = \text{NH}_2 + \text{H}_2\text{O}$	0.080	2.45

### 3. Effect of diffusion of OH, H and O radicals in the flames

#### 3.1. Objectives and methodology

This part of the study focuses on the understanding of ammonia flame structure and chemistry, and more specifically on the role of the diffusion of O, OH and H radicals in the flame and its impact on flame propagation and extinction characteristics. It could be seen in previous Section 2.3 that OH radicals play a predominant role in ammonia combustion as their reaction with ammonia leads to high heat release through a fast reaction that dominates the ammonia oxidation path. Sensitivities of burning velocity and extinction stretch rate but also NO production toward this reaction as well as OH production through  $H + O_2 = O + OH$  are high, showing great dependence on OH production and consumption mechanism. In contrast, dependence in OH radical was not observed to such an extent in methane flame. Drawing a parallel with a study on hydrogen flame structure [123], for which H radical back-diffusion to the flame front is a critical and limiting step in hydrogen combustion, the role of OH back-diffusion on ammonia flame characteristics was further investigated. Ammonia flame features were compared to two extensively studied fuels, CH<sub>4</sub> and H<sub>2</sub> to highlight NH<sub>3</sub> fuel specificities. Finally, the effect of radical diffusion in the CH<sub>4</sub>/NH<sub>3</sub> mixtures was investigated.

The study has been performed on Chemkin-Pro software, using the Premix code for the determination of laminar burning velocity (FPF), and the Oppdiff code for the determination of the extinction stretch rate (PCF). The chemistries employed here are Miller [44] for H<sub>2</sub>, GRI-Mech 3.0 [122] for CH<sub>4</sub>, and Tian [69] for NH<sub>3</sub> and Okafor [63] for CH<sub>4</sub>/NH<sub>3</sub> mixture at  $E = 0.30$ . Even though those mechanisms can be questioned in their capability to fully model with accuracy the flames studied, they are commonly used and allow to model the laminar burning velocity and extinction stretch rate of those flames with enough accuracy for this study, which compares trends only.

Looking at the conservation equations implemented in the Premixed code for the resolution of 1D freely propagating flames (FPF) problems, it can be seen diffusion phenomenon is expressed through the diffusion velocity of specie in both energy and species equations. The diffusion model used in this study is the mixture-average transport properties where the diffusion velocity of specie  $k$  is expressed as follows [124][120]:

$$V_k = V_k + W_k + V_c \quad (2.3)$$

Where  $V_k$  is the ordinary diffusion velocity from Curtiss-Hirschfelder approximation, dependent on the mole fraction of specie  $k$  and the mixture-average diffusion coefficient  $D_{km}$ ;  $W_k$  is the thermal diffusion velocity, dependent on the specie  $k$  mole fraction and the mixture-average diffusion coefficient  $D_{km}$  and temperature and  $V_c$  is the correction velocity to insure mass fractions sum to unity.

$$V_k = -D_{km} \frac{1}{X_k} \frac{dX_k}{dx} \quad (2.4)$$

$$W_k = D_{km} \theta_k \frac{1}{T} \frac{dT}{dx} \quad (2.5)$$

$$D_{km} = \frac{1 - Y_k}{\sum_{j \neq k} \frac{X_j}{D_{kj}}} \quad (2.6)$$

$$D_{kj} = \frac{3}{16} \frac{\sqrt{\frac{2\pi k_B^3 T^3}{m_{kj}}}}{p \pi \sigma_{kj}^2 \Omega^{(1,1)*}} \quad (2.7)$$

Where  $D_{jk}$  is the Lennard Jones binary diffusion coefficient for  $j$  and  $k$ ,  $\Omega^{(1,1)*}$  is the collision integral,  $k_b$  the Boltzmann constant,  $T$  the temperature,  $m_{jk}$  the reduced mass of  $j$  and  $k$ , and  $\sigma_{jk}$  is the reduced collision diameter as expressed in Eq. ( 2.8 ).

$$\sigma_{jk} = \frac{1}{2} (\sigma_j + \sigma_k) \quad (2.8)$$

where  $\sigma_j$  is the collision diameter of specie  $j$ .

In this study, the diffusion velocity of the radicals of interest has been modified through the modification of the radicals' Lennard Jones collision diameter. Modifying the Lennard-Jones collision diameter of OH, H, and O independently allows us to observe the effect of OH, H, and O diffusion in the flame independently. By reducing or increasing the collision diameter, the diffusion velocity of those species is increased or decreased. The changes in the flame characteristics observed can thus be attributed to the change in the diffusion properties of those radicals only, through the artificial modification of diffusion velocities.

The modification of collision diameters might also impact the calculation of thermal conductivity of the mixture  $\lambda$ , as well as the mixture viscosity  $\mu$ , as pure species thermal conductivities and viscosity depend on collision diameter. However, those parameters are mixture averaged and as only one radical collision diameter is changed at once, this effect is assumed to be negligible overall.

The parameter  $X$ , as expressed in Eq. ( 2.9 ), was introduced to be able to compare the effect of each radical diffusion on laminar burning velocity and extinction stretch rate. The parameter  $X$  introduced is here varying between 0 and 8 corresponding to the variation of the collision diameter from 1/3 to 3 times their initial value and follows the variations of binary diffusion parameter with the collision diameter.  $X = 1$  corresponds to the true physical collision diameter, while smaller values correspond to reduced diffusion and larger value to emphasized diffusion cases.

$$X = \left( \frac{\sigma_{jn}}{\sigma_{jp}} \right)^2 \quad ( 2.9 )$$

Where  $\sigma_{jn}$  is the true physical collision diameter of specie  $j$  and  $\sigma_{jp}$  is the parametric collision diameter of specie  $j$  which is modified artificially.

## 3.2. Comparison of methane, ammonia and hydrogen

### 3.2.1. Effect of radical diffusion on laminar burning velocity

Figs. 2.25a, b, and c represent the laminar burning velocity of  $H_2$ ,  $CH_4$ , and  $NH_3$  premixed flames at stoichiometry under atmospheric conditions, respectively. It can be seen in Fig. 2.25a that enhanced diffusion of H radicals leads to an increase in the laminar burning velocity of the hydrogen flame. This can be related to the faster back-diffusion of H radical from the burnt gas region upstream, at the leading edge of the flame, where they are consumed in the reaction  $H + O_2 + M = HO_2 + M$  and  $H + HO_2 = OH + OH$ , major heat generators on the upstream part of the reaction zone [123]. From Fig. 2.25a, it can also be seen that O and OH radicals' diffusion plays a marginal role if any. This confirms the methodology employed here.

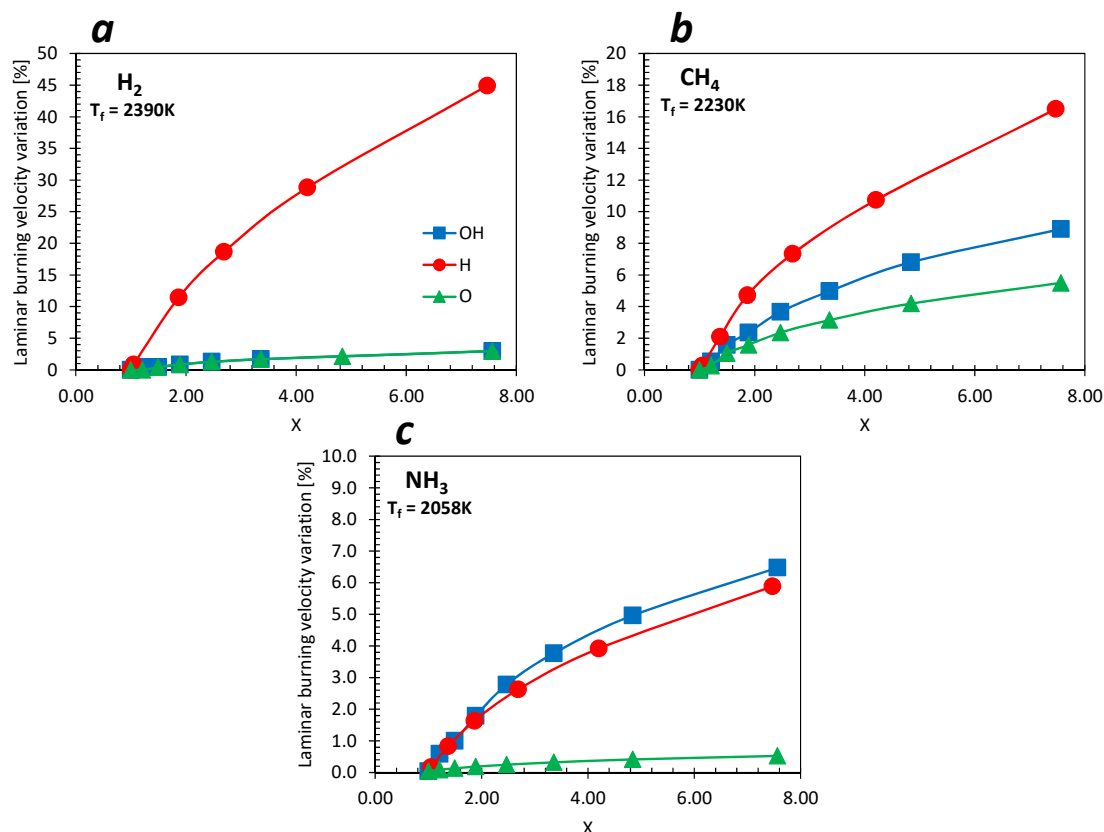


Fig. 2.25. Effect of enhanced radical diffusion on the laminar burning velocity of 1D freely propagating flames (FPF) at  $\phi = 1.0$ : (a)  $H_2$ /air flame; (b)  $CH_4$ /air flame; (c)  $NH_3$ /air flame.  $\square$ ,  $\circ$ ,  $\Delta$  represents OH, H and O, respectively.

In the case of premixed methane flame, it can be seen from Fig. 2.25b that enhanced diffusions of O, OH, and H radicals all lead to increases in the laminar burning velocity. However, for the same  $X$  value, an increase in laminar burning velocity varies in order depending on the radical. H radicals enhanced diffusion leads to the larger increase in laminar burning velocity, followed by OH and O radicals. This order corresponds to the radicals overall production rate order, with a large production of H radical in the downstream part of reaction zone corresponding to  $OH + CO = H + CO_2$  and  $OH + H_2 = H + H_2O$ , which are consumed upstream to produce  $CH_3$  through  $H + CH_4 = CH_3 + H_2$  (produce 40% of  $CH_3$  from reaction path analysis), as observed in Law's work [123] and Section 2.3. OH, and O radicals are also produced downstream and back-diffuse for  $CH_3$  production as first H dissociation from  $CH_4$  is also done through  $CH_4 + OH = CH_3 + H_2O$  (produce 37% of  $CH_3$ ) and  $CH_4 + O = CH_3 + OH$  (produce 13% of  $CH_3$ ). The radicals enhanced diffusion thus leads to greater laminar burning velocity.

Ammonia case shows a slightly different picture as presented in Fig. 2.25c. The OH radical diffusion is here predominant over H diffusion, while O diffusion has few or no effect. This difference can be understood in terms of the essential role of OH consumption with  $\text{NH}_3$  in the upstream part of the flame region which is both the fastest reaction and the largest heat contributor of the mechanism. This reaction is thus essential and leads to a specific role of OH radical in ammonia combustion, relatively to other well-known fuels which are  $\text{CH}_4$  and  $\text{H}_2$ . The first H dissociation from  $\text{NH}_3$  is done mainly through  $\text{NH}_3 + \text{OH} = \text{NH}_2 + \text{H}_2\text{O}$ , which is responsible for around 80% of  $\text{NH}_2$  radical production, the first step in ammonia oxidation. Contrary to methane case, in ammonia flame, the production rate of OH radical is dominant over H and O, and OH back-diffuses upstream for  $\text{NH}_2$  production, corresponding to the observation done on the effect of the diffusion of those radicals on the laminar burning velocity.

### 3.2.2. Effect of radical diffusion on extinction stretch rate

In this section, the study is reduced to the case of methane and ammonia which are the main targets of this thesis. From Figs. 2.26a and b, it could be observed that radicals enhanced diffusion leads to a lower extinction stretch rate. This is especially true for H radical diffusion, while OH radical effect is smaller for both  $\text{CH}_4$  and  $\text{NH}_3$  premixed twin flames (PCF). The enhanced OH radical diffusion even increases the extinction stretch rate in the methane case. To better understand these phenomena, the use of flame structure analysis is necessary.

From the  $\text{NH}_3$  flame structure, it can be seen that OH, O, and H radicals production rates in Fig. 2.27 are facing a large drop compared to what was observed in the 1D freely propagating flame case (FPF) in Fig. 2.12. As the stretch rate is increased, OH and H radical productions are decreased, and their relative order is changed. H diffusion becomes prevalent in chemistry. The reduced radical production, is related to the reduced residence time, as H, OH, O radicals are produced downstream of the flame region, close to the stagnation plane as mentioned in section 2.3.2. The same observation can be done for methane flame. The rates of production are lower, though the relative order for O, OH, H is conserved, as shown in Fig. 2.27b.

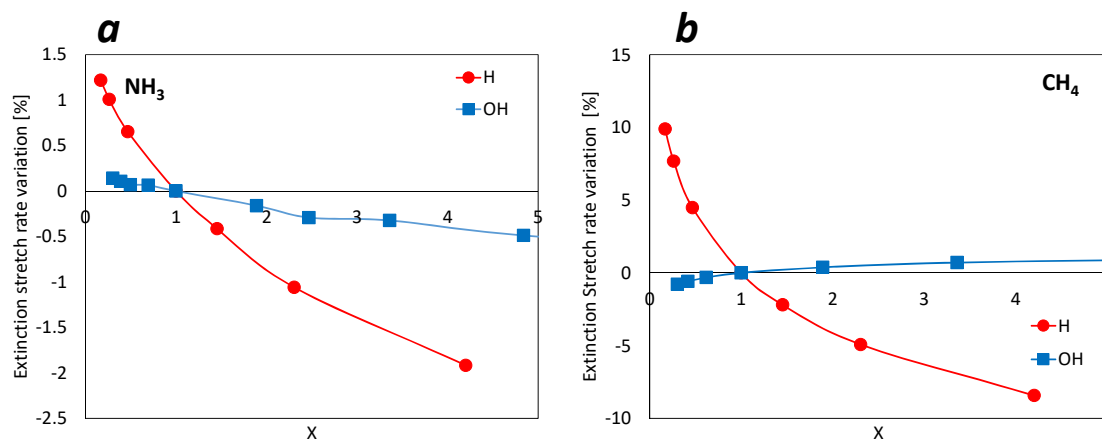


Fig. 2.26. Effect of enhanced diffusion on the extinction stretch rate of counterflow premixed twin flames (PCF) for  $\phi = 1.0$ : (a)  $\text{NH}_3$ /air flame; (b)  $\text{CH}_4$ /air flame.

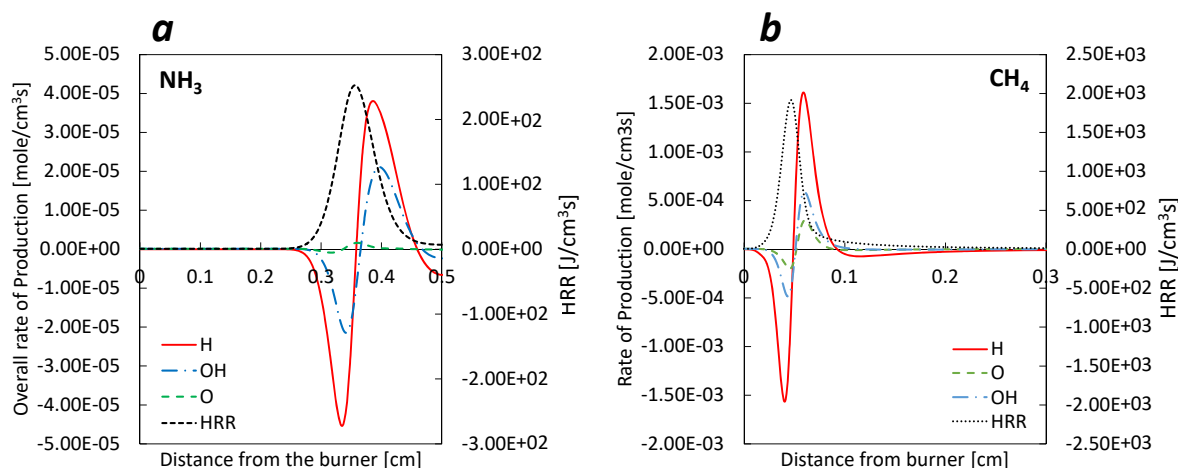


Fig. 2.27. Rate of production of O, OH, H in counterflow premixed twin flames structure (PCF), for a stretch rate of  $40 \text{ s}^{-1}$ : (a) ammonia/air flame and (b) methane/air flame.

Flame position relative to the burner lip, region limited to one of the twin flame observation.

When artificially increasing the diffusion of radicals, the flame thickness is increased both toward the flame, feeding the first step of fuel oxidation reactions, as well as toward the burnt region where they are lost as they don't contribute to main oxidation chemistry. The decrease is, in order, reflecting the role of the radical in the flame chemistry: Enhanced diffusion of H leads to a larger decrease in extinction stretch rate than OH in the two cases observed.  $\text{NH}_3$  extinction stretch rate also appears to be much less affected by the variation in radical diffusion than the one of  $\text{CH}_4$ , with variation between +/- 2% for  $\text{NH}_3$  to compare with +10% to -5% for  $\text{CH}_4$ . This is also true for  $\text{NH}_3$  laminar burning velocity

results (less than 9%). Thus even though that diffusion of radicals is important, it is a less critical parameter for  $\text{NH}_3$  compared to  $\text{CH}_4$  or  $\text{H}_2$  flames.

### 3.3. The case of methane/ammonia flames

The effect of radical diffusion for methane/ammonia  $E = 0.3$  flames laminar burning velocity is presented in Fig. 2.28. It can be observed that the predominance of H radical effect is lowered but remains essential in this case, while the one of OH is becoming slightly more important as it could be expected from the previous discussion in Fig. 2.25. For these mixtures, the mole fraction of  $\text{NH}_3$  in the mixture is larger than the one of  $\text{CH}_4$ . However, the H radical diffusion remains predominant compared with OH, even for the large quantity of ammonia introduced, which is consistent with the relative order in the rate of production of radicals in the flame as in Fig. 2.29.

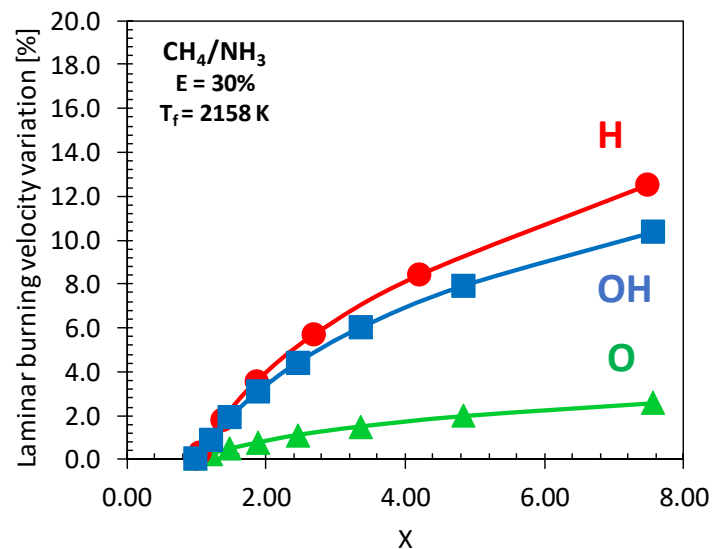


Fig. 2.28. Effect of the enhanced diffusion of radicals on the laminar burning velocity of ammonia/methane flame (FPF). Mixture of  $E = 0.30$  and  $\phi = 1.0$ .  $\square$ ,  $\circ$ ,  $\Delta$  represents OH, H and O, respectively.

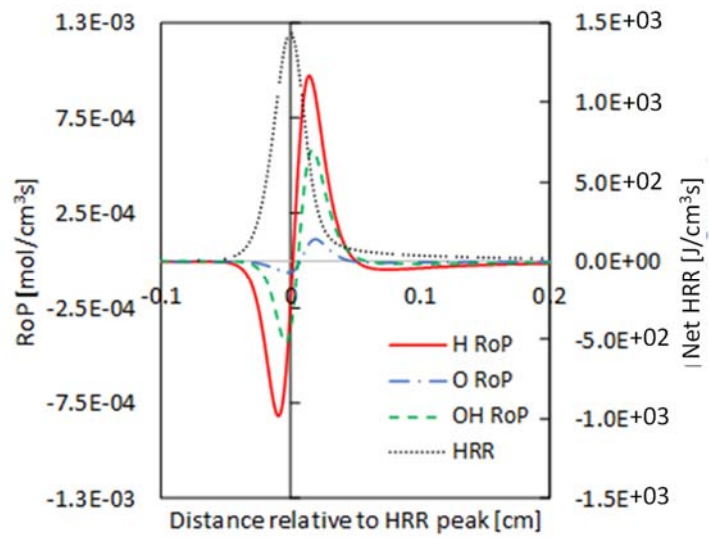


Fig. 2.29. Rate of Production (RoP) of H, OH, and H in an ammonia/methane/air 1D freely propagation flame (FPF) of at  $E = 0.3$ .

## 4. NO emission index for ammonia/methane premixed flames and effect of flame stretch

### 4.1. Method and objectives

Study in Section 2.2 already investigated the main features of the burnt gas emissions, and particularly the NO<sub>x</sub>, in relation to the flame structure and using reaction path analysis. The present study completes the first approach and aims to understand the effect of stretch rate on NO formation/consumption. It has indeed been observed that, for ammonia/air counterflow premixed twin flames, the mole fraction of NO at the stagnation plane is gradually getting lower as the stretch rate is increased. However, due to the shorter residence time which leads to higher unburnt gas quantity when getting close to extinction, unburnt ammonia amount is also increasing as flame stretch rate increases.

To compare the NO emission amount for different flame configurations, the use of the NO emission index, EINO, is relevant. Emission indexes have been widely used in the literature [125,126] and are defined as the ratio of the mass of NO produced on the mass of fuel burnt. This definition can be extended to other pollutant emissions such as NO<sub>2</sub> or NO<sub>x</sub> in general.

The NO emission indexes of counterflow premixed twin flames (PCF) were thus compared for various residence time to the one of an unstretched 1D freely propagating flame (FPF). The calculations were done on Chemkin-Pro software, using the freely propagating flame code as well as the opposed flow flame code. The details of the calculation for the NO emission index are explained and the results for the present study are discussed.

### 4.2. Definition of the flame front and beginning of consumption of fuel

To define the residence time, as well as the emission index, a common reference point for the calculation is necessary for both flames. In the present study, the flame front, where the temperature starts rising, and the reactions occurring, has been selected for all the configurations investigated. To define the threshold of temperature to be considered as the beginning of the flame zone, the variations of the NH<sub>3</sub> profile were studied carefully.

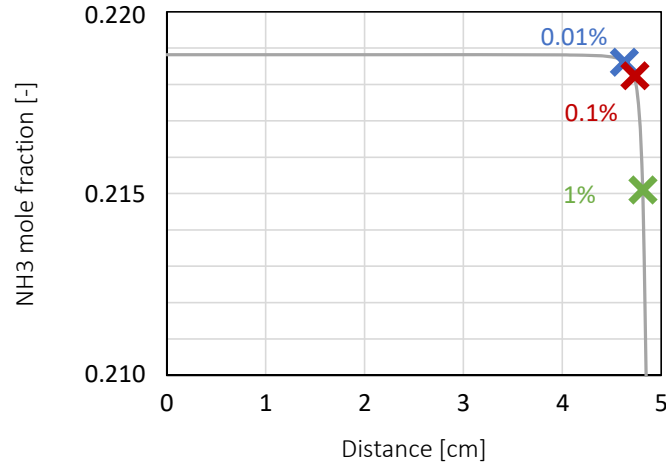


Fig. 2.30.  $\text{NH}_3$  mole fraction profile for a 1D freely propagating flame (FPF). The crosses represent the value of  $\text{NH}_3$  mole fraction when the temperature is 1% of the temperature rise in green, 0.1% of the temperature rise in red, or 0.01% of the temperature rise in blue.

Using 1% of temperature rise as a threshold, the consumption of  $\text{NH}_3$  has already started as shown in Fig. 2.30, and the mole fraction decreased by around 2%. To be closer to the plateau region, the beginning of the flame region for calculation should be taken at 0.1% or 0.01% of temperature rise, corresponding to less than 1% decrease of  $\text{NH}_3$  mole fraction. The value of 0.01% of the temperature rise was selected as a reference for the present study. The positions for this value are noted  $X_0$  and  $Z_0$  for 1D freely propagating flame (FPF) and counterflow premixed twin flames (PCF), respectively.

### 4.3. Residence time definition

The residence time definition based on the integral of density,  $\tau_1$ , as in Eq. ( 2.10 ) was selected for it is handily usable in both configurations. It was compared to the total residence time in each sub-grid in the case of the 1D freely propagating flame,  $\tau_2$ , as in Eq. ( 2.11 ) to ensure the validity of the definition. The results are plotted in Fig. 2.31.

$$\tau_1 = \frac{\int_{X_0}^{X_s} \rho dx}{\rho(X_0)U(X_0)} \quad (2.10)$$

$$\tau_2 = \sum_{X_0}^{X_s} \frac{\Delta x_i}{|U_i|} \quad (2.11)$$

where  $\rho$  is the density of the mixture and  $U$ , the velocity.  $X_0$  is the origin position, as defined in the previous paragraph and  $X_s$  is the position corresponding to the defined residence time and vary between  $X_0$  and the end of the calculation domain when  $\tau_1$  is increasing. From Fig. 2.31, it could be observed that the two definitions are strictly equivalent. The residence time  $\tau = \tau_1$  will be considered in the following.

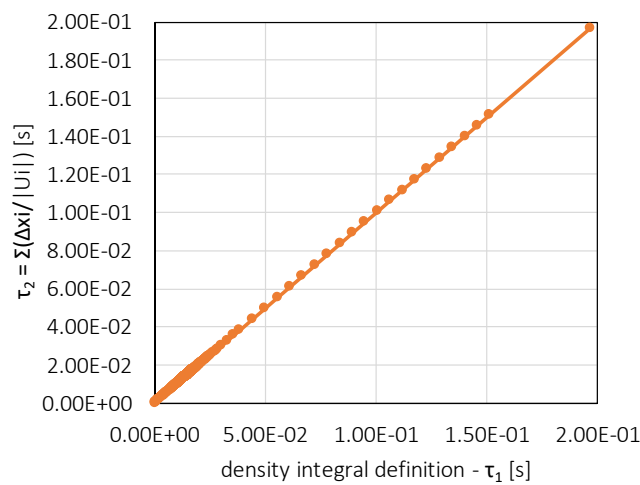


Fig. 2.31. Validation of density definition of residence time for 1D freely propagating flame (FPF).

In the case of the counterflow premixed twin flames,  $X_0$  is replaced by  $Z_0$  and  $X_s$  become  $Z_s$ , the position of the stagnation plane in Eq. ( 2.10 ).

The relation between the defined residence time,  $\tau$ , and the calculation domain was further studied to see if meshing can potentially affect the results. In the case of the 1D freely propagating flame, the evolution of  $\tau$  with the length of the integration domain is almost linear, at the exception of the very beginning of the reaction zone, where the slope is larger. This corresponds to the entrance in the reaction zone where a large density gradient is observed. For larger  $X_s - X_0$ , some differences can be observed and are attributed to the different mesh sizes when moving away from the reaction zone, from finer to coarser mesh. Indeed, the spacing between points appears to change brutally at the junction between two regions. The trend remains however linear as observed in Fig. 2.32.

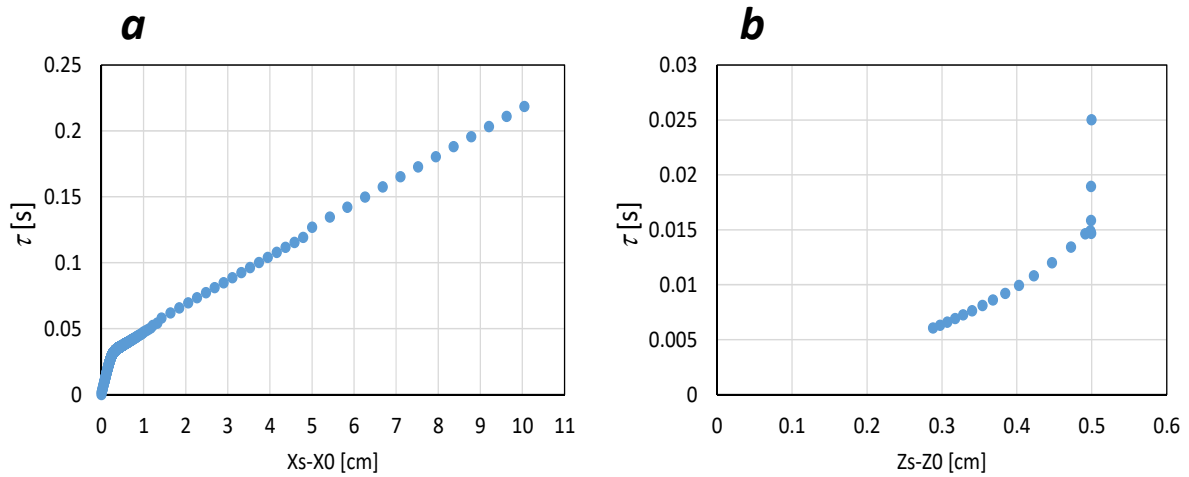


Fig. 2.32. Evolution of  $\tau$  depending on the integrated distance: (a) FPF; (b) PCFF.

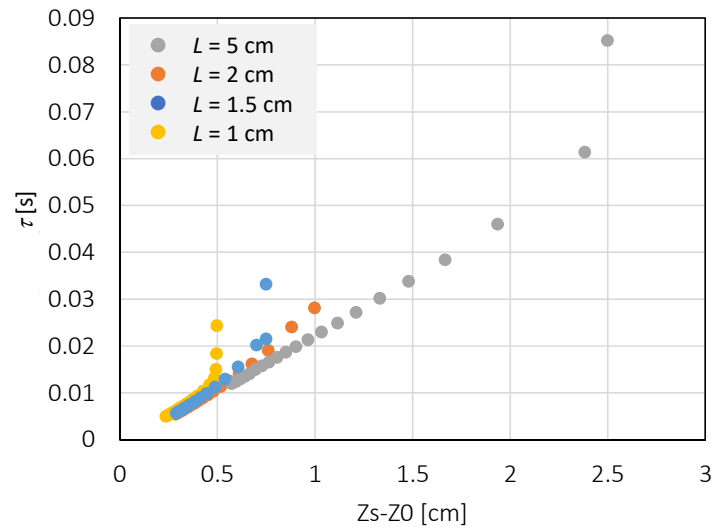


Fig. 2.33. Evolution of  $\tau$ :  $L = 5$  cm, grey;  $L = 2$  cm, orange;  $L = 1.5$  cm, blue;  $L = 1$  cm, yellow.

For the counterflow premixed twin flames, the graph in Fig. 2.32b was obtained from a calculation on a domain of  $L = 10$  mm, corresponding to the distance between the burners. The change in the trend observed in the graph representing  $\tau_l$  as a function of  $Z$  corresponds to the case where the calculated flames are too close to the burner outlet. Numerical aberration might result in this change of trend for some limit-cases. This has been confirmed by modifying the length of domain  $L$  selected. For different  $L$ , one, two, or three points of this type could be observed as presented in Fig. 2.33. Special attention to the mesh is thus necessary, and the distance selected between the burners for calculation should be considered as discussed in the next section.

#### 4.4. EINO in ammonia flame case

The first case investigated in this study is the ammonia/air premixed flame, at  $\phi = 1$ . The EINO is calculated for both 1D freely propagating flames and counterflow premixed twin flames using the calculation results obtained from Chemkin pro software. The EINO is then calculated according to the two following formulas:

$$EINO_{free} = \frac{\int_{X_0}^{X_s} W_{NO} \dot{\omega}_{NO} dx}{\int_{X_0}^{\infty} W_{NH_3} \dot{\omega}_{NH_3} dx} \quad (2.12)$$

$$EINO_{counter} = \frac{\int_{Z_0}^{Z_s} W_{NO} \dot{\omega}_{NO} dz}{\int_{Z_0}^{Z_s} W_{NH_3} \dot{\omega}_{NH_3} dz} \quad (2.13)$$

$\dot{\omega}_X$  is the rate of production of specie  $X$  corresponding to the mole production by unit volume and unit time of the specie  $X$ . This includes surface and gas-phase reactions.  $W_X$  is the molar mass of the specie  $X$ .  $X_0$  remains as defined before (temperature increase of 0.01%).  $X_s$  is the end of the integration region for freely propagating flame, and is changed according to  $\tau$  as introduced before.  $Z_0$  corresponds to  $X_0$ , in the case of the counterflow premixed twin flames, and  $Z_s$  is the stagnation plane position.

In the same way that has been discussed for the residence time, it could be observed that the point corresponding to flames too close to the burners in the counterflow premixed twin flames case leads to numerical error. This is represented in Fig. 2.34. To cover a wide range of residence time, it is thus necessary to increase the distance between the burners to reach the lower stretch cases.

Comparing EINO for 1D flame at  $\tau$  tending to infinity (or large values), and EINO for counterflow premixed twin flames, it can be observed that their values are converging toward each other. Indeed, large  $\tau$  corresponds to low stretch rates in the counterflow flame, with a configuration becoming closer to the freely propagating one. For small values of residence time, EINO is almost divided by two near the extinction compared with its value for the 1D freely propagating flame. Flame stretch as thus a positive effect on NO emission reduction.

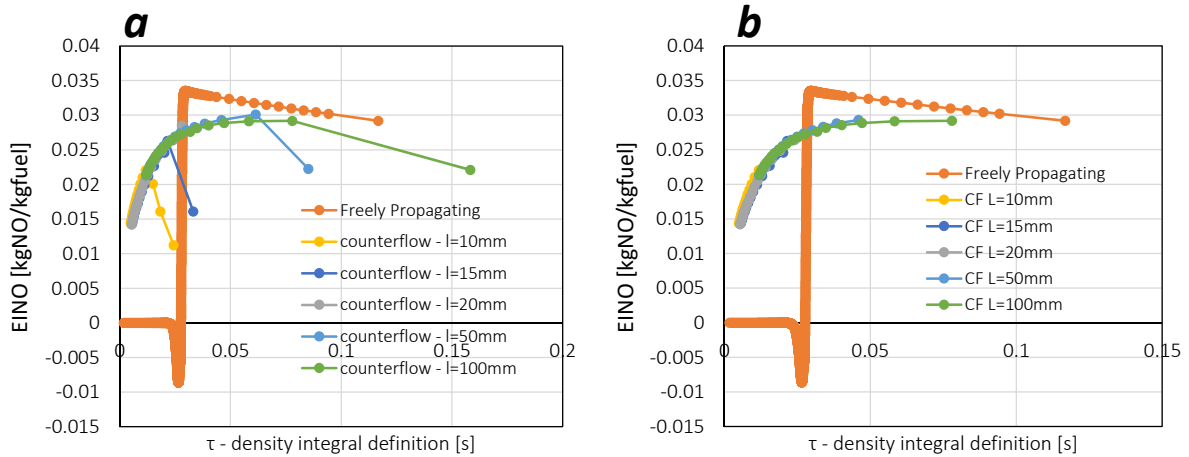


Fig. 2.34. EINO of FPF and PCF depending on the residence time. FPF is in orange, other curves correspond to PCF results with various  $L$ . Numerical error (flames too close to the burner) are kept in (a) and removed in (b).

#### 4.5. EINO in methane flame case

Methane flames have been observed the same way the ammonia flames were studied in the previous section. EINO curves obtained are presented in Fig. 2.35. Contrary to ammonia flame case, stretch here has few to no influence in NO production. Indeed, the curves of EINO obtained from various stretch conditions follow that of the 1D freely propagating flame.

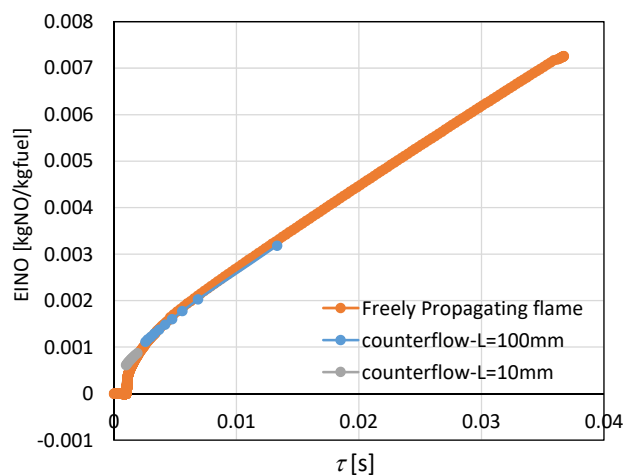


Fig. 2.35. EINO for methane FPF (orange) and PCF with  $L = 10$  mm (grey) and 100 mm (blue).

A comparison between ammonia and methane case shows that the response of EINO to flame stretch is different from one flame to the other. This can be related to the different chemical mechanisms involved in the two cases. While NO is mainly obtained from the thermal path for methane flames, it is

the fuel-NO mechanisms that are predominant in ammonia flame. Both mechanisms appear to have a very different sensitivity to stretch and residence time.

## 4.6. EINO in the case of ammonia/methane flames

Finally, methane/ammonia mixtures have been studied, for various  $E$ . In this case, the EINO expression was re-written to take into account the two fuels:

$$EINO_{free} = \frac{\int_{x_0}^{x_s} W_{NO} \dot{\omega}_{NO} dx}{\int_{x_0}^{\infty} (W_{NH_3} \dot{\omega}_{NH_3} + W_{CH_4} \dot{\omega}_{CH_4}) dx} \quad (2.14)$$

$$EINO_{counter} = \frac{\int_{z_0}^{z_s} W_{NO} \dot{\omega}_{NO} dz}{\int_{z_0}^{z_s} (W_{NH_3} \dot{\omega}_{NH_3} + W_{CH_4} \dot{\omega}_{CH_4}) dz} \quad (2.15)$$

The results for 1D freely propagating flames are presented in Fig. 2.36. Considering its value when  $\tau$  is relatively small ( $\tau < 0.2 - 0.4$  s), it can be observed that the EINO has a non-monotonic variation with ammonia addition. The EINO increases quickly at first when adding a small amount of ammonia in the methane flame and then is reduced to a value corresponding to  $NH_3$  flame EINO. The variation of EINO with residence time is also fundamentally different in methane and ammonia/methane cases. While the first increases gradually before stabilization to a plateau value, the second one shows a sharp increase for small residence time ( $\tau < 0.1$  s) before gradually decreasing up to a plateau value. This can be related to the different mechanisms of the formation of NO for the two different fuel mixtures. In the first case, NO comes primarily from thermal-NO production. NO is formed in the burnt gas region, where the temperature is high enough. A large residence time corresponds to a large region of production of NO in the burnt gases. In the second case, NO comes essentially from fuel-NO. It is formed in the reaction zone, explaining the large peak observed in the EINO for small  $\tau$ . NO can be later reduced in  $N_2O$  or  $N_2$  by reactions with the  $NH_i$ , explaining the reduction to the plateau value for larger  $\tau$ .

It can be observed that for a larger introduction of  $NH_3$ , the peak value observed is gradually shifted to a larger value of  $\tau$  ( $\tau = 0 - 0.05$  s). Stabilization up to the plateau EINO value is also longer: for  $E = 0.15$  s at  $\tau > 0.8$ , for  $E = 0.30$  at  $\tau > 1$  s and for  $E = 0.60$  at  $\tau > 1.2$  s.

It is also interesting to observe that for large  $\tau$ , the value of EINO for methane flame is larger than the one of ammonia/methane flames. The largest EINO value observed correspond to short residence time, and mixtures close to  $E = 0.15$ , with a rise in fuel-NO<sub>x</sub> in addition to the classical dominant thermal NO<sub>x</sub> production route. This value is decreased for higher ammonia concentration and longer residence times, as the larger concentration of ammonia allows for the reduction of NO<sub>x</sub> in the burnt gases.

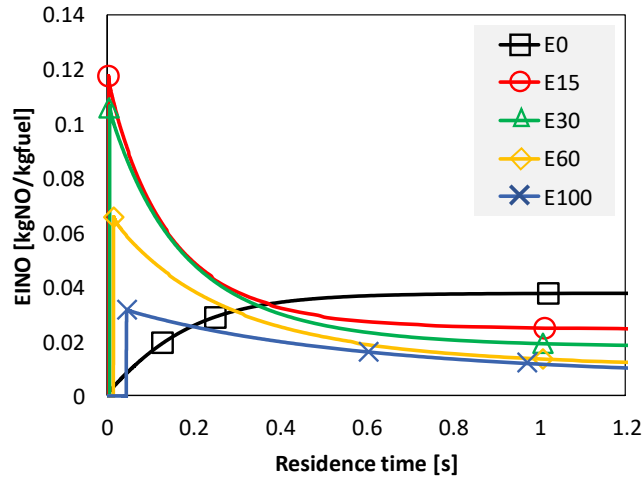


Fig. 2.36. EINO in freely propagating flame (FPF) for ammonia/methane mixtures at stoichiometry.

The evolution of EINO with  $\tau$  for premixed counterflow twin flames is presented in Fig. 2.37. The calculation for large residence time requires to perform calculations on extensively longer domains, as explained earlier. For this reason, only  $\tau < 0.1$  s are presented in this figure. The trend for those values of  $\tau$  is the same as the ones observed for freely propagating flames. The peak observed is however smaller in the small  $\tau$  region.

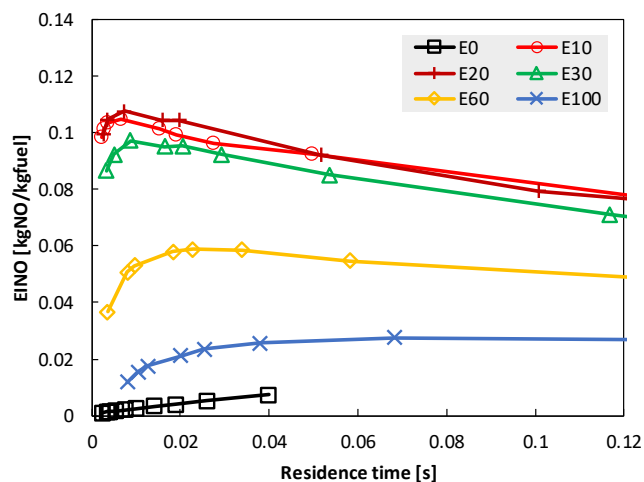


Fig. 2.37. EINO in PCF for ammonia/methane mixtures at stoichiometry.

To compare the stretched and unstretched case, the EINO for freely propagating flame and premixed counterflow twin flames is presented in Fig. 2.38 for  $E = 0, 0.3, \text{ and } 1$ . As observed earlier for simple methane or ammonia case, the value of the EINO of the two flames tends to converge for large  $\tau$  (small stretch rates), while being slightly smaller for small  $\tau$  (large stretch rates).

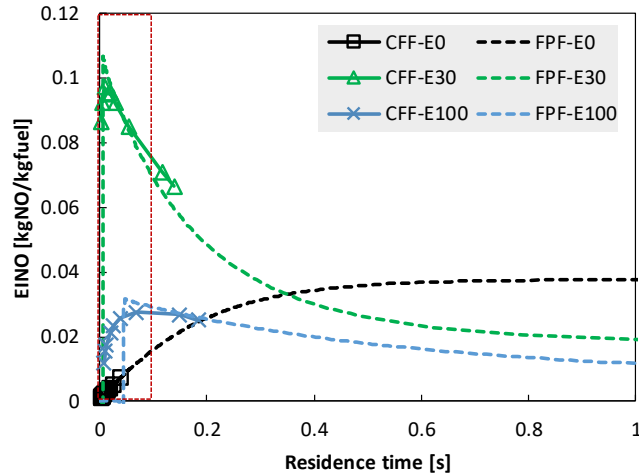


Fig. 2.38. EINO of PCF in plain lines and symbols, and FPF in dashed lines, for fuel mixing ratio  $E = 0, 0.3, \text{ and } 1$ . The dashed red rectangle corresponds to the region shown in Fig. 2.37.

## 5. Conclusions

Ammonia, methane and ammonia/methane flames were investigated numerically in this chapter from the viewpoint of combustion chemistry and the main characteristics of those flames were highlighted. A global approach, using reaction path, flame structure, heat release, and emission analysis was developed in Section 0. This was followed by a study of the effect of the radical diffusion, and more specifically back-diffusion, on laminar burning velocity and extinction stretch rate, both fundamental propagation characteristics of the flames in Section 3. Finally, Section 4 focused more specifically on NO emission index in stretched counterflow ammonia/methane flames and the impact of the reduced residence time on the emissions. The main results of the present chapter are summarized in the following.

From the global flame study, it could be observed that:

- A comparison between ammonia and methane flames structures allows identifying the similarity between the flames but also the main singularities observed for ammonia. One specificity of the ammonia flame is the predominance of the OH radical in the flame chemistry, with a key role in main reaction sub-paths, heat release, and a preponderant impact on flame properties.
- Ammonia/methane flame reaction path remains, overall, similar to that of the two fuels taken separately. However, interactions between the two oxidation paths, though being minor are of interest as they are responsible for the emissions of pollutants (HCN, CN...) and as they interact with the NO<sub>x</sub> formation/reduction. These interactions involve indeed NO and N species interacting with the CH<sub>i</sub> radicals and HCCO to form HCNO, H<sub>2</sub>CN, HCN, CN, and NCO, joining the ammonia oxidation path by reduction to NH, and to lower extent NH<sub>2</sub> and N<sub>2</sub>O, and the production of CO.
- The interactions between the two oxidations path were found to be more pronounced in the range  $E = 0.1 - 0.3$ , merely investigated in the literature, also corresponding to a higher production of NO<sub>2</sub> and N<sub>2</sub>O, HCN and CN, and unburnt methane. Unburnt ammonia and NO showed a peak for greater values of  $E$ , close to  $E = 0.6$ .
- The NO formation and reduction mechanisms were studied in detail. It could be observed that the NO formation path is highly dependent on the quantity of ammonia in the fuel mixture, with fuel-

NO routes becoming gradually more important and changing the overall chemistry. The impact on the NH consumption is particularly important, changing from N and NO production routes, previously observed in the literature, to N<sub>2</sub>O and N<sub>2</sub> direct reduction as well as N<sub>2</sub>H, N<sub>2</sub>H<sub>2</sub> production, emphasizing the N<sub>2</sub>H<sub>2</sub> → N<sub>2</sub>H → N<sub>2</sub> reaction branch of ammonia oxidation path. The C-N interactions and their impact on the NO<sub>x</sub> formation chemistry were found to be highly dependent on the availability of NH and CH<sub>3</sub> radicals in the flames, in addition to the H, O, and OH radical pool.

From the radical diffusion study, the following conclusions can be drawn:

- Laminar burning velocity was found to increase with enhanced diffusion of H, O, and OH radicals in the flame. The importance of these radicals diffusion is however different depending on the flame. Whereas H is a key limiting parameter in the H<sub>2</sub> flame propagation, H and OH enhanced diffusion are, in this order, stimulating the methane flame propagation. In the case of ammonia, OH was found to be predominant. These observations were found to be consistent with the relative importance of the radicals inside the flame, and particularly in the first reactions occurring at the beginning of the reaction zone, initiating the combustion. The case of ammonia/methane was shown to corresponds to the observation on methane and ammonia flame, with a larger dependence on OH when ammonia is gradually introduced.
- The effect of radical diffusion on the extinction stretch rate was found to be lower than for the laminar burning velocity, and eventually reducing the extinction stretch rate. This was related to the broadening of the reaction zone and the loss of radicals in the burnt gas region as the residence time is reduced.

From the NO emission study in stretched flames, it could be seen that:

- From the 1D freely propagating flame (FPF) observation it could be seen that short residence time leads to higher NO emissions in the flame. However, for longer residence time, thanks to the

reduction of the NO in the burnt gas region for larger ammonia mixing ratios, the EINO was found to be decreasing.

- For counterflow premixed twin flames (PCF), it was found that for small residence time, EINO is smaller than the one of freely propagating flame (FPF), and converge to the same value for larger residence time.

# Appendix

## 2A. Detailed reaction path with Okafor's mechanism

The detail of the reaction path summarized by sub-paths in Chapter 2 is detailed in the following tables. All the tables are obtained using the freely propagating model (FPF), at  $\phi = 1.0$  and 1atm.

Table 2A. 1. Detailed reaction path with Okafor's mechanism.

### a) Methane oxidation

Sub-path	Nb	Reaction	<i>E</i>						
			0	0.05	0.10	0.15	0.20	0.30	0.60
CH → HCO	128	CH+O <sub>2</sub> = O+HCO	0.051	0.041	0.034	0.029	0.024	0.017	0.005
C <sub>2</sub> H <sub>2</sub> → C <sub>2</sub> H	23	O+C <sub>2</sub> H <sub>2</sub> = OH+C <sub>2</sub> H	0.000	0.000	0.000	0.000	0.000	0.000	0.000
	112	OH+C <sub>2</sub> H <sub>2</sub> = C <sub>2</sub> H+H <sub>2</sub> O							
C <sub>2</sub> H <sub>2</sub> → CH <sub>2</sub> CO	110	OH+C <sub>2</sub> H <sub>2</sub> = H+CH <sub>2</sub> CO	0.000	0.000	0.000	0.000	0.000	0.000	0.000
C <sub>2</sub> H <sub>2</sub> → CO	24	O+C <sub>2</sub> H <sub>2</sub> = CO+CH <sub>2</sub>	0.005	0.005	0.005	0.005	0.005	0.005	0.002
C <sub>2</sub> H <sub>2</sub> → HCCO	22	O+C <sub>2</sub> H <sub>2</sub> = H+HCCO	0.009	0.010	0.010	0.010	0.010	0.009	0.004
C <sub>2</sub> H <sub>2</sub> → HCCOH	111	OH+C <sub>2</sub> H <sub>2</sub> = H+HCCOH	0.000	0.000	0.000	0.000	0.000	0.000	0.000
C <sub>2</sub> H <sub>3</sub> → C <sub>2</sub> H <sub>2</sub>	72	H+C <sub>2</sub> H <sub>2</sub> (+M) = C <sub>2</sub> H <sub>3</sub> (+M)	0.013	0.015	0.015	0.015	0.015	0.014	0.006
	74	H+C <sub>2</sub> H <sub>3</sub> = H <sub>2</sub> +C <sub>2</sub> H <sub>2</sub>							
C <sub>2</sub> H <sub>3</sub> → CH <sub>2</sub> CHO	188	C <sub>2</sub> H <sub>3</sub> +O <sub>2</sub> = O+CH <sub>2</sub> CHO	0.007	0.007	0.007	0.007	0.006	0.005	0.002
C <sub>2</sub> H <sub>3</sub> → CH <sub>2</sub> CO	25	O+C <sub>2</sub> H <sub>3</sub> = H+CH <sub>2</sub> CO	0.001	0.001	0.001	0.001	0.000	0.000	0.000
C <sub>2</sub> H <sub>4</sub> → C <sub>2</sub> H <sub>2</sub>	177	C <sub>2</sub> H <sub>4</sub> (+M) = H <sub>2</sub> +C <sub>2</sub> H <sub>2</sub> (+M)	0.000	0.000	0.000	0.000	0.000	0.000	0.000
C <sub>2</sub> H <sub>4</sub> → C <sub>2</sub> H <sub>3</sub>	76	H+C <sub>2</sub> H <sub>4</sub> = C <sub>2</sub> H <sub>3</sub> +H <sub>2</sub>	0.025	0.027	0.027	0.026	0.025	0.022	0.009
	115	OH+C <sub>2</sub> H <sub>4</sub> = C <sub>2</sub> H <sub>3</sub> +H <sub>2</sub> O							
C <sub>2</sub> H <sub>4</sub> → CH <sub>2</sub> CHO	181	O+C <sub>2</sub> H <sub>4</sub> = H+CH <sub>2</sub> CHO	0.004	0.004	0.004	0.003	0.003	0.002	0.001
C <sub>2</sub> H <sub>4</sub> → HCO	26	O+C <sub>2</sub> H <sub>4</sub> = CH <sub>3</sub> +HCO	0.007	0.007	0.007	0.006	0.006	0.005	0.002
C <sub>2</sub> H <sub>5</sub> → C <sub>2</sub> H <sub>4</sub>	75	H+C <sub>2</sub> H <sub>4</sub> (+M) = C <sub>2</sub> H <sub>5</sub> (+M)	0.020	0.024	0.025	0.025	0.025	0.023	0.011
	178	C <sub>2</sub> H <sub>5</sub> +O <sub>2</sub> = HO <sub>2</sub> +C <sub>2</sub> H <sub>4</sub>							
C <sub>2</sub> H <sub>5</sub> → C <sub>3</sub> H <sub>8</sub>	206	CH <sub>3</sub> +C <sub>2</sub> H <sub>5</sub> (+M) = C <sub>3</sub> H <sub>8</sub> (+M)	0.001	0.001	0.001	0.001	0.001	0.000	0.000
C <sub>2</sub> H <sub>5</sub> → CH <sub>3</sub> CHO	182	O+C <sub>2</sub> H <sub>5</sub> = H+CH <sub>3</sub> CHO	0.004	0.004	0.003	0.002	0.002	0.001	0.000
C <sub>2</sub> H <sub>6</sub> → C <sub>2</sub> H <sub>5</sub>	28	O+C <sub>2</sub> H <sub>6</sub> = OH+C <sub>2</sub> H <sub>5</sub>	0.062	0.059	0.054	0.048	0.043	0.032	0.011
	79	H+C <sub>2</sub> H <sub>6</sub> = C <sub>2</sub> H <sub>5</sub> +H <sub>2</sub>							
C <sub>3</sub> H <sub>8</sub> → C <sub>3</sub> H <sub>7</sub>	116	OH+C <sub>2</sub> H <sub>6</sub> = C <sub>2</sub> H <sub>5</sub> +H <sub>2</sub> O	0.001	0.001	0.001	0.001	0.001	0.000	0.000
	207	O+C <sub>3</sub> H <sub>8</sub> = OH+C <sub>3</sub> H <sub>7</sub>							
	208	H+C <sub>3</sub> H <sub>8</sub> = C <sub>3</sub> H <sub>7</sub> +H <sub>2</sub>							
	209	OH+C <sub>3</sub> H <sub>8</sub> = C <sub>3</sub> H <sub>7</sub> +H <sub>2</sub> O							
CH → C	50	H+CH = C+H <sub>2</sub>	0.010	0.008	0.006	0.005	0.004	0.002	0.000
CH → CH <sub>2</sub> O	130	CH+H <sub>2</sub> O = H+CH <sub>2</sub> O	0.018	0.017	0.016	0.015	0.014	0.012	0.005
CH <sub>2</sub> (S) → CH <sub>2</sub>	145	CH <sub>2</sub> (S)+N <sub>2</sub> = CH <sub>2</sub> +N <sub>2</sub>	0.118	0.106	0.095	0.085	0.075	0.058	0.022
	151	CH <sub>2</sub> (S)+H <sub>2</sub> O = CH <sub>2</sub> +H <sub>2</sub> O							
CH <sub>2</sub> (S) → CH <sub>2</sub> O	156	CH <sub>2</sub> (S)+CO <sub>2</sub> = CO+CH <sub>2</sub> O	0.009	0.009	0.008	0.008	0.007	0.005	0.002

$\text{CH}_2(\text{S}) \rightarrow \text{CH}_2\text{OH}$	63	$\text{H}+\text{CH}_2\text{OH} = \text{CH}_2(\text{S})+\text{H}_2\text{O}$	0.003	0.003	0.003	0.003	0.003	0.003	0.002
$\text{CH}_2(\text{S}) \rightarrow \text{CH}_3\text{OH}$	150	$\text{CH}_2(\text{S})+\text{H}_2\text{O}(+\text{M}) = \text{CH}_3\text{OH}(+\text{M})$	0.003	0.003	0.003	0.003	0.003	0.002	0.001
$\text{CH}_2(\text{S}) \rightarrow \text{CO}$	147	$\text{CH}_2(\text{S})+\text{O}_2 = \text{H}+\text{OH}+\text{CO}$	0.045	0.038	0.034	0.029	0.026	0.020	0.008
	148	$\text{CH}_2(\text{S})+\text{O}_2 = \text{CO}+\text{H}_2\text{O}$							
$\text{CH}_2 \rightarrow \text{CH}$	129	$\text{CH}+\text{H}_2 = \text{H}+\text{CH}_2$	0.087	0.077	0.067	0.059	0.051	0.038	0.012
	95	$\text{OH}+\text{CH}_2 = \text{CH}+\text{H}_2\text{O}$							
$\text{CH}_2 \rightarrow \text{CH}_2\text{O}$	94	$\text{OH}+\text{CH}_2 = \text{H}+\text{CH}_2\text{O}$	0.027	0.024	0.023	0.021	0.019	0.016	0.008
	185	$\text{CH}_2+\text{O}_2 = \text{O}+\text{CH}_2\text{O}$							
$\text{CH}_2 \rightarrow \text{CO}$	138	$\text{CH}_2+\text{O}_2 \Rightarrow \text{OH}+\text{H}+\text{CO}$	0.035	0.033	0.030	0.028	0.026	0.022	0.011
$\text{CH}_2 \rightarrow \text{CO}_2$	184	$\text{CH}_2+\text{O}_2 \Rightarrow 2\text{H}+\text{CO}_2$	0.041	0.038	0.035	0.032	0.030	0.025	0.013
$\text{CH}_2\text{CO} \rightarrow \text{HCCO}$	81	$\text{H}+\text{CH}_2\text{CO} = \text{HCCO}+\text{H}_2$	0.004	0.004	0.004	0.004	0.003	0.003	0.001
	117	$\text{OH}+\text{CH}_2\text{CO} = \text{HCCO}+\text{H}_2\text{O}$							
$\text{CH}_2\text{COH} \rightarrow \text{CH}_2\text{CO}$	198	$\text{H}+\text{CH}_2\text{CO}(+\text{M}) = \text{CH}_2\text{CHO}(+\text{M})$	0.011	0.011	0.011	0.010	0.010	0.008	0.003
	16	$\text{O}+\text{CH}_2\text{O} = \text{OH}+\text{HCO}$							
$\text{CH}_2\text{O} \rightarrow \text{HCO}$	59	$\text{H}+\text{CH}_2\text{O} = \text{HCO}+\text{H}_2$	0.440	0.390	0.349	0.312	0.280	0.224	0.104
	104	$\text{OH}+\text{CH}_2\text{O} = \text{HCO}+\text{H}_2\text{O}$							
	164	$\text{CH}_3+\text{CH}_2\text{O} = \text{HCO}+\text{CH}_4$							
$\text{CH}_2\text{OH} \rightarrow \text{CH}_2\text{O}$	57	$\text{H}+\text{CH}_2\text{O}(+\text{M}) = \text{CH}_2\text{OH}(+\text{M})$	0.035	0.033	0.031	0.029	0.028	0.024	0.014
	172	$\text{CH}_2\text{OH}+\text{O}_2 = \text{HO}_2+\text{CH}_2\text{O}$							
$\text{CH}_3 \rightarrow \text{C}_2\text{H}_6$	161	$2\text{CH}_3(+\text{M}) = \text{C}_2\text{H}_6(+\text{M})$	0.061	0.059	0.053	0.048	0.042	0.032	0.011
$\text{CH}_3 \rightarrow \text{CH}_2\text{O}$	10	$\text{O}+\text{CH}_3 = \text{H}+\text{CH}_2\text{O}$	0.272	0.233	0.201	0.174	0.150	0.111	0.041
	97	$\text{OH}+\text{CH}_3 = \text{H}_2+\text{CH}_2\text{O}$							
	159	$\text{CH}_3+\text{O}_2 = \text{OH}+\text{CH}_2\text{O}$							
$\text{CH}_3 \rightarrow \text{C}_2\text{H}_4$	141	$\text{CH}_2+\text{CH}_3 = \text{H}+\text{C}_2\text{H}_4$	0.010	0.009	0.008	0.007	0.006	0.005	0.001
$\text{C}_2\text{H}_5 \rightarrow \text{CH}_3$	162	$2\text{CH}_3 = \text{H}+\text{C}_2\text{H}_5$	0.035	0.030	0.024	0.018	0.014	0.007	0.000
$\text{CH}_3 \rightarrow \text{CH}_2$	99	$\text{OH}+\text{CH}_3 = \text{CH}_2+\text{H}_2\text{O}$	0.026	0.025	0.023	0.021	0.020	0.016	0.008
	139	$\text{CH}_2+\text{H}_2 = \text{H}+\text{CH}_3$							
$\text{CH}_3 \rightarrow \text{CH}_2(\text{S})$	100	$\text{OH}+\text{CH}_3 = \text{CH}_2(\text{S})+\text{H}_2\text{O}$	0.240	0.218	0.197	0.177	0.159	0.126	0.053
	149	$\text{CH}_2(\text{S})+\text{H}_2 = \text{CH}_3+\text{H}$							
$\text{CH}_3 \rightarrow \text{CH}_2\text{OH}$	62	$\text{H}+\text{CH}_2\text{OH} = \text{OH}+\text{CH}_3$	0.018	0.017	0.017	0.016	0.015	0.013	0.007
$\text{CH}_3 \rightarrow \text{CH}_3\text{O}$	122	$\text{HO}_2+\text{CH}_3 = \text{OH}+\text{CH}_3\text{O}$	0.076	0.067	0.061	0.057	0.053	0.047	0.030
$\text{CH}_3 \rightarrow \text{CH}_3\text{OH}$	98	$\text{OH}+\text{CH}_3(+\text{M}) = \text{CH}_3\text{OH}(+\text{M})$	0.016	0.014	0.013	0.011	0.010	0.008	0.004
$\text{CH}_3 \rightarrow \text{CO}$	11	$\text{O}+\text{CH}_3 = \text{H}+\text{H}_2+\text{CO}$	0.174	0.148	0.127	0.109	0.094	0.068	0.024
$\text{CH}_3\text{CHO} \rightarrow \text{CH}_2\text{CHO}$	193	$\text{H}+\text{CH}_3\text{CHO} = \text{CH}_2\text{CHO}+\text{H}_2$	0.001	0.001	0.001	0.001	0.001	0.001	0.000
$\text{CH}_3\text{O} \rightarrow \text{CH}_2\text{O}$	58	$\text{H}+\text{CH}_2\text{O}(+\text{M}) = \text{CH}_3\text{O}(+\text{M})$	0.067	0.063	0.060	0.057	0.054	0.049	0.033
	173	$\text{CH}_3\text{O}+\text{O}_2 = \text{HO}_2+\text{CH}_2\text{O}$							
$\text{CH}_3\text{OH} \rightarrow \text{CH}_2\text{OH}$	19	$\text{O}+\text{CH}_3\text{OH} = \text{OH}+\text{CH}_2\text{OH}$	0.015	0.014	0.012	0.011	0.010	0.008	0.004
	69	$\text{H}+\text{CH}_3\text{OH} = \text{CH}_2\text{OH}+\text{H}_2$							
	107	$\text{OH}+\text{CH}_3\text{OH} = \text{CH}_2\text{OH}+\text{H}_2\text{O}$							
$\text{CH}_3\text{OH} \rightarrow \text{CH}_3\text{O}$	108	$\text{OH}+\text{CH}_3\text{OH} = \text{CH}_3\text{O}+\text{H}_2\text{O}$	0.004	0.003	0.003	0.003	0.002	0.002	0.001
$\text{CH}_4 \rightarrow \text{CH}_3$	12	$\text{O}+\text{CH}_4 = \text{OH}+\text{CH}_3$	1.000	0.895	0.801	0.715	0.637	0.502	0.216
	54	$\text{H}+\text{CH}_4 = \text{CH}_3+\text{H}_2$							
	101	$\text{OH}+\text{CH}_4 = \text{CH}_3+\text{H}_2\text{O}$							
$\text{CH}_4 \rightarrow \text{C}_2\text{H}_4$	133	$\text{CH}+\text{CH}_4 = \text{H}+\text{C}_2\text{H}_4$	0.005	0.003	0.003	0.002	0.002	0.001	0.000
$\text{CO} \rightarrow \text{CO}_2$	102	$\text{OH}+\text{CO} = \text{H}+\text{CO}_2$	0.745	0.667	0.600	0.538	0.482	0.384	0.172
	123	$\text{HO}_2+\text{CO} = \text{OH}+\text{CO}_2$							

HCCO → CH <sub>2</sub> (S)	80	H+HCCO = CH <sub>2</sub> (S)+CO	0.010	0.009	0.009	0.008	0.008	0.006	0.002
HCCO → CO	179	HCCO+O <sub>2</sub> = OH+2CO	0.005	0.005	0.005	0.005	0.005	0.005	0.003
HCCOH → CH <sub>2</sub> CO	83	H+HCCOH = H+CH <sub>2</sub> CO	0.000	0.000	0.000	0.000	0.000	0.000	0.000
	169	HCO+H <sub>2</sub> O = H+CO+H <sub>2</sub> O							
HCO → CO	170	HCO+M = H+CO+M	0.439	0.397	0.360	0.325	0.294	0.238	0.110
	171	HCO+O <sub>2</sub> = HO <sub>2</sub> +CO							

## b) Ammonia oxidation

Sub-path	Nb	Reaction	<i>E</i>						
			0	0.05	0.10	0.15	0.20	0.30	0.60
HNO → NO	271	H+NO+M = HNO+M							
	272	HNO+O = NO+OH							
	273	HNO+H = H <sub>2</sub> +NO	0.000	0.051	0.087	0.116	0.139	0.173	0.216
	274	HNO+OH = NO+H <sub>2</sub> O							
	275	HNO+O <sub>2</sub> = HO <sub>2</sub> +NO							
N → N <sub>2</sub>	254	NH <sub>2</sub> +N = N <sub>2</sub> +2H	0.000	0.000	0.001	0.002	0.003	0.005	0.011
N → NO	221	N+O <sub>2</sub> = NO+O	0.001	0.011	0.015	0.018	0.021	0.025	0.034
	222	N+OH = NO+H							
N <sub>2</sub> H <sub>2</sub> → N <sub>2</sub> H <sub>3</sub>	283	N <sub>2</sub> H <sub>3</sub> = N <sub>2</sub> H <sub>2</sub> +H	0.000	0.001	0.003	0.005	0.006	0.009	0.012
N <sub>2</sub> H <sub>2</sub> → N <sub>2</sub> H	288	N <sub>2</sub> H <sub>2</sub> +H = NNH+H <sub>2</sub>							
	289	N <sub>2</sub> H <sub>2</sub> +O = NNH+OH							
	291	N <sub>2</sub> H <sub>2</sub> +OH = NNH+H <sub>2</sub> O	0.000	0.002	0.005	0.010	0.015	0.028	0.076
	292	N <sub>2</sub> H <sub>2</sub> +NH = NNH+NH <sub>2</sub>							
N <sub>2</sub> H <sub>3</sub> → N <sub>2</sub> H <sub>2</sub>	284	N <sub>2</sub> H <sub>3</sub> +H = N <sub>2</sub> H <sub>2</sub> +H <sub>2</sub>							
	285	N <sub>2</sub> H <sub>3</sub> +HO <sub>2</sub> = N <sub>2</sub> H <sub>2</sub> +H <sub>2</sub> O <sub>2</sub>	0.000	0.001	0.003	0.005	0.007	0.009	0.013
	287	N <sub>2</sub> H <sub>3</sub> +NH = N <sub>2</sub> H <sub>2</sub> +NH <sub>2</sub>							
N <sub>2</sub> H <sub>4</sub> → N <sub>2</sub> H <sub>3</sub>	286	N <sub>2</sub> H <sub>3</sub> +HO <sub>2</sub> = N <sub>2</sub> H <sub>4</sub> +O <sub>2</sub>	0.000	0.000	0.000	0.000	0.000	0.000	0.001
N <sub>2</sub> O → N <sub>2</sub>	225	N <sub>2</sub> O+H = N <sub>2</sub> +OH	0.000	0.009	0.019	0.029	0.038	0.052	0.070
N <sub>2</sub> O → N <sub>2</sub>	227	N <sub>2</sub> O(+M) = N <sub>2</sub> +O(+M)	0.000	0.000	0.001	0.001	0.002	0.004	0.012
N <sub>2</sub> O → N <sub>2</sub> H	262	NNH+O = N <sub>2</sub> O+H	0.000	0.000	0.001	0.001	0.001	0.002	0.003
NH → HNO	234	NH+OH = HNO+H							
	236	NH+O <sub>2</sub> = HNO+O	0.000	0.012	0.020	0.028	0.035	0.048	0.079
	280	NH+CO <sub>2</sub> = HNO+CO							
NH → N <sub>2</sub>	238	2NH = N <sub>2</sub> +2H	0.000	0.000	0.000	0.001	0.001	0.002	0.005
NH → N <sub>2</sub> H <sub>2</sub>	252	NH <sub>2</sub> +NH = N <sub>2</sub> H <sub>2</sub> +H	0.000	0.002	0.005	0.010	0.016	0.030	0.079
NH → NO	233	NH+O = NO+H	0.000	0.017	0.025	0.031	0.035	0.039	0.038
	237	NH+O <sub>2</sub> = NO+OH							
NH <sub>2</sub> → NH	245	NH <sub>2</sub> +H = NH+H <sub>2</sub>							
	247	NH <sub>2</sub> +O = NH+OH							
	248	NH <sub>2</sub> +OH = NH+H <sub>2</sub> O	0.000	0.060	0.111	0.157	0.200	0.274	0.430
	251	2NH <sub>2</sub> = NH <sub>3</sub> +NH							
NH <sub>2</sub> → H <sub>2</sub> NO	250	NH <sub>2</sub> +O <sub>2</sub> = H <sub>2</sub> NO+O	0.000	0.000	0.000	0.000	0.000	0.001	0.001
NH <sub>2</sub> → HNO	246	NH <sub>2</sub> +O = HNO+H	0.000	0.039	0.066	0.087	0.103	0.124	0.135
NH <sub>2</sub> → N <sub>2</sub> H <sub>4</sub>	281	2NH <sub>2</sub> = N <sub>2</sub> H <sub>4</sub>	0.000	0.000	0.000	0.000	0.000	0.001	0.001

NH <sub>3</sub> → NH <sub>2</sub>	277	NH <sub>3</sub> +H = NH <sub>2</sub> +H <sub>2</sub>							
	278	NH <sub>3</sub> +OH = NH <sub>2</sub> +H <sub>2</sub> O	0.000	0.105	0.199	0.285	0.363	0.498	0.784
	279	NH <sub>3</sub> +O = NH <sub>2</sub> +OH							
N <sub>2</sub> H → N <sub>2</sub>	260	NNH = N <sub>2</sub> +H							
	265	NNH+O <sub>2</sub> = N <sub>2</sub> +HO <sub>2</sub>	0.000	0.006	0.017	0.028	0.041	0.066	0.139
	266	NNH+O <sub>2</sub> = N <sub>2</sub> +H+O <sub>2</sub>							
NO → N <sub>2</sub>	220	N+NO = N <sub>2</sub> +O							
	242	NH+NO = N <sub>2</sub> +OH	-0.001	0.019	0.039	0.055	0.069	0.089	0.115
	256	NH <sub>2</sub> +NO = N <sub>2</sub> +H <sub>2</sub> O							
NO → N <sub>2</sub> O	240	NH+NO = N <sub>2</sub> O+H	0.000	0.009	0.020	0.031	0.041	0.058	0.085
	241	NH+NO = N <sub>2</sub> O+H							
NO → N <sub>2</sub> H	257	NH <sub>2</sub> +NO = NNH+OH	0.000	0.005	0.011	0.019	0.026	0.038	0.062
	263	NNH+O = NH+NO							
NO → NO <sub>2</sub>	228	HO <sub>2</sub> +NO = NO <sub>2</sub> +OH	0.000	0.026	0.032	0.033	0.032	0.029	0.018
	229	NO+O+M = NO <sub>2</sub> +M							
NO <sub>2</sub> → HONO	243	NH+HONO = NH <sub>2</sub> +NO <sub>2</sub>	0.000	0.000	0.000	0.000	0.000	0.000	0.000
	276	HNO+NO <sub>2</sub> = HONO+NO							
NH → N	232	NH+H = N+H <sub>2</sub>	0.000	0.023	0.038	0.049	0.058	0.071	0.087
	235	NH+OH = N+H <sub>2</sub> O							
NO <sub>2</sub> → NO	231	NO <sub>2</sub> +H = NO+OH	0.000	0.026	0.031	0.032	0.031	0.028	0.018

## c) Interactions

Sub-path	Nb	Reaction	<i>E</i>						
			0	0.05	0.10	0.15	0.20	0.30	0.60
CH → HCN	326	CH+NO = HCN+O	0.000	0.002	0.003	0.003	0.003	0.002	0.001
CH → HCNN	321	CH+N <sub>2</sub> (+M) = HCNN(+M)	0.000	0.000	0.000	0.000	0.000	0.000	0.000
C → CN	324	C+NO = CN+O	0.000	0.000	0.000	0.000	0.000	0.000	0.000
CH → NCO	327	CH+NO = H+NCO	0.000	0.001	0.001	0.001	0.001	0.001	0.000
NCO → CO	303	NCO+H = NH+CO	0.000	0.007	0.008	0.009	0.009	0.008	0.003
HOCN → HNCO	353	HOCN+H = H+HNCO	0.000	0.001	0.001	0.001	0.001	0.001	0.001
HNCO → CO	345	HNCO+H = NH <sub>2</sub> +CO	0.000	0.006	0.008	0.008	0.008	0.008	0.004
HNCO → NCO	344	HNCO+O = NCO+OH	0.000	0.001	0.002	0.002	0.002	0.002	0.001
	347	HNCO+OH = NCO+H <sub>2</sub> O							
HCN → CN	299	CN+H <sub>2</sub> O = HCN+OH							
	301	CN+H <sub>2</sub> = HCN+H	0.000	0.002	0.003	0.003	0.003	0.003	0.001
	313	HCN+O = CN+OH							
HCN → HNCO	315	HCN+OH = HNCO+H	0.000	0.000	0.000	0.000	0.000	0.000	0.000
HCN → HOCN	314	HCN+OH = HOCN+H	0.000	0.001	0.001	0.001	0.001	0.001	0.001
HCN → NCO	311	HCN+O = NCO+H	0.000	0.004	0.006	0.006	0.006	0.005	0.002
HCNO → HCN	351	HCNO+H = OH+HCN	0.000	0.000	0.000	0.000	0.000	0.000	0.000
HCNO → HNCO	350	HCNO+H = H+HNCO	0.000	0.002	0.002	0.003	0.003	0.002	0.001
HCCO → HCNO	354	HCCO+NO = HCNO+CO	0.000	0.001	0.002	0.002	0.002	0.002	0.001
H <sub>2</sub> CN → HCN	317	H+HCN(+M) = H <sub>2</sub> CN(+M)	0.000	0.003	0.004	0.005	0.005	0.005	0.003
CN → NCO	298	CN+OH = NCO+H	0.000	0.002	0.002	0.002	0.003	0.002	0.001
	300	CN+O <sub>2</sub> = NCO+O							

## Appendix 2A Detailed reaction path with Okafor's mechanism

CH <sub>3</sub> → H <sub>2</sub> CN	336	CH <sub>3</sub> +NO = H <sub>2</sub> CN+OH	0.000	0.003	0.004	0.005	0.005	0.005	0.003
	355	CH <sub>3</sub> +N = H <sub>2</sub> CN+H							
CH <sub>3</sub> → HCN	335	CH <sub>3</sub> +NO = HCN+H <sub>2</sub> O	0.000	0.001	0.002	0.002	0.002	0.002	0.001
	356	CH <sub>3</sub> +N = HCN+H <sub>2</sub>							
CH <sub>2</sub> → HCN	330	CH <sub>2</sub> +NO = OH+HCN	0.000	0.001	0.001	0.001	0.001	0.001	0.001
CH <sub>2</sub> → HCNO	331	CH <sub>2</sub> +NO = H+HCNO	0.000	0.001	0.001	0.001	0.001	0.001	0.000
CH <sub>2</sub> → HNCO	329	CH <sub>2</sub> +NO = H+HNCO	0.000	0.005	0.006	0.007	0.007	0.006	0.003
CH <sub>2</sub> (S) → HCNO	334	CH <sub>2</sub> (S)+NO = H+HCNO	0.000	0.001	0.001	0.001	0.001	0.001	0.000
	332	CH <sub>2</sub> (S)+NO = H+HNCO							

## 2B. Reaction path using other chemistries

The reaction path of ammonia/methane flames was investigated for 3 other mechanisms, Tian's [69], GRI-Mech 3.0 [122], and UCSD mechanisms [96], in addition to the Okafor's mechanism for which results are presented in Section 2.1. No major differences were observed. The minor differences observed between those mechanisms were, as summarized in Section 2.1, related to the  $N_2H_x$  reaction subset, and its presence or not in the mechanisms. The full tables for the reaction paths using those mechanisms are introduced in the following.

Simulations were performed on Chemkin-pro, using the 1D FPF model. The equivalence ratio is equal to 1 in all the simulations. The reaction numbering corresponds to the reaction numbering within each mechanism. Reactions are gathered by sub-paths as in Section 2.1, but some difference exists in the subpaths due to the differences in the reaction subsets of the mechanisms.

NNH and  $N_2H$  correspond to the same species, written using one or the other formulation depending on the mechanism. Sub-paths are written with  $N_2H$ , following the nomenclature in this thesis, but the individual reactions are written as in the original mechanisms used.

### Reaction path with Tian's mechanism

Table 2A. 2. Reaction path with Tian's mechanism

a) Methane oxidation

Sub-paths	Nb	Reaction	E = 0	E = 0.15	E = 0.30	Trend
<b>CH<sub>4</sub> → CH<sub>3</sub></b>	59	CH <sub>4</sub> +H = CH <sub>3</sub> +H <sub>2</sub>	1.000	0.705	0.496	↘↘
	60	CH <sub>4</sub> +O = CH <sub>3</sub> +OH				
	61	CH <sub>4</sub> +OH = CH <sub>3</sub> +H <sub>2</sub> O				
	574	CH <sub>4</sub> +NH <sub>2</sub> = CH <sub>3</sub> +NH <sub>3</sub>				
<b>CH<sub>3</sub> → CH<sub>2</sub>O</b>	68	CH <sub>3</sub> +O = CH <sub>2</sub> O+H	0.234	0.138	0.085	↘↘
	75	CH <sub>3</sub> +O <sub>2</sub> = CH <sub>2</sub> O+OH				
<b>CH<sub>3</sub> → CH<sub>2</sub>OH</b>	124	CH <sub>2</sub> OH+H = CH <sub>3</sub> +OH	0.329	0.241	0.175	↘
<b>CH<sub>3</sub> → CO</b>	69	CH <sub>3</sub> +O = H <sub>2</sub> +CO+H	0.077	0.044	0.026	↘↘
	76	CH <sub>3</sub> +HCO = CH <sub>4</sub> +CO				
<b>CH<sub>3</sub> → CH<sub>2</sub></b>	66	CH <sub>3</sub> +H = CH <sub>2</sub> +H <sub>2</sub>	0.043	0.028	0.018	↘↘
	70	CH <sub>3</sub> +OH = CH <sub>2</sub> +H <sub>2</sub> O				
<b>CH<sub>3</sub> → CH<sub>2</sub>*</b>	67	CH <sub>2</sub> (S)+H <sub>2</sub> = CH <sub>3</sub> +H	0.017	0.012	0.008	↘
	71	CH <sub>3</sub> +OH = CH <sub>2</sub> (S)+H <sub>2</sub> O				

	92	$\text{CH}_2(\text{S})+\text{M} = \text{CH}_2+\text{M}$				
	93	$\text{CH}_2(\text{S})+\text{N}_2 = \text{CH}_2+\text{N}_2$				
<b><math>\text{CH}_2^* \rightarrow \text{CH}_2</math></b>	95	$\text{CH}_2(\text{S})+\text{H} = \text{CH}_2+\text{H}$	0.068	0.037	0.021	$\Downarrow\Downarrow$
	99	$\text{CH}_2(\text{S})+\text{O}_2 = \text{CH}_2+\text{O}_2$				
	100	$\text{CH}_2(\text{S})+\text{H}_2\text{O} = \text{CH}_2+\text{H}_2\text{O}$				
<b><math>\text{CH}_2 \rightarrow \text{CH}</math></b>	81	$\text{CH}_2+\text{H} = \text{CH}+\text{H}_2$	0.0329	0.0192	0.0111	$\Downarrow\Downarrow$
<b><math>\text{CH}_2^* \rightarrow \text{CH}</math></b>	96	$\text{CH}_2(\text{S})+\text{H} = \text{CH}+\text{H}_2$	0.0005	0.0003	0.0001	$\Downarrow\Downarrow$
	73	$\text{CH}_3+\text{HO}_2 = \text{CH}_3\text{O}+\text{OH}$				
	74	$\text{CH}_3+\text{O}_2 = \text{CH}_3\text{O}+\text{O}$				
<b><math>\text{CH}_3 \rightarrow \text{CH}_3\text{O}</math></b>	139	$\text{CH}_3\text{O}+\text{H} = \text{CH}_3+\text{OH}$	0.056	0.047	0.038	$\Downarrow$
	551	$\text{CH}_3+\text{NO}_2 = \text{CH}_3\text{O}+\text{NO}$				
	593	$\text{CH}_3+\text{H}_2\text{NO} = \text{CH}_3\text{O}+\text{NH}_2$				
	122	$\text{CH}_2\text{OH}(\text{+M}) = \text{CH}_2\text{O}+\text{H}(\text{+M})$				
<b><math>\text{CH}_2\text{OH} \rightarrow \text{CH}_2\text{O}</math></b>	127	$\text{CH}_2\text{OH}+\text{OH} = \text{CH}_2\text{O}+\text{H}_2\text{O}$	0.321	0.236	0.172	$\Downarrow$
	129	$\text{CH}_2\text{OH}+\text{O}_2 = \text{CH}_2\text{O}+\text{HO}_2$				
<b><math>\text{CH}_3\text{O} \rightarrow \text{CH}_2\text{O}</math></b>	137	$\text{CH}_3\text{O}(\text{+M}) = \text{CH}_2\text{O}+\text{H}(\text{+M})$	0.053	0.044	0.036	$\Downarrow$
	44	$\text{CH}_2\text{O}+\text{H} = \text{HCO}+\text{H}_2$				
<b><math>\text{CH}_2\text{O} \rightarrow \text{HCO}</math></b>	45	$\text{CH}_2\text{O}+\text{O} = \text{HCO}+\text{OH}$	0.682	0.471	0.329	$\Downarrow$
	47	$\text{CH}_2\text{O}+\text{OH} = \text{HCO}+\text{H}_2\text{O}$				
	49	$\text{CH}_2\text{O}+\text{CH}_3 = \text{HCO}+\text{CH}_4$				
	50	$\text{HCO} = \text{H}+\text{CO}$				
<b><math>\text{HCO} \rightarrow \text{CO}</math></b>	51	$\text{HCO}+\text{H} = \text{CO}+\text{H}_2$	0.663	0.437	0.305	$\Downarrow\Downarrow$
	54	$\text{HCO}+\text{OH} = \text{CO}+\text{H}_2\text{O}$				
	55	$\text{HCO}+\text{O}_2 = \text{CO}+\text{HO}_2$				
<b><math>\text{CO} \rightarrow \text{CO}_2</math></b>	34	$\text{CO}+\text{OH} = \text{CO}_2+\text{H}$	0.770	0.545	0.381	$\Downarrow$
	35	$\text{CO}+\text{OH} = \text{CO}_2+\text{H}$				
<b><math>\text{CH}_3 \rightarrow \text{C}_2\text{H}_6</math></b>	78	$2\text{CH}_3(\text{+M}) = \text{C}_2\text{H}_6(\text{+M})$	0.053	0.034	0.021	
	150	$\text{C}_2\text{H}_6+\text{H} = \text{C}_2\text{H}_5+\text{H}_2$				
<b><math>\text{C}_2\text{H}_6 \rightarrow \text{C}_2\text{H}_5</math></b>	151	$\text{C}_2\text{H}_6+\text{O} = \text{C}_2\text{H}_5+\text{OH}$	0.053	0.033	0.020	$\Downarrow$
	152	$\text{C}_2\text{H}_6+\text{OH} = \text{C}_2\text{H}_5+\text{H}_2\text{O}$				
	156	$\text{C}_2\text{H}_6+\text{CH}_3 = \text{C}_2\text{H}_5+\text{CH}_4$				
<b><math>\text{C}_2\text{H}_5 \rightarrow \text{C}_2\text{H}_4</math></b>	158	$\text{C}_2\text{H}_4+\text{H}(\text{+M}) = \text{C}_2\text{H}_5(\text{+M})$	0.058	0.038	0.023	$\Downarrow\Downarrow$
	165	$\text{C}_2\text{H}_5+\text{O}_2 = \text{C}_2\text{H}_4+\text{HO}_2$				
<b><math>\text{C}_2\text{H}_4 \rightarrow \text{C}_2\text{H}_3</math></b>	170	$\text{C}_2\text{H}_3+\text{H}(\text{+M}) = \text{C}_2\text{H}_4(\text{+M})$	0.058	0.037	0.022	$\Downarrow\Downarrow$
	172	$\text{C}_2\text{H}_4+\text{H} = \text{C}_2\text{H}_3+\text{H}_2$				
	180	$\text{C}_2\text{H}_4+\text{OH} = \text{C}_2\text{H}_3+\text{H}_2\text{O}$				
<b><math>\text{C}_2\text{H}_3 \rightarrow \text{C}_2\text{H}_2</math></b>	186	$\text{C}_2\text{H}_2+\text{H}(\text{+M}) = \text{C}_2\text{H}_3(\text{+M})$	0.041	0.027	0.017	$\Downarrow\Downarrow$
	187	$\text{C}_2\text{H}_3+\text{H} = \text{C}_2\text{H}_2+\text{H}_2$				
	190	$\text{C}_2\text{H}_3+\text{OH} = \text{C}_2\text{H}_2+\text{H}_2\text{O}$				
<b><math>\text{C}_2\text{H}_2 \rightarrow \text{HCCO}</math></b>	208	$\text{C}_2\text{H}_2+\text{O} = \text{HCCO}+\text{H}$	0.027	0.017	0.011	$\Downarrow\Downarrow$
<b><math>\text{HCCO} \rightarrow \text{C}_2\text{O}</math></b>	287	$\text{HCCO}+\text{OH} = \text{C}_2\text{O}+\text{H}_2\text{O}$	0.005	0.003	0.002	$\Downarrow$

## b) Ammonia oxidation

Sub-paths	Nb	Reaction	E = 0	E = 0.15	E = 0.30	Trend
<b>NH<sub>3</sub> → NH<sub>2</sub></b>	352	NH <sub>3</sub> +H = NH <sub>2</sub> +H <sub>2</sub>				
	353	NH <sub>3</sub> +O = NH <sub>2</sub> +OH	0.000	0.295	0.504	↗ ↗
	354	NH <sub>3</sub> +OH = NH <sub>2</sub> +H <sub>2</sub> O				
<b>NH<sub>2</sub> → NH</b>	356	NH <sub>2</sub> +H = NH+H <sub>2</sub>				
	358	NH <sub>2</sub> +O = NH+OH				
	359	NH <sub>2</sub> +O = NH+OH	0.000	0.147	0.250	↗ ↗
	360	NH <sub>2</sub> +OH = NH+H <sub>2</sub> O				
	365	2NH <sub>2</sub> = NH <sub>3</sub> +NH				
<b>NH<sub>2</sub> → HNO</b>	357	NH <sub>2</sub> +O = HNO+H	0.000	0.067	0.097	↗
<b>NH<sub>2</sub> → H<sub>2</sub>NO</b>	361	NH <sub>2</sub> +HO <sub>2</sub> = H <sub>2</sub> NO+OH	0.000	0.034	0.049	↗
	374	NH <sub>2</sub> +NO <sub>2</sub> = H <sub>2</sub> NO+NO				
<b>H<sub>2</sub>NO → HNO</b>	444	H <sub>2</sub> NO+H = HNO+H <sub>2</sub>	0.000	0.015	0.022	↗
	447	H <sub>2</sub> NO+OH = HNO+H <sub>2</sub> O				
<b>NH → HNO</b>	377	NH+OH = HNO+H	0.000	0.026	0.043	↗
	379	NH+O <sub>2</sub> = HNO+O				
<b>NH → N</b>	375	NH+H = N+H <sub>2</sub>	0.000	0.040	0.060	↗
	378	NH+OH = N+H <sub>2</sub> O				
<b>NH → NO</b>	376	NH+O = NO+H	0.000	0.024	0.031	↗
	380	NH+O <sub>2</sub> = NO+OH				
<b>HNO → NO</b>	304	HNO+H = NO+H <sub>2</sub>				
	305	HNO+O = NO+OH				
	306	HNO+OH = NO+H <sub>2</sub> O	0.000	0.112	0.130	↗
	307	HNO+O <sub>2</sub> = HO <sub>2</sub> +NO				
	310	NO+H(+M) = HNO(+M)				
<b>N → NO</b>	388	N+OH = NO+H	0.001	0.017	0.025	↗
	389	N+O <sub>2</sub> = NO+O				
<b>NO → N<sub>2</sub>O</b>	383	NH+NO = N <sub>2</sub> O+H	0.000	0.032	0.058	↗
	384	NH+NO = N <sub>2</sub> O+H				
<b>N<sub>2</sub>O → NH</b>	384	NH+NO = N <sub>2</sub> O+H	0.000	0.012	0.022	↗
<b>NO → NO<sub>2</sub></b>	311	NO+O(+M) = NO <sub>2</sub> (+M)				
	314	NO+HO <sub>2</sub> = NO <sub>2</sub> +OH	0.000	0.007	0.005	↗
	315	NO <sub>2</sub> +H = NO+OH				
<b>NO → N<sub>2</sub></b>	370	NH <sub>2</sub> +NO = N <sub>2</sub> +H <sub>2</sub> O				
	385	NH+NO = N <sub>2</sub> +OH	-0.001	0.050	0.084	↗
	390	N+NO = N <sub>2</sub> +O				
<b>N<sub>2</sub>O → N<sub>2</sub></b>	343	N <sub>2</sub> O(+M) = N <sub>2</sub> +O(+M)	0.000	0.031	0.056	↗
	345	N <sub>2</sub> O+H = N <sub>2</sub> +OH				
<b>NH (+NH<sub>2</sub>) → N<sub>2</sub>H<sub>2</sub></b>	366	NH <sub>2</sub> +NH = N <sub>2</sub> H <sub>2</sub> +H	0.000	0.007	0.021	↗
<b>N<sub>2</sub>H<sub>2</sub> → N<sub>2</sub>H</b>	422	N <sub>2</sub> H <sub>2</sub> +M = NNH+H+M				
	423	N <sub>2</sub> H <sub>2</sub> +H = NNH+H <sub>2</sub>	0.000	0.006	0.017	↗
	424	N <sub>2</sub> H <sub>2</sub> +O = NNH+OH				
	426	N <sub>2</sub> H <sub>2</sub> +OH = NNH+H <sub>2</sub> O				
<b>NO → N<sub>2</sub>H</b>	371	NH <sub>2</sub> +NO = NNH+OH	0.000	0.023	0.043	↗
	395	NNH+O = NH+NO				
<b>N<sub>2</sub>O → N<sub>2</sub>H</b>	393	NNH+O = N <sub>2</sub> O+H	0.000	0.001	0.002	↗

$N_2H \rightarrow N_2$	397	$NNH+O_2 = N_2+HO_2$	0.001	0.016	0.032	↗
	398	$NNH+O_2 = N_2+H+O_2$				

## c) Interactions

Sub-paths	Nb	Reaction	E = 0	E = 0.15	E = 0.30	Trend
$HCO \rightarrow HNO$	543	$HCO+NO = HNO+CO$	0.000	0.027	0.021	↗ ↘
$C_2O \rightarrow NCO$	640	$C_2O+NO = CO+NCO$	0.000	0.002	0.001	↗ ↘
$NCO \rightarrow NH$	523	$NCO+H = CO+NH$	0.000	0.011	0.010	↗ ↘
$CH_3 \rightarrow CH_3NH_2$	577	$CH_3+NH_2 = CH_3NH_2$	0.000	0.002	0.002	↗ ⇒
$CH_3NH_2 \rightarrow CH_2NH_2$	647	$CH_3NH_2+H = CH_2NH_2+H_2$	0.000	0.001	0.001	↗ ⇒
	649	$CH_3NH_2+O = CH_2NH_2+OH$				
	651	$CH_3NH_2+OH = CH_2NH_2+H_2O$				
	655	$CH_3NH_2+NH_2 = CH_2NH_2+NH_3$				
$CH_3 \rightarrow CH_2NH_2$	578	$CH_3+NH_2 = CH_2NH_2+H$	0.000	0.001	0.001	↗ ⇒
$CH_2NH_2 \rightarrow CH_2NH$	657	$CH_2NH_2 = CH_2NH+H$	0.000	0.002	0.002	↗ ⇒
	658	$CH_2NH_2+H = CH_2NH+H_2$				
	663	$CH_2NH_2+O_2 = CH_2NH+HO_2$				
$CH_3 \rightarrow CH_2NH$	583	$CH_3+NH = CH_2NH+H$	0.000	0.014	0.018	↗
$CH_2^* \rightarrow CH_2NH$	605	$CH_2(S)+NH_3 = CH_2NH+2H$	0.000	0.003	0.004	↗
$CH_2NH \rightarrow HCNH$	672	$CH_2NH+H = HCNH+H_2$	0.000	0.011	0.014	↗
	674	$CH_2NH+O = HCNH+OH$				
	677	$CH_2NH+OH = HCNH+H_2O$				
	681	$CH_2NH+NH_2 = HCNH+NH_3$				
$HCNH \rightarrow HCN$	691	$HCNH = HCN+H$	0.000	0.010	0.013	↗
	693	$HCNH+H = HCN+H_2$				
$CH_2NH \rightarrow H_2CN$	671	$CH_2NH+H = H_2CN+H_2$	0.000	0.007	0.009	↗
	673	$CH_2NH+O = H_2CN+OH$				
	676	$CH_2NH+OH = H_2CN+H_2O$				
	678	$CH_2NH+CH_3 = H_2CN+CH_4$				
	680	$CH_2NH+NH_2 = H_2CN+NH_3$				
$CH_3 \rightarrow H_2CN$	585	$CH_3+N = H_2CN+H$	0.000	0.004	0.004	↗ ⇒
	592	$CH_3+NO = H_2CN+OH$				
$H_2CN \rightarrow HCN$	682	$H_2CN = HCN+H$	0.000	0.008	0.010	↗
	683	$H_2CN+H = HCN+H_2$				
$HCN \rightarrow CN$	468	$CN+H_2 = HCN+H$	0.000	0.004	0.004	↗ ⇒
	472	$HCN+OH = CN+H_2O$				
$HCN \rightarrow NCO$	469	$HCN+O = NCO+H$	0.000	0.007	0.007	↗ ⇒
$CN \rightarrow NCO$	483	$CN+OH = NCO+H$	0.000	0.006	0.006	↗ ⇒
	484	$CN+O_2 = NCO+O$				

Reaction path with GRI-Mech 3.0

Table 2A. 3. Reaction path with GRI-Mech 3.0

a) Methane oxidation

Sub-path	Nb	Reactions	$E = 0$	$E = 0.15$	$E = 0.30$	Trend
$\text{CH}_4 \rightarrow \text{CH}_3$	11	$\text{O} + \text{CH}_4 = \text{OH} + \text{CH}_3$				
	53	$\text{H} + \text{CH}_4 = \text{CH}_3 + \text{H}_2$	1.000	0.719	0.510	$\searrow \searrow$
	98	$\text{OH} + \text{CH}_4 = \text{CH}_3 + \text{H}_2\text{O}$				
$\text{CH}_3 \rightarrow \text{CH}_2\text{O}$	10	$\text{O} + \text{CH}_3 = \text{H} + \text{CH}_2\text{O}$	0.272	0.173	0.107	$\searrow \searrow$
$\text{CH}_2\text{O} \rightarrow \text{HCO}$	15	$\text{O} + \text{CH}_2\text{O} = \text{OH} + \text{HCO}$				
	58	$\text{H} + \text{CH}_2\text{O} = \text{HCO} + \text{H}_2$	0.439	0.307	0.215	$\searrow$
	101	$\text{OH} + \text{CH}_2\text{O} = \text{HCO} + \text{H}_2\text{O}$				
$\text{HCO} \rightarrow \text{CO}$	55	$\text{H} + \text{HCO} = \text{H}_2 + \text{CO}$				
	100	$\text{OH} + \text{HCO} = \text{H}_2\text{O} + \text{CO}$				
	166	$\text{HCO} + \text{H}_2\text{O} = \text{H} + \text{CO} + \text{H}_2\text{O}$	0.500	0.350	0.245	$\searrow \searrow$
	167	$\text{HCO} + \text{M} = \text{H} + \text{CO} + \text{M}$				
	168	$\text{HCO} + \text{O}_2 = \text{HO}_2 + \text{CO}$				
$\text{CO} \rightarrow \text{CO}_2$	99	$\text{OH} + \text{CO} = \text{H} + \text{CO}_2$	0.737	0.534	0.382	$\searrow \searrow$
$\text{CH}_3 \rightarrow \text{CH}_2^*$	97	$\text{OH} + \text{CH}_3 = \text{CH}_2(\text{S}) + \text{H}_2\text{O}$	0.189	0.139	0.102	$\searrow$
	146	$\text{CH}_2^* + \text{H}_2 = \text{CH}_3 + \text{H}$				
$\text{CH}_2^* \rightarrow \text{CH}_2$	142	$\text{CH}_2^* + \text{N}_2 = \text{CH}_2 + \text{N}_2$				
	148	$\text{CH}_2^* + \text{H}_2\text{O} = \text{CH}_2 + \text{H}_2\text{O}$	0.174	0.132	0.094	$\searrow$
	151	$\text{CH}_2^* + \text{CO} = \text{CH}_2 + \text{CO}$				
	152	$\text{CH}_2^* + \text{CO}_2 = \text{CH}_2 + \text{CO}_2$				
$\text{CH}_3 \rightarrow \text{CH}_2$	96	$\text{OH} + \text{CH}_3 = \text{CH}_2 + \text{H}_2\text{O}$	0.018	0.016	0.013	$\searrow$
	136	$\text{CH}_2 + \text{H}_2 = \text{H} + \text{CH}_3$				
$\text{CH}_2 \rightarrow \text{CH}$	93	$\text{OH} + \text{CH}_2 = \text{CH} + \text{H}_2\text{O}$	-0.070	-0.043	-0.024	$\nearrow$
	126	$\text{CH} + \text{H}_2 = \text{H} + \text{CH}_2$				
$\text{CH} \rightarrow \text{HCO}$	125	$\text{CH} + \text{O}_2 = \text{O} + \text{HCO}$	0.048	0.025	0.013	$\searrow$
$\text{CH}_3 \rightarrow \text{CO}$	284	$\text{O} + \text{CH}_3 = \text{H} + \text{H}_2 + \text{CO}$	0.181	0.115	0.071	$\searrow$
$\text{CH}_3 \rightarrow \text{C}_2\text{H}_6$	158	$2\text{CH}_3(+\text{M}) = \text{C}_2\text{H}_6(+\text{M})$	0.058	0.050	0.039	$\Rightarrow \searrow$
$\text{C}_2\text{H}_6 \rightarrow \text{C}_2\text{H}_5$	27	$\text{O} + \text{C}_2\text{H}_6 = \text{OH} + \text{C}_2\text{H}_5$				
	78	$\text{H} + \text{C}_2\text{H}_6 = \text{C}_2\text{H}_5 + \text{H}_2$	0.059	0.051	0.039	$\Rightarrow \searrow$
	113	$\text{OH} + \text{C}_2\text{H}_6 = \text{C}_2\text{H}_5 + \text{H}_2\text{O}$				
$\text{C}_2\text{H}_5 \rightarrow \text{C}_2\text{H}_4$	74	$\text{H} + \text{C}_2\text{H}_4(+\text{M}) = \text{C}_2\text{H}_5(+\text{M})$	-0.015	-0.023	-0.025	$\searrow$
$\text{C}_2\text{H}_5 \rightarrow \text{CH}_3\text{CHO}$	286	$\text{O} + \text{C}_2\text{H}_5 = \text{H} + \text{CH}_3\text{CHO}$	0.005	0.003	0.001	$\searrow$
$\text{CH}_3\text{CHO} \rightarrow \text{CH}_2\text{CHO}$	299	$\text{H} + \text{CH}_3\text{CHO} = \text{CH}_2\text{CHO} + \text{H}_2$	0.001	0.001	0.000	$\Rightarrow$
$\text{C}_2\text{H}_4 \rightarrow \text{C}_2\text{H}_3$	75	$\text{H} + \text{C}_2\text{H}_4 = \text{C}_2\text{H}_3 + \text{H}_2$	0.023	0.026	0.026	$\Rightarrow$
	112	$\text{OH} + \text{C}_2\text{H}_4 = \text{C}_2\text{H}_3 + \text{H}_2\text{O}$				
$\text{C}_2\text{H}_4 \rightarrow \text{CH}_2\text{CHO}$	285	$\text{O} + \text{C}_2\text{H}_4 = \text{H} + \text{CH}_2\text{CHO}$	0.004	0.004	0.003	$\Rightarrow$
$\text{C}_2\text{H}_3 \rightarrow \text{CH}_2\text{CHO}$	294	$\text{C}_2\text{H}_3 + \text{O}_2 = \text{O} + \text{CH}_2\text{CHO}$	0.006	0.007	0.006	$\Rightarrow$
$\text{CH}_2\text{CHO} \rightarrow \text{CH}_2\text{CO}$	304	$\text{H} + \text{CH}_2\text{CO}(+\text{M}) = \text{CH}_2\text{CHO}(+\text{M})$	-0.010	-0.011	-0.010	$\Rightarrow$
	309	$\text{H} + \text{CH}_2\text{CHO} = \text{CH}_2\text{CO} + \text{H}_2$				

<b>C<sub>2</sub>H<sub>3</sub> → C<sub>2</sub>H<sub>2</sub></b>	71	H+C <sub>2</sub> H <sub>2</sub> (+M) = C <sub>2</sub> H <sub>3</sub> (+M)				
	73	H+C <sub>2</sub> H <sub>3</sub> = H <sub>2</sub> +C <sub>2</sub> H <sub>2</sub>	-0.006	-0.011	-0.014	↘
	111	OH+C <sub>2</sub> H <sub>3</sub> = H <sub>2</sub> O+C <sub>2</sub> H <sub>2</sub>				
<b>C<sub>2</sub>H<sub>2</sub> → HCCO</b>	21	O+C <sub>2</sub> H <sub>2</sub> = H+HCCO	0.009	0.010	0.011	↗
<b>CH<sub>2</sub>CO → HCCO</b>	80	H+CH <sub>2</sub> CO = HCCO+H <sub>2</sub>	0.007	0.007	0.006	↘
	114	OH+CH <sub>2</sub> CO = HCCO+H <sub>2</sub> O				
<b>CH → C</b>	49	H+CH = C+H <sub>2</sub>	0.009	0.004	0.002	↘↘

## b) Ammonia oxidation

Sub-path	Nb	Reactions	E = 0	E = 0.15	E = 0.30	Trend
<b>NH<sub>3</sub> → NH<sub>2</sub></b>	277	NH <sub>3</sub> +H = NH <sub>2</sub> +H <sub>2</sub>				
	278	NH <sub>3</sub> +OH = NH <sub>2</sub> +H <sub>2</sub> O	0.000	0.281	0.490	↗↗
	279	NH <sub>3</sub> +O = NH <sub>2</sub> +OH				
<b>NH<sub>2</sub> → NH</b>	200	NH <sub>2</sub> +O = OH+NH				
	202	NH <sub>2</sub> +H = NH+H <sub>2</sub>	0.000	0.197	0.360	↗
	203	NH <sub>2</sub> +OH = NH+H <sub>2</sub> O				
<b>NH → N</b>	191	NH+H = N+H <sub>2</sub>	0.000	0.055	0.072	↗
	193	NH+OH = N+H <sub>2</sub> O				
<b>NH → HNO</b>	192	NH+OH = HNO+H				
	194	NH+O <sub>2</sub> = HNO+O	0.000	0.058	0.112	↗↗
	197	NH+H <sub>2</sub> O = HNO+H <sub>2</sub>				
<b>NH<sub>2</sub> → HNO</b>	201	NH <sub>2</sub> +O = H+HNO	0.000	0.096	0.143	↗
<b>HNO → NO</b>	212	H+NO+M = HNO+M				
	213	HNO+O = NO+OH				
	214	HNO+H = H <sub>2</sub> +NO	0.000	0.199	0.252	↗
	215	HNO+OH = NO+H <sub>2</sub> O				
	216	HNO+O <sub>2</sub> = HO <sub>2</sub> +NO				
<b>NO → NO<sub>2</sub></b>	186	HO <sub>2</sub> +NO = NO <sub>2</sub> +OH				
	187	NO+O+M = NO <sub>2</sub> +M	0.000	0.087	0.089	↗⇒
	189	NO <sub>2</sub> +H = NO+OH				
<b>NO → N<sub>2</sub></b>	178	N+NO = N <sub>2</sub> +O	-0.001	0.032	0.048	↗
<b>NO → N<sub>2</sub>O</b>	199	NH+NO = N <sub>2</sub> O+H	0.000	0.054	0.113	↗↗
<b>N<sub>2</sub>O → N<sub>2</sub></b>	183	N <sub>2</sub> O+H = N <sub>2</sub> +OH	0.000	0.052	0.104	↗↗
<b>N → NO</b>	179	N+O <sub>2</sub> = NO+O	0.001	0.021	0.021	↗⇒
	180	N+OH = NO+H				

## c) Interactions

Sub-path	Nb	Reactions	$E = 0$	$E = 0.15$	$E = 0.30$	Trend
<b>HCCO</b> → <b>HCNO</b>	274	HCCO+NO = HCNO+CO	0.000	0.003	0.004	↗
<b>CH<sub>2</sub></b> → <b>HCNO</b>	251	CH <sub>2</sub> +NO = H+HCNO	0.000	0.002	0.003	↗
<b>CH<sub>2</sub>*</b> → <b>HCNO</b>	252	CH <sub>2</sub> *+NO = H+HNCO	0.000	0.001	0.001	⇒
<b>HCNO</b> → <b>HNCO</b>	270	HCNO+H = H+HNCO	0.000	0.004	0.006	↗
<b>CH<sub>2</sub></b> → <b>HNCO</b>	249	CH <sub>2</sub> +NO = H+HNCO	0.000	0.009	0.010	↗⇒
<b>HNCO</b> → <b>NH<sub>2</sub></b>	265	HNCO+H = NH <sub>2</sub> +CO	0.000	0.011	0.011	↗⇒
<b>HNCO</b> → <b>NCO</b>	264	HNCO+O = NCO+OH	0.000	0.003	0.005	↗
	266	HNCO+H = H <sub>2</sub> +NCO				
	267	HNCO+OH = NCO+H <sub>2</sub> O				
<b>CH</b> → <b>NCO</b>	247	CH+NO = H+NCO	0.000	0.001	0.001	⇒
<b>CH<sub>3</sub></b> → <b>H<sub>2</sub>CN</b>	256	CH <sub>3</sub> +NO = H <sub>2</sub> CN+OH	0.000	0.005	0.004	↗↘
	275	CH <sub>3</sub> +N = H <sub>2</sub> CN+H				
<b>H<sub>2</sub>CN</b> → <b>HCN</b>	237	H+HCN(+M) = H <sub>2</sub> CN(+M)	0.000	-0.005	-0.004	↘
<b>CH<sub>3</sub></b> → <b>HCN</b>	255	CH <sub>3</sub> +NO = HCN+H <sub>2</sub> O	0.000	0.002	0.003	↗
	276	CH <sub>3</sub> +N = HCN+H <sub>2</sub>				
<b>CH<sub>2</sub></b> → <b>HCN</b>	250	CH <sub>2</sub> +NO = OH+HCN	0.000	0.002	0.002	↗⇒
<b>CH</b> → <b>HCN</b>	246	CH+NO = HCN+O	0.000	0.003	0.003	↗⇒
<b>HCN</b> → <b>NCO</b>	231	HCN+O = NCO+H	0.000	0.007	0.006	↗↘
<b>C</b> → <b>CN</b>	244	C+NO = CN+O	0.000	0.000	0.000	⇒
	219	CN+H <sub>2</sub> O = HCN+OH				
	221	CN+H <sub>2</sub> = HCN+H				
<b>HCN</b> → <b>CN</b>	233	HCN+O = CN+OH	0.000	-0.001	-0.001	↘⇒
	218	CN+OH = NCO+H				
<b>CN</b> → <b>NCO</b>	220	CN+O <sub>2</sub> = NCO+O	0.000	0.002	0.002	↗⇒
	223	NCO+H = NH+CO				

Reaction path with UCSD mechanism

Table 2A. 4. Reaction path with UCSD mechanism

## a) Methane oxidation

Sub-path	Nb	Reaction	E = 0	E = 0.15	E = 0.3	Trend
CH <sub>4</sub> → CH <sub>3</sub>	41	CH <sub>4</sub> +H = H <sub>2</sub> + CH <sub>3</sub>				
	42	CH <sub>4</sub> +OH = H <sub>2</sub> O+ CH <sub>3</sub>				
	43	CH <sub>4</sub> +O = CH <sub>3</sub> +OH	1.000	0.736	0.531	↘
	44	CH <sub>4</sub> +O <sub>2</sub> = CH <sub>3</sub> +HO <sub>2</sub>				
	56	H+ CH <sub>3</sub> +M = CH <sub>4</sub> +M				
CH <sub>3</sub> → CH <sub>2</sub>	46	CH <sub>3</sub> +H = T-CH <sub>2</sub> + H <sub>2</sub>	0.023	0.017	0.012	↘
CH <sub>3</sub> → CH <sub>2</sub> *	47	CH <sub>3</sub> +H = S-CH <sub>2</sub> + H <sub>2</sub>	0.199	0.149	0.108	↘
	48	CH <sub>3</sub> +OH = S-CH <sub>2</sub> + H <sub>2</sub> O				
CH <sub>3</sub> → CH <sub>2</sub> O	49	CH <sub>3</sub> +O = CH <sub>2</sub> O+H	0.402	0.287	0.202	↘↘
	52	CH <sub>3</sub> + O <sub>2</sub> = CH <sub>2</sub> O+OH				
CH <sub>3</sub> → C <sub>2</sub> H <sub>4</sub>	50	CH <sub>3</sub> +T-CH <sub>2</sub> = C <sub>2</sub> H <sub>4</sub> +H	0.018	0.012	0.008	↘↘
CH <sub>3</sub> → CH <sub>3</sub> O	51	CH <sub>3</sub> + HO <sub>2</sub> = CH <sub>3</sub> O+OH	0.013	0.011	0.009	↘
	53	CH <sub>3</sub> + O <sub>2</sub> = CH <sub>3</sub> O+O				
CH <sub>2</sub> * → CO	59	S-CH <sub>2</sub> + O <sub>2</sub> = CO+OH+H	0.032	0.023	0.016	↘↘
CH <sub>2</sub> * → CH <sub>2</sub>	61	S-CH <sub>2</sub> +M = T-CH <sub>2</sub> +M	0.169	0.127	0.092	↘↘
CH <sub>2</sub> → CH	62	T-CH <sub>2</sub> +H = CH+H <sub>2</sub>	0.021	0.015	0.011	↘
	64	T-CH <sub>2</sub> +OH = CH+ H <sub>2</sub> O				
CH <sub>2</sub> → CH <sub>2</sub> O	63	T-CH <sub>2</sub> +OH = CH <sub>2</sub> O+H	0.021	0.016	0.011	↘
CH <sub>2</sub> → CO	65	T-CH <sub>2</sub> +O = CO+2	0.096	0.071	0.052	↘
	68	T-CH <sub>2</sub> + O <sub>2</sub> = CO+OH+H				
CH <sub>2</sub> → CO <sub>2</sub>	67	T-CH <sub>2</sub> + O <sub>2</sub> = CO <sub>2</sub> +H <sub>2</sub>	0.030	0.023	0.018	↘
CH → HCO	71	CH+ O <sub>2</sub> = HCO+O	0.016	0.009	0.006	↘↘
CH <sub>2</sub> OH → CH <sub>2</sub> O	129	CH <sub>2</sub> OH+H = CH <sub>2</sub> O+H <sub>2</sub>				
	131	CH <sub>2</sub> OH+OH = CH <sub>2</sub> O+ H <sub>2</sub> O	0.064	0.054	0.045	↘
	132	CH <sub>2</sub> OH+ O <sub>2</sub> = CH <sub>2</sub> O+ HO <sub>2</sub>				
	133	CH <sub>2</sub> OH+M = CH <sub>2</sub> O+H+M				
CH <sub>3</sub> O → CH <sub>2</sub> O	79	CH <sub>3</sub> O+M = CH <sub>2</sub> O+H+M	0.019	0.016	0.014	↘
CH <sub>2</sub> O → HCO	36	CH <sub>2</sub> O+H = HCO+H <sub>2</sub>				
	37	CH <sub>2</sub> O+O = HCO+OH	0.521	0.384	0.280	↘
	38	CH <sub>2</sub> O+OH = HCO+ H <sub>2</sub> O				
HCO → CO	28	HCO+M = CO+H+M				
	29	HCO+H = CO+H <sub>2</sub>				
	32	HCO+OH = CO+ H <sub>2</sub> O	0.544	0.403	0.295	↘
	33	HCO+ O <sub>2</sub> = CO+ HO <sub>2</sub>				
	34	HCO+ CH <sub>3</sub> = CO+CH <sub>4</sub>				
CO → CO <sub>2</sub>	24	CO+O+M = CO <sub>2</sub> +M	0.679	0.508	0.372	↘
	25	CO+OH = CO <sub>2</sub> +H				
CH <sub>3</sub> → C <sub>2</sub> H <sub>6</sub>	57	2 CH <sub>3</sub> +M = C <sub>2</sub> H <sub>6</sub> +M	0.062	0.049	0.036	↘

$C_2H_6 \rightarrow C_2H_5$	80	$C_2H_6+H = C_2H_5+H_2$				
	81	$C_2H_6+O = C_2H_5+OH$				
	82	$C_2H_6+OH = C_2H_5+ H_2O$	0.062	0.049	0.036	↘
	83	$C_2H_6+CH_3 = C_2H_5+CH_4$				
	84	$C_2H_6+M = C_2H_5+H+M$				
$C_2H_5 \rightarrow C_2H_4$	86	$C_2H_5+H = C_2H_4+H_2$				
	89	$C_2H_5+ O_2 = C_2H_4+ HO_2$	0.045	0.043	0.034	↘
	94	$C_2H_5+M = C_2H_4+H+M$				
$C_2H_4 \rightarrow C_2H_3$	95	$C_2H_4+H = C_2H_3+H_2$	0.047	0.041	0.031	↘
	96	$C_2H_4+OH = C_2H_3+ H_2O$				
$C_2H_4 \rightarrow HCO$	97	$C_2H_4+O = CH_3+HCO$	0.015	0.012	0.008	↘
$C_2H_4 \rightarrow CH_2CHO$	98	$C_2H_4+O = CH_2CHO+H$	0.008	0.006	0.004	↘
$C_2H_3 \rightarrow C_2H_2$	105	$C_2H_3+H = C_2H_2+H_2$	0.022	0.019	0.014	↘
	106	$C_2H_3+M = C_2H_2+H+M$				
$C_2H_3 \rightarrow CH_2CHO$	108	$C_2H_3+ O_2 = CH_2CHO +O$	0.016	0.015	0.012	↘
$C_2H_2 \rightarrow HCCO$	110	$C_2H_2+O = HCCO+H$	0.012	0.009	0.006	↘↘
$C_2H_2 \rightarrow CO$	111	$C_2H_2+O = T-CH_2+CO$	0.006	0.005	0.003	↘↘
$C_2H_2 \rightarrow CH_2CO$	113	$C_2H_2+OH = CH_2CO+H$	0.009	0.009	0.007	↘
$CH_2CO \rightarrow CO$	115	$CH_2CO+H = CH_3+CO$	0.031	0.028	0.022	↘
	135	$CH_2CO+OH = CH_2OH+CO$				
$CH_2CHO \rightarrow CH_2CO$	144	$CH_2CHO = CH_2CO+H$	0.024	0.022	0.017	↘
$HCCO \rightarrow CO$	119	$HCCO+H = S-CH_2+CO$	0.010	0.007	0.005	↘↘
	122	$HCCO+ O_2 = 2CO+OH$				

## b) Ammonia oxidation

Sub-path	Nb	Reaction	E = 0	E = 0.15	E = 0.3	Trend
$NH_3 \rightarrow NH_2$	300	$NH_3+M = NH_2+H+M$				
	301	$NH_3+H = NH_2+ H_2$	0.000	0.264	0.469	↗↗
	302	$NH_3+O = NH_2+OH$				
	303	$NH_3+OH = NH_2+ H_2O$				
$NH_2 \rightarrow NH$	295	$NH_2+H = NH+ H_2$	0.000	0.177	0.314	↗↗
	297	$NH_2+OH = NH+ H_2O$				
$NH_2 \rightarrow HNO$	296	$NH_2+O = HNO+H$	0.000	0.049	0.076	↗↗
$NH \rightarrow HNO$	290	$NH+OH = HNO+H$	0.000	0.061	0.112	↗↗
	292	$NH+ O_2 = HNO+O$				
$NH \rightarrow N$	288	$NH+H = N+ H_2$	0.000	0.033	0.054	↗
	291	$NH+OH = N+ H_2O$				
$NH \rightarrow NO$	289	$NH+O = NO+H$	0.000	0.036	0.051	↗
$HNO \rightarrow NO$	309	$HNO+H = NO+ H_2$				
	310	$HNO+OH = NO+ H_2O$	0.000	0.111	0.188	↗↗
	308	$HNO+M = H+NO+M$				

<b>N → NO</b>	270	$N + O_2 = NO + O$	0.001	0.014	0.023	↗
	271	$N + OH = NO + H$				
<b>NO → N<sub>2</sub>O</b>	293	$NH + NO = N_2O + H$	0.000	0.036	0.072	↗
<b>N<sub>2</sub>O → NH</b>	293	$NH + NO = N_2O + H$	0.000	-0.036	-0.072	↗
<b>NO → NO<sub>2</sub></b>	318	$NO_2 + M = NO + O + M$	0.000	0.000	0.000	⇒
	319	$NO + HO_2 = NO_2 + OH$				
	320	$NO_2 + H = NO + OH$				
	321	$NO_2 + O = NO + O_2$				
<b>NO → N<sub>2</sub></b>	298	$NH_2 + NO = N_2 + H_2O$	-0.001	0.014	0.026	↗↗
	294	$NH + NO = N_2 + OH$				
	269	$O + N_2 = NO + N$				
<b>N<sub>2</sub>O → N<sub>2</sub></b>	314	$N_2O + M = N_2 + O + M$	0.000	0.035	0.071	↗↗
	315	$N_2O + H = N_2 + OH$				
	317	$N_2O + OH = N_2 + HO_2$				
<b>NO → N<sub>2</sub>H</b>	299	$NH_2 + NO = N_2H + OH$	0.000	0.022	0.046	↗↗
<b>N<sub>2</sub>O → N<sub>2</sub>H</b>	306	$N_2H + O = N_2O + H$	0.000	0.001	0.001	⇒
<b>N<sub>2</sub>H → N<sub>2</sub></b>	304	$N_2H = N_2 + H$	0.000	0.022	0.047	↗↗

## c) Interactions

Sub-path	Nb	Reaction	E = 0	E = 0.15	E = 0.3	Trend
<b>CH → HCN</b>	272	$N_2 + CH = HCN + N$	0.000	0.003	0.002	↗↘
	313	$NO + CH = HCN + O$				
<b>HCN → NCO</b>	273	$HCN + O = NCO + H$	0.000	0.002	0.002	↗⇒
<b>NCO → NH</b>	275	$NCO + H = CO + NH$	0.000	0.004	0.003	↗↘
<b>NCO → HNCO</b>	277	$NCO + H_2 = HNCO + H$	0.000	-0.001	-0.001	↗⇒
<b>HCCO → HNCO</b>	278	$HCCO + NO = HNCO + CO$	0.000	0.001	0.001	↗⇒
<b>HNCO → CO</b>	279	$HNCO + M = NH + CO + M$	0.000	0.000	0.000	⇒
<b>HNCO → NCO</b>	281	$HNCO + O = NCO + OH$	0.000	0.002	0.002	↗⇒
	283	$HNCO + OH = NCO + H_2O$				
<b>HCN → CN</b>	284	$CN + H_2 = HCN + H$	0.000	-0.001	-0.001	↗⇒
	285	$CN + H_2O = HCN + OH$				
<b>CN → NCO</b>	286	$CN + OH = NCO + H$	0.000	0.001	0.001	↗⇒
	287	$CN + O_2 = NCO + O$				
<b>CH<sub>2</sub> → HNCO</b>	312	$NO + T-CH_2 = HNCO + H$	0.000	0.005	0.004	↗↘

# Chapter 3

## Assessment of detailed chemistry models for ammonia/methane flames by comparison with experiments using the counterflow configuration

### 1. Introduction

#### 1.1. Objectives of the chapter

As developed in the introduction to Chapter 2, nitromethane chemistry has been widely investigated in the past. These various studies lead to the development of several new kinetics, and kinetics updates and improvements. The main features of the chemistry of hydrocarbon fuels with the introduction of nitrogen compounds, here methane and ammonia, are globally understood, as presented in Chapter 2. Nonetheless, even though most of the mechanisms developed agree on the main reaction kinetics, differences in minor branches of the reaction path could be observed between them. And, slight changes in the reaction parameters from one mechanism to another can lead to large discrepancies in the evaluation of flame characteristics. Thus, though the global scheme of reaction been quite well understood using existing kinetics, the quantitative prediction of the combustion process requires validation of those mechanisms over a wide range of flame characteristics, under a broad range of conditions and various configurations to ensure their validity, and pave the way to the prediction of flame behavior in more complex environments, such as boilers or gas turbines. Moreover, in addition to their use for chemistry validation, those fundamental flame properties are important in the analysis of the flame behavior in actual combustion systems. They are commonly used as tool for prediction particularly in early stages of the design of combustors, before moving to the 3D simulation analysis representing the details of the burners.

The present chapter has for objective the validation of existing kinetics over a wide range of ammonia/methane fuel mixtures through the comparison of the existing mechanism prediction to the experimental observation in a simple burner. The mechanism selected in this study are further described in Section 1.2, as well as the selected counterflow flame configuration in Section 1.3, and the consideration taken to adequately model it in Sections 1.4 and 1.5.

The parameters selected for the chemistry validation are the extinction stretch rate and the OH and NO distributions in the flame. As previously stated, those criteria are both of interest for chemistry validation. The experimental results and their comparison to the numerical predictions are developed in the following sections. Section 2 focuses on the extinction stretch rate of the counterflow premixed twin flames. The extinction stretch rate of the counterflow non-premixed flame is presented in Section 3, followed by the results on OH and NO distributions in the premixed twin flame in Section 4.

## 1.2. Overview of existing mechanisms and selection of four kinetics for ammonia/methane flames

Since the early work of Miller and Bowmann [44], a large number of detailed kinetics (also called detailed reaction mechanisms, or detailed chemistry) have been developed and can be found in the literature when considering the simulation of nitro-methane chemistry. A non-exhaustive list of some of the main mechanisms in the literature is presented in the following.

- *Miller and Bowmann's mechanism (1990)* [44]:

Compiling early work on combustion kinetics, two mechanisms were proposed. The first for light hydrocarbons in most of the common combustion situations including 234 reactions and 49 species; and the second corresponding to ammonia oxidation, with 73 and 19 species. Though being limited to 24 hydrocarbon species, the hydrocarbon set is sufficient for the simulation of the C<sub>1</sub>-C<sub>2</sub> hydrocarbon and include some cyanide and nitrogen species involved in the formation of NO<sub>x</sub>. The N<sub>2</sub>H<sub>2</sub> specie and the related reactions as well as some other nitrogen reactions, included in the ammonia oxidation mechanism provided in [44], are not included in the first hydrocarbon-nitrogen set, for which nitrogen subset was more limited.

Due to its relatively low number of reactions and species, this mechanism is convenient for capturing the main combustion kinetics, but fails in reproducing accurately and quantitatively the experimental trends, overestimating for example the laminar burning velocity of ammonia flames [87].

- Lindstedt's mechanism (1994) [127]:

To expand the validity of existing mechanisms in a broader range of conditions, particularly regarding the NO<sub>x</sub> formation, a work based on experimental results on argon diluted ammonia and NO seeded hydrogen-oxygen premixed flames in a low-pressure environment lead to an updated 21 species and 95 reactions mechanism for ammonia oxidation. The predicted values of the laminar burning velocity of ammonia flame with this mechanism are similar to the ones by Miller and Bowmann, overestimating the laminar burning velocity of the flame in both atmospheric and high-pressure conditions [87] and will not be further discussed here.

- GRI-Mech 3.0 (2000) [122]:

Developed by the University of California Berkley, GRI-Mech 3.0 includes 53 species and 325 reactions. It has been optimized based on a great number of experimental results, including ignition delay measurements, laminar burning velocity, and profile measurement in a shock tube and flow reactors. GRI-Mech 3.0 has been used in several studies on methane blends with an overall good estimation of their properties [128–132]. Moreover, though aiming at hydrocarbons combustion, fair estimates of the laminar burning velocity of ammonia and ammonia-methane flames could be observed [63,87]. Furthermore, this mechanism is of reasonable size and attractive when considering later simulations in more complex configurations, close to the industrial applications. This mechanism was thus selected for the present study.

- Konnov's mechanism (2007-2010) [133,134]:

Based on a first mechanism [134] including 127 species and 1207 reactions and validated on the laminar burning velocity and NO emission measurements in a methane-hydrogen flame, an updated version of the mechanism was proposed by Shmakov et al. [133] based on work in the literature as

well as complementary measurements for NO and NH<sub>3</sub> doped hydrogen flames aiming at a better prediction of the NO<sub>x</sub> formation. The updated mechanism, was well-validated on species profiles taken on these flames, including the major reactants H<sub>2</sub>, O<sub>2</sub>, H<sub>2</sub>O, H, OH, NH<sub>3</sub>, and NO. However, only traces of ammonia were used in the validation experiment and it was shown that the mechanism overestimates dramatically the extinction stretch rate of ammonia flame as well as its laminar burning velocity [43] and thus was not selected for the present study.

- Tian, Mendiara and Glarborg's mechanism (2009) [47,69]:

Based on work on methane/ammonia/oxygen/argon flame, detailed kinetics was proposed by Tian et al. [69] updated by Mendiara and Glarborg [47] for ammonia oxidation in the oxy-fuel combustion of methane with a high content of CO<sub>2</sub>. Recent review work by Glarborg et al. [78] on nitrogen chemistry in combustion proposed an updated mechanism based on this earlier work. Tian's mechanism includes 84 species and 702 reactions while Mendiara's does include 97 species and 779 reactions. Glarborg mechanism accounts for 153 species and 1397 reactions. Both Tian's and Glarborg's mechanism over-estimates the laminar burning velocity of ammonia [88], but Glarborg's to a larger extent. Moreover, Tian's mechanism also gave a good estimate of the extinction stretch rate for ammonia flames [89], and present a reasonable number of species and equations and was thus considered here.

- AramcoMech 2.0 (2013-2016) [80,90–95]:

AramcoMech 2.0 is a well-developed mechanism available for a large variety of hydrocarbons and developed by NUI Galway and its partners. This mechanism presents a much better accuracy, as well as many detailed frames of reactions, providing usually better agreement with the simulation for natural gas combustion [129,131]. Due to its large number of reactions and species (close to 500 species), AramcoMech 2.0 was employed here only for methane flame and in specific cases for greater discussion in Section 2.3.

- Nakamura's mechanism (2016) [77]:

From the observation of weak flames in a micro-flow reactor, Nakamura proposed new kinetics based on Miller and Bowman kinetics with updates from both Konnov and Mathieu. This updated mechanism includes 159 species and 1072 reactions. It showed better agreement to the laminar burning velocity of ammonia flame as presented by Kobayashi et al. [43] than Konnov mechanism, with results close to those with Tian's mechanism.

- Okafor's mechanism (2018-2019) [63,88]:

Okafor's mechanism was proposed on the base of GRI-Mech 3.0 with the addition of some of the nitrogen reactions of Tian's mechanism, related to the ammonia oxidation, and some updates of rate constants as discussed by Okafor et al. [63]. The updated mechanism resulted in 59 species and 356 reactions and was well-validated on laminar velocity results for methane/ammonia flames up to a large content of ammonia (close to 52% in mole fraction).

- UCSD mechanism [96]:

University California of San Diego mechanism constituted of 72 species and 321 reactions (corresponding to the C<sub>1</sub>-C<sub>2</sub> subset + nitrogen subset), aims at hydrocarbons flames prediction, but include a sufficiently detailed nitrogen subset, as well as several carbon-nitrogen interaction species. This mechanism was also well-validated for small hydrocarbon such as methane and is thus included in the present study.

In the limited scope of this study, the detailed comparison of all those mechanisms was not performed, but it was decided to focus on four mechanisms. The selection of those four mechanisms was done taking into account the set of species in the mechanisms and the existing validations in the literature, with specific attention on the ability of the mechanisms to model ammonia flame characteristics. Thus, and according to the previously given description, GRI-Mech 3.0, Tian's, UCSD mechanism, and Okafor's mechanisms were selected for chemistry validation of ammonia/methane flames.

### 1.3. Counterflow flame experimental setup

The experimental configuration selected for this study is the counterflow configuration. This common configuration is historically used for the observation of both premixed and non-premixed flame as it allows for the observation of plane flame, closed to one dimension. In the case of this study, two identical burners are facing each other. They are constituted of an inner converging duct surrounded by an outer converging coflow. The inner duct is supplied with the reactant gases, whereas the coflow is supplied with nitrogen, and acts as a curtain to prevent the reaction with the surrounding air as introduced in Fig. 3.1. Depending on if the burners are supplied with the same mixture of fuel and air as presented on Fig. 3.1a, or separately supplied with air on one side and fuel on the other like on Fig. 3.1b, premixed twin flames or non-premixed flame (also called diffusion flame) can be observed. In both the inner and outer ducts, honeycombs plates are introduced sufficiently upstream to break eventual large flow structure and ensure a good velocity profile at the burner outlet.

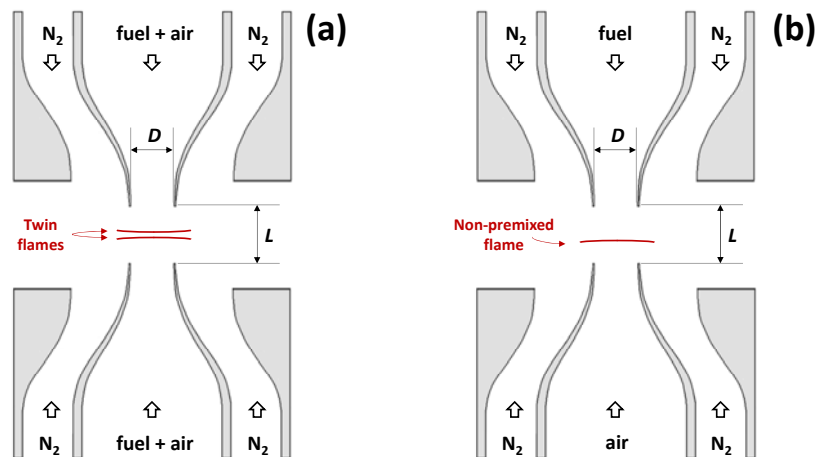


Fig. 3.1. Representation of the counterflow burners: (a) premixed twin flames configuration; (b) non-premixed flame configuration.

The produced flames are illustrated in Fig. 3.2. They are close to a 1D flame, particularly on the burner axis, where the curvature is negligible and the stretch experienced by the flame is limited to the strain. Flames are steady and laminar and because they are not attached to the burner lip, the heat losses to the burner are considered neglectable. This configuration is thus really attractive as it can be relatively easily modeled as further detailed in Section 1.4. It is also highly flexible and might be used in other

configurations than the presented ones, such as lean-rich flames and so on, which were not investigated in the present work.

Geometries of the configuration are of importance as it will be developed in both Sections 1.4 and 1.5. The diameter of the burners in this study,  $D$ , is fixed to 10 mm, but the distance between the burners,  $L$ , is adjustable.

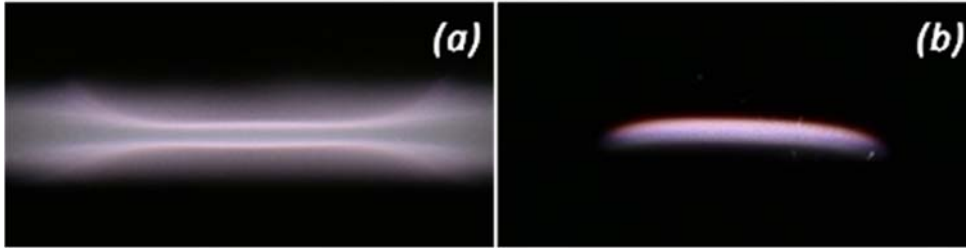


Fig. 3.2. Flame direct picture,  $E = 0.15$ : (a) twin premixed flame configuration; (b) non-premixed flame configuration.

## 1.4. 1D modeling and its limits

### 1.4.1. 1D modeling

For calculations, 1D opposed-flow code from Chemkin-pro software is used. The model used reduces the 3 dimensions of the problem to a 1D axisymmetric problem using similarity transformation [135]. Axial velocity, temperature, and mass fractions of the species are assumed to be a function of  $z$  only (the axis direction). The radial velocity component is assumed to vary linearly with the radial coordinate  $r$  and even if thermodynamic pressure is assumed to be constant, its gradients are still conserved. Those assumptions are used to reduce the conservation equations for calculation and are presented in Appendix 3A.

Diffusion velocities formulation was set here as mixture-average. The Soret effect is considered neglectable and is not included for the premixed cases but was considered for non-premixed flames.

A first solution is calculated on a coarse mesh, with parameters for the TWOPT solver set usually at 6 initial grid points, 10 adaptative points, and 0.03 for both curvature and gradient refining parameters. This solution is set as an input for the final solution calculation for which the solver parameters were set as an initial grid of 10 pt, with a refining parameter of 0.01 on the gradient and of 0.01 for the curvature. The number of adaptative points was selected between 25 to 50. These parameters give a sufficiently refined mesh for all the cases studied. Using coarse mesh solution as input usually allowed to get better

and faster convergence to the solution. The numerical boundary conditions were set in agreement with the experimental conditions.

To obtain the extinction stretch rate, the flame case just before extinction was calculated by increasing gradually the burners outlet velocities up to extinction. The first calculation is done far from extinction and is used as an initial solution for the second calculation at  $U + \Delta U$ , up to the extinction case. Calculations are then reiterated, taking the last solution before extinction as an initial solution for this new series of calculations with a smaller  $\Delta U$ . This is reproduced until  $\Delta U < 0.1$  cm/s. The temperature-stretch rate curves were checked for all the mixture cases investigated to ensure the simulation converged well to the extinction (beginning of the S-curve).

For the numerical simulation, the stretch rate at extinction is calculated from the last flame case simulated before extinction. For non-premixed flames, it is calculated from the velocity at the burner outlet following the work of Cheliah et al. [136] and corresponds to the velocity gradient on the oxidizer side. For premixed twin flames, the maximum axial velocity gradient before the flame front is calculated from the simulated axial velocity.

A general definition of stretch rate is presented in the following, as well as the derivation of simpler expressions of use for the experimental measurement of the extinction stretch rate for non-premixed and premixed counterflow flames.

- General definition of stretch rate,  $\varepsilon$ :

$$\varepsilon = \frac{1}{A} \frac{dA}{dt} \quad (3.1)$$

where  $A$  is the flame surface. This equation can be reformulated as in the work of Matalon [137]:

$$\varepsilon = -\mathbf{n} \cdot \nabla \times (\mathbf{v}_s \times \mathbf{n}) + (\mathbf{V}_f \cdot \mathbf{n})(\nabla \cdot \mathbf{n}) \quad (3.2)$$

where  $\mathbf{v}_s$  is the flow velocity at the flame,  $\mathbf{V}_f$  the flame surface velocity and  $\mathbf{n}$  the normal vector to the flame surface pointing to the upstream flame region. This general expression is convenient for the derivation of the stretch rate in the counterflow configuration as introduced in the following.

- Counterflow premixed twin flames:

In the case of the counterflow twin flames, the flame is stationary, and  $V_f = 0$ . Thus,  $(\mathbf{V}_f \cdot \mathbf{n})(\nabla \cdot \mathbf{n}) = 0$ . The flame is considered as 1D, so the curvature is equal to zero, and  $(\nabla \cdot \mathbf{n}) = 0$ . Describing the counterflow between the two burners spaced by distance  $L$  as potential flow, with  $\mathbf{v}_s$  such as  $\mathbf{v}_s = c r \mathbf{e}_r - 2c z \mathbf{e}_z$  and  $c$  constant, and considering the boundary condition such as  $\mathbf{v}_{s,(z=-\frac{L}{2},r=0)} = U \mathbf{e}_z$ , one gets:

$$\varepsilon = \frac{2U}{L} \quad (3.3)$$

This expression relates the stretch rate of the flame to the velocity boundary condition, which is convenient for experimental measurement,  $L$  being known, and  $U$  being measurable from flow rate measurement. However, the potential flow assumption might be restrictive, and differ from the experimental condition, depending on various parameters such as geometrical configuration for instance. Thus, this stretch rate expression may differ from the actual stretch rate observed by the flame, which corresponds to the axial velocity gradient before the flame front.

In previous work, Kitano and Kobayashi [138] measured the actual velocity gradient before the flame front, corresponding to the actual stretch rate, with LDV measurement in methane and propane flames. Then, they compared this measured value to the previously defined global stretch rate  $\varepsilon = 2U/L$ . They could observe that by considering the ratio of burner inter-distance and burner diameter, a linear relationship between the two quantities could be obtained. This empirical expression is written as follows:

$$\varepsilon_{corr} = \varepsilon \cdot \left( 0.73 \left( \frac{L}{D} \right) + 0.5 \right) \quad (3.4)$$

Using this expression allows for the direct comparison of the gradient before the flame front observed experimentally and numerically. The expression being empirical, its validity for the wide range of mixture conditions observed in the present study will be further discussed in Sections 1.4.2 and 1.5.

- Counterflow non-premixed flame:

In the case of counterflow non-premixed flame, a similar convenient expression has been derived by Seshadri and Williams [139] and will be directly introduced here:

$$\varepsilon = \frac{2U_{ox}}{L} \left( 1 + \frac{U_{fuel}}{U_{ox}} \sqrt{\frac{\rho_{fuel}}{\rho_{ox}}} \right) \quad (3.5)$$

This expression has been widely used in literature for various type of mixture, which allows comparison with many different published works [136,139–142]. In this case too, proper characterization of the velocity profiles has been performed and is the object of Section 1.5.

#### 1.4.2. *Limits of the 1D model*

As mentioned in the previous section, the adequation between the theoretical 1D model and the experimental observation might be a source of uncertainty when trying to validate the chemistry. Several parameters can affect the velocity profiles, and lead to errors in the measurement of species for observation of the flame structure as well as in the measurement of the extinction stretch rate. The unidimensionality, adiabaticity, stability, and laminarity of the counterflow flames are assumed in the 1D model, but those strong assumptions are not perfectly observed in experiments, and discrepancies can thus be observed between the model and experiment.

Even though these assumptions, and the conditions under which they might not be perfectly fulfilled, have not been the subject of detailed study in the present work, they were still considered and reviewed quickly:

- The curvature of the flame can lead to discrepancies between numerical and experimental results. Even though, flames can be considered, locally at the burner center axis, like 1D, they remain slightly curved, which might affect the results observed. The curvature is however in the present study really small as can be seen from a typical flame in Fig. 3.2, and this effect is considered as neglectable in most of the cases. It should however be noticed that a particularly low stretch rate tends to lead to flame presenting a larger curvature. Those cases were thus excluded from the present study.
- The flame considered in the model is adiabatic, which is not the case experimentally. However, the heat losses to the surroundings through the burner are neglectable in the present configuration, the flame being detached from the burner. The effect of radiative heat losses on the extinction limit has been investigated by Ju et al. [143]. It was found that radiative heat losses should be considered for extinction near the flammability limit. In the methane case studied, the difference

in the results obtained with and without radiative heat loss consideration appeared for equivalence ratios lower than 0.5 and stretch rate lower than  $50 \text{ s}^{-1}$ . In the present study, the extinction limits were observed sufficiently far from the flammability limit, and radiative heat losses could thus be neglected.

- The burner co-axiality or geometrical defaults can create asymmetry between the burners and affect the position of the stagnation point, and consequently, the flames positions. Similarly, even though they have the same design, the upper and lower burner might present some differences, such as honeycomb defaults, leading to flow unbalance. Those points have been carefully considered whenever changing the configuration of the burners. The observation of the flames' symmetry and positions showed that these effects be neglected.
- Flame instabilities might also lead to discrepancies between model and experiment. Small fluctuations of flow rate might affect the strain and in turn the flame. The perturbed flame, through the fluctuations of the flame position, temperature, and heat released might also, in turn, affect the local strain [144,145]. This type of fluctuations, as it affects the local strain, affects the extinction stretch rate. Unsteady counterflow flames have been the subject of several studies and are not further investigated in the present work [146,147]. The extinction stretch rate of methane/air flames, for near stoichiometric cases, might be the case which can be the most prone to be affected by these instabilities due to the larger flow rate used. However, flame oscillations have not been observed during experiments, and instabilities due to upstream flow perturbations were limited thanks to the design of the burner. These instabilities are thus considered neglectable.
- Finally, the velocity flow field considered for the derivation of flame stretch in Eq. ( 3.3 ) is modeled by a potential flow field. The real experimental velocity flow field, though, tends to differ from this model and can be a major source of discrepancy. The geometrical configuration of the burner has an impact on the evaluation of the extinction stretch rate as investigated by Kobayashi and Kitano [138]. Rather than the extinction stretch rate as in Eq. ( 3.3 ), consideration of the experimental maximum axial velocity gradient before the flame front should be considered and used for comparison with the simulations. In the present study, the effect of the geometrical configuration on the velocity profiles was thus more specifically examined. Following this

investigation, both optimal experimental configurations, limiting the deviation from the model, and stretch rate empirical correction, as in Eq. ( 3.4 ) were considered as developed in the following.

In the case of counterflow premixed twin flames, and as previously mentioned in Section 1.4.1, the geometrical ratio  $L/D$  was shown to impact the velocity profiles and the extinction stretch rate. Indeed, small  $L/D$  were shown to lead to an M-shape velocity profile at the burner outlets [138,141]. This might lead to an erroneous value of stretch rate if not properly considered. This was considered by Kobayashi and Kitano and yielded the expression in Eq. ( 3.4 ). The validity of this empirical equation, obtained for different gases than the present ones, is further investigated in Section 1.5.

Counterflow non-premixed flames are also expected to be sensitive to the velocity flow field conditions, and for this reason, have been the subject of special attention in the present study. Preliminary study on the impact of the geometrical configuration on the velocity profiles and the extinction stretch rate was thus performed. As a first approach, extinction stretch rate was obtained experimentally for different configurations: the  $L/D$  ratio was varied and both equal momentum (EM) and equal velocity (EV) outlet conditions were considered. The results on the extinction stretch rate of methane-air non-premixed flame, as defined in Eq. ( 3.5 ), are presented in Table 3.1.

Table 3.1. Extinction stretch rate obtained for the methane-air counterflow non-premixed flame in different configurations. Measurement using Eq. ( 3.5 ).

Geometrical configuration	Extinction stretch rate [s <sup>-1</sup> ]
$L/D = 1$ for EV	524
$L/D = 1$ for EM [136]	610
$L/D = 1.2$ for EV	423
$L/D = 1.2$ for EM	469
$L/D = 1.5$ for EV	349
$L/D = 2$ for EV	259
$L/D = 2$ for EM	282

It could be observed that increasing the distance between the burners led to a reduction of the extinction stretch rate. Moreover, extinction stretch rate obtained from equal momentum (EM) condition were systematically higher than the one observed for equal velocity (EV) condition. From these results, it can be observed that the methodology and the configuration employed can highly affect the results

obtained. A good geometrical configuration is thus of primary importance and its impacts on the velocity profiles were investigated experimentally using PIV measurement in Section 1.5.

## 1.5. Velocity profiles considerations for modeling

### 1.5.1. Objective and methodology

PIV measurements allow the observation of the velocity profiles simultaneously at all points between the two burners. The aim of this 2D velocity mapping is first to quantify the difference between the experimentally observed velocity profiles and the 1D simulated velocity profile using bulk velocity measurement and to propose empirical correction for the adequate comparison of the experimental and numerical results for the chemistry validation. Special attention has been paid to the velocities profiles at the burner outlets, and to the velocity profile along the center-axis of the burners which corresponds respectively to the velocity boundary conditions provided in the 1D model for the numerical simulations and the 1D velocity profile along the burner axis obtained from the simulations.

The effects on the burner outlet velocity profile of boundary layers at the burner lip and of the pressure gradient at the stagnation plane could be seen and quantified. Once quantified, they were therefore used as input for numerical simulations in the Chemkin-Pro numerical environment, to remove flow modeling uncertainty and to perform a proper evaluation of the chemistry.

The ratio  $L/D$  is known to impact the velocity profiles in counterflow flames experiments [138,141,148]. This ratio is usually recommended to be large enough so that the static pressure gradient does not affect the velocity profile at the outlet of the burner. On the opposite, a too-large distance might lead to a more unstable flame, more sensitive to outside perturbation. The ratio  $L/D$  is usually taken between 1 and 5 [149]. Nonetheless, it was observed in Section 1.4.2 that an increase in the  $L/D$  ratio between only 1 and 2 tends to lower the extinction stretch rate for methane non-premixed flames suggesting a greater instability of the flame. The same conclusion was done with ammonia addition, as well as for premixed flames. The premixed twin flames, though being more stables than the non-premixed ones, became more unstable for greater  $L$  values. The ratio selected in this study was thus a tradeoff value and was kept close to 1 for all the cases investigated. The selected values are introduced in Table 3.2.

Table 3.2. Geometric configurations selected in this study.

Study cases	L/D
Extinction of premixed twin flames for NH <sub>3</sub> /CH <sub>4</sub> /air (except NH <sub>3</sub> /air)	1.2
Extinction of premixed twin flames for NH <sub>3</sub> /air	1.0
Extinction of non-premixed flames	1.0
OH-PLIF and NO-PLIF measurements	1.0

Once the optimal geometrical configurations were determined, the velocity profiles were examined in these conditions for both non-premixed and premixed flames.

The velocity profiles for non-premixed flames were clarified for both equal velocity (EV) and equal momentum (EM) conditions to understand the differences observed in the extinction stretch rate calculated in those conditions. From those measurements, empirical corrections for the velocity at the boundary conditions were obtained.

Premixed flames for various fuel mixtures (methane, methane/ammonia, ammonia) and various equivalence ratio were investigated. The objective was to establish relations between the velocity at the centerline of the burner outlet, the radial gradient at the burner outlet, and the flame stretch (defined as the maximum gradient just upstream of flame front) to the velocity obtained from the mass flow rates. Using those relations, and the opposed flow flame model in Chemkin-Pro, it is possible to reproduce in the simulation the axial velocity profile observed in the experiment. Those relations were then used for modeling the cases corresponding to the PLIF measurement developed in Section 4 as well as ensure the validity of the empirical correction of extinction stretch rate by Kobayashi and Kitano [138] for the present study.

The experimental setup consists of a double pulse laser at 532 nm, going through a set of cylindrical lenses, and a beam expander to create a laser sheet going through the region of investigation. To avoid too bright images that complicate the data post-treatment, and be able to regulate the laser intensity, a beam intensity attenuator is positioned on the beamline before the lenses. The particles seeded were SiO<sub>2</sub> (Nipsil SS-50F particle, mean diameter of 2 μm) in the cold flow cases, and TiO<sub>2</sub> particles (Fujifilm Wako Pure Chemical, mean diameter < 5 μm) in the flame cases. The flow rates considered in this study are small, especially for ammonia flame cases. The entrainment of particles is thus difficult. To ensure good seeding, a specific swirling seeding system was developed and presented in Appendix 3B. The collection of the images is done using a CCD camera (Ikegami SKC-133) mounted with Nikon lenses

(Nikkor, 135 mm, f2.8) and a 532nm band-pass filter. The camera and laser pulses were commanded using a delay generator, controlled by a computer. The delay between the pulses was selected depending on the case investigated and maximum velocities considered. It was varied within the range 50  $\mu$ s to 1.5 ms. Schematics of the experimental setup is introduced in Fig. 3.3.

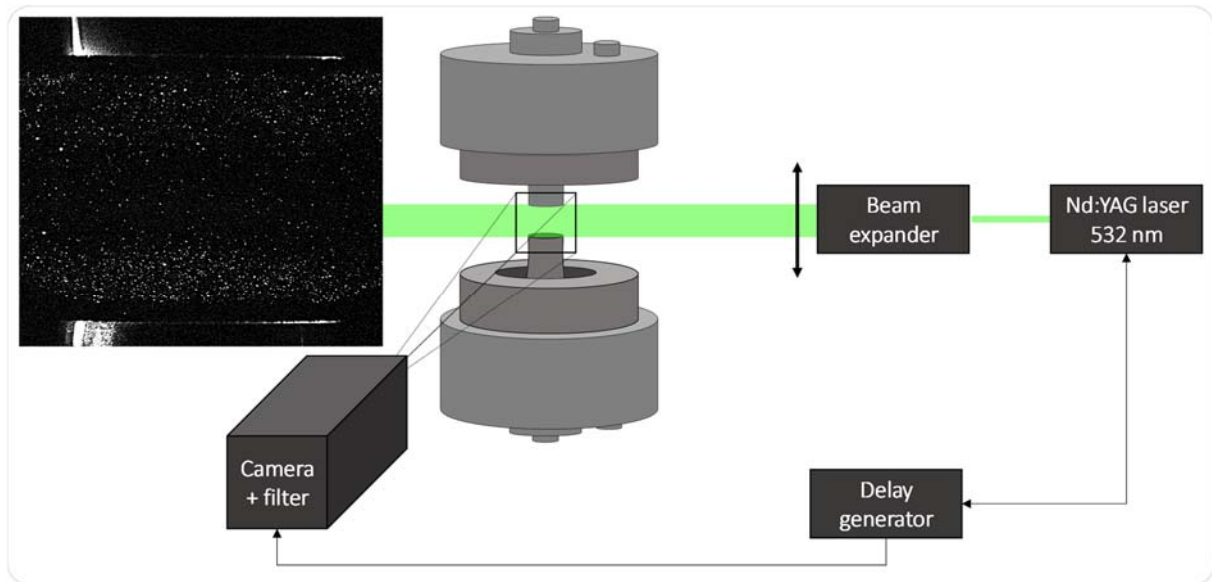


Fig. 3.3. Schematics of PIV measurement experimental setup.

Image processing is done on the software FtrPIV from Flowtech Research [150]. Analysis for one case is done on a set of at least 100 pairs of images, with the same parameters. The increment time between the two images is set as the one input for the laser pulse delay and depends on the case studied. Indeed, for each case, a different  $\Delta t$  has been calculated such as particles move within 5 pixels during this spend of time (considering the maximum velocity estimated at the burner outlet from the mass flow rates set as input). Scaling is done from the images directly, as the two burners' lips can be seen on the images, and burners inter-distance is carefully set to a specific value (10, 15 and 20 mm). Interrogation regions for vector calculation are set to 33 pixels by 33 pixels, with window overlapping of 10 pixels in both  $r$  and  $z$  directions. The vectors obtained with a correlation factor between 0.2 and 1.0 are selected, all the other removed. Among those vectors, second filtering is applied: vector corresponding to a displacement of more than 10 pixels are excluded as not physical, considering the flow patterns of the counterflow burner, the large velocity gradient along the  $z$ -axis, as well as the large increase of the radial velocity component with  $z$  going close to the stagnation plane axis, the angle deviation, and the vector length variation compared with the mean and median value of the vectors calculated in the nearby region,

have been increased compared with their nominal value up to 50 degrees and 75%. No interpolation is done to obtain the vectors in the regions of small particle density or where the analysis could not be performed. The mean velocity profiles are then obtained from the velocity field obtained for each pair. The specific region of interest for the study is the region along the burner axis, as well as the one at the burners' lips.

### 1.5.2. Non-premixed flames

Counterflow non-premixed methane flames were studied for both momentum equality and velocity equality, and various stretch values. Fig. 3.4 and Fig. 3.5 compare experimentally measured axial velocity profile with 1D simulation integrating different boundary conditions in the simulation. The full velocity map between the two burners obtained from PIV analysis is also included in the figures.

Three different boundary conditions were investigated:

- (A) Velocity boundaries based on the bulk velocity obtained from the mass flow meter.
- (B) Velocity boundaries based on the velocity on the burner axis and at the burner outlet measured from PIV.
- (C) Velocity boundaries based on the velocity on the burner axis and at the burner outlet measured from PIV and the radial velocity gradient at the burner outlet.

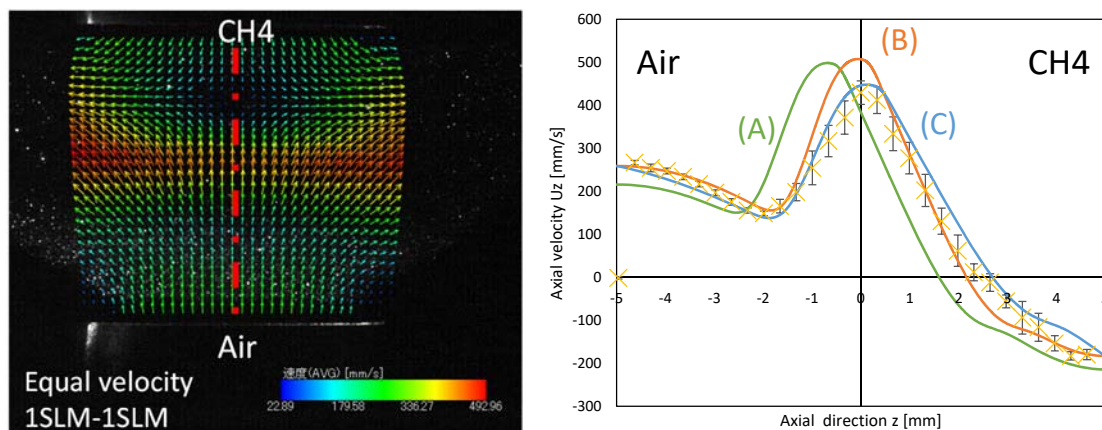


Fig. 3.4. Methane counterflow non-premixed flame in equal velocity (EV) conditions,  $U = 210$  mm/s: Velocity mapping; Axial velocity profile from experiment and simulations with conditions (A), (B) and (C).

For each flow condition, 3 sets of 200 images have been taking, giving 100 pairs for analysis on Flowtech PIV software. As the flame is stable, the mean value of the results of the analysis of the 100 pairs is considered. The experimental plot in Figs. 3.4 and 3.5, in crosses, corresponds to this mean value, and the error bar to the variation around this mean value in the full set.

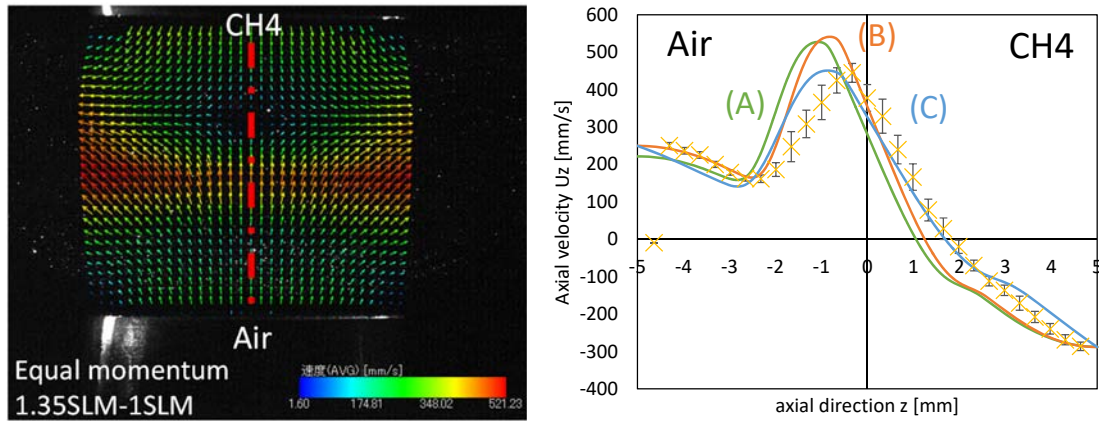


Fig. 3.5. Methane counterflow non-premixed flame in equal momentum boundary condition for  $U_{air} = 210$  mm/s and  $U_{CH_4} = 290$  mm/s. Velocity mapping; Axial velocity profile from experiment and simulations with conditions (A), (B) and (C).

While simulations with boundary conditions (A) are not able to reproduce the axial velocity profile observed experimentally, its reproduction in cases (B) and (C) is acceptable. The knowledge of the measured velocity at the burner outlet, on the burner axis, is thus necessary for the good reproduction of the experiments. The difference in the simulation between condition (B) and (C) are relatively small and barely affects the velocity gradient before the flame front on the oxidizer side as well as the minimum velocity position on the oxidizer side. Indeed, the radial velocity gradients at the burner outlet are small in the range of velocities investigated for non-premixed flames, and the main parameter of importance for proper modeling of the experimental results is thus the axial velocity on the burner axis at the burner exit.

Measuring the velocity profiles simultaneously to the extinction experiment is however not recommended as the introduction of particles in the flow field might lead to greater heat losses due to particles and earlier extinction. The strategy adopted here was thus to relate the bulk velocity obtained from mass flow rate measurements with the actual measured velocity on the burner axis at the burner

exit. This relation is then later used to calculate the actual outlet velocity value for a given bulk velocity value and used in the calculation of the experimental extinction stretch rate.

To obtain this relation between the bulk velocity obtained from the mass flow rates and the one at the burner outlets, measurements were performed on a broad range of mass flow rates. The results are presented in Fig. 3.6.

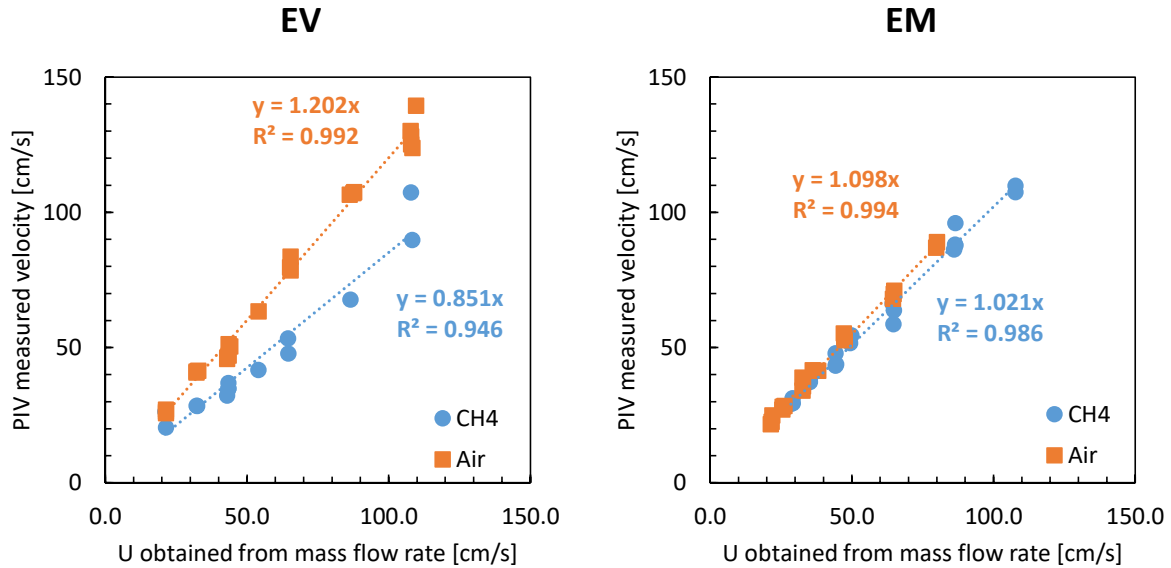


Fig. 3.6. Relations between bulk velocity and the one measured using PIV at the burner outlet: (a) equal velocity (EV) condition; (b) and the equal momentum (EM) condition.

Linear relations between the two velocities can be observed in both equal momentum and equal velocity conditions. However, while velocities at the burner outlet do not differ in the equal momentum condition ( $y = x$  relation), in the case of the equal velocity condition, unbalance is observed: for the air burner, the relation becomes  $y = ax$ , with  $a > 1$  and  $y = ax$  with  $a < 1$  for fuel side, and can be associated with the difference between the fuel and oxidizer densities. When ammonia is introduced in the mixture, the fuel density is slightly modified. However, this variation remains small when compared to the difference of density between fuel and oxidizer, and the relations are thus not expected to change.

The origin of the evolution of the velocity at the burner outlet as presented in Fig. 3.6 can be further understood by looking in more details to the velocity profiles for the two conditions as summarized in Figs. 3.7 and 3.8.

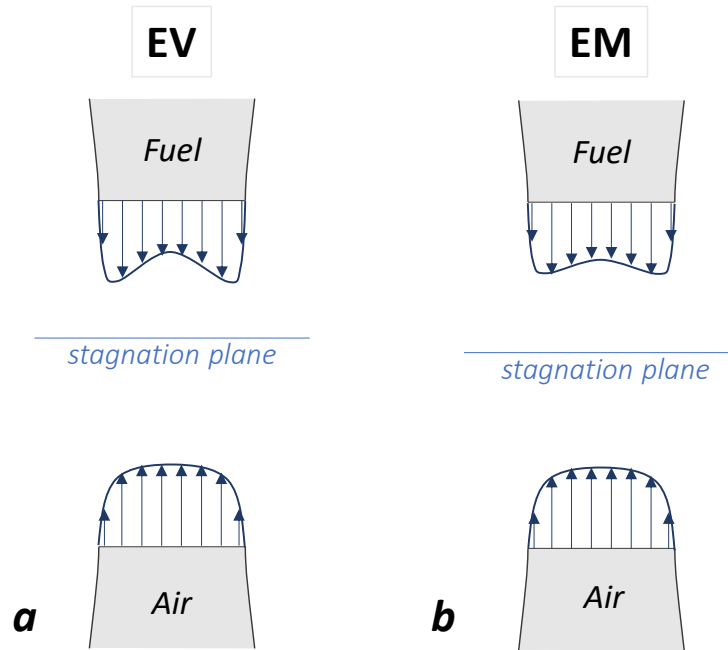


Fig. 3.7. Schematics of the observations on velocity profiles at the burner outlets: (a) equal velocity condition; (b) equal momentum condition.

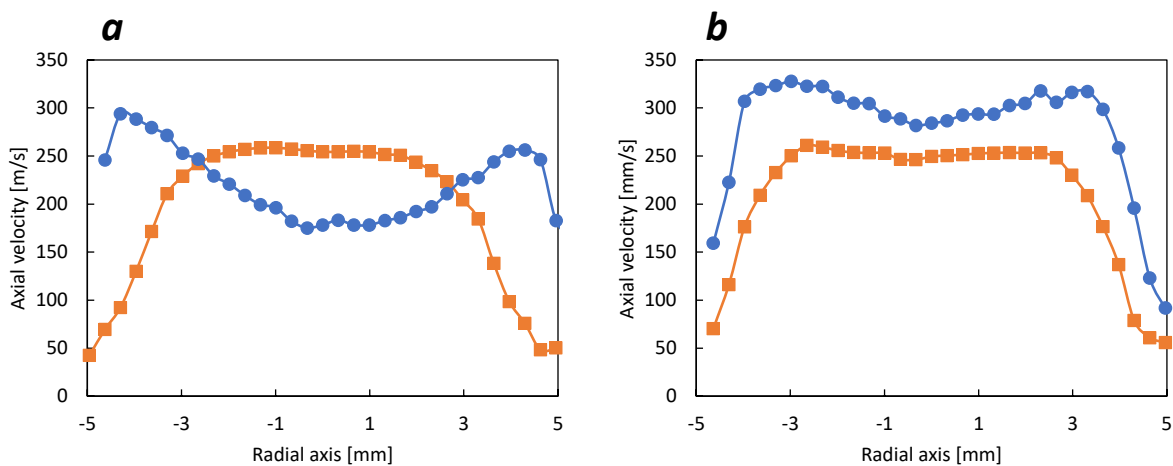


Fig. 3.8. Axial velocity profile at the air outlet ( $\square$ ) and fuel outlet ( $\circ$ ): (a) equal velocity (EV) with  $U = 210$  mm/s; (b) equal momentum (EM) conditions with  $U_{air} = 210$  mm/s and  $U_{CH_4} = 290$  mm/s.

For both cases, a slight unbalance leads to an M-shape at the fuel outlet while a reversed U shape is observed for the oxidizer outlet. However, the unbalance impact in burner momentum equality (EM) condition remains small, while the one for equal velocity (EV) condition is more pronounced.

In the EM condition, the outlet velocity profile remains close to the expected reverse U for both burners and the velocities at the center axis remain close to the one calculated from mass flow rates. On

the opposite, in the EV condition, the difference between the two profiles becomes more noticeable, with a clear M shape on the fuel side.

In the M-shape case, the axial velocity first increases from the burner lip ( $r = +/- 5$  mm) similarly to the profile due to the boundary layer, and then decreases when getting close to the center ( $r = 0$  mm). The lower velocity at  $r = 0$  mm is due to the closer stagnation plane, which proximity with the burner impacts the upstream flow field.

Using the measurement presented in Fig. 3.6, it is possible to correct the velocity at extinction obtained from mass flow rate measurement to obtain the one observed experimentally in the configuration and the for the burner used in this study. The Eq. ( 3.5 ) can thus be re-written:

$$\varepsilon = \frac{2U_{ox,z=0}}{L} \left( 1 + \frac{U_{fuel,z=L}}{U_{ox,z=0}} \sqrt{\frac{\rho_{fuel}}{\rho_{ox}}} \right) \quad (3.6)$$

with  $U_{ox,z=0}$  and  $U_{fuel,z=L}$  the actual velocities at the burner outlet, which are  $U_{ox,z=0} = 1.098U_{ox}$  and  $U_{fuel,z=L} = 1.021U_{fuel}$  in the case of the equal momentum (EM) condition, and  $U_{ox,z=0} = 1.202U_{ox}$  and  $U_{fuel,z=L} = 0.851U_{fuel}$  in the case of the equal velocity (EV) condition.

The use of either EV or EM condition is similar to the present correction, and EV condition was selected in the following experiment on the extinction stretch rate for practical reasons.

### 1.5.3. Premixed flames

Similar to what was observed for the counterflow non-premixed flames, the experimental velocity profiles for counterflow premixed twin flames can deviate from the potential flow estimated in the numerical simulation, particularly for small  $L/D$  and large flow rates. If not properly considered, this can lead to an erroneous conclusion when comparing the numerical and experimental extinction stretch rate, but also flame structure. Empirical correction of the extinction stretch rate as derived by Kobayashi and Kitano [138] was used in this study to take into account the impact of the selected  $L/D$ . To confirm the validity of the empirical correction for the range of velocity investigated in the present work, as well as the fuel considered, the velocity profiles also studied for premixed flames. Clarification of the velocity profiles is moreover necessary for the comparison of experimental and numerical profiles of reacting species as investigated in Section 4. The ammonia mixing ratio,  $E$ , was set to 0, 0.15, 0.30, and 1 for the PIV experiments, and equivalence ratios of 0.8, 1.0 and 1.2 have been investigated, for the range of inlet

flow velocity corresponding to the minimum velocity necessary for stabilization to the velocity just before extinction.

The same way it was done for non-premixed flames, for each flame case, the axial velocity at the centerline of the burners' outlet,  $U_{z0}$ , is obtained and compared to the one obtained from the mass flow meter measurements,  $U$ . Similarly, the radial gradient at the center of the burner outlet,  $g_r$ , was compared to  $U$ .

Moreover, for comparison with the expression of Eq. ( 3.4 ), the maximum axial velocity gradient before the flame front,  $g_z$ , was obtained from the PIV measurements. To obtain  $g_z$ , polynomial fitting of the experimental axial velocity profile of the region of interest has been done to the order 5. The derivative of the fitting curve is then calculated and its absolute maximum value in the region of interest is defined as  $g_z$ . Details of the fitting are available in Appendix 3B. The following relations were investigated:

a.  $U_{z0}=f(U)$

b.  $g_{r0}=f(U)$

c.  $g_z=f(g_n)=f(2U/L)$

For all the mixtures investigated, the relations  $a$ ,  $b$  and  $c$  are linear. The scatter to the linear trend is more or less pronounced depending on the relation. The largest uncertainties correspond to the relation  $b$  on the radial velocity gradient. Depending on the equivalence ratio and the mixing, the leading coefficients for those relations differ slightly. The relations  $a$  and  $b$  are summarized in Table 3.3 and were used for the boundary conditions inputs for numerical simulations for the comparison of species profiles. The relation  $c$ , relating the measured gradient velocity before the flame front and the global stretch as expressed in Eq. ( 3.3 ), is also included in Table 3.3. A comparison with the results from Kobayashi and Kitano [138] is also presented in Fig. 3.9. A larger scattering for the present data can be observed and might be attributed to the variation in fuel composition and on the equivalence ratio as well as the larger uncertainty for small flow rate measurements. Leading coefficients are slightly larger than expected for  $L/D = 1$  but in reasonable agreement with the previous data. The Eq. (3.5) was thus conserved.

Table 3.3. Relations  $U_{z0} - U$ ,  $g_{r0} - U$  and  $g_z - g_n$ , with  $U$  in cm/s for ammonia/methane/air flames.

$E$	$U_{z0}$ [cm/s]	$g_{r0}$ [ $s^{-1}$ ]	$g_z$ [ $s^{-1}$ ]
0	$U_{z0} = 0.8317 \cdot U$	$g_{r0} = 0.585 \cdot U + 59.093$	$g_z = 1.4952g_n$
0.15	$U_{z0} = 0.8513 \cdot U$	$g_{r0} = 0.7958 \cdot U + 19.527$	$g_z = 1.5456g_n$
0.30	$U_{z0} = 0.8729 \cdot U$	$g_{r0} = 0.78 \cdot U + 1.7684$	$g_z = 1.3896g_n$
0.60	$U_{z0} = 0.8647 \cdot U$	$g_{r0} = 0.788 \cdot U + 18.413$	$g_z = 1.5602g_n$
1	$U_{z0} = 1.0777 \cdot U$	$g_{r0} = 0.724 \cdot U + 13.389$	$g_z = 1.6281g_n$

Similarly to the analysis on non-premixed flames, the measured and simulated velocity profiles were compared for methane flame case, for which the chemistry is relatively well known, to ensure that the experimental axial velocity profile can be reproduced using the 1D axisymmetric numerical simulation in Chemkin-pro numerical environment and the actual experimental boundary conditions. A detailed comprehensive study is proposed in Appendix 3B, but the main conclusions are recalled here.

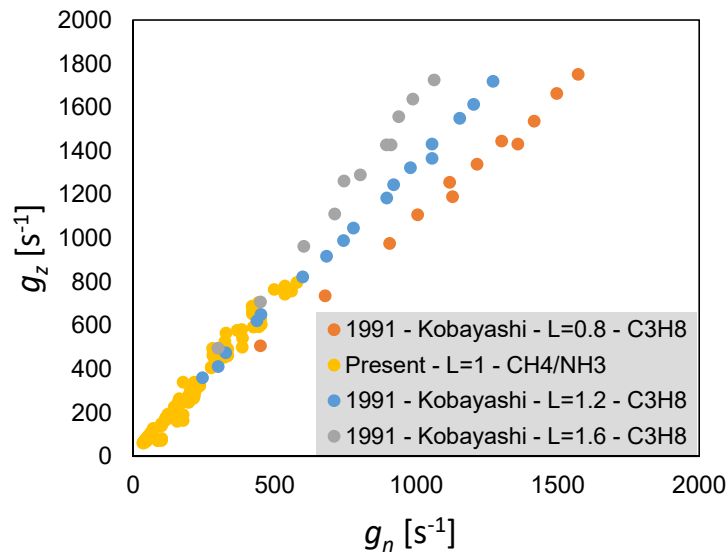


Fig. 3.9. Comparison of  $g_z$  as a function of  $g_n$  in the present study to previous experiments results by Kobayashi and Kitano [138].

The use of the boundary conditions obtained from PIV measurements and the derived relations between  $U$ ,  $U_{z0}$ ,  $g_z$ , and  $g_{r0}$ , previously introduced in Table 3.3. Relations  $U_{z0} - U$ ,  $g_{r0} - U$  and  $g_z - g_n$ , Table 3.3, allows for a better estimate of the experimental velocity profiles as introduced in Fig. 3.10. The remaining uncertainty might be attributed to the combined limitations of the 1D axisymmetrical model and the chemistry modeling, as well as experimental measurement limitations.

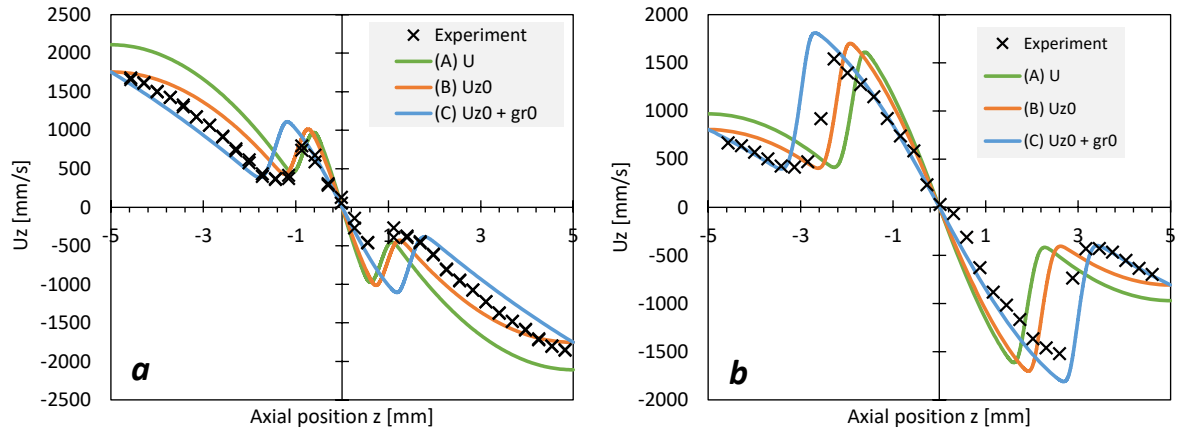


Fig. 3.10. Velocity profiles for methane/air counterflow premixed twin flames: (a)  $\phi = 0.8$  and  $U = 210.6$  cm/s; (b)  $\phi = 1.2$  and  $U = 96.9$  cm/s.  $\times$  represent the PIV experimental results, the plain lines are the simulations results.

## 2. Experimental analysis of the extinction stretch rate of counterflow premixed twin flames

### 2.1. Conditions of study

Experiments were performed using the setup described in Section 1.3 of this chapter, following the methodology described in Sections 1.4 and 1.5. The region of the investigation was defined as  $\phi = 0.6$  to  $\phi = 1.3$ , corresponding to the range of stoichiometry for which the methane flame can be observed on the present burner. The ammonia mixing ratios  $E = 0, 0.05, 0.1, 0.15, 0.2, 0.25, 0.3, 0.4, 0.6$  and  $1$  were investigated. Distance between the burners was set to  $L = 1.2$  cm, giving a ratio  $L/D$  of  $1.2$  at the exception of ammonia/air flame which could be stabilized only for  $L/D = 1$ . The simulation environment is Chemkin-Pro from ANSYS [120], with the opposed-flow model [124] as described in Section 1.4.1.

### 2.2. Experimental results and comparisons with numerical simulations

The experimental extinction stretch rate for different ammonia mixing ratios,  $E$ , is represented as a function of the equivalence ratio,  $\phi$ , in Fig. 3.11. It could be observed that the extinction stretch rate of ammonia/air premixed flames is extremely low compared with the one of methane/air premixed flames, presenting maximum values close to  $130 \text{ s}^{-1}$  and  $1600 \text{ s}^{-1}$ , respectively. The extinction stretch rate of methane/ammonia/air premixed flames decreases drastically as ammonia is introduced in the mixture, as expected from the particularly low values of the extinction stretch rate of ammonia/air flames observed.

For all the ammonia mixing ratio considered,  $E$ ,  $\varepsilon_{ext}$  increases when  $\phi$  increases, up to a maximum between  $\phi = 0.9 - 1.0$  and then decreases in the rich region. The observation of a maximum value in the lean region can be attributed to a non-equidiffusive phenomenon combined with stretch effect as stated by Law [123]. Both  $\text{NH}_3/\text{air}$  and  $\text{CH}_4/\text{air}$  lean flames have a Lewis number,  $Le$  (= thermal to mass diffusivity)  $< 1$ , whereas for rich flames,  $Le > 1$ , as detailed in Table 3.4. The positive stretch is thus expected to enhance the flame temperature in the lean region for  $Le < 1$ , and to lower it in the rich region for  $Le > 1$ , leading to a maximum extinction stretch rate in the leaner region.

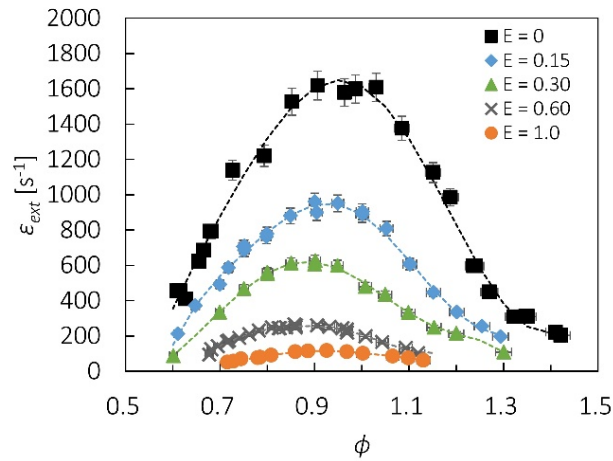


Fig. 3.11. Extinction stretch rate of ammonia/methane/air counterflow premixed twin flames for several  $E$  and  $\phi$ .

Table 3.4. Lewis number of ammonia/methane/air mixtures calculated following work by Fairbanks and Wilke [151] and transport and thermal data from Okafor et al. [63].

Equivalence ratio	0.8	1.2
Methane/air	0.96	1.10
Ammonia/air	0.94	1.09

For kinetics validation, 3 specific equivalence ratios are more specifically investigated:  $\phi = 0.7$ , in the lean region, corresponding to the limit observable with the experimental setup used in the case of pure ammonia flame;  $\phi = 0.9$ , near the maximum extinction stretch rate obtained for all the mixtures considered; and  $\phi = 1.2$ , in the rich region. The results are plotted in Fig. 3.12, for various  $E$ .

From Fig. 3.12, it can be observed that an increase in  $E$  led to a decrease in  $\epsilon_{ext}$ , corresponding to the lower combustion intensity of ammonia flame as also observed in Fig. 3.11. Experimental data for  $\phi = 0.9$  are well correlated into one curve, whereas the scattering is larger for the data at  $\phi = 0.7$  and  $\phi = 1.2$ . These larger discrepancies might be attributed to experimental limitations as buoyancy becomes more important for smaller values of  $\epsilon$ .

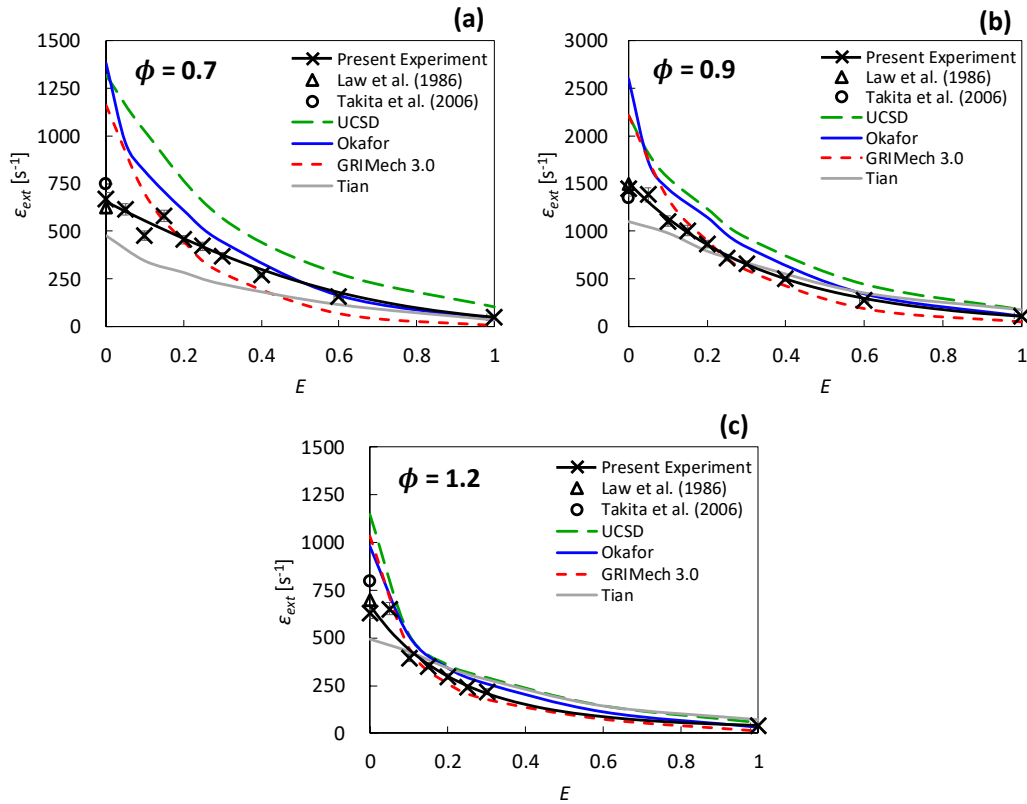


Fig. 3.12. Extinction stretch rate of ammonia/methane/air premixed twin flames with ammonia mixing ratio,  $E$ : (a)  $\phi = 0.7$ ; (b)  $\phi = 0.9$ ; (c)  $\phi = 1.2$ .

Comparing the four selected mechanisms simulation results to the experimental one, it can be noticed that none of the mechanisms allow reproducing the experimental trend for all the stoichiometries and all the ammonia mixing ratio considered. The largest discrepancies are observed in the lean case at  $\phi = 0.7$ . This discrepancy appears between experimental data and numerical results but also between mechanisms. It is reduced when the stoichiometry is increased up to  $\phi = 1.2$ . In the rich case, all mechanisms are in reasonable agreement with the experimental results. This larger discrepancies for lean flames might be attributed to some limitations of the hydrocarbon subsets of the mechanisms selected in this study. This is developed in greater details in Section 2.3. Looking more specifically at the different estimates given by the four mechanisms, the following observations could be drawn:

- Tian's mechanism underestimates the stretch rate in all the cases investigated at the exception of pure  $\text{NH}_3$  case, but especially for pure  $\text{CH}_4$  flames as can be seen in Fig. 3.12. This can be related to the  $\text{HCO} \rightarrow \text{CO}$  conversion step as discussed by Okafor et al. [63]. Competition in the set of

reactions associated with this conversion leads to a reduction in the production of H radical, lowering the flame reactivity and thus the extinction stretch rate.

- GRI-Mech3.0 fails to reproduce the extinction stretch rate by systematically underestimating the extinction stretch rate for a large quantity of  $\text{NH}_3$ . This can be understood as some key-reactions for ammonia combustion, which are relevant for large ammonia introduction, are not included in GRI-Mech 3.0 [63]. Comparing Okafor's mechanism and GRI-Mech 3.0 predictions, one can see that this problem is mostly corrected by introducing some essential reactions involving the  $\text{NH}_i$  radicals.
- UCSD mechanism produces results that are close to the one obtained by Okafor's mechanism at the exception of the case of  $\phi = 0.7$  as soon as  $\text{NH}_3$  is introduced in the mixture. This difference might thus be attributed to  $\text{NH}_3$  chemistry. From reaction path analysis in lean  $\text{NH}_3$ /air premixed flames, the sub-paths corresponding to HNO production ( $\text{NH}_2, \text{NH} \rightarrow \text{HNO}$ ) and reduction to NO seem to have a more important role than in stoichiometric and rich flames [43]. Moreover, these paths differ in the two mechanisms and might explain to some extent the difference observed. Some reactions from the  $\text{NH}_i\text{-CH}_i$  interactions set might also be involved.

On the overall, none of the chemical mechanisms used in this study were able to reproduce all the cases considered. Further studies are thus necessary to develop the current mechanisms especially concerning lean flames chemistry.

## 2.3. Further discussion on lean flames

It could be observed that the case of pure methane was not adequately reproduced by the mechanisms proposed in this study. This might be reasonably attributed to some reactions in the carbon set which are under-developed. Indeed, the four mechanisms all included a minimum carbon subset, corresponding to the major reaction path for methane combustion, but variations can be observed for this subset within each mechanism: reaction constants are taken from different sources, some minor intermediates are included in some but not all of them. More specifically, the UCSD mechanism is the one which is the more developed within the 4 sets tested, with the largest set of intermediate species and reactions. GRI-

Mech3.0 and Tian's mechanism presents a much more limited carbon reaction set. Okafor's mechanism carbon reaction set is even more limited. Those differences can first explain the divergences observed in the simulation results for lean methane flames as recalled in Fig. 3.13.

For further discussion, calculations were performed with AramcoMech 2.0 for methane case. This later mechanism presents an extensive set of reactions, a compilation of gradually well-validated chemical subsets (from H<sub>2</sub>-O<sub>2</sub> subset, C<sub>1</sub> subset, to larger hydrocarbons), on a broad range of experiments and conditions [95]. The results were shown to be much closer to experimental results, as shown in Fig. 3.13, confirming that the methane subset of the mechanisms presently selected, though being sufficient for some of the methane flame combustion characteristics including the laminar burning velocity, are not able to reproduce experimental trends for stretch flames.

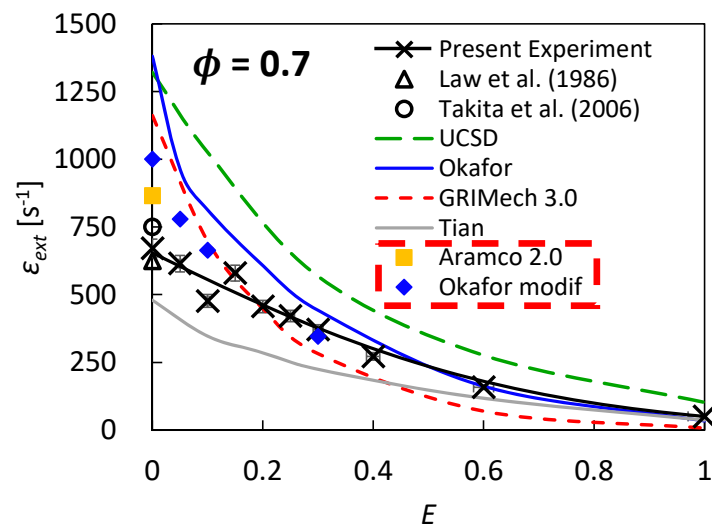


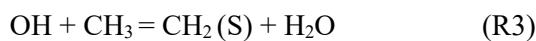
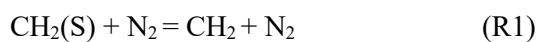
Fig. 3.13. Experimental and numerical results of the extinction stretch rate at  $\phi = 0.7$  with  $E$ , for comparison with AramcoMech 2.0 and Okafor's mechanism after modification in this study.

To identify more specifically which reactions are predominant for the lean flame chemistry, near flame extinction, and restrict the reactions subset to investigate, reaction path as been observed at  $\phi = 0.9$  and  $\phi = 0.7$ . This has been done for both Okafor's mechanism [63] and Tian's mechanism [69], as they show opposite trends relative to the extinction stretch rate. Flames investigated are 1D opposed twin flames, close to extinction (with stretch rate between 90% and 100% of the extinction stretch rate value obtained by simulation for the two mechanisms). Complete results are presented in Appendix 3C and summarized here. For both mechanisms, the reactions associated with OH radical becomes more

important. Major changes between  $\phi = 0.9$  and  $\phi = 0.7$  concern the conversion of  $\text{HCO} \rightarrow \text{CO}$  and  $\text{CO} \rightarrow \text{CO}_2$ . The first one becomes faster as more  $\text{O}_2$  is available for the reaction  $\text{HCO} + \text{O}_2 = \text{HO}_2 + \text{CO}$ . The second becomes also faster as both CO production and OH production are emphasized as more  $\text{O}_2$  is available leading to faster  $\text{CO} + \text{OH} = \text{CO}_2 + \text{H}$ . The conversions  $\text{CH}_3 \rightarrow \text{CH}_2\text{O}$  and  $\text{CH}_2\text{O} \rightarrow \text{HCO}$  are also emphasized but to a lower degree. These reactions, and reactions competing with these reactions, have a large impact on the global chemistry of lean highly stretched flames and should be investigated in priority.

Extinction stretch rate sensitivity analysis has also been performed. The extinction stretch rate was calculated iteratively, with the variation of the pre-exponential factor,  $A$ , of each reaction. These variations of  $A$  were in the range  $\pm 5\%$  of their original values and the extinction stretch rate was calculated for each case, as well as the sensitivity. Due to the computational cost, the calculations have been done for Okafor's mechanism only, and on coarse mesh. The sensitivity of both the velocity at the outlet of the burner just before extinction (corresponding to the global, also called normal stretch  $g_{ext} = 2U_{ext}/L$ ) and maximum axial velocity gradient upstream of the flame front just before extinction are plotted in Fig. 3.14.

The extinction stretch rate, like the laminar burning velocity [63], is strongly positively sensitive to the chain branching reaction  $\text{H} + \text{O}_2 = \text{O} + \text{OH}$ . This can be understood as this reaction is at the origin of most of the radicals O and OH produced in the flame. Reaction  $\text{CO} + \text{OH} = \text{CO}_2 + \text{H}$  figures among the reactions which are producing the more heat in the flame. This explains the strong positive sensitivity observed here. The other reactions with positive sensitivity are:



Among those 5 reactions, (R2), (R4) and (R5) are related to the production of H and OH radicals. The role of (R1) and (R3) and how it affects stretch rate is less evident. The reactions with negative sensitivity correspond all to H consumption to more stable species.

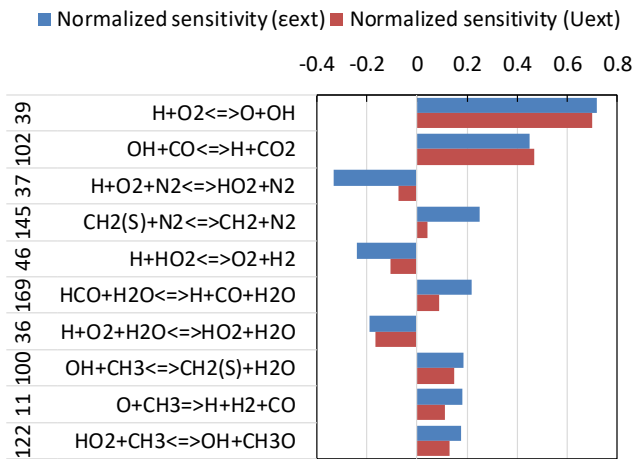


Fig. 3.14. The sensitivity of extinction stretch rate for methane/air lean flame.

The modification of any of these reactions in the four studied mechanisms leads to a large difference in the extinction stretch rate simulation results. As an example, the sole modification of one unique reaction was shown to have a great impact on the extinction stretch rate as presented in Fig. 3.13, through the example of the modification of the reaction coefficients from  $\text{HO}_2 + \text{CH}_3 = \text{OH} + \text{CH}_3\text{O}$  in Okafor's mechanism.  $\text{HO}_2 + \text{CH}_3 = \text{OH} + \text{CH}_3\text{O}$  reaction coefficients were identical to the one in GRI-Mech 3.0 and were changed to fit the coefficient proposed in AramcoMech 2.0, updated from a work by Jasper et al. [152]. A drastic decrease in the extinction stretch rate was observed, showing a better fit to the experimental data.

### 3. Experimental analysis of the extinction stretch rate of counterflow non-premixed flame

#### 3.1. Conditions of study

Two main objectives can be presented here. The first one is the determination of the extinction stretch rate of ammonia non-premixed flame, as well as the observation of the evolution of the extinction stretch rate of ammonia/methane mixture for an increasing ammonia mixing ratio. Extinction stretch rate is an essential parameter in the comprehension of the turbulent flame. Indeed, the extinction stretch rate corresponds to the inverse of the smallest residence time under which flame cannot be sustained and characterise the flame behavior. Determination of extinction stretch rate of ammonia, and

ammonia/methane non-premixed flame have been reported recently in the literature [70], but data remain scarce and is part of the objective of the study.

The second objective concern mechanisms validation for non-premixed stretched flames. Non-premixed flames present different structures than premixed flames, which might correspond to some differences in the kinetics considered. Validation towards both premixed and non-premixed flames has thus an interest.

Extinction stretch rate has been obtained using a counterflow burner, fuelled in one side by a mixture of ammonia and methane, and on the other side by air. In the case of pure ammonia fuel, the airside was doped with  $O_2$  to dope the reactivity and stabilize the flame. Indeed, flames could not be stabilized using pure ammonia toward air jet, even when reducing the distance  $L$  between the burners. The extinction stretch rate was obtained using Eq. (3.7), which relates the extinction stretch rate to the velocity at the burner outlet. The bulk velocity at the burner outlet was obtained from the mass flow rates and corrected to get the actual velocity at the centreline using the relations obtained from PIV measurements. Extinction stretch rate has been obtained by gradually increasing the velocity at the outlet of the burners while keeping equal velocity conditions for fuel and air.

## 3.2. Experimental results and comparison with numerical simulations

The results of the extinction stretch rate of counterflow non-premixed flames are first presented in Fig. 3.15 for pure ammonia fuel and  $O_2$ -enriched air as the oxidizer, and followed by the one for methane/ammonia fuel and air as the oxidizer in Fig. 3.16. The ammonia counterflow non-premixed flame could not be stabilized with air as the oxidizer, even by reducing the burner inter-distance, and enrichment with  $O_2$  was thus considered. The choice of  $O_2$  enrichment was driven by the chemistry validation purpose of this study. For the same reason, and to remain as close as possible of the  $NH_3$  chemistry in the air, the study was limited to a small addition of  $O_2$  (25% and 30% only). The extinction stretch rate obtained is particularly small, even with  $O_2$ -enrichment, with a value close to  $150 \text{ s}^{-1}$  at 25% of  $O_2$  in the oxidizer close to the value obtained for premixed stoichiometric flames. This value increases to  $400 \text{ s}^{-1}$  for 30% of oxygen in the oxidizer. The extinction stretch rate thus increases drastically when the content of  $O_2$  in the air is increased, as 5% more of  $O_2$  doubles the value of the extinction stretch

rate. This important increase is to be associated with the greater availability of OH and O radicals, which are of particular importance in ammonia chemistry as discussed in Chapter 2.

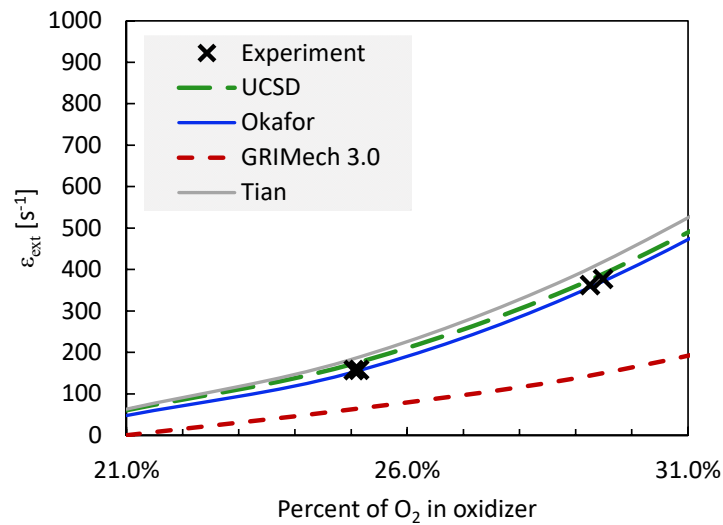


Fig. 3.15. Extinction stretch rate of ammonia counterflow non-premixed flames. Oxidizer: air enriched with O<sub>2</sub>, N<sub>2</sub>/O<sub>2</sub> between 0.75/0.25 and 0.70/0.30.

Numerical simulations were performed using the four mechanisms previously selected. It can be observed from Fig. 3.15, that similarly to premixed flames [43], GRI-Mech 3.0 tend to underestimate the extinction stretch rate, while Tian's, UCSD and Okafor's mechanisms give estimates close to the experimental results. The order between the mechanisms remains the same as observed for premixed flames, but the agreement with the experimental results is much better, except for GRI-Mech 3.0. Tian's, UCSD, and Okafor's mechanisms can thus be validated toward the extinction criteria for non-premixed flame and considered for the numerical simulations of non-premixed ammonia flames.

Following the discussion on the extinction of ammonia counterflow non-premixed flames, ammonia/methane blended fuel is investigated. It can be observed in Fig. 3.16 that introduction of ammonia in the non-premixed flame is, as in the premixed case, leading to a near exponential decrease of the extinction stretch rate. Whereas the extinction stretch rate for ammonia non-premixed flame was estimated to be close to the maximum extinction stretch rate for premixed flames (close to 100 s<sup>-1</sup>), the value obtained for the non-premixed methane flames are much smaller (non-premixed flame close to 600 s<sup>-1</sup>; premixed flame close to 1600 s<sup>-1</sup>) and the extinction stretch rate of ammonia/methane non-premixed flame ranges between 100 and 600 s<sup>-1</sup>.

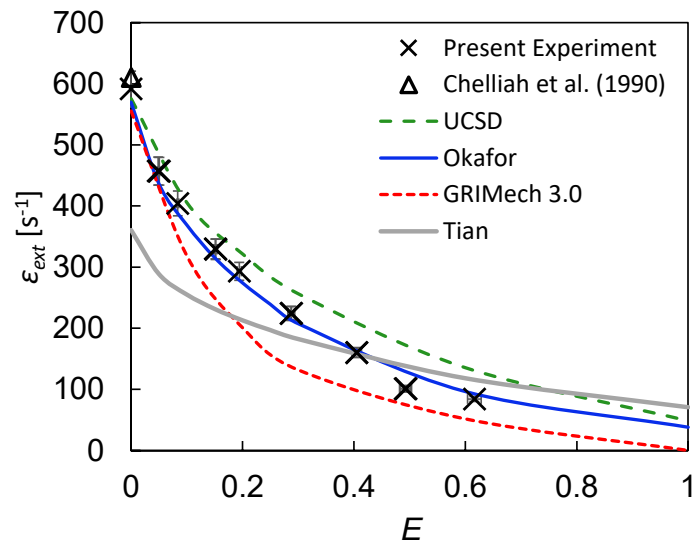


Fig. 3.16. Extinction stretch rate of methane/ammonia counterflow non-premixed flame. Oxidizer: air.

The experimental results were compared to the simulation results using the UCSD mechanism, GRI-Mech 3.0, Tian's, and Okafor's mechanisms in Fig. 3.16. First, comparing numerical and experimental trends, it can be seen that the extinction stretch rate is better reproduced by the Okafor's mechanism in the range of experimental conditions investigated, followed by UCSD mechanism. It can also be observed that Tian's mechanism greatly underestimates the methane flame extinction stretch rate and globally fail to reproduce the experimental extinction stretch rate. The origin of the underestimation can be reasonably attributed to the same reactions as discussed in Section 2 for premixed flames. The same way, GRI-Mech3.0 tends to underestimate the extinction stretch rate when ammonia is added, as for premixed flames and ammonia non-premixed flames, highlighting the lack in its nitrogen chemistry.

Second, the largest differences between the simulations with Okafor's, or the experimental results, and UCSD mechanism and the experiment are observed at  $E = 0.3$ . This corresponds to nearly 50% of ammonia in terms of mole fraction. In such mixing, both ammonia and methane reaction paths have comparable reaction rates, but the heat release process is still essentially sustained by methane oxidations reactions. Interactions between the two oxidation paths, through radicals such as  $\text{CH}$ ,  $\text{CH}_2$ ,  $\text{CH}_2(\text{S})$ ,  $\text{HCCO}$  on methane side, and  $\text{NO}$  and  $\text{NH}$  on ammonia side are more important than for the other mixings  $E$  as discussed in Chapter 2.

Thus, the overestimation by UCSD mechanism in this specific region tends to suggest that interaction reactions between ammonia oxidation path and methane oxidation path might be responsible for the

discrepancy observed. Their impact on the mixture reactivity might be underestimated in the UCSD mechanism. Comparison between the reactions parameters of both mechanism as well as sensitivity analysis combined with reaction path analysis would however be necessary to conclude definitely on this point.

## 4. Evaluation of the chemistry based on OH and NO distributions in the flame using OH and NO-PLIF

### 4.1. Objective and investigated conditions

Greater discrepancies between the experimental results and the numerical results of extinction stretch rate could be observed in the premixed counterflow twin flame cases. Indeed, in this case, none of the selected mechanisms were able to reproduce the experimental trend. More detailed investigations are thus necessary for those flames. The premixed twin flames structure was thus investigated, using OH and NO-PLIF, to identify the origin of the discrepancy more particularly.

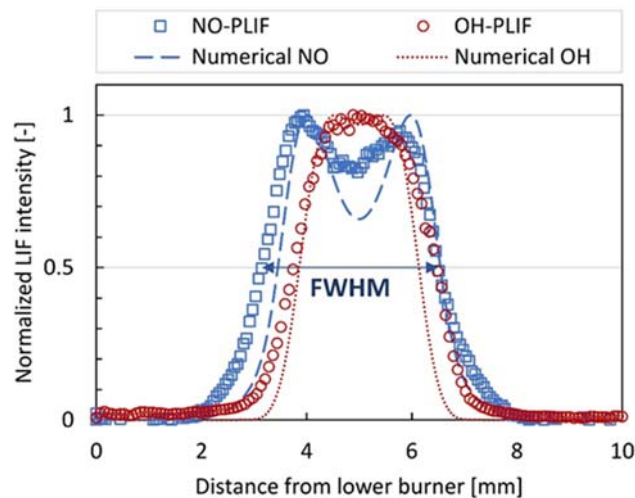


Fig. 3.17. Example of OH and NO-PLIF profiles for counterflow premixed twin flames at  $E = 1$  and

$$\phi = 1.2.$$

In the counterflow premixed twin flames configuration, profiles of temperature and species are symmetric to the stagnation plane as seen in Fig. 3.17. The FWHM (Full-Width-Half-Maximum) parameter, selected in this study, corresponds to the distance between the front of apparition of the

species in the two flames. This parameter, as well as the distance between two flames in counterflow twin flames configuration, varies with  $\varepsilon$ ,  $\phi$  and  $E$ . The FWHM of OH and NO profiles can thus be related to the rates of formation and consumption of these species. Thus, comparisons of the FWHM experimental values with the numerical ones of different chemical mechanisms enable the validation of those kinetics for stretched premixed  $\text{NH}_3/\text{CH}_4/\text{air}$  twin flames. Moreover, it allows for the identification of the associated subsets of reactions which require updates. An example of a comparison of numerical and experimental FWHM is shown in Fig. 3.17.

To investigate the chemistry in a broad range of mixtures, different cases have been selected. They are presented in Table 3.5. Ammonia mixing ratio,  $E$ , was varied between 0 and 1, and for each  $E$ , three equivalence ratios,  $\phi = 0.8$  (lean),  $\phi = 1.0$  (stoichiometric), and  $\phi = 1.2$  (rich) were investigated. The ratio  $L/D$  was kept constant and equal to 1. Stretch rate was not kept constant for practical reasons: the maximum extinction stretch rate variations for  $E$  between 0 and 1 are between  $2000 \text{ s}^{-1}$  and  $100 \text{ s}^{-1}$ . Moreover, for the same  $E$ , the extinction stretch rate highly depends on the stoichiometry. Rather than setting a constant stretch rate for all the flames observed, the choice which has been done here is to select a convenient stretch rate between 30% and 60% of its value at extinction for the flame case studied, as presented in Fig. 3.18. A stretch rate a value leading to stable flame with limited curvature neither too close to burner lips nor too close to extinction was considered as convenient.

Table 3.5. Cases studied for OH and NO profiles.

$E$	$\phi$	$U$ [cm/s]	$U_{z0}$ [cm/s]	$g_{r0}$ [s <sup>-1</sup> ]
0	0.8	210.4	175.0	182.2
	1	298.9	248.6	234
	1.2	97.1	80.8	115.9
0.15	0.8	166.7	141.9	152.2
	1	196.1	166.9	175.6
	1.2	103.6	88.2	102
0.3	0.8	103.1	90.0	82.15
	1	81.5	71.1	65.32
	1.2	42.4	37.0	34.85
0.6	0.8	36.5	31.5	47.21
	1	30.0	25.9	42.1
	1.2	25.7	22.2	38.7
1	0.8	23.7	25.6	30.58
	1	24.8	26.7	31.36
	1.1	23.1	24.9	30.11

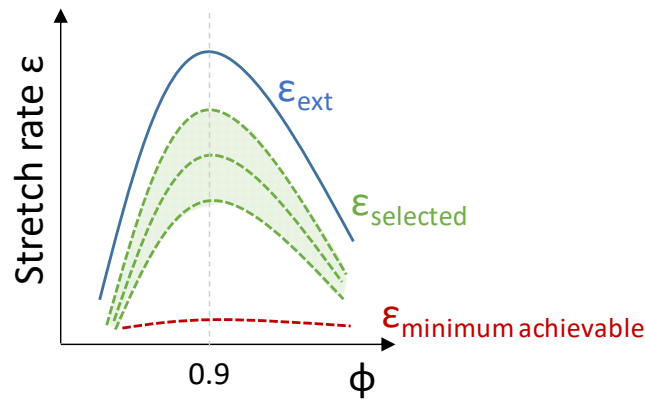


Fig. 3.18. Schematics of the region of study for OH and NO-PLIF profiles.

## 4.2. Experimental setup and method

The OH and NO profiles were obtained along the center axis of the burners using PLIF measurements. For the OH-PLIF, the laser beam was generated using an Nd-YAG pulsed laser (Spectra-Physics GCR-250-10 at 532 nm) pumping a dye laser (Lumonics HD-500 for Rhodamine 6G) tuned at 565.858 nm and frequency-doubled (Lumonics HT-1000) at 282.929 nm to excite the OH  $A^2\Sigma^+ \leftarrow X^2\Pi$  (1,0) band with an energy of about 12 mJ per shot. The fluorescence was collected at approximately 310 nm using an intensified charge-coupled device camera (Andor iStar CCD) mounted with UV lenses (UV-Nikkor 105 mm F4.5) with a combination of a UG-11 filter and 313 nm band-pass filter.

For the NO-PLIF, the beam was generated using an Nd-YAG pulsed laser (Spectra-Physics GCR-250-10 at 355 nm) pumping a dye laser (Sirah with a frequency doubling unit for Coumarin 450) tuned at 452.596 nm, frequency-doubled at 226.298 nm for excitation of the NO  $A^2\Sigma \leftarrow X^2\Pi$  (0,0) band. Because the effectiveness of the Coumarin dye degrades with time, the laser energy was measured for each flame case, and used in post-processing. The energy range was 1 – 6 mJ per shot, corresponding to the linear fluorescence regime. For fluorescence signal collection, a band-pass filter centered at 236.3 nm was used.

For both OH-PLIF and NO-PLIF, a laser sheet of approximately 50 mm in height and 60  $\mu\text{m}$  thickness was created using a set of fused silica cylindrical lenses. The energy uniformity of the laser sheet was controlled by the fluorescence emitted by an acetone cell. Settings for fluorescence collection through the ICCD camera were kept identical for each flame case, to allow for the comparison between

them and with the simulated profiles from numerical analysis. The experimental setup is summarized in Fig. 3.19.

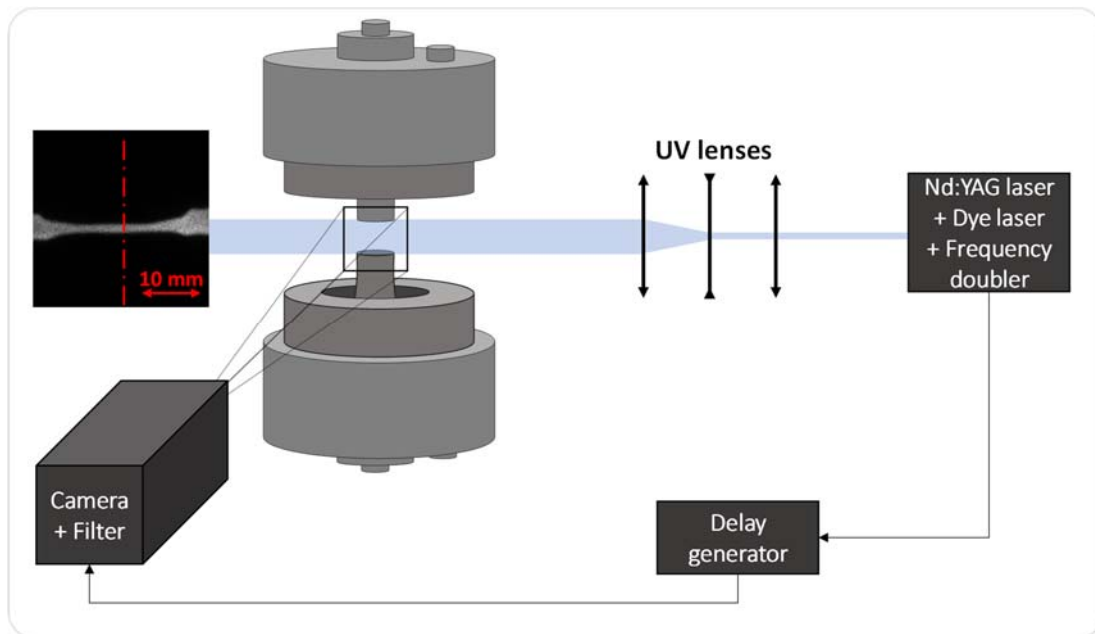


Fig. 3.19. Schematics of the PLIF experimental setup.

The images of OH-PLIF and NO-PLIF were first time-averaged over 250 raw images of the same flame case. A typical PLIF image before time averaging is presented in Fig. 3.20, with the space between the burner represented as a dashed square, and the burner axis with a dashed line. For comparison of the experimental profiles with numerical simulations, the region of interest is the burners axis. Moreover, because the counterflow flames observed experimentally were curved only far from the axis, as seen in Fig. 3.2 or Fig. 3.20, the fluorescence intensity profiles of OH and NO were then taken from the time-averaged images by spatially averaging across a 10 pixels width running perpendicular to the burner axis. This corresponds to a region where flame curvature is neglectable. Background images were processed using the same method and subtracted. A correction factor obtained was obtained from the acetone cell measurement for the laser sheet energy profile and then applied.

The FWHM (Full-Width-Half-Maximum) of the PLIF profiles, corresponding to the signal width at which the signal is 50% of its maximum value, were then employed for comparison with the numerical analysis. The variations of the experimental FWHM calculated shot by shot remained under 10% for all the flame cases investigated. The spatial resolution was about  $60 \mu\text{m}/\text{pixel}$ . An example of normalized

PLIF profiles and numerical simulation results for OH and NO profiles using Okafor's mechanism [63] is provided in Fig.3.17 for rich  $\text{NH}_3/\text{air}$  flames. The present OH-PLIF and NO-PLIF are not simultaneous, and thus the centers of the OH and NO profiles, i.e. the stagnation plane, are not strictly identical. This is due to slight changes in the flow balance between the burners when repeating the experiment. The error introduced remains minor and is evaluated by the standard deviation on the FWHM for the repetition of the same case and presented in Appendix 3D.

For the comparison of the FWHM of these OH and NO experimental profiles with the numerical one, careful considerations on quenching and temperature dependencies are essential and are argued in Section 4.3.

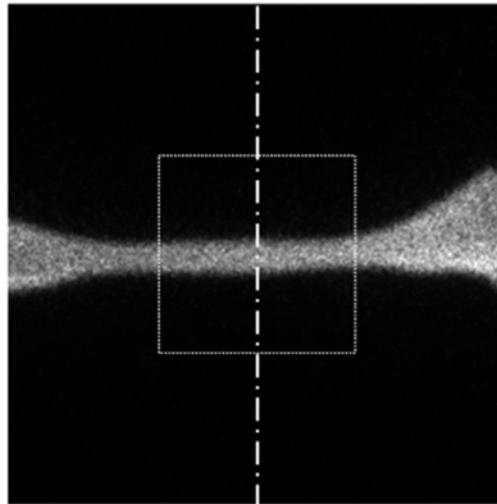


Fig. 3.20. Example of OH-PLIF image:  $E = 0.15$ ,  $\phi = 0.8$ ,  $U = 196.1$  cm/s. The dashed line is the burner axis, the square represents the region between the burners.

## 4.3. Quantitative evaluation based on FWHM of the OH and NO-PLIF measurements

### 4.3.1. Relationship between PLIF and mole fraction profiles

The relationship between the measured fluorescence intensity profiles and the mole fraction profiles is in general not directly proportional as discussed by Eckbreth [153] and Battles and Hanson [154]. Indeed, the fluorescence dependence on temperature and quenching is a major challenge. Depending on the laser intensity, those dependencies vary, and different fluorescence regimes can be observed. Thus, it is first necessary to investigate the fluorescence regime. To do so, the fluorescence intensity

dependence on laser intensity output for both OH and NO was checked by varying the laser energy output for similar flame configuration and taking the mean value of the resulting LIF intensity image by image. The results are presented in Fig. 3.21.

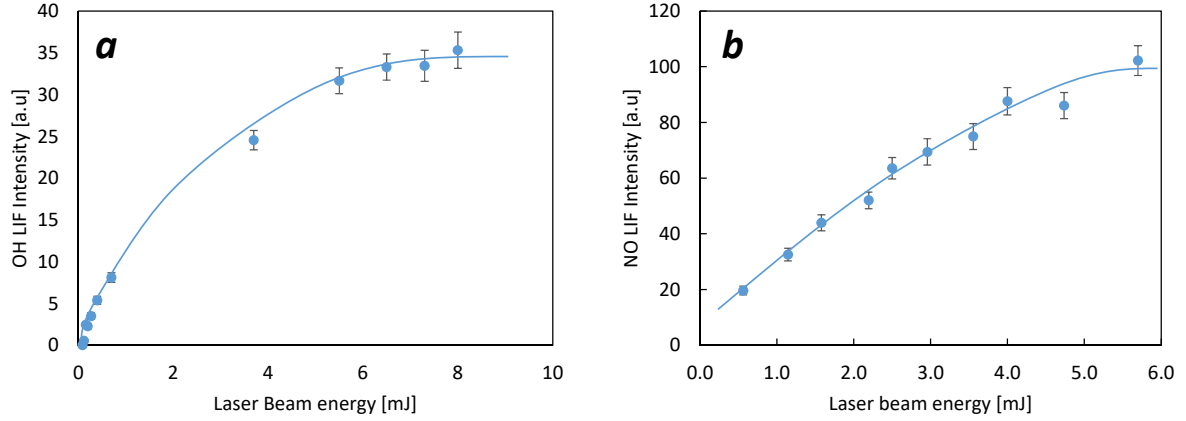


Fig. 3.21. Fluorescence intensity evolution with laser beam energy: (a) OH; (b) NO.

It can be observed that in the case of OH, for laser energy above 8 mJ per shot, like in the present experiment, the fluorescence regime can be considered as saturated. For this reason, the quenching effect on the OH FWHM can be considered as neglectable in the present experiment. In the case of NO-PLIF measurements, the fluorescence regime was linear. Quenching cannot be neglected in this case and its estimation was performed.

In the case of NO, the global quenching rate,  $Q$ , was obtained using the following equations by Eckbreth [153]:

$$Q = \sum_i k_{Q_i} \rho_{n_i} \quad (3.7)$$

$$k_{Q_i} = \bar{v}_i \sigma_{Q_i} \quad (3.8)$$

$$\bar{v}_i = \left[ \frac{8kT}{\pi\mu_i} \right]^{1/2} \quad (3.9)$$

With  $k_{Q_i}$  the rate coefficient,  $\rho_{n_i}$  the number density of the deactivating species. The quenching cross-sections,  $\sigma_{Q_i}$ , are those introduced by Paul et al. [155], based on the harpooned model, which takes into account the variations of the quenching cross-section with the temperature. Deactivation species

considered were limited to CH<sub>4</sub>, C<sub>2</sub>H<sub>6</sub>, C<sub>3</sub>H<sub>8</sub>, C<sub>2</sub>H<sub>4</sub>, C<sub>2</sub>H<sub>2</sub>, CO, CO<sub>2</sub>, CH, H<sub>2</sub>, O<sub>2</sub>, O, H, OH, H<sub>2</sub>O, N<sub>2</sub>, N<sub>2</sub>O, NO, NO<sub>2</sub>, NH<sub>3</sub>, NH.

Temperature and species concentration are obtained from numerical simulations on Chemkin-Pro software using the opposed flow code. The global quenching rate,  $Q$ , is calculated across the flame using the previous Eqs. ( 3.7 ), ( 3.8 ) and ( 3.9 ) for all the PLIF cases considered.

Then, the temperature dependence of the fluorescence signal through the Boltzmann fraction was considered. In the case of OH-PLIF measurements, due to the appropriate selection of specific excitation wavelengths, the fluorescence dependence on temperature, through the Boltzmann fraction, can be considered as neglectable. Indeed, in this study, the OH radicals were present in a region of the flame for which the temperature varied between 1400 K and 2100 K. According to the study of McManus et al. [156], and for this range of temperature, the fluorescence intensity dependence on temperature for the OH  $Q_1(6)$  transition can be neglected.

For NO, the 226.298 nm air (226.365 nm vacuum) wavelength for excitation of the NO (0,0) ( $A^2\Sigma - X^2\Pi$ ) band was selected in this study, corresponding to the P<sub>1</sub>(7.5), P<sub>1</sub>(8.5), P<sub>1</sub>(9.5), P<sub>1</sub>(10.5), Q<sub>12</sub>(22.5), P<sub>2</sub>(22.5) transition lines. The Boltzmann fraction was calculated following expression derived in work by van Gessel et al. [157] and is shown in Fig. 3.22.

$$F_{B,J} = \frac{(2J + 1)}{Q_{rot}Q_{vib}} \exp\left(-\frac{E_J}{kT}\right) \quad (3.10)$$

with

$$Q_{rot} = \frac{kT}{B_v}; \quad Q_{vib} = \frac{1}{1 - \exp\left(-\frac{hc\omega_v}{kT}\right)}; \quad E_J = -\frac{hcB_vJ(J + 1) + K_e}{kT} \quad (3.11)$$

and  $B_v$ ,  $K_e$ ,  $\omega_v$  constants are quoted from van Gessel et al. [157] and Hubert and Herzberg [158].

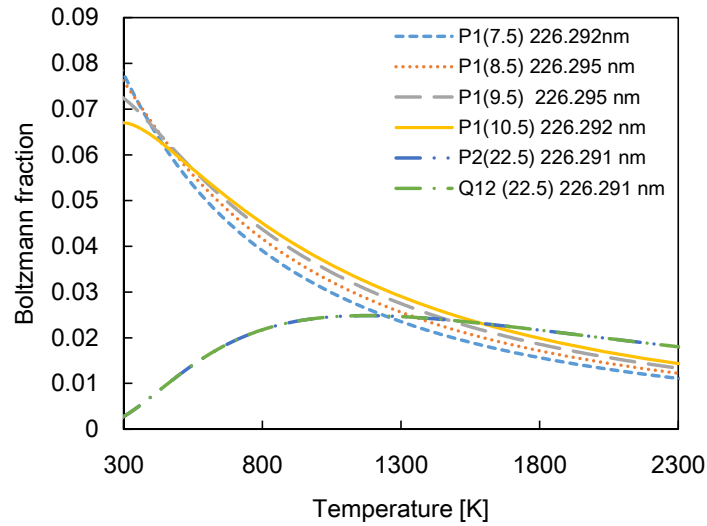


Fig. 3.22. Boltzmann fraction for the P<sub>1</sub>(7.5), P<sub>1</sub>(8.5), P<sub>1</sub>(9.5), P<sub>1</sub>(10.5), Q<sub>12</sub>(22.5), P<sub>2</sub>(22.5) transition lines.

The fluorescence can now be expressed as a function of the radical concentrations. For OH-PLIF, and as shown in Fig. 3.21, the laser intensity was large enough to reach the saturated fluorescence regime. In those conditions, quenching might be neglected and fluorescence intensity  $F$  can be expressed as in Eq. ( 3.12) as derived in Eckbreth's work [153]:

$$F = CN_{OH}F_j \propto X_{OH} \frac{P}{kT} \quad (3.12)$$

where  $X$  is the mole fraction,  $P$  the pressure,  $k$  the Boltzmann constant, and  $T$  the temperature. The coefficient  $C$  depends on experimental parameters and Einstein coefficients for spontaneous and stimulated emission and absorption and is constant along the flame front.  $N_{OH}$  is the OH particle density and  $F_j$  is the Boltzmann fraction, which assumed constant in this case as previously discussed. The relationship between  $F$  and  $X_{OH}P/kT$  is thus proportional along the burner axis across the flame front. The comparison of the FWHM of the experimental OH fluorescence profiles with the ones of the  $X_{OH}P/kT$  quantity is thus possible.  $X_{OH}P/kT$  is obtained from the numerical simulation from the selected kinetic mechanisms.

For NO-PLIF, the laser energy was much lower than for OH, and the study on the variation of the NO fluorescence intensity for different laser energies showed that the fluorescence regime was linear.

In this regime, fluorescence intensity can be related to the mole fraction of NO,  $X_{NO}$ , as introduced in Eq. ( 3.13 ) from Eckbreth [153]:

$$F = CX_{NO} \frac{P}{kT} F_J I \Phi \quad (3.13)$$

where  $C$  is constant along the flame,  $I$  is laser excitation irradiance,  $\Phi$  the fluorescence efficiency. The fluorescence signal was corrected for laser sheet non-uniformity and normalized considering the variation of the laser energy between each measurement to allow comparison between them.

This normalized fluorescence,  $f$ , relationship with the NO mole fraction,  $X_{NO}$ , is then given in Eq. ( 3.14 ) :

$$f \propto X_{NO} \frac{P}{kT} F_J \Phi_J \quad (3.14)$$

As several rotational levels,  $J$ , are excited here, in Eq. ( 3.14 ) can be written as the sum over the different excited states yielding:

$$f \propto X_{NO} \frac{P}{kT} \sum_J F_J \Phi_J \quad (3.15)$$

The right-hand side of Eq. ( 3.15 ) was calculated from numerical simulations using the selected chemical mechanisms and the expression for  $Q$  and  $F_J$  derived earlier.

#### 4.3.2. Mechanisms quantitative evaluation based on the OH and NO FWHM

To compare the experimental and numerical FWHM of OH and NO in counterflow premixed flames, those data were represented against each other for the four selected mechanisms. Moreover, the correlations to the trend obtained for each mechanism, as shown in Fig. 3.23, were examined. The determination coefficients,  $R^2$ , were calculated for lean, stoichiometric, and rich flames as shown in Fig. 3.24. The figures cover values of equivalence ratios,  $\phi$ , of 0.8, 1.0, 1.1 and 1.2, and ammonia mixing ratios,  $E$ , of 0, 0.15, 0.30, 0.60, and 1.0 in the present measurements. The experimental uncertainty in terms of quantitative evaluation of OH and NO FWHMs from PLIF measurements is represented by the error bars in Fig. 3.23. A table of the data is included in Appendix 3D.

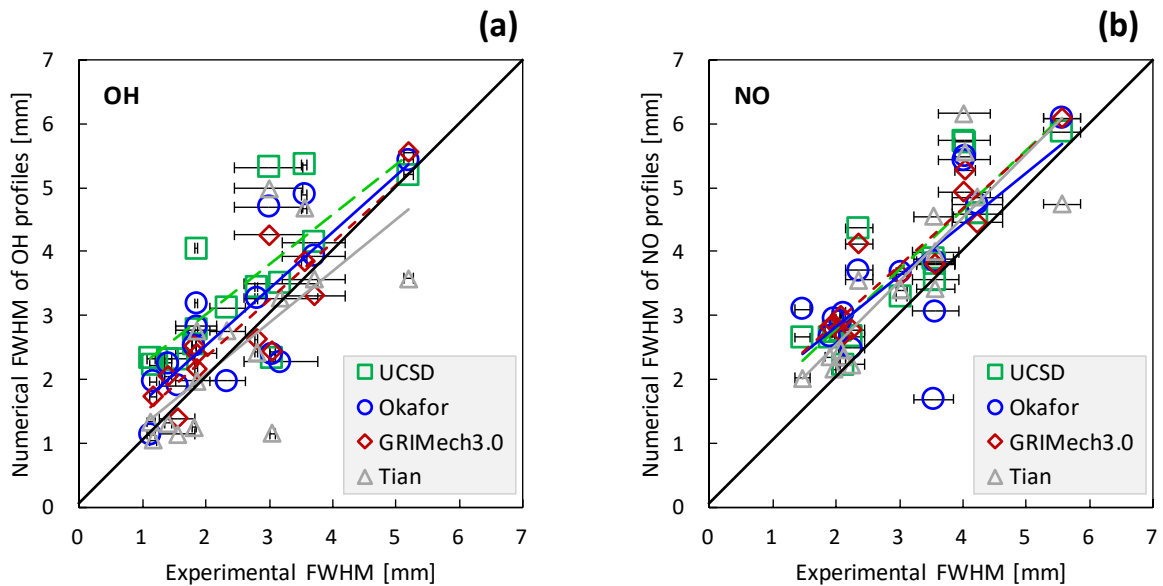


Fig. 3.23. Comparison of the experimental and numerical FWHM: (a) OH; (b) NO.

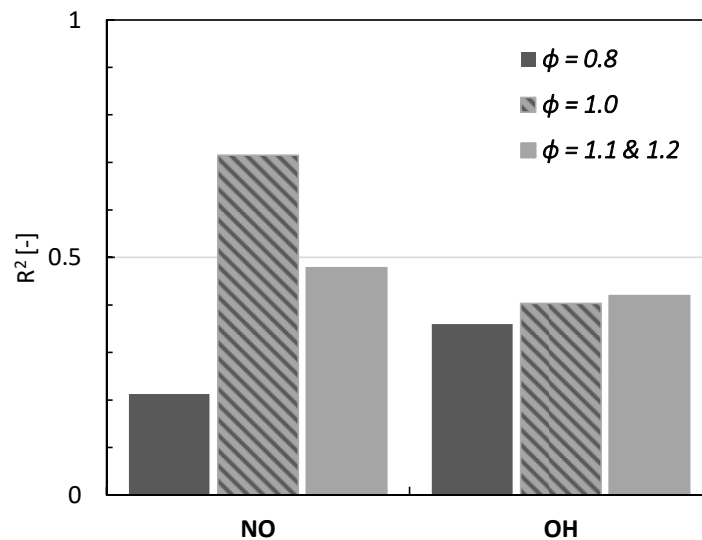


Fig. 3.24. Determination coefficient by equivalence ratio.

Although data are scattered, the characteristics of the selected mechanisms can be observed in Fig. 3.23 as well as some common features depending on the values of the equivalence ratio,  $\phi$ , in Fig. 3.24. Before discussion on each mechanism, the effects of  $\phi$  on  $R^2$  are considered. As seen in Fig. 3.24, for fuel-lean condition ( $\phi = 0.8$ ),  $R^2$  is smaller than for richer cases, corresponding to the previous observations on the extinction stretch rate of lean flames shown in Figs. 3.12a and b. On the other hand, for stoichiometric and rich cases,  $R^2$  increases, indicating smaller scattering, also observed for the extinction stretch rates of the rich flames as presented in Fig. 3.12c. The fact that trends obtained from

the quantitative analysis of the FWHMs of OH and NO and extinction stretch rate are corresponding, indicate the potential of the present method based on PLIF measurements for evaluating detailed chemical mechanisms.

In the following, each chemistry is further examined. Linear regression was obtained using the least square method on the present data set for each mechanism and is represented in Fig. 3.23. The regression lines for OH radical represented on Fig. 3.23a. are all located over the  $y = x$  line, corresponding to the equality between the experimental and numerical FWHM, except for Tian's mechanism. Indeed, Tian's mechanism is the only mechanism which tends to predict the apparition of the OH radical downstream to the experimental results for most of the cases observed. The same trend for OH production and for the extinction stretch rate can be observed here again. Tian's mechanism is then followed in order by GRI-Mech 3.0, Okafor's mechanism, and UCSD mechanism when gradually going above the  $y = x$  line, which all over-predicted, in the same order, the extinction stretch rate in Fig. 3.12. For NO in Fig. 3.23b., all the linear regression trends are located above the  $y = x$  line, showing a general over-prediction of NO production, too. The trends are closer to each other than for OH, with few differences in the NO prediction by the four selected mechanisms. While Tian's mechanism gave particularly scattered data in the case of OH, the scatter is smaller for NO. Okafor's mechanism, on the opposite, presents much more scattered data for NO, suggesting some lacks in the nitrogen subsets included in the chemistry.

## 5. Conclusions

Ammonia/methane fuel counterflow flames were investigated experimentally and numerically in this chapter. Extinction stretch rate and OH and NO profiles in the flames were measured by PLIF in these configurations. A careful comparison of the present experimental results with 1D numerical simulations leads to the evaluation of a selected set of mechanisms toward those criteria. The main results of this study are summarized in the following.

The study developed in Section 1 showed the importance of the consideration of the actual velocity profiles as observed in the experiment. From the PIV measurements and the comparison of the experimental velocity profile to the numerical one, it could be highlighted that:

- For both counterflow premixed twin flame and counterflow non-premixed flames, the velocity profiles at the outlet of the burner are affected by the pressure gradient at the stagnation plane, leading to M-shape velocity profiles. This is particularly pronounced for the non-premixed flames in the equal velocity boundary condition where the momentum unbalance amplified the M-shape on the fuel burner side but was also observed for equal momentum boundary condition, as well as premixed flames.
- Relations between the bulk velocity obtained from mass flow rates and the actual velocity as the burner outlet center axis were however found to be linear. In the same way, the radial velocity gradient at the burner outlet and the actual axial velocity gradient before the flame front, i.e. the stretch rate, could be related to the bulk velocity. Prediction of those quantities is thus possible from the knowledge of the bulk velocity.
- Though perfect reproduction of the experimental velocity profiles could not be done using the 1D opposed-flow model of Chemkin-Pro software, the introduction of the measured boundary velocity values ( $U_{z0}, g_{r0}$ ) reduces the uncertainty on the axial velocity profile compared with the case where only bulk velocity is considered and is thus recommended to limit the error in the comparison of the experimental results and 1D model.

The extinction stretch rate of premixed twin flames was then investigated experimentally and numerically on a broad range of ammonia mixing ratio,  $E$ , and equivalence ratio,  $\phi$ , in Section 2. From this study, the following results were obtained:

- The ammonia introduction led to a large decrease in the extinction stretch rate, as expected from the lower burning intensity. For all the ammonia mixing ratio investigated, the extinction stretch rate peaks between 0.9 and 0.95, shifting slightly on the leaner side to 0.9 as ammonia is gradually introduced. The position of these peaks on the lean side was attributed to the Lewis number under the unity of the lean mixtures.
- The comparison of the experimental results with the numerical simulation results using the four selected mechanisms highlighted the fact that none of the mechanisms was able to reproduce the experimental trend in all the conditions investigated.
- A large discrepancy was observed between mechanisms and experimental results for lean flames. This larger discrepancy might reasonably be attributed to a lack in the methane chemistry for those flames and should be considered as a perspective of this work.

Next, the extinction stretch rate of ammonia O<sub>2</sub>-enriched air non-premixed flames and ammonia/methane-air counterflow non-premixed flames was investigated both experimentally and numerically in Section 3 and led to the following results:

- Ammonia-air non-premixed flames could not be stabilized on the present burner, and O<sub>2</sub>-enriched air was used as the oxidizer to observe the flame in conditions close to the ammonia-air non-premixed configuration. All of the mechanisms investigated, at the exclusion of GRI-Mech 3.0, were able to reproduce the ammonia non-premixed flames extinction stretch rate experimental trend contrary to what has been observed for premixed flames.
- The addition of ammonia in methane non-premixed flame leads to a nearly exponential decrease in the extinction stretch rate. The comparison of numerical simulations and experimental results showed that only Okafor's mechanism was able to reproduce the experimental trend for methane/ammonia premixed flame in the range of fuel mixing  $E$  investigated. GRI-Mech 3.0, Tian's and UCSD mechanism could not follow the experimental trend, due to lack in respectively nitrogen, hydrocarbons, and their interactions in each chemistry.

Finally, OH and NO-PLIF measurements were performed for the quantitative determination of the FWHM of the profiles of OH and NO for counterflow premixed flames in Section 4. They were then compared with those obtained by numerical analysis using four mechanisms. The following results were obtained:

- The lower determination coefficients,  $R^2$ , in the lean region for both OH and NO suggest that further investigation in this region is necessary for mechanisms improvement, similar to what was observed from the extinction stretch rate measurements.
- All the detailed chemistries, at the exception of Tian's mechanism for OH, over-predicted the apparition of both OH and NO. Improvement of the present mechanism is thus necessary for the accurate prediction of NO<sub>x</sub> emissions in those flames.

As a perspective of this work, other species might be considered for PLIF measurement in the premixed twin flames such as NH, CH, or CH<sub>2</sub>O which are key species in ammonia and methane chemistries. A similar study for non-premixed flames might also be considered particularly to validate the present model toward the NO profiles in the flames for example.

Another parameter of interest for mechanism validation, and which was not considered in the present study, is the measurement of temperature profiles. This is particularly challenging in the counterflow configuration as the introduction of a thermocouple highly disturbs the local velocity flow field and generate disturbances of the flame. Laser diagnostics might be considered such as Raman spectrometry for example.

Another perspective of this work, in relation with the Section 1 of this chapter, would be to further investigate the relations obtained from the PIV measurement in the present configuration to a broader range of conditions, with variations of the  $L/D$  ratio, but also through the use of different fuel and oxidizer mixtures, to be able to generalize the present results.

# Appendix

## 3A. 1D modeling of counterflow flames

The model used here is a 1D axisymmetric counterflow flame as in the work by Kee et al. [135] applied in the OPPDIFF code of Chemkin-Pro (ANSYS v19) [124] and re-introduced here. The 3D problem is reduced to the 1D axisymmetric problem by assuming that the stream can be described by the stream function  $\psi(r, z) = r^2 F(z)$ . To ensure mass continuity, this function is set as:

$$\begin{cases} -\frac{\partial \psi}{\partial z} = r\rho v = -r^2 \frac{dF}{dz}, \\ \frac{\partial \psi}{\partial r} = r\rho u = 2rF(z), \end{cases}$$

where  $\rho$  is the density,  $u$  the axial velocity, and  $v$  the radial velocity.

The axial velocity  $u$  is assumed to depend on  $z$  only, and the radial velocity  $v$  is to vary linearly with  $r$ . This linear variation of  $v$  with  $r$  which is observed experimentally, when staying close to the burners' axis as presented in Fig. 3A. 1.

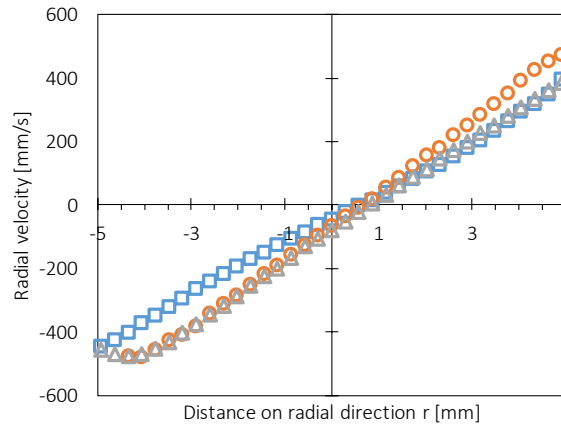


Fig. 3A. 1. Radial velocity as a function of  $r$ , for various  $z$  position, from PIV measurement on an ammonia/air counterflow premixed twin flames.

The temperature,  $T$ , and the mass fraction,  $Y_k$ , of the species  $k$  are also assumed to be dependent on  $z$  only. Pressure,  $p$ , is assumed constant in the flow field, but the gradients are kept in the momentum equations. The flame is assumed to be steady and adiabatic. The buoyancy effect is also neglected.

Neglecting the buoyancy is acceptable in most of the cases studied when considering the high velocities observed experimentally.

The momentum equation can then be reduced to:

Momentum in  $z$ :

$$\frac{\partial p}{\partial z} = -4U \frac{d}{dz} \left( \frac{U}{\rho} \right) - 2\mu \frac{d}{dz} \left( \frac{1}{\rho} \frac{dU}{dz} \right) + \frac{4}{3} \frac{d}{dz} \left[ 2\mu \frac{d}{dz} \left( \frac{U}{\rho} \right) + \nu \frac{dU}{dz} \right]$$

Momentum in  $r$ :

$$\frac{1}{r} \frac{\partial p}{\partial r} = \frac{d}{dz} \left( \frac{2U}{\rho} \frac{dU}{dz} \right) - \frac{3}{\rho} \left( \frac{dU}{dz} \right)^2 - \frac{d}{dz} \left[ \mu \frac{d}{dz} \left( \frac{1}{\rho} \frac{dU}{dz} \right) \right]$$

From the 2nd equation, it can be seen that  $\frac{1}{r} \frac{\partial p}{\partial r}$  can be a function of  $z$  only, and is constant as  $\frac{\partial}{\partial z} \left( \frac{1}{r} \frac{\partial p}{\partial r} \right) = \frac{1}{r} \frac{\partial}{\partial r} \left( \frac{\partial p}{\partial z} \right) = 0$

For numerical implementation in Chemkin-pro software, this constant is called  $H$ , and a function  $G(z)$  is introduced such as:

$$G(z) = \frac{dF}{dz}$$

The problem can then be re-written as a set of the following equations:

$$\begin{aligned} G(z) &= \frac{dF}{dz} \\ H - 2 \frac{d}{dz} \left( \frac{FG}{\rho} \right) + \frac{3G^2}{\rho} + \frac{d}{dz} \left[ \mu \frac{d}{dz} \left( \frac{G}{\rho} \right) \right] &= 0 \\ 2F \frac{dT}{dz} - \frac{1}{c_p} \frac{d}{dz} \left( \lambda \frac{dT}{dz} \right) + \frac{\rho}{c_p} \sum_k c_{pk} Y_k V_k \frac{dT}{dz} + \frac{1}{c_p} \sum_k h_k \dot{\omega}_k &= 0 \\ 2F \frac{dY_k}{dz} + \frac{d}{dz} (\rho Y_k V_k) - \dot{\omega}_k W_k &= 0 \end{aligned}$$

Where  $c_p$  is the specific heat,  $h_k$  species molar enthalpies,  $W_k$  the species molar mass, and the viscosity  $\mu$ , thermal diffusivity  $\lambda$  and diffusion velocities  $V_k$  are calculated from mixture average formulation:

$$\begin{aligned} V_k &= -\frac{1}{X_k} D_{km} \frac{dX_k}{dz} - \frac{D_k^T}{\rho Y_k T} \frac{dT}{dz} \\ D_{km} &= \frac{1 - Y_k}{\sum_{j \neq k} \frac{X_j}{D_{jk}}} \end{aligned}$$

The boundary conditions are usually implemented as:

At  $z = 0$ :

$$F = \frac{\rho_0 u_0}{2}; G = 0; T = T_{0,0}; \rho u Y_k + \rho Y_k V_k = (\rho u Y_k)_0$$

At  $z = L$ :

$$F = \frac{\rho_L u_L}{2}; G = 0; T = T_{L,0}; \rho u Y_k + \rho Y_k V_k = (\rho u Y_k)_L$$

However, for a better representation of the experimental conditions, introduction of the radial gradient at  $(z, r)=(0, 0)$  and  $(L, 0)$ ,  $g_{r0}$  and  $g_{rL}$  respectively, can be introduced in the simulation:

$$g_{r,0 \text{ or } L} = \left( \frac{\partial v}{\partial r} \right)_{r=0, z=0 \text{ or } L} = \left( \frac{v}{r} \right)_{z=0 \text{ or } L} = \left( -\frac{G}{\rho} \right)_{z=0 \text{ or } L}$$

The boundary conditions are then modified such as:

At  $z = 0$ :

$$F = \frac{\rho_0 u_0}{2}; G = -\rho_0 g_{r,0}; T = T_0; \rho u Y_k + \rho Y_k V_k = (\rho u Y_k)_0$$

At  $z = L$ :

$$F = \frac{\rho_L u_L}{2}; G = -\rho_L g_{r,L}; T = T_L; \rho u Y_k + \rho Y_k V_k = (\rho u Y_k)_L$$

## 3B. Details of PIV measurements

### Seeding system

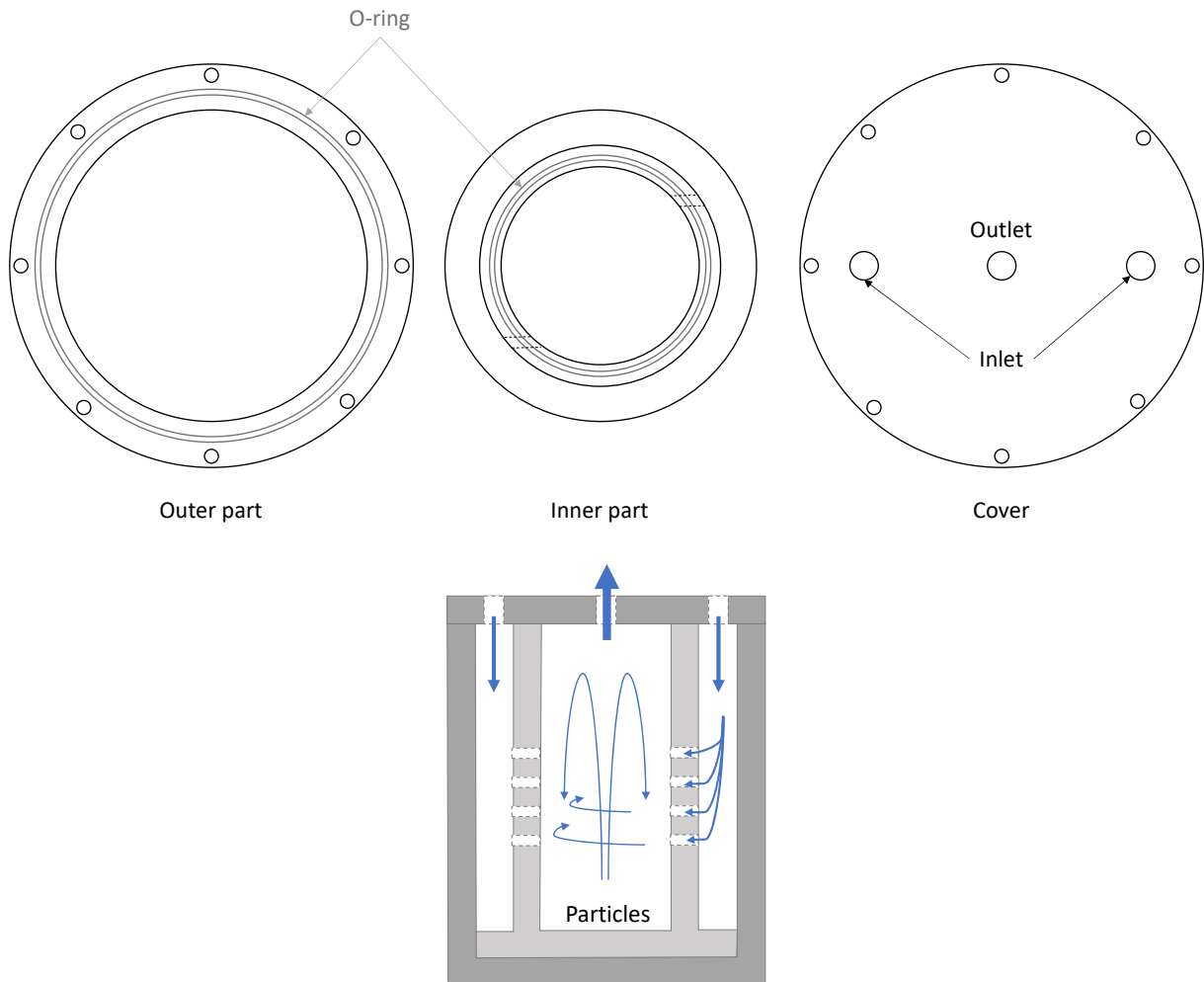


Fig. 3B.1. Schematics of the seeding system.

### Velocity profiles polynomial fitting

To get the actual stretch rate observed by the premix twin flames, i.e. the maximum axial velocity gradient before the flame front [65], the PIV measured velocity profiles were post-processed. The focus here is done on the axial velocity profile  $U_z$  as a function of  $z$ , the axial position. The region of interest, in red circles in Fig. 3B.2, is limited to the region before flame front where the velocity profile is decreasing monotonically.

The PIV measurements produce discrete curves, and to get the gradient with the best accuracy possible, the axial velocity was fitted by polynomial function in the region of interest, from which the

derivative was taken.  $g_z$  corresponds to the maximum obtained by the derivative in the region of interest. The polynomial fitting has been done using the least squared method, and the order of polynomial researched was order 5. The region was defined by calculating the derivate of the velocity function and looking at its sign. The region for fitting was thus chosen to be between the burner to the local minimum (maximum) which corresponds to a plus/minus sign change.

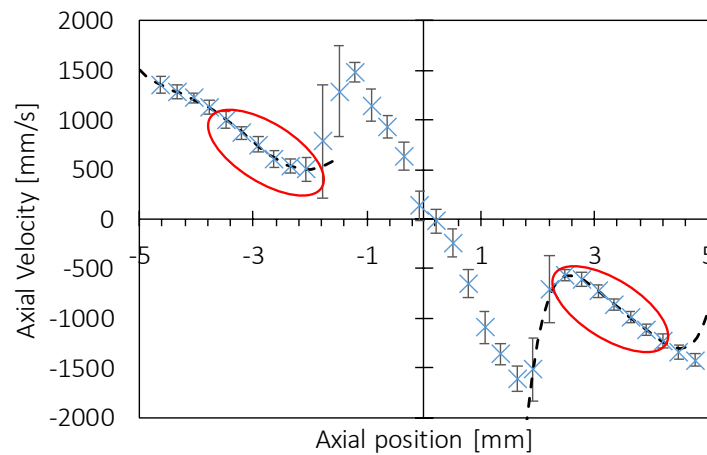


Fig. 3B.2. Axial velocity profile of a methane counterflow premixed twin flames at  $\phi = 1.0$  and  $g_z = 490 \text{ s}^{-1}$ : PIV experiment in blue crosses; fitting curves in black dashed line.

## Comparison of numerical simulations with experiments in methane case

To ensure that the methodology developed in Section 1.5.3 for premixed flame allows proper modeling of the present experiment, the measured and simulated velocity profiles were compared for methane flame case, for which the chemistry is relatively well known. In methane case, the chemistry has been widely studied, and the uncertainty in the modeling associated with it is assumed to be limited. This comparison thus ensures that the experimental axial velocity profile can be reproduced using the 1D axisymmetric numerical simulation in Chemkin-pro numerical environment and the actual experimental boundary conditions.

To limit as much as possible the modeling uncertainty related to the detailed chemistry, the mechanism chosen here is AramcoMech 2.0 mechanism [80,90–95], which includes 493 species and 2716 reactions. This mechanism has been well validated for a wide set of hydrocarbons. To ensure the phenomenon observed is really related to the modeling of the velocity profile and not the mechanism, it

has been repeated with the UCSD mechanism (update of 2016, which is equally well-validated) [96], and the same results were observed.

The simulations had been performed using the relation  $U_{z0} = f(U)$  (simulation case B) and both  $U_{z0} = f(U)$  and  $g_{r0} = f(U)$  (simulation case C), obtained from the PIV measurements described in Section 1.5.3, to impose the correct boundary conditions fitting to experiment. The numerically simulated velocity profiles in cases B and C are then compared to the one experimentally observed as represented in Fig. 3B.3 reproduced from Section 1.5.3.

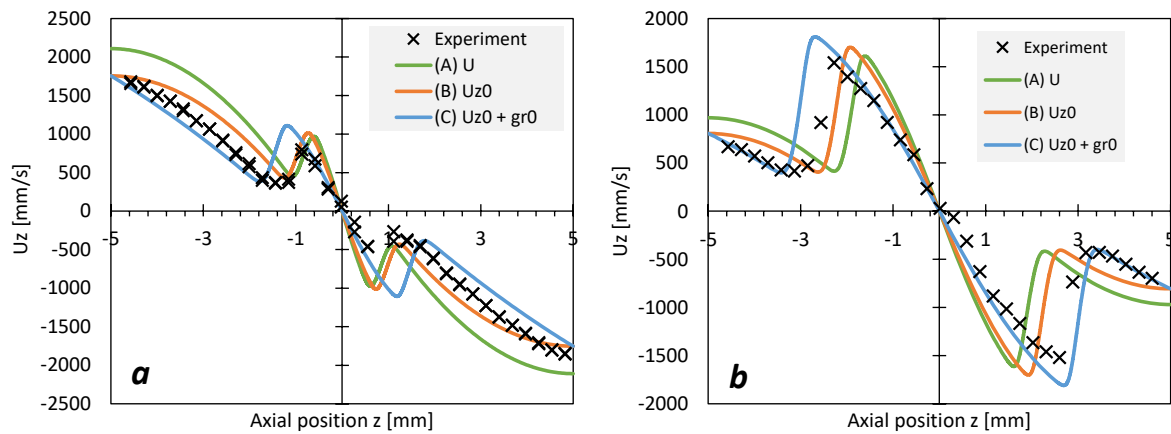


Fig. 3B.3. Comparison of experimental and numerical results for a methane/air counterflow premixed twin flames: (a)  $\phi = 0.8$  and  $U = 210.4$  cm/s (b)  $\phi = 1.2$  and  $U = 97.1$  cm/s.

Counterflow premixed twin flames present symmetry at the stagnation plane so that one can focus on the velocity profile between one burner and the stagnation plane, as represented in Fig. 3B.4. From the lower burner outlet, in  $z = -5$  mm, the velocity decreases, up to a local minimum, then increases due to the temperature gradient at the flame front, up to a maximum, and finally decreases to zero at the stagnation plane at  $z = 0$  mm. The profile can thus be divided into 3 regions: region I between the burner outlet and the local minimum, region II between the local minimum and local maximum, region III between the local maximum and the stagnation plane.

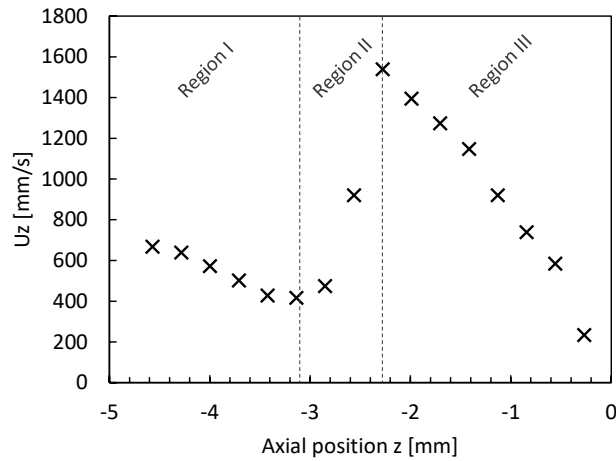


Fig. 3B.4. Experimental velocity profile between the burner and the stagnation plane and region identified for modeling validation.

As can be observed in Fig. 3B.3, there is no perfect fitting of simulation and experiment curves on all 3 regions. The analysis should then be pursued further on the 3 regions and on the way the simulation can reproduce the velocity local peaks ( $z_{min}$ ,  $V_{min}$ ) and ( $z_{max}$ ,  $V_{max}$ ). In region I, the experimentally measured profile is observed in between simulation B and C, closer to case C. This can be observed in Figs. 3B.3 a and b but is equally true for all the cases studied. From this point of view, and in this region, considering the radial gradient at the boundary (case C) is preferable.

The results for the flame region, region II, are more complicated to assess. Indeed, values for the minimum velocity (entrance of flame region) are well reproduced in both cases B and C, while values for the maximum velocity (exit of the flame region) are overestimated in both cases, case B, being slightly closer. When looking at the axial position of those peaks, position for the maximum velocity is well reproduced in the case B while overestimated in the case C. Position of minimum velocity shows more complex feature and is located, as can be seen in Fig. 3B.5, between the position given in case B and case C. It is important to recall at this stage that the particles introduced in the flow might also affect the measurement through heat losses, particularly in the flame region, and might explain to some extent the present observation in this region.

In region III, where velocity decreases up to the stagnation plane, a better agreement is obtained with the simulations corresponding to case C inputs, as it can be seen in the 2 cases presented in Fig. 3B.3.

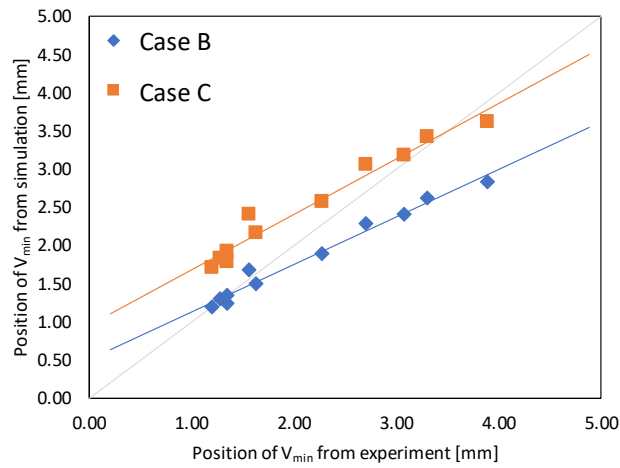


Fig. 3B.5. Simulated  $z_{min}$  as a function of the experimental one.

Overall, though not perfectly reproducing the experimental velocity profile, the introduction of the actual velocity and the radial gradient at the burner outlet in the 1D counterflow model allow for better adequation of the simulated profiles with the experimental result.

## 3C. Reaction path for lean methane counterflow premixed twin flames

The reaction path for the lean methane premixed flame has been further investigated as developed in Section 2. The detailed results for the main sub-paths of the reaction path are presented in the following tables. First, the evolution of the reaction path when getting leaner ( $\phi = 0.9$  and  $\phi = 0.7$ ) is investigated with Okafor's mechanism [63], and then with Tian's mechanism [121]. The reactions which are crossed out were present in Okafor's mechanism but not in Tian's.

Finally, the results for the two mechanisms are compared for the two stoichiometries.

### 3C.1. For Okafor's mechanism

Table 3C.1. Reaction path coefficients for lean methane premixed flames with Okafor's mechanism.

Reaction	Sub-path	$\phi = 0.9$	$\phi = 0.7$	Trend	$\phi = 0.9$	$\phi = 0.7$
$\text{OH} + \text{CH}_4 = \text{CH}_3 + \text{H}_2\text{O}$					<b>52%</b>	<b>61%</b>
$\text{H} + \text{CH}_4 = \text{CH}_3 + \text{H}_2$	$\text{CH}_4 \rightarrow \text{CH}_3$	1	1		34%	21%
$\text{O} + \text{CH}_4 = \text{OH} + \text{CH}_3$					15%	18%
$\text{O} + \text{CH}_3 = \text{H} + \text{CH}_2\text{O}$	$\text{CH}_3 \rightarrow \text{CH}_2\text{O}$	0.2717	0.2885	bit up	97%	97%
$\text{OH} + \text{CH}_3 \Rightarrow \text{H}_2 + \text{CH}_2\text{O}$					3%	3%
$\text{H} + \text{CH}_2\text{O} = \text{HCO} + \text{H}_2$	$\text{CH}_2\text{O} \rightarrow \text{HCO}$	0.3975	0.4097	bit up	56%	41%
$\text{OH} + \text{CH}_2\text{O} = \text{HCO} + \text{H}_2\text{O}$					<b>44%</b>	<b>59%</b>
$\text{HCO} + \text{O}_2 = \text{HO}_2 + \text{CO}$					<b>42%</b>	<b>60%</b>
$\text{HCO} + \text{H}_2\text{O} = \text{H} + \text{CO} + \text{H}_2\text{O}$	$\text{HCO} \rightarrow \text{CO}$	0.4326	0.4596	up	30%	19%
$\text{HCO} + \text{M} = \text{H} + \text{CO} + \text{M}$					28%	21%
$\text{OH} + \text{CO} = \text{H} + \text{CO}_2$	$\text{CO} \rightarrow \text{CO}_2$	0.4251	0.4988	up	100%	100%
$\text{OH} + \text{CH}_3 = \text{CH}_2^* + \text{H}_2\text{O}$	$\text{CH}_3 \rightarrow \text{CH}_2^*$	0.2220	0.2266	constant	100%	100%
$\text{CH}_2^* + \text{N}_2 = \text{CH}_2 + \text{N}_2$	$\text{CH}_2^* \rightarrow \text{CH}_2$	0.1669	0.1542	down	70%	73%
$\text{CH}_2^* + \text{H}_2\text{O} = \text{CH}_2 + \text{H}_2\text{O}$					30%	27%
$\text{CH} + \text{H}_2 = \text{H} + \text{CH}_2$	$\text{CH}_2 \rightarrow \text{CH}$	0.0621	0.0289	down	100%	100%
$\text{CH} + \text{O}_2 = \text{O} + \text{HCO}$	$\text{CH} \rightarrow \text{HCO}$	0.0432	0.0250	down	100%	100%
$2\text{CH}_3 (+\text{M}) = \text{C}_2\text{H}_6 (+\text{M})$	$\text{CH}_3 \rightarrow \text{C}_2\text{H}_6$	0.0571	0.0440	down	100%	100%
$\text{O} + \text{CH}_3 \Rightarrow \text{H} + \text{H}_2 + \text{CO}$	$\text{CH}_3 \rightarrow \text{CO}$	0.1756	0.1873	up	100%	100%

## 3C.2. For Tian's mechanism

Table 3C.2. Reaction path coefficients for lean methane premixed flames with Tian's mechanism.

Reaction	Sub-path	$\phi = 0.9$	$\phi = 0.7$	Trend	$\phi = 0.9$	$\phi = 0.7$
$\text{OH} + \text{CH}_4 = \text{CH}_3 + \text{H}_2\text{O}$					<b>49%</b>	<b>60%</b>
$\text{H} + \text{CH}_4 = \text{CH}_3 + \text{H}_2$	$\text{CH}_4 \rightarrow \text{CH}_3$	1	1		33%	17%
$\text{O} + \text{CH}_4 = \text{OH} + \text{CH}_3$					19%	23%
$\text{O} + \text{CH}_3 = \text{H} + \text{CH}_2\text{O}$	$\text{CH}_3 \rightarrow \text{CH}_2\text{O}$	0.2360	0.2871	up	100%	100%
<del><math>\text{OH} + \text{CH}_3 \Rightarrow \text{H}_2 + \text{CH}_2\text{O}</math></del>					0%	0%
$\text{H} + \text{CH}_2\text{O} = \text{HCO} + \text{H}_2$	$\text{CH}_2\text{O} \rightarrow \text{HCO}$	0.5874	0.6010	up	29%	18%
$\text{OH} + \text{CH}_2\text{O} = \text{HCO} + \text{H}_2\text{O}$					71%	82%
$\text{HCO} + \text{O}_2 = \text{HO}_2 + \text{CO}$					100%	100%
<del><math>\text{HCO} + \text{H}_2\text{O} = \text{H} + \text{CO} + \text{H}_2\text{O}</math></del>	<b><math>\text{HCO} \rightarrow \text{CO}</math></b>	<b>0.2232</b>	<b>0.3696</b>	<b>up</b>	0%	0%
<del><math>\text{HCO} + \text{M} = \text{H} + \text{CO} + \text{M}</math></del>					0%	0%
$\text{OH} + \text{CO} = \text{H} + \text{CO}_2$	$\text{CO} \rightarrow \text{CO}_2$	<b>0.5333</b>	<b>0.5971</b>	<b>up</b>	19%	23%
$\text{OH} + \text{CO} = \text{H} + \text{CO}_2$ (duplicate)					81%	77%
$\text{OH} + \text{CH}_3 = \text{CH}_2^* + \text{H}_2\text{O}$	$\text{CH}_3 \rightarrow \text{CH}_2^*$	0.0409	0.0471	constant	100%	100%
$\text{CH}_2^* + \text{N}_2 = \text{CH}_2 + \text{N}_2$	$\text{CH}_2^* \rightarrow \text{CH}_2$	0.0465	0.0377	down	67%	71%
$\text{CH}_2^* + \text{H}_2\text{O} = \text{CH}_2 + \text{H}_2\text{O}$					33%	29%
$\text{CH} + \text{H}_2 = \text{H} + \text{CH}_2$	$\text{CH}_2 \rightarrow \text{CH}$	0.0240	0.0094	down	100%	100%
$\text{CH} + \text{O}_2 = \text{O} + \text{HCO}$	$\text{CH} \rightarrow \text{HCO}$	0.0108	0.0059	down	100%	100%
$2\text{CH}_3 (+\text{M}) = \text{C}_2\text{H}_6 (+\text{M})$	$\text{CH}_3 \rightarrow \text{C}_2\text{H}_6$	0.0513	0.0510	constant	100%	100%
$\text{O} + \text{CH}_3 \Rightarrow \text{H} + \text{H}_2 + \text{CO}$	$\text{CH}_3 \rightarrow \text{CO}$	0.0513	0.0624	up	100%	100%

## 3C.3. Comparison between mechanisms

Table 3C.3. Reaction path coefficients comparison for Tian's and Okafor's mechanisms.

Reaction	Sub-path	$\phi = 0.9$			$\phi = 0.7$		
		Okafor	Tian	Trend	Okafor	Tian	Trend
$\text{OH} + \text{CH}_4 = \text{CH}_3 + \text{H}_2\text{O}$							
$\text{H} + \text{CH}_4 = \text{CH}_3 + \text{H}_2$	$\text{CH}_4 \rightarrow \text{CH}_3$	1	1		1	1	
$\text{O} + \text{CH}_4 = \text{OH} + \text{CH}_3$							
<b><math>\text{O} + \text{CH}_3 = \text{H} + \text{CH}_2\text{O}</math></b>	<b><math>\text{CH}_3 \rightarrow \text{CH}_2\text{O}</math></b>	<b>0.272</b>	<b>0.236</b>	<b>smaller</b>	<b>0.289</b>	<b>0.287</b>	<b>same</b>
<del><math>\text{OH} + \text{CH}_3 \Rightarrow \text{H}_2 + \text{CH}_2\text{O}</math></del>							
$\text{H} + \text{CH}_2\text{O} = \text{HCO} + \text{H}_2$	$\text{CH}_2\text{O} \rightarrow \text{HCO}$	0.3975	0.5874	larger	0.410	0.601	larger
$\text{OH} + \text{CH}_2\text{O} = \text{HCO} + \text{H}_2\text{O}$							
$\text{HCO} + \text{O}_2 = \text{HO}_2 + \text{CO}$							
$\text{HCO} + \text{H}_2\text{O} = \text{H} + \text{CO} + \text{H}_2\text{O}$	$\text{HCO} \rightarrow \text{CO}$	0.4326	0.2232	smaller	0.460	0.370	smaller
<del><math>\text{HCO} + \text{M} = \text{H} + \text{CO} + \text{M}</math></del>							
<b><math>\text{OH} + \text{CO} = \text{H} + \text{CO}_2</math></b>	<b><math>\text{CO} \rightarrow \text{CO}_2</math></b>	<b>0.4251</b>	<b>0.5333</b>	<b>larger</b>	<b>0.500</b>	<b>0.137</b>	<b>smaller</b>
$\text{OH} + \text{CH}_3 = \text{CH}_2^* + \text{H}_2\text{O}$	$\text{CH}_3 \rightarrow \text{CH}_2^*$	0.2220	0.0409	smaller	0.227	0.047	smaller
$\text{CH}_2^* + \text{N}_2 = \text{CH}_2 + \text{N}_2$	$\text{CH}_2^* \rightarrow \text{CH}_2$	0.1669	0.0465	smaller	0.154	0.038	smaller
$\text{CH}_2^* + \text{H}_2\text{O} = \text{CH}_2 + \text{H}_2\text{O}$							
$\text{CH} + \text{H}_2 = \text{H} + \text{CH}_2$	$\text{CH}_2 \rightarrow \text{CH}$	0.0621	0.0240	smaller	0.029	0.009	smaller
$\text{CH} + \text{O}_2 = \text{O} + \text{HCO}$	$\text{CH} \rightarrow \text{HCO}$	0.0432	0.0108	smaller	0.025	0.006	smaller
$2\text{CH}_3 (+\text{M}) = \text{C}_2\text{H}_6 (+\text{M})$	$\text{CH}_3 \rightarrow \text{C}_2\text{H}_6$	0.0571	0.0513	constant	0.044	0.051	larger
$\text{O} + \text{CH}_3 \Rightarrow \text{H} + \text{H}_2 + \text{CO}$	$\text{CH}_3 \rightarrow \text{CO}$	0.1756	0.0513	smaller	0.187	0.062	smaller

### 3D. Experimental OH and NO FWHM results

Table 3D.1. Experimental OH and NO FWHM results.

E	$\phi$	U [cm/s]	U <sub>z0</sub> [cm/s]	g <sub>r0</sub> [1/s]	FWHM OH PLIF [cm]			FWHM NO PLIF [cm]		
					Mean	$\sigma$ Repeat. 3 cases	$\sigma$ shot by shot	Mean	$\sigma$ Repeat. 3 cases	$\sigma$ shot by shot
0	0.8	210.4	175.0	182.2	0.181	0.003	0.004	0.211	0.004	**
	1	298.9	248.6	234	0.305	0.004	0.004	0.196	0.003	**
	1.2	97.1	80.8	115.9	0.519	0.008	0.005	0.556	0.030	**
0.15	0.8	166.7	141.9	152.2	0.117	0.005	0.004	0.191	0.007	0.005
	1	196.1	166.9	175.6	0.140	0.005	0.004	0.207	0.002	0.006
	1.2	103.6	88.2	102	0.185	0.032	0.005	0.303	0.008	0.012
0.3	0.8	103.1	90.0	82.15	0.155	0.028	0.003	0.225	0.021	0.010
	1	81.5	71.1	65.32	0.279	0.003	0.004	0.356	0.030	0.012
	1.2	42.4	37.0	34.85	0.370	0.050	0.009	0.423	0.040	0.022
0.6	0.8	36.5	31.5	47.21	0.185	0.002	0.005	0.236	0.021	0.008
	1	30.0	25.9	42.1	0.355	0.004	0.007	0.403	0.016	0.013
	1.2	25.7	22.2	38.7	0.299	0.055	0.016	0.402	0.041	0.022
1	0.8	23.7	25.6	30.58	0.113	0.006	0.006	0.147	0.012	0.009
	1	24.8	26.7	31.36	0.234	0.028	0.016	0.356	0.036	0.017
	1.1	23.1	24.9	30.11	0.318	0.058	0.022	0.354	0.031	0.024

\*\* Signal/noise too small if not time-averaged which leads to error in the detection of the 50% threshold on an image by image basis. Resolution: 0.006 cm

The variations of the FWHM obtained were evaluated using the standard deviation,  $\sigma$ , on three repetition of the same flame cases (3 series of images), and the standard deviation within one serie of image, due to fluctuation of the laser energy shot by shot. The largest standard deviation are reported on the shape of error bars in Fig. 3.23.

# Chapter 4

## Fundamental characteristics of ammonia/methane-air non-premixed jet flames

### 1. Introduction

#### 1.1. Stabilization issues

Flame stabilization is a fundamental concern when developing combustion systems. Indeed, knowledge of flame stabilization regimes is needed to ensure the combustion system reaches a steady condition and to limit flame instabilities triggering safety, efficiency and emissions issues. In some cases, the research for a particular stabilization regime might also be motivated by other practical limitations, such as material deformation or degradation in a high-temperature environment, leading to some specific concern on the location of the flame stabilization. Good knowledge of the flame stabilization physics is thus essential to ensure reliable and performant industrial applications.

As explained in Chapter 1, ammonia flame stabilization is problematic due to its extraordinarily low burning intensity. Demonstrations of turbine-like combustors [60] are encouraging, but the use of ammonia in industrial burners remains challenging mostly due to NO<sub>x</sub> emission, as detailed in Chapters 2 and 3, but also to stabilization issues. Several strategies can be applied to tackle the ammonia flame stabilization issues. Among them are pre-heating or fuel-mixing. The use of a swirl burner can also be considered as investigated by Hayakawa et. al. [109]. In such configuration, the recirculation structures generated by the swirling flow driving the mixing of some of the burnt gases with the fresh ones were considered for explaining the flame stabilization [110]. The flame stabilization was consequently greatly influenced by the modification of injection angles or liner geometry as they change the swirling flow structure [43,61,109].

Stabilization is a multiparameter mechanism and thus complex to apprehend. Coupled aerodynamical, thermal and chemical parameters impact flame stabilization and their contribution is difficult to assess,

especially in a complex environment like in the works aforementioned. Moreover, fuel mixing affects number of parameters in combustion. The different properties of the fuels mixed lead to chemical changes as developed in Chapter 2 and affect fundamental flame properties as introduced in Chapter 3. Interactions of the flame with the burner and its environment will thus also face changes, and stabilization process is expected to change and was thus selected as the object of this chapter. More specifically, and because ammonia mixtures stabilization mechanisms remain merely examined in the literature from a fundamental perspective, a more comprehensive fundamental study is required.

## 1.2. Introduction on non-premixed jet flames

This study aiming at the investigation of the fundamental aspects of ammonia/methane flames stabilization, the non-premixed jet flame configuration was selected. Indeed, the use of a non-premixed jet flame is convenient as it allows for the observation of the flame in a configuration that is close to some applications but also simple and readily usable for understanding the physics of the stabilization phenomena. Jet flame has been extensively studied in the and the main mechanisms of the jet flame stabilization are globally understood as successively reviewed by Buckmaster, Chung, Lyons, Lawn and Linan [159–163].

The classical jet flame configuration consists of a fuel jet in a free air stream or air coflow. Once ignited, a non-premixed jet flame might stabilize in the interface between the fuel and oxidizer stream. A reaction region at this interface, where chemical reaction and composition changes occur can be defined. The diffusion of fresh reactants from the oxidizer and the fuel side to the reaction region and hot burnt product from this region to the fuel and oxidizer is then observed. The jet flame structure, as observed experimentally in laminar jet flame in the early works of Smyth [164] and Hottel and Hawthorne [165] can be represented as in Fig. 4.1. The fuel and oxygen concentrations are gradually decreased when getting closer to the flame front at which the products concentration peaks. This flame front also corresponds to the highest temperatures when scanning the flame radially for a fixed height above the burner. The mixture fraction,  $Z$ , is a useful quantity used for the description structure of the non-premixed flame and corresponds to the fuel ratio in the mixture, as expressed in equation ( 4.1 ).

$$Z = \frac{sY_F - Y_O + Y_O^0}{sY_F^0 + Y_O^0} \quad (4.1)$$

with  $s$  the stoichiometric fraction,  $Y_i$  the mass fraction of specie  $i$  and the subscripts  $O$  and  $F$  denote the oxidant and fuel, and the superscript 0 the boundary condition.  $s$  might be expressed as follows:

$$s = \frac{\vartheta_O M_O}{\vartheta_F M_F} \quad (4.2)$$

With  $\vartheta$  the stoichiometric coefficient of species  $i$  and  $M_i$  their molar mass.

Then, assuming an irreversible infinitely fast reaction, the stoichiometric mixture fraction,  $Z_{st}$ , can be calculated as the value of  $Z$  when both fuel and oxidant are fully consumed and  $Y_O = Y_F = 0$ .

$$Z_{st} = \frac{1}{1 + \frac{sY_F^0}{Y_O^0}} \quad (4.3)$$

Theoretical work by Burke and Schumann [166], under a certain number of restrictive assumptions, including the infinitely fast reaction assumption and the resulting flame reacting surface, constant radial only diffusion, mixing from diffusion only and constant air and fuel velocities, allowing for the prediction of the flame shape and height, in reasonable agreement with experimental results.

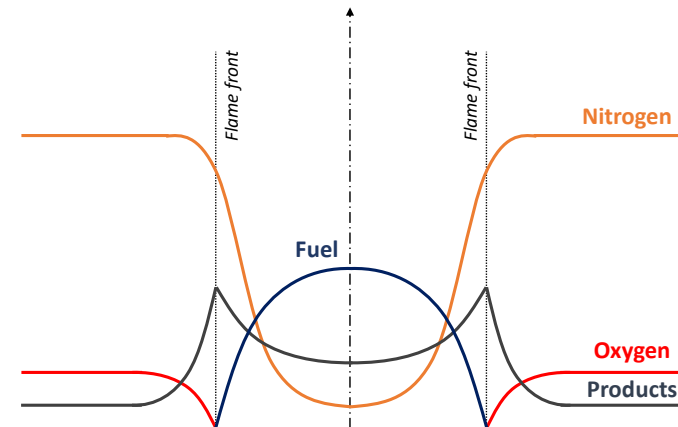


Fig. 4.1. Representation of a non-premixed fuel-air jet flame structure at a fixed height above the burner.

The aerodynamics of the jet is of primary importance when studying jet flames. As the velocity of the jet is increased, the jet will transit from laminar to turbulent and the flame dynamics will change as

reported by Hawthorne et al. [167] and represented in Fig. 4.2: Flame height is first linearly increasing as the jet velocity is increased. Then, as the jet velocity is further increased, instability will appear in the jet flame and turbulence will develop from that breakpoint position, which is gradually decreasing toward the burner lip. The jet will finally become fully turbulent as the jet velocity keeps increasing. When the fully turbulent jet is developed, the flame height remains constant.

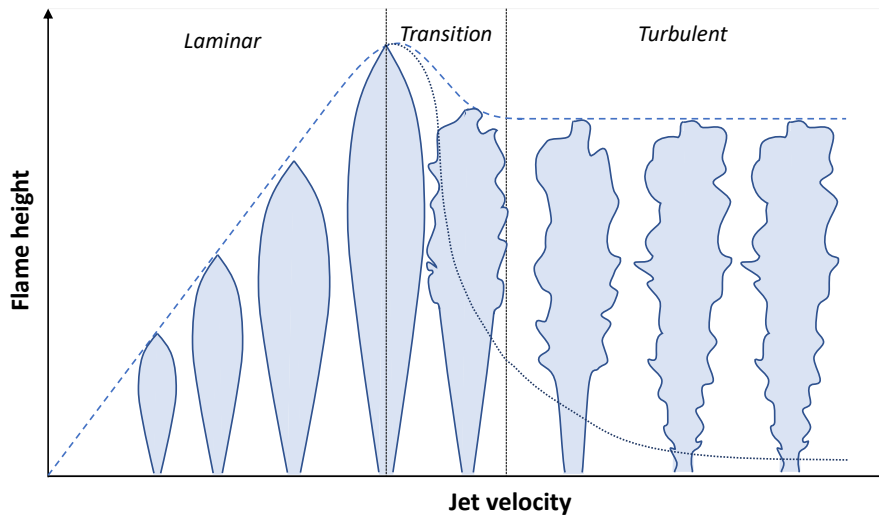


Fig. 4.2. Flame shape evolution with the jet velocity.

Observation of the different stabilization regime of the jet flames has been the subject of several studies [160–162,168–170]. The aerodynamic of the jet was revealed to have a large impact on the flame stabilization and mappings of the different stabilization regimes were consequently proposed.

In the present configuration [117–119,171], the following stabilization regimes can be observed: when increasing the jet velocity, the flame, initially attached to the burner and stabilizing a few millimeters away from the burner lip, lifts for a critical velocity,  $U_{LO}$ , and stabilizes further downstream at a distance corresponding to few times the burner outlet diameter. The lifted flame will then eventually blow out if increasing the jet velocity or will re-attach if the jet velocity is reduced. The re-attachment velocity,  $U_A$ , at which the flame gets re-attached is smaller than the lifting velocity,  $U_{LO}$ , showing a characteristic hysteresis behavior first mentioned by Scholefield and Garside [172]. Both attached and lifted flames are illustrated in Fig. 4.3 in the case of ammonia/methane flame.

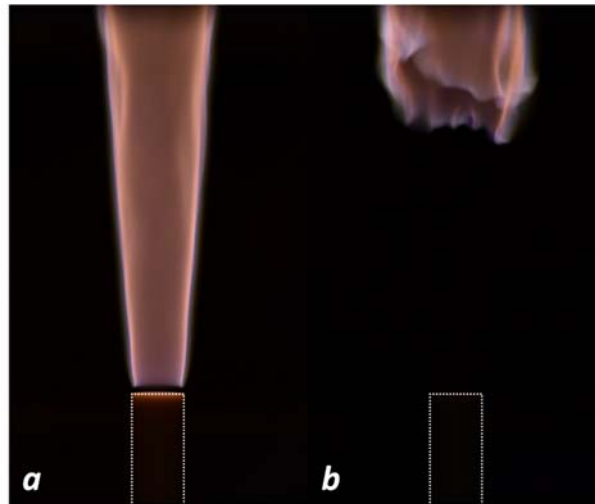


Fig. 4.3. Ammonia/methane non-premixed jet flame in the present configuration: (a) attached flame before liftoff, (b) lifted flame after liftoff.

Characterizing the transition from one stabilization regime to another is essential. The knowledge of the liftoff and blowout limit is particularly critical. Therefore, to understand the mechanisms which will lead to the flame blowoff, the evolution of the lifted flame has been the subject of special attention. Several attempts for their prediction led to different models as reviewed in a work by Lyons [161]. For laminar lifted flames, the triple-flame theoretical concept was developed and well-validated from experimental measurements. However, for turbulent lifted flames, several theories can be distinguished:

- **The premixed model** describes the lifted flame base as premixed, and the flame is expected to stabilize where its local burning velocity balances the one of the jet as developed in works by Eickhoff et al. and Kalghatgi [173,174].
- **The leading edge model** described by Buckmaster [175] and supported by several experimental observations [161,162,176,177] support the concept of that partial mixing will occur in some region in a non-premixed environment such as the edges of the non-premixed flame sheet. This leading-edge consists of a premixed flame supporting a diffusion flame behind and presents a tri-brachial structure.
- **The scalar dissipation model** is developed on the concept that the flame stabilization depends on the local extinction of diffusion flamelets, and the flame thus stabilizes in the region where the scalar dissipation rate becomes lower than a characteristic value.

- **The large-eddy model** [178] emphasizes the importance of large eddy structure in the flame stabilization. In this model, the flame leading edge is connected to the large eddy structure and somehow jumps from one structure to the next ensuring the flame stabilization.

Each of these models does not, alone, explain all the flame characteristics observed through the experiments on the lifted flames. They however all contribute to the understanding of the lifted flame stabilization, as they all highlight specific aspects of these flames.

Though extensively studied and the main mechanisms of the jet flame stabilization being globally understood [159–163], the study on the stabilization of non-premixed jet flame remains of interest. The effects of dilution and preheating are of particular interest because of the potential industrial applications with burnt gas recirculation aiming at emissions reduction [118,160,171,179–182]. More recently, the search for alternative fuels leads to the study of fuel gas mixtures, especially with the introduction of carbon-free fuel to hydrocarbon jets [183,184]. Those studies revealed differences with classical dilution study as the gas introduced is chemically active. This study falls within this context, with the ammonia addition to a methane jet being the core of the present investigation.

### 1.3. Objectives of this chapter

The purpose of this study is first to clarify the effect of ammonia addition on the stabilization of a methane jet flame in an air coflow. Jet stabilization regimes, and more specifically liftoff and re-attachment, were first investigated with ammonia gradual introduction with a low air coflow velocity. To do so, the velocities  $U_{LO}$  and  $U_A$  were determined for various fuel mixing ratio up to the cases where flame could not be stabilized anymore.

Then, the stabilization domain was observed under the combined effect of ammonia addition and increasing air coflow velocity. A peculiar re-attachment behavior being observed under these conditions, a more detailed study of the lifted flame in the hysteresis region was performed to clarify the importance of both aspects in the apparition of the behavior. To investigate this, the jet structure and lifted flame positions were investigated using shadowgraph imaging.

The attached flame was later studied to understand the impact of ammonia addition on the aero-thermo-chemical couplings leading to the liftoff. For this purpose, flame position evolution was

observed using  $\text{CH}^*$  fluorescence images. The temperature at the burner lip and the heat transfers to the burner were also studied to observe the change in the thermo-chemical coupling. Those measurements were completed by a flame temperature cartography, near the burner lip to further understand the evolution of the flame up to liftoff for different ammonia mixing ratio,  $E$ .

The experimental setup and the methods deployed to answer to the present objectives are further detailed in the following Section 1.4.

## 1.4. Experimental setup

### 1.4.1. Experimental setup overview

The experimental setup consists of a vertical non-premixed fuel jet surrounded by an air coflow. It is constituted of a central straight pipe of 6 mm inner diameter,  $D_i$ , and 10 mm outer diameter,  $D_o$ , with a 2 mm burner rim thickness,  $e$ , from which is injected the fuel as presented in Fig. 4.4. Pipe length,  $L$ , is 950 mm ( $L/D_i > 150$ ) and gives a fully developed velocity profile at the burner outlet, with a maximum jet velocity of 30 m/s for methane jet. The air coflow is supplied from 4 symmetrical opposite inlets and goes through two perforated plates for relaminarization, before entering a convergent to provide a uniform velocity profile at the pipe outlet, ranging under 0.3 m/s.

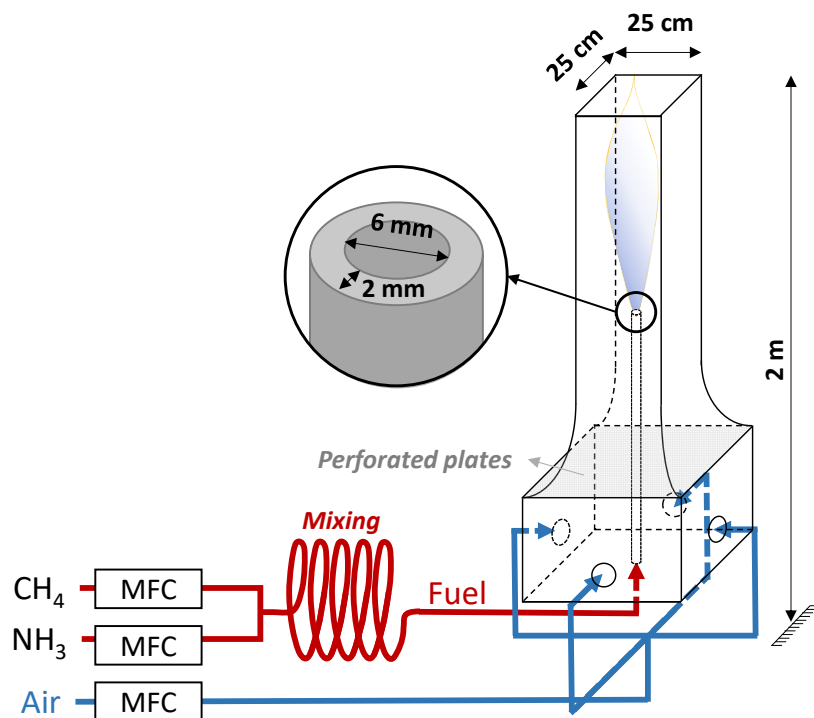


Fig. 4.4. Experimental setup.

The jet flame is developing in a chamber of 250 x 250 mm as represented in Fig. 4.4 preventing from outside disturbances. The chamber was designed to be large enough so that no direct interaction between the flame and the wall occurs and no large scale recirculations were observed [185]. The material of the pipe, and particularly its conductivity, were shown to impact the experimental results on the flame stabilization [119], as well as on the transition between the stabilization regimes. As a first approach, the material selected in this study is common stainless steel (E24) with a conductivity of 54 W/(m·K) at 295K.

The flow rates are adjusted using thermal mass flow controllers (BROOKS SLA series), with a precision of 0.7% of the mass flow rate, more 0.2% of the full range. Methane (with purity over 99.95%) and ammonia (with a purity of 99.96%) are mixed before the injection inside the burner. Fuel mixing can be expressed in different manners, such as volumetric or massic fraction. The heat fraction of the fuel was selected in the present study, following the definition given in works by Okafor et al. and Ichikawa et al. [63,64] as in previous chapters but is recalled here. The ammonia mixing ratio,  $E$ , is defined as in the following equation, where  $X_i$  is the mole fraction of the specie  $i$  and  $LHV_i$  is the lower heating value of the specie  $i$ , with  $LHV_{CH_4} = 802.3$  kJ/kmol and  $LHV_{NH_3} = 316.8$  kJ/kmol.

$$E = \frac{X_{NH_3} \cdot LHV_{NH_3}}{X_{NH_3} \cdot LHV_{NH_3} + X_{CH_4} \cdot LHV_{CH_4}} \quad (4.4)$$

Stabilization regimes were obtained by the gradual increase of the fuel flow rate for a constant value of fuel mixing ratio,  $E$  and air coflow velocity. The mean jet exit velocity,  $U_J$ , and the mean air coflow velocity,  $U_{co}$ , refer to the velocities calculated from the mass flow rates. Previous laser doppler anemometry measurements [118] were performed to characterize the present setup and show good agreement (within 6% or error) between the mean velocity from the velocity profile measurement at the outlet of the pipe and the bulk velocity calculated from the mass flow rates.

#### 1.4.2. Jet structure and lifted flame position observation

To observe the jet flow evolution in the velocity range of interest as well as its evolution when adding ammonia or varying the air coflow velocity, in both cold flow and flame configurations, the use of shadowgraph images was selected. This method allows for the observation of the aerodynamics of the jet without the generation of disturbances contrary to sampling or seeding methods. Avoiding flow

disturbances is essential in the case of the study of ammonia and ammonia blended fuels as the low reactivity of such mixtures makes the flame prompt to destabilization and sensitive to any variations in the flow field. Shadowgraph method thus allows, in this case, to get sufficient information on the jet aerodynamics, while preventing from measurement bias.

The shadowgraph images were obtained using a He-Ne laser combined with a spatial filter, expanded using a lens to produce an afocal beam before going through the flame and being collected on the other side of the setup using a tracing paper screen, associated to an intensified camera with high-speed shutter for recording (PI-MAX 2, exposure time 0.2 ms). The position of the flame was estimated on each image as the upstream-most position of highest intensity region corresponding to the light deviation due to thermal expansion as presented in Fig. 4.5. The average lifted flame position or lift height,  $H_L$ , was obtained from 50 images of the same flame. In the same way, the jet breakpoint position,  $H_T$ , was obtained using the average of the position at which turbulence develops for 50 images.

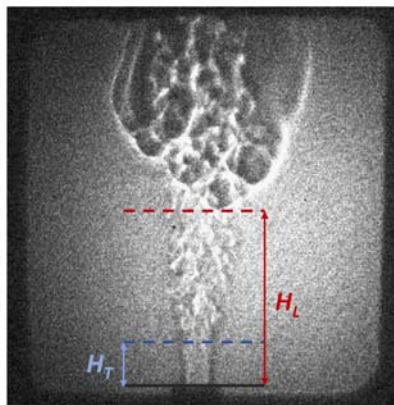


Fig. 4.5. Lifted flame height,  $H_L$ , and jet breakpoint height,  $H_T$ , on a shadowgraph image.

Other methods than the present one could be considered, particularly regarding the determination of the lifted flame position, such as PLIF or chemiluminescence. The present method however allows the simultaneous observation of the jet structure and lifted flame and is sufficient for observation of the relative variations of  $H_L$  and  $H_T$  considered in this study.

### 1.4.3. Attached flame position measurements

To analyze the evolution of the attached flame with ammonia addition, a local detailed study, close to the burner lip was performed. This study included flame tip position measurement, burner lip temperature measurement and temperature mapping in the vicinity of the burner lip.

Measurement of flame tip position was performed by using simple CH\* chemiluminescence imaging. Chemiluminescence imaging is an attractive methodology for flame visualization as it requires limited material. Moreover, CH radicals, emitting at 431 nm, are known to be a good marker of the flame front in methane flames. One of the main drawbacks of this method is that chemiluminescence is collected from all the radicals in the flame. To obtain the flame front position, the jet flame was thus considered as an axisymmetric cone and Abel deconvolution was used to obtain the flame contour corresponding to the 3D chemiluminescence emission. Deconvoluted CH\* images and OH PLIF images were compared in previous studies [117] and gave satisfactory agreement. The deconvolution performed, flame tip height,  $H_a$ , and flame tip radius,  $R_a$ , were obtained based on the selection of a threshold intensity value as described in greater detail in Appendix 4A.

As already mentioned, CH radicals are good markers for the heat released region in the case of methane flames, but in the case of ammonia/methane flames, the CH radical profile peak moves toward the fuel region when increasing ammonia content. This shift remains however moderated and was thus considered neglectable. The choice of CH as a marker for the flame also leads to images with a smaller signal to noise ratio when ammonia content is increased, due to the lower quantity of CH radicals, potentially leading to larger uncertainty in the analysis and should be mentioned as a drawback of the present method.

The flame tip position was observed using this methodology under various fuel mixing conditions and a broad range of jet velocities, covering the whole attached flame regime, from a jet velocity of 0.05 m/s to liftoff. For each flame case, 3 series of 300 images were used. The mean value of both  $H_a$  and  $R_a$  from the analysis of each image is reported in the results.

#### 1.4.4. Burner lip temperature and conductive heat flux measurements

The local interaction of the flame with the burner was also observed considering the evolution of the burner temperature. For that purpose, two K thermocouples (Chromel/Alumel) with branches of 75  $\mu\text{m}$  in a sleeve of 0.5 mm were inserted inside the burner, at the lip level ( $z = 0$ ) and within the burner ( $z = -6$  mm). A representation of the burner end with thermocouples is presented in Fig. 4.6. The temperatures at the burner lip and within the lip were thus observed in parallel of the flame tip position, for the same range of velocity and mixing. The conductive heat flux,  $Q$ , was then simply estimated as:

$$Q = \frac{\lambda \cdot \Delta T}{d_{th}} \quad (4.5)$$

With  $\lambda$  the thermal conductivity of the burner at the mean temperature  $(T_{lip} + T_{-6mm})/2$ ,  $\Delta T = T_{lip} - T_{-6mm}$ , and  $d_{th}$ , the distance between the two thermocouples.

The monitoring of these temperatures during the experiment was also used as a way to control that thermal equilibrium was reached before taking the chemiluminescence imaging.

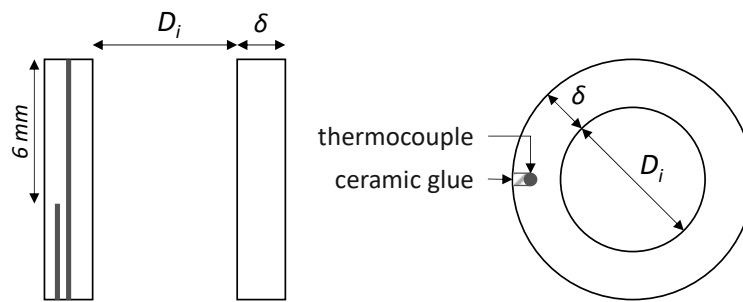


Fig. 4.6. Burner end and thermocouple positions.

The aero-thermo-chemical coupling was further analyzed by temperature mapping measurements, above the burner lip using an R-thermocouple (Pt-Pt/Rh13%), with branches of 50  $\mu\text{m}$ . The region above the burner lip between  $z = 2$  mm and  $z = 8$  mm was explored between  $r = 0$  mm and  $r = 15$  mm. Temperature measurement between  $z = 0$  and 2 mm could not be taken for practical reasons. Details on the measurements are introduced in Appendix 4B. The objective being here to follow the evolution of the temperature profiles with ammonia introduction, correction from the thermocouple measurements were not considered here and the direct measurement evolution is proposed. The maximum temperature at 8 mm above the burner, where the maximum temperature stabilizes, varied in the velocity range investigated, between a maximum of 1850 – 1950 K, for methane flame to values of 1840 – 1870 K for ammonia-methane flame at  $E = 0.3$ . The values for methane case were in general agreement with the observation from Lamige [117].

## 2. Effect of ammonia addition on stabilization regimes of methane non-premixed jet flames

Flame stabilization is a phenomenon corresponding to aerodynamic, chemical and thermal couplings. Any modification of one of these parameters can lead to a substantial change in the flame stabilization. The addition of ammonia to a methane jet flame is thus expected to impact its stabilization. The purpose of this section is to clarify the effect of ammonia addition on the stabilization regimes of a methane non-premixed jet flame in an air coflow, and more specifically liftoff and re-attachment. An exhaustive review of the parameters influencing those stabilization regimes is not done in the present study but some fundamental aspects, necessary for putting into perspective the present work, are recalled in Section 2.1. More specifically, the stabilization regimes and the hysteresis region generally show dependence on the use of an air coflow, as noted by Takahashi and Schmoll and Leung and Wierzba [169,186], and on dilution of both fuel and oxidizer [118,160,187,188]. Both aspects being essential for the understanding of the present work, are developed in the following.

### 2.1. Previous works on the effects on stabilization regimes of the air coflow velocity and dilution of the fuel jet

The stabilization regimes for methane flames in an air coflow were obtained for the present configuration in previous works [118,171,188]. Both liftoff and re-attachment showed neglectable dependence on the air coflow velocity in the range investigated. This independence, attributed to burner rim thickness, was also observed in Takahashi and Schmoll's work [169] reproduced in Fig. 4.7. In this figure, the jet velocity,  $U_J$ , corresponding to the liftoff limit,  $U_{jc}$ , is represented against the air coflow velocity,  $U_{co}$ , named  $U_a$  Takahashi and Schmoll's work, for different burner lip thicknesses. For a burner lip thickness of the same order,  $\delta = 2.4$  mm, to compare to  $\delta = 2$  mm in our study, and an air coflow velocity range of the same order (Takahashi and Schmoll: 0.2 – 0.4 m/s; present: 0.05 – 0.3 m/s), a similar region, independent on the air coflow velocity is observed, whereas for smaller burner lips, variations with the air coflow velocity are more pronounced.

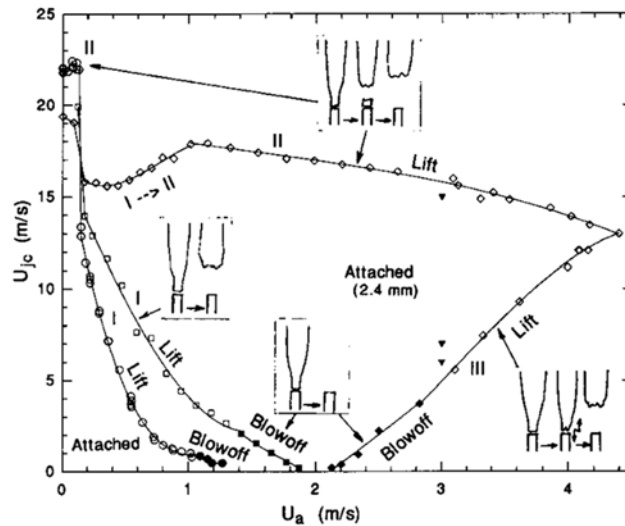


Fig. 4.7. Stabilization map as a function of the air coflow velocity and for different lip thickness,  $\delta$ , from Takahashi and Schmoll [169]: circles  $\delta = 0.2$  mm; squares  $\delta = 1.2$  mm; diamonds  $\delta = 2.4$  mm.

Through a preliminary study, it could be though observed that this independence was not conserved with ammonia addition. The combined effect of the air coflow velocity and ammonia addition has thus been the subject of particular attention in the following Section 2.2

Mixing and dilution were investigated in previous works [180,182–184,188,189] which have shown that the dilution of both the jet and the air coflow has a large impact on the lifted flame height. This impact is however highly dependent on the nature of the diluent. With the gradual addition of inert diluent, lifted flames were shown to be stabilizing further downstream due to the combination of pure dilution (reduction of the concentration of the reactants), thermal and chemical effects. The studies by Guo et al., Min et al. and Lamige et al. [118,171,190] have shown that those diluents could be ranked according to their ability in breaking flame stabilization. The pure dilution effect was shown to be dominant. It was followed by the thermal and chemical effect, depending on the gas used, the first one being usually of greater importance, and the heat capacity of the diluent gas being a good marker for ranking the inert gases in most of the cases. The comparative study of the addition of  $\text{CO}_2$ ,  $\text{N}_2$  and Ar on a methane flame thus led to the  $\text{CO}_2 > \text{N}_2 > \text{Ar}$  destabilization ranking.

Additionally, self-similar behaviors using the fuel jet Peclet number,  $Pe_f = U_J D_i / \alpha$ , and the diluent mass flow rate ratio  $Q_d/Q_f$  or  $Q_d/Q_{ox}$ , with  $U_J$  the fuel jet velocity,  $D_i$  the inner diameter of the burner,  $\alpha$  the thermal diffusivity,  $Q_d$  the diluent mass flow rate and  $Q_f$  the fuel-side mass flow rate (fuel + diluent), were shown to characterize the liftoff limit for those inert diluents as shown in Fig. 4.8. The constants

of the self-similar relation introduced in Fig. 4.8 for the methane-side dilution are recalled in Table 4.1. Using this expression, a single coefficient,  $K_{d,f}$ , for each diluent  $d$ , is sufficient for characterizing the flame liftoff evolution with the introduction of the diluent  $d$ . This coefficient accounts for all the phenomena (pure dilution, thermal, chemical) observed when adding the diluent  $d$ .

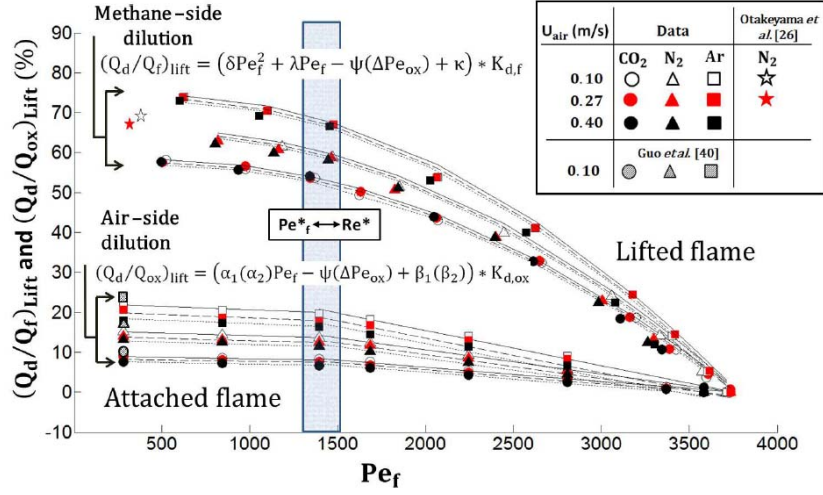


Fig. 4.8. Liftoff limit  $(Q_d/Q_{ox})_{\text{lift}}$  and  $(Q_d/Q_f)_{\text{lift}}$  as a function of the fuel jet Pelet number,  $Pe_f$ , from the work by Marin [191].

Table 4.1. Coefficients for the self-similar relation  $(Q_d/Q_f)_{\text{lift}} = (\delta \cdot Pe_f^2 + \lambda \cdot Pe_f - \psi \cdot \Delta Pe_{ox} + \kappa) \cdot K_{d,f}$  from the work by Marin [191].

Parameter	Value
$\delta$ ( $10^{-6}$ )	-5.3
$\lambda$ ( $10^{-3}$ )	4.8
$\kappa$	57.0
$\psi$	0.035
$K_{CO_2,f}$	1
$K_{N_2,f}$	1.13
$K_{Ar,f}$	1.28

Dilution with another reacting gas, or mixing, like in the present study, is however different due to the nature of the gas, and as the chemical aspects become far from neglectable. This was well-illustrated in the study by Wu et al. [192], where the effects of the dilution of  $H_2$  jet flame with  $CO_2$  and propane ( $C_3H_8$ ) were studied. The addition of the latter on to the hydrogen jet led to a faster decrease of the lift height than for  $CO_2$ . This difference was attributed to the drastic reduction of the laminar burning

velocity when adding propane, its addition acting as a sink for OH and H radicals in the flame. It is thus essential to carefully investigate the effect of gas mixing on the stabilization process.

## 2.2. Experiment on ammonia/methane jet flames

The results on the evolution of the stabilization domain with ammonia addition are first introduced in the case of a small air coflow velocity,  $U_{co} = 0.026$  m/s, close to the free-jet configuration. The objective of this section is first to describe the effect of ammonia alone on the stabilization of the jet flames. The air coflow velocity and the ratio of fuel jet and air coflow momentum is of importance in the study of jet flames, and though the range of the air coflow velocity investigated being small, its variation in the case of ammonia/methane mixtures revealed important changes in the stabilization domain and is thus investigated in a second time. The peculiar behaviors observed could not be simply explained from the analysis of global parameters of the fuel jet, and the re-attachment was further investigated by observation of the lifted flame height and jet aerodynamic structure in the hysteresis region. The study was first performed for low air coflow velocity to highlight the effect of ammonia addition, and then, with larger air coflow velocities.

### 2.2.1. Evolution of the stabilization regimes

- **Effect of ammonia addition for low air coflow velocity ( $U_{co} = 0.026$  m/s)**

The evolution of the stabilization domain of a methane non-premixed flame was first studied in the case of a low air coflow velocity,  $U_{co} = 0.026$  m/s, to observe the effect of the ammonia addition alone. The bulk velocity at liftoff,  $U_{LO}$ , as well as the one for re-attachment,  $U_A$ , are plotted against the ammonia fuel mixing ratio,  $E$ , in Fig. 4.9. The corresponding Reynolds numbers of the jet is  $Re_J = D_i U_J / \nu$ , with  $U_J$  the bulk velocity of the jet,  $D_i$ , the burner inner diameter, 6mm, and  $\nu$  has been calculated for each mixture using multicomponent mixture approximation for viscosity [193].

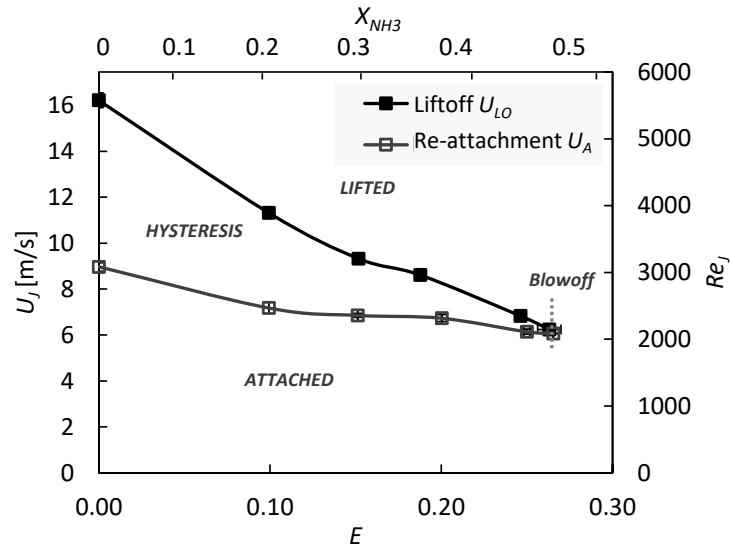


Fig. 4.9. Evolution of the stabilization regimes with  $E$  for  $U_{co} = 0.026$  m/s.

From Fig. 4.9, it is seen that the addition of ammonia leads to both slower  $U_{LO}$  and  $U_A$ , and therefore, to a reduction of the stabilization range. The lift-off velocity,  $U_{LO}$ , is sharply reduced from around 16 m/s, in the case of pure methane, to less than 7 m/s for  $E = 0.26$ . The re-attachment velocity,  $U_A$ , is also decreasing until  $E = 0.26$  but at a slower rate. The hysteresis domain, in between the lift-off and re-attachment is thus gradually reduced when ammonia is added as  $U_{LO}$  and  $U_A$  are getting close to each other. This region covers Reynolds number,  $Re_J$ , from 5600 to 2100, corresponding to jets in turbulent conditions to jets close to the transition from laminar to turbulent flow in a pipe, classically considered at  $Re_J = 2300$  [194–196]. For  $E = 0.26$ ,  $U_{LO}$  and  $U_A$  become so close that an unstable flame could be observed, flipping from the attached to the lifted position. At the end of the hysteresis domain ( $E > 0.26$ ), where the ammonia mole fraction reaches 50% in the fuel jet, the flame cannot be stabilized on the burner anymore.

In the case of dilution by inert gas ( $N_2$ , Ar,  $CO_2$ ) [171,197], it was found that flame was destabilized and that the lift-off would occur by the combined effects of pure dilution, thermal and chemical effect. The ratio  $(Q_d/Q_f)_{lft}$ , corresponding to the flow rate ratio of diluent on the total amount of fuel mixture injected through the pipe at lift-off, was shown to be a good parameter to rank the ability of the diluent in breaking the flame stability. In previous work [191], for the same burner configuration and air coflow velocity (0.1 m/s), the largest  $(Q_d/Q_f)_{lft}$  obtained for Ar,  $N_2$  and  $CO_2$  dilution were respectively equal to 74%, 63% and 58%, compared to 48% in the present case for ammonia. The decrease in the lift-off

velocity is thus particularly sharp in the case of ammonia addition. The liftoff self-similar relations obtained in the work by Marin [191] for inert diluent, is compared to the one obtained with ammonia dilution in Fig. 4.10. The trend is overall reproduced with a value of  $K_{NH_3,f} = 0.85$ . However, some slight changes can be noticed looking more specifically in the turbulent and laminar region independently, as the auto-similar relation deviates slightly from the present experimental observation.

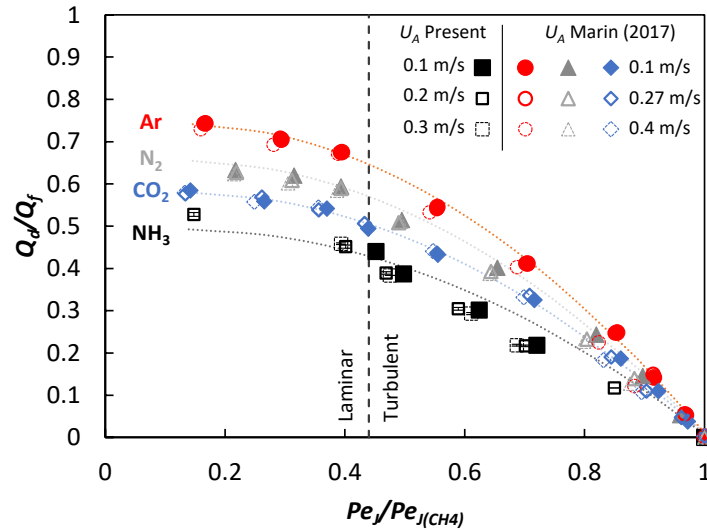


Fig. 4.10. Self-similar relation at liftoff from the work by Marin [191] for inert gases, and ammonia from the present study. The dashed line represents the laminar-to-turbulent transition in a pipe flow.

The molar heat capacity,  $C_{pm}$ , of the diluent was shown to be of importance in ranking the ability of the diluent to break flame stabilization [117,191]. Their values were, at 298 K,  $C_{pm,Ar} = 20.8$  J/(mol·K),  $C_{pm,N_2} = 29.2$  J/(mol·K) and  $C_{pm,CO_2} = 37.3$  J/(mol·K) [117]. The molar heat capacity of ammonia at 298 K,  $C_{pm,NH_3}$ , is 36.5 J/(mol·K), relatively close to the one of  $CO_2$ . The difference observed between the two gases in Fig. 4.10 might thus reasonably be attributed to the changes in the chemistry due to the introduction of ammonia, which is a reactive gas.

The laminar burning velocity of a mixture has been shown to have a dominant impact on flame stabilization and liftoff [117,197,198]. As the laminar burning velocity decreases, liftoff is expected to occur for smaller jet velocities [118,197]. The lifted flames position also being related to the laminar burning velocity [174,181], a variation of the laminar burning velocity might be expected to affect the re-attachment. To compare the evolution of the laminar burning velocity and the liftoff and re-attachment velocity of the mixtures investigated, the ratio  $C$  of the liftoff  $U_{LO}$  and re-attachment  $U_A$  velocities on the laminar burning velocity  $S_{L0}$ ,  $C_L (= U_{LO}/S_{L0})$  and  $C_A (= U_A/S_{L0})$  respectively have been

calculated and summarized in Fig. 4.11. Assuming the stabilization of the non-premixed flame in near stoichiometric conditions, the laminar burning velocity obtained experimentally by Han et al. [101] for stoichiometric flames were considered as a first approximation.

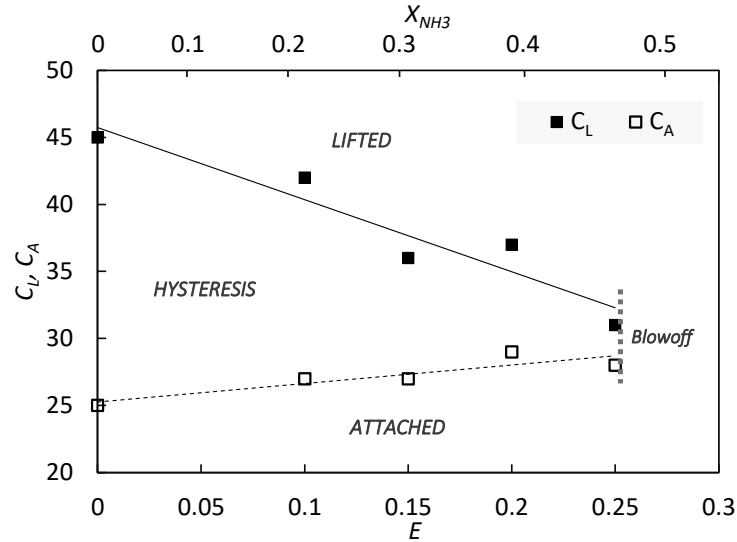


Fig. 4.11. Evolution of  $C_L$  and  $C_A$  with  $E$  for  $U_{co} = 0.026$  m/s.

As noted in Fig. 4.11, both  $C_L$  and  $C_A$  ratios are varying with ammonia concentration.  $C_L$  values are much larger than the  $C_A$  ones. Whereas  $C_A$  variations are small and a general trend cannot be observed with ammonia addition,  $C_L$  shows a clear variation between  $E = 0$  and  $0.25$ , gradually decreasing when ammonia is introduced. The dependence on flame properties might thus also vary with ammonia introduction and the balance between the aerodynamic, kinetics and thermal contributions change. The evolution of the stabilization domain with ammonia addition cannot thus be simply reduced to the laminar burning velocity variations of stoichiometric flames.

Overall, both liftoff and re-attachment velocity decreased with ammonia addition to a methane non-premixed jet flame and led to a particularly large reduction of the stabilization domain, especially when compared with inert diluents such as Ar,  $N_2$  or  $CO_2$ . For a non-neglectable part, this phenomenon might be associated with kinetics change as discussed bases on the results in Fig. 4.10. However, the relative part of these changes is not constant, with no simple relationship with the decrease in the laminar burning velocity as observed in Fig. 4.11, suggesting that other mechanisms should be considered to fully understand the stabilization domain reduction and particularly the liftoff velocity decrease.

• **Coupled effect of higher air coflow velocities and ammonia addition on the stabilization regimes**

As mentioned in the introduction of this work, the presence of an air coflow and its specific velocity might affect the stabilization region of a non-premixed jet flame and was thus investigated. Air coflow velocities were thus varied between the initial value  $U_{co} = 0.026$  m/s, close to free-jet condition, up to a velocity of  $U_{co} = 0.3$  m/s. The experimental liftoff and re-attachment limits are shown in Fig. 4.12 where the jet Reynolds number,  $Re_J$ , corresponding to the different cases investigated (liftoff:  $U_J = U_{LO}$ , re-attachment:  $U_J = U_A$ ) are plotted for various air coflow velocities,  $U_{co}$ , and various mixing ratio,  $E$ . Whereas, similarly to the previous studies for methane flames on the same burner [117], no major variations of the liftoff line were noticed, the present study shows some variations of the re-attachment line. Indeed, when ammonia is increased up to  $E = 0.15$ ,  $U_A$  gradually decreases with higher  $U_{co}$ . The apparition of the dependence in the air coflow velocity coincides with the laminar-to-turbulent transition in a pipe flow classically considered at  $Re_J = 2300$ .

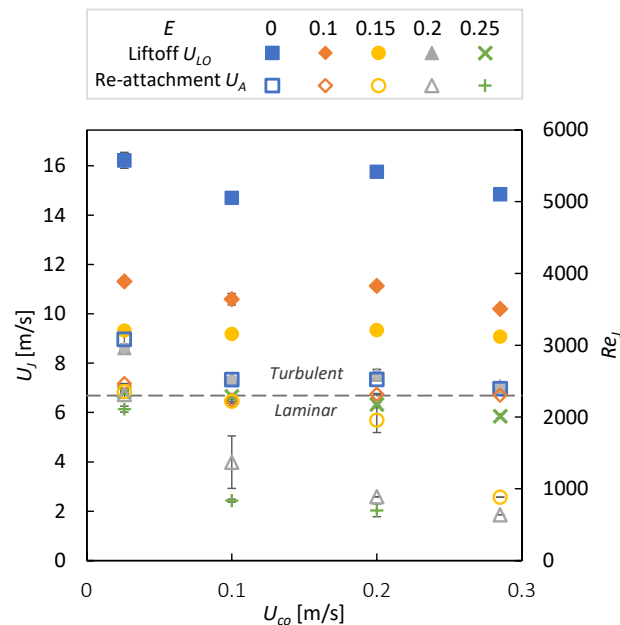


Fig. 4.12. Evolution of the liftoff re-attachment with  $U_{co}$  for  $E = 0, 0.1, 0.15, 0.2$  and  $0.25$ . The dashed line represents the laminar-to-turbulent transition in pipe flow.

To study more specifically the combined effect of the higher air coflow velocity with ammonia addition on the hysteresis region, both liftoff velocity and re-attachment velocity are plotted against the fuel mixing ratio for a selected air coflow velocity,  $U_{co} = 0.2$  m/s in Fig. 4.13.

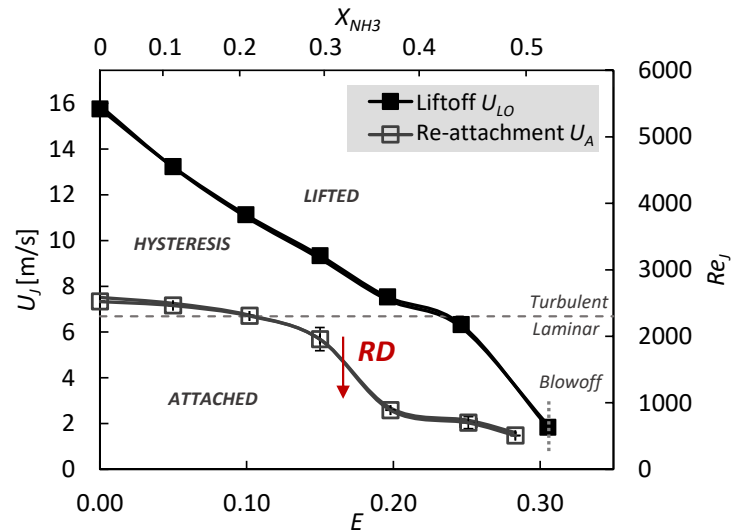


Fig. 4.13. Hysteresis region for ammonia addition at  $U_{co} = 0.2$  m/s. The dashed line indicates the laminar-to-turbulent transition in pipe flow ( $Re_j = 2300$ ).

First, it can be seen in Fig. 4.13 that for this larger air coflow velocity, the liftoff appears for lower velocities as ammonia is introduced, similarly to Fig. 4.9. However, this decrease is larger than for low air coflow velocity case and the jet Reynolds number at liftoff is reduced from 5400 for methane flames, to 630 for  $E = 0.3$ . Another noticeable change corresponds to an evolution of the slope of the liftoff Reynolds curve close to the laminar to turbulent transition. This was mentioned in previous studies on fuel jet and air coflow dilution with inert gases [171,197] where lifted jet flames are mainly controlled by dilution phenomenon in the laminar range (with a large  $U_{LO}$  slope relative to  $E$ ), whereas for turbulent range less diluent addition is needed for destabilizing the flame and combined aerodynamics and dilution are key to the destabilization. The stability domain is also slightly expanded with the end of the hysteresis region, going from  $E = 0.26$  at  $U_{co} = 0.026$  m/s, to  $E = 0.30$  at  $U_{co} = 0.2$  m/s.

However, as presented in Fig. 4.14, it can be noticed that this expansion disappears when the air coflow velocity keeps increasing, as in the case of  $U_{co} = 0.3$  m/s with a direct blowoff at  $E = 0.25$ , and was not further studied here. Overall, the liftoff transition obtained for different ammonia concentrations is only slightly affected by a variation of the air coflow velocity as shown in both Figs. 4.12 and 4.14.

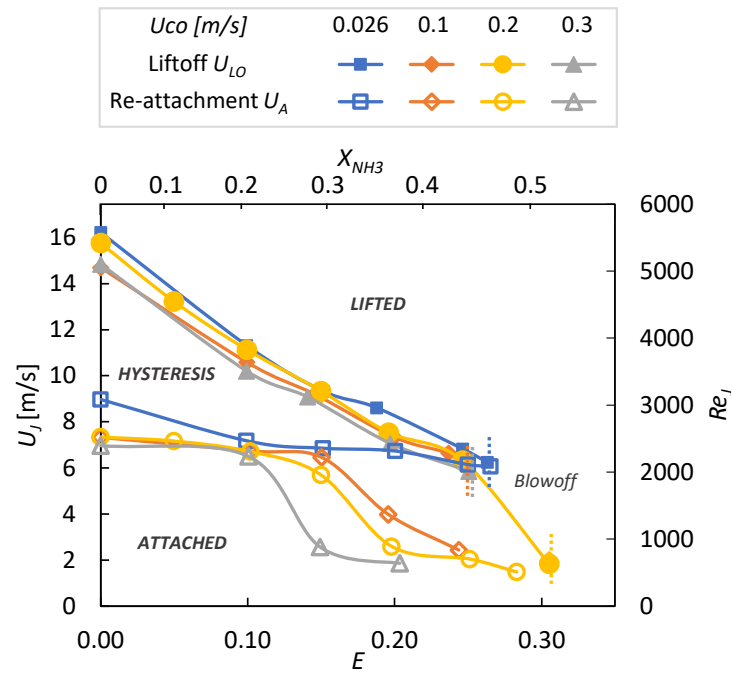


Fig. 4.14. Evolution of the hysteresis region with  $E$  for  $U_{co} = 0.026, 0.1, 0.2, 0.3$  m/s.

Secondly, focusing now on the re-attachment line in Fig. 4.13, a significant difference with Fig. 4.9 can be noticed: a sudden drop in terms of jet Reynolds number  $Re_J$  appears. This drop will be called hereafter as “Re-attachment Drop” (RD) and represented by a red arrow in Fig. 4.13. It coincides with the laminar-to-turbulent transition of the jet and significantly increases the hysteresis region. This re-attachment drop, occurring for mixtures between  $E = 0.15$  and  $E = 0.2$  for the air coflow velocity ( $U_{co} = 0.2$  m/s) represented in Fig. 4.13, is dependent on  $U_{co}$ . Indeed, as highlighted in Fig. 4.14, a larger air coflow velocity leads to a re-attachment drop for a smaller ammonia mixing ratio  $E$ .

The relationship between the re-attachment drop (RD), the ammonia mixing ratio and the air coflow velocity is not straightforward. As ammonia is added, the jet re-attachment velocities,  $U_A$ , are becoming smaller and the relative impact of the air coflow on the jet aerodynamics, and the mixing of fuel and air, might be greater. This could in turn impact the local flame velocity and its stabilization and should be investigated. Indeed, lifted flames are expected to stabilize in a region where the local velocity balances the local flame speed. When ammonia is introduced in greater quantity in the jet, the local flame speed is reduced. Moreover, modification of the air coflow velocity, particularly larger air coflow velocities, is also expected to destabilize the flame as their increase leads to a larger local velocity where flame stabilizes. Thus, both air coflow velocity increase and ammonia addition change the local velocity

balance corresponding to flame stabilization, through variations of local velocity, fuel/air mixing and fuel reactivity.

As a first global approach in understanding the re-attachment drop (RD), the critical value of air coflow velocity,  $U_{co,c}$ , above which RD appears for a fixed ammonia concentration is thus compared to the laminar burning velocity of this mixture at stoichiometry and introduced in Table 4.2 with the ratio  $C_{co} = U_{co,c} / S_{L0}$ . Comparison with the laminar burning velocity of the mixture shows that the critical air coflow velocity is smaller than the laminar burning velocity, for all the cases investigated. The ratio  $C_{co}$  also tends to decrease with ammonia addition and becomes particularly small when getting closer to the end of the hysteresis region, at  $E = 0.25$ , suggesting the flame becomes particularly sensitive to slight changes in its environment and more prompt to re-attachment drop as greater amounts of ammonia are added. This first approach, confirming the sensitivity of the jet with high ammonia content to the air coflow velocity, is however not sufficient to conclude on the origin of the re-attachment drop. Thus, a more comprehensive study of the lifted flames in the hysteresis region, particularly of their position in the jet, is necessary to conclude on the apparition of the re-attachment drop and developed in the next sections.

Table 4.2. Evolution of the critical air coflow velocity  $U_{co,c}$  for various  $E$ .

$E$	$X_{NH_3}$ molar fraction	$U_{co,c}$ [m/s]	$S_{L0}$ [101] [m/s]	$C_{co}$ (= $U_{co,c} / S_{L0}$ )
-	-	[m/s]	[m/s]	-
0	0	*	0.35	*
0.1	0.22	*	0.27	*
0.15	0.31	0.2	0.25	0.8
0.2	0.39	0.026-0.1	0.22	0.45-0.12
0.25	0.46	0.026	0.21	0.12

\*  $U_{co,c} > 0.3$  m/s not investigated due to experimental limitations.

So, this study emphasizes two particular phenomena: first the drastic decrease in the stabilization domain of a methane non-premixed jet flame due to ammonia addition, but also a specific behavior, the re-attachment drop, linked to combined effects of air coflow velocity and fuel dilution. As the analysis of the global characteristics of the jet flame could not satisfactorily explain the present results, the evolution of the lifted flame height in the hysteresis region, as well as the evolution of jet structure, was further investigated as presented in the next section.

### 2.2.2. Ammonia/methane lifted flames behavior in hysteresis region and re-attachment

To explain the singular re-attachment drop observed, the aerodynamic of the jet and the lifted flame position in the hysteresis region were investigated using shadowgraph imaging. The sole effect of ammonia is first introduced before studying the combined effect of ammonia and air coflow velocity to understand the contribution of both fuel mixing and air coflow velocity.

- **Effect of ammonia addition for low air coflow velocity ( $U_{co} = 0.026$  m/s)**

As ammonia is introduced in the jet, the thermal and diffusion properties of the mixtures are changed as introduced in Table 4.3. To confirm that these variations do not introduce a dramatic change in the aerodynamic of the jet, the effect of ammonia addition was first viewed for a cold flow jet expanding in the lowest air coflow ( $U_{co} = 0.026$  m/s), in the velocity range corresponding to the re-attachment velocity observed for mixtures between  $E = 0$  and  $E = 0.2$ .

Table 4.3. Thermal and diffusion properties of ammonia/methane mixtures at 298 K and 1 atm.

$E$	$\rho$ [kg/m <sup>3</sup> ]	$\nu$ [mm <sup>2</sup> /s]	$\alpha$ [mm <sup>2</sup> /s]	$C_p$ [J/kg/K]
0	0.654	17.38	24.5	2225
0.1	0.663	16.98	23.95	2193
0.15	0.667	16.81	23.74	2179
0.2	0.670	16.67	23.55	2168
0.25	0.673	16.55	23.38	2158

As shown in Fig. 4.15, the breakpoint of both jets, above which the turbulence develops, decreases in this velocity range which is within the laminar-to-turbulent transition region denoted by the dashed line at 2300. No major difference appears in the aerodynamic of the two jets and the evolution of the jet breakpoint height normalized by the burner inner diameter,  $D_i$ ,  $H_T/D_i$ , presented in Fig. 4.15, is similar for the two jets in the hysteresis region. The origin of the reduction of the re-attachment velocity noted in Fig. 4.9 cannot be explained by the variation of the jet aerodynamic alone and the lifted flame observation is necessary.

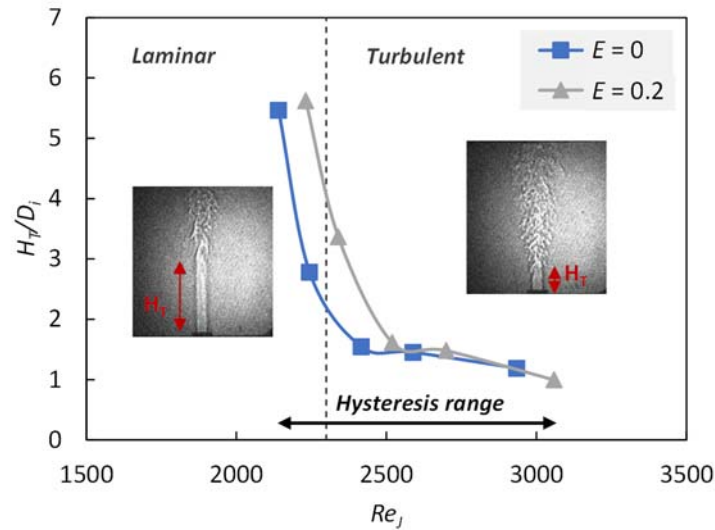


Fig. 4.15. Variation of  $H_T/D_i$  with  $Re_J$  for  $E = 0$  and  $E = 0.2$ . The dashed line corresponds to the pipe flow transition at  $Re_J = 2300$ .

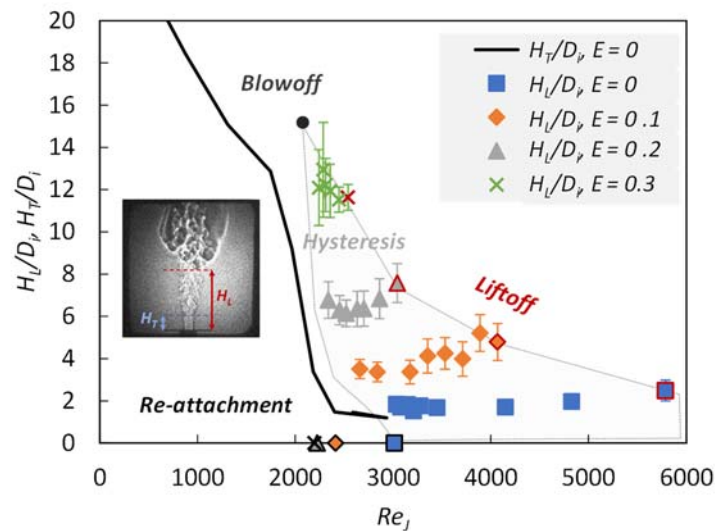


Fig. 4.16. Evolution of  $H_T/D_i$  and  $H_L/D_i$  with  $E$  and  $Re_J$  for  $U_{co} = 0.026$  m/s.

The evolution of the lifted flame height normalized by the burner inner diameter,  $D_i$ ,  $H_L/D_i$ , within the hysteresis region was explored more specifically and presented in Fig. 4.16 for a fixed air coflow velocity of 0.026 m/s and  $E$  varying within 0 – 0.25. For each ammonia concentration curve, the rightmost data point corresponds to the height at liftoff highlighted by a red contour, and the leftmost one, highlighted by black contour, corresponds to re-attachment. The jet breakpoint evolution obtained from the shadowgraph imaging in the cold flow jet (cf. Fig. 4.15) is also reported.

The normalized lifted flame height,  $H_L/D_i$ , is increased as ammonia is introduced in the jet and the laminar burning velocity of the mixture decreased as discussed in the literature for other diluents [180,182]. Indeed, as diluent is introduced in the jet, the burning velocity of the mixture will decrease, and for a same jet outlet velocity, the flame will tend to stabilize in the upper region of the jet where the local velocity is lower and can be balanced by the mixture burning velocity. In the range of mixing ratio investigated,  $E = 0 - 0.25$ , the lifted flame position varied between 4 and 15 times the value of the jet diameter,  $D_i$ , in the hysteresis region. The increase is particularly pronounced for the largest ammonia additions, with a variation between the cases  $E = 0.20$  and  $E = 0.25$  which is particularly large compared to the corresponding laminar burning velocity change. The jet velocities in these cases are also smaller and it can be noticed that as ammonia is introduced in the mixture, for the same fuel jet velocity the fluctuations of the flame position are larger, as identified by the fluctuation range in the figure, corresponding to the standard deviation to the mean value of the flame position in the 50 images investigated, in Fig. 4.16, traducing the greater instability of the flame.

For all the mixtures, the lifted flame height,  $H_L$ , decreases from the liftoff height position,  $H_{LO}$ , as the jet velocity decreases toward the re-attachment limit, which corresponds to the common observation in previous studies on blended fuels [183,184]. Results also point out that when the jet velocity is further decreased up to the point where the lifted flame height, is joined by the jet breakpoint height, re-attachment occurs.

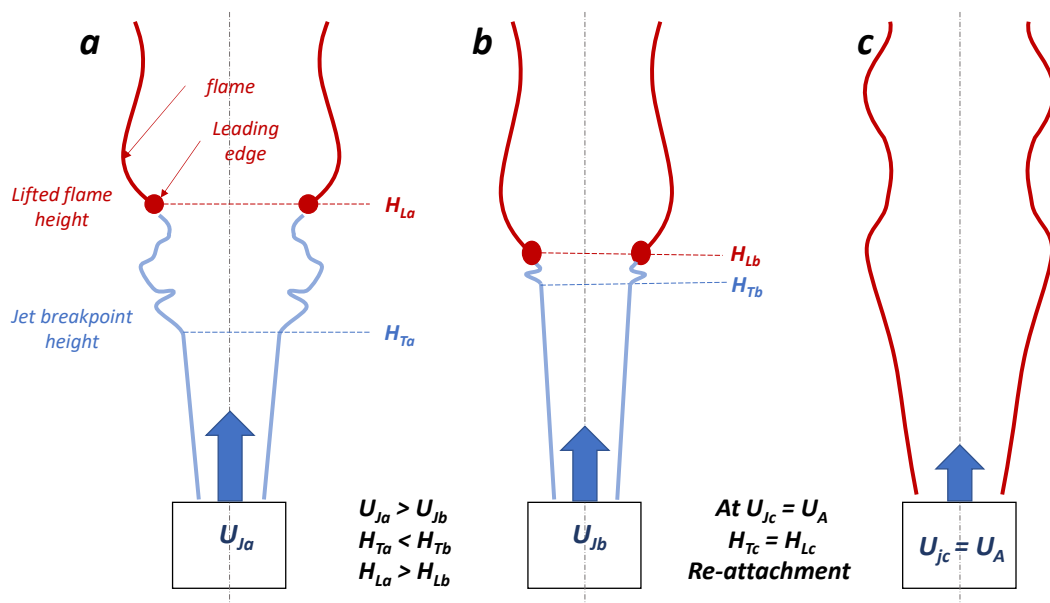


Fig. 4.17. Schematics of flame re-attachment.

This is summarized in Fig. 4.17, where 3 jet velocity cases are represented such as  $U_{Ja} > U_{Jb} > U_{Jc}$ . The turbulent lifted flame in the hysteresis region is located above the jet breakpoint, such as  $H_{La} > H_{Ta}$ . When the jet velocity is decreased,  $H_L$  is reduced and  $H_T$  is increased. The two points eventually join for  $U_{Jc} = U_A$ , the re-attachment velocity, and the flame gets re-attached. A higher liftoff height thus leads to a smaller re-attachment velocity to get  $H_L = H_T$ , as visible in Fig. 4.9.

- **Coupled effect of higher air coflow velocities and ammonia addition**

The air coflow velocity was shown to have a particularly important impact on the stabilization domain of ammonia/methane flame. To understand this effect, the jet aerodynamic is first investigated by varying the air coflow velocity from 0.026 m/s, for which no re-attachment drop was observed, to 0.2 m/s. For flames in the hysteresis region, these values lead to ratio  $U_{co}/U_J$  between 0.002, for methane flames at liftoff and 0.1 in the case of the largest ammonia content at re-attachment. Even though these ratios remain small, a larger impact of the air coflow is to be expected for the smallest jet velocity as previously mentioned.

The same way the jet breakpoint was obtained for both methane and ammonia-methane flame for a small air coflow velocity in Fig. 4.15, its variations were compared in Fig. 4.18 for two air coflow velocities,  $U_{co} = 0.026$  m/s and  $U_{co} = 0.2$  m/s, for the range of jet velocities corresponding to the hysteresis region.

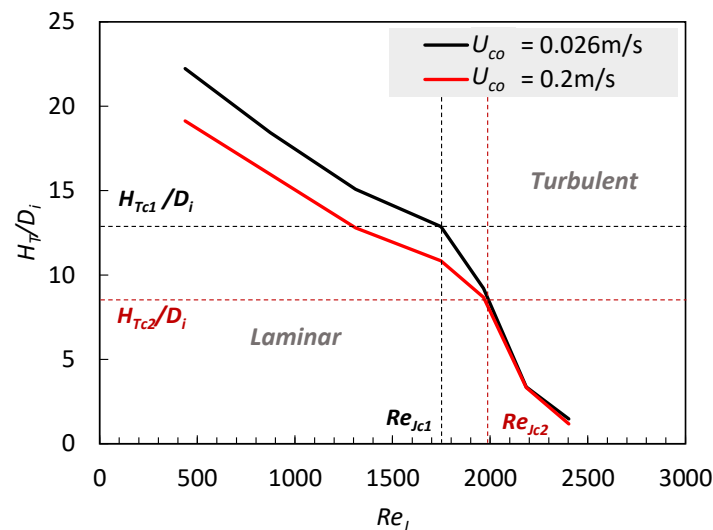


Fig. 4.18. Evolution of  $H_T/D_i$  for  $U_{co} = 0.026$  m/s and 0.2 m/s with  $Re_J$ . Subscripts 1 and 2 correspond to the change in the decreasing slope observed for  $U_{co} = 0.026$  m/s and  $U_{co} = 0.2$  m/s, respectively.

As previously discussed, the normalized jet breakpoint height,  $H_T/D_i$ , decreases when the Reynolds number increases. For both air coflow velocities, a change in the decreasing slope of the jet breakpoint is noticed at  $Re_J$  close to 2000, near the laminar-turbulent theoretical transition [199], and at a normalized height,  $H_{Tc1}/D_i$ , between 10 and 13  $D_i$ . These changes are denoted by the dashed line in Fig. 4.18,  $H_{Tc1}$  corresponding to the change for  $U_{co} = 0.026$  m/s and  $H_{Tc2}$  to  $U_{co} = 0.2$  m/s. However, for smaller  $Re_J$  numbers, increasing the air coflow velocity leads to a sensibly lower position of the jet breakpoint while the evolution is similar for the largest  $Re_J$ . Thus, the velocity flow field in the jet is expected to be more sensitive to the air coflow velocity for lower jet velocity and height above  $H_{Tc}$ .

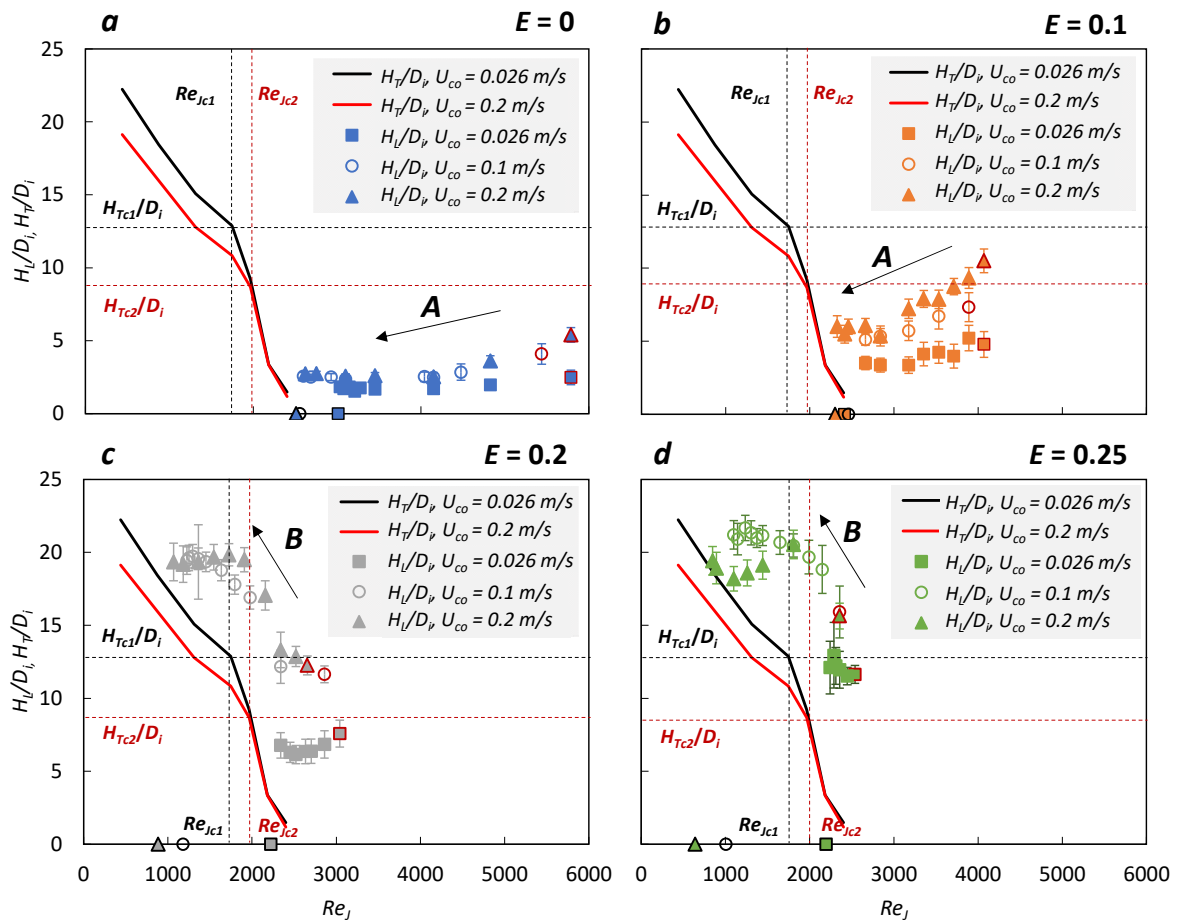


Fig. 4.19. Evolution of lift height with  $Re_J$  for  $U_{co} = 0.026$  m/s, 0.1 m/s and 0.2 m/s: (a)  $E = 0$ ; (b)  $E = 0.1$ ; (c)  $E = 0.20$  and (d)  $E = 0.25$ .

The evolution of the normalized lifted flames height,  $H_l/D_i$ , for ammonia mixing ratio  $E = 0, 0.1, 0.2$  and  $0.25$  with three different air coflow velocities  $U_{co} = 0.026$  m/s, 0.1 m/s and 0.2 m/s, is presented in Fig. 4.19, with the evolution of the normalized jet breakpoint height,  $H_T/D_i$ , as represented in Fig.

4.18. The rightmost points contoured in red correspond to the liftoff cases whereas the leftmost ones, contoured in black, correspond to re-attachment.

As in the case of the low air coflow velocity, as ammonia is introduced, the normalized lifted flame height,  $H_L/D_i$ , is increased. It can also be noticed that for all the mixtures, a larger air coflow velocity leads to a higher normalized lifted flame height,  $H_L/D_i$ , as mentioned in several studies [162,170]. Indeed, and as discussed in these studies, for a higher air coflow velocity, the jet velocity profiles at the same jet height are broader, and thus, the local velocity being larger, the flame stabilizes slightly higher in the jet where the local flame velocity is balanced.

Moreover, another peculiar change occurs with the increase in the ammonia mixing ratio,  $E$ . Indeed, whereas for the smaller  $E$  cases the normalized lifted flame height,  $H_L/D_i$ , presents a decreasing trend when decreasing the jet Reynolds number,  $Re_J$ , for the larger  $E$  cases, an increasing trend can be observed. In the first case,  $H_L/D_i$  remains under the normalized liftoff height,  $H_{L0}/D_i$ , as  $H_L/D_i$  decreases. However, in the other case, as  $H_L/D_i$  increases, it becomes larger than  $H_{L0}/D_i$ , reaching values close to 20. These two flame behaviors are further detailed in the following.

- **Re-attachment drop mechanism**

From these results, two re-attachment behaviors are thus exhibited and will be referred to as behaviors A and B as follow: the re-attachment behavior A corresponds to a usual decrease in  $H_L$  when  $Re_J$  decreases, while behavior B refers to the singular increase of  $H_L$  associated to a decrease in  $Re_J$ . Behaviors A and B are represented by black arrows in Fig. 4.19. These behaviors can furthermore be related to the re-attachment drop as previously presented in Fig. 4.13 and Fig. 4.14. Indeed, whereas behavior A corresponds to the re-attachment cases before Re-attachment Drop, the behavior B matches to the cases after the Re-attachment Drop, with particularly low re-attachment velocities. Indeed, in the B case, the jet velocity needs to be further decreased to get a laminar jet up to this higher lift position. The re-attachment drop is thus explained by those two specific evolutions as summarized in Fig. 4.20.

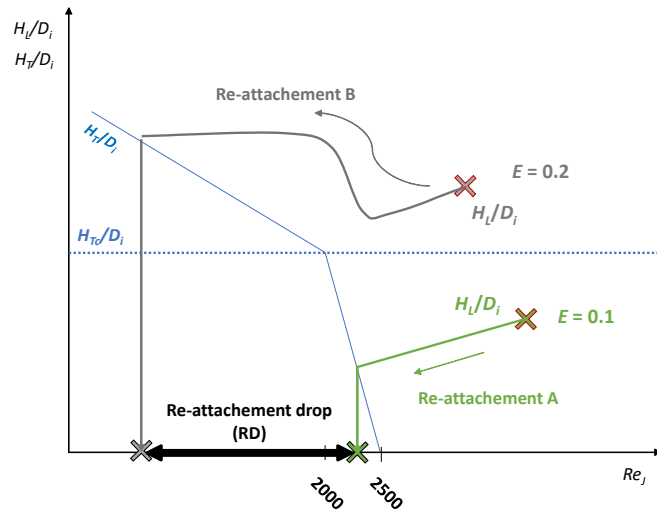


Fig. 4.20. Schematics of the re-attachment behaviors A and B and the re-attachment drop (RD).

To explain the transition between behaviors A and B, the critical length,  $H_{Tc}$ , which corresponds to the change in the slope of breakpoint evolution as introduced previously in Fig. 4.18, should be considered. If the lifted flame is stabilized under this critical length when  $Re_J$  decreases, this decrease will lead both to a sharp increase of the normalized jet breakpoint position,  $H_T/D_i$ , and to a decrease of the normalized flame lifted height,  $H_L/D_i$ . So, the flame is directly re-attached for  $H_T/D_i = H_L/D_i < H_{Tc}/D_i$ , following behavior A, as it has been obtained for all the mixing investigated when the air coflow velocity is low. This behavior A is summarized in Fig. 4.22, which details the evolution of the flow structure and flame position when the jet velocity decreases. In these conditions, as ammonia is introduced in the jet, the lifted flame gets higher and the relaminarization of the jet up to this upper position is observed for a slightly lower jet velocity, explaining why the re-attachment velocity,  $U_A$ , decreases. However, in this case,  $Re_J$  remains above  $Re_{Jc}$  and for this range of Reynolds, the increase in the jet breakpoint position is sharp on a small span of jet velocity, explaining the low dependence in ammonia addition and the limited decrease of  $U_A$ .

On the opposite, for larger air coflow, which leads to higher liftoff height, the increase in ammonia will lead to the largest ammonia amounts to  $H_L/D_i > H_{Tc}/D_i$  at  $Re_J = Re_{Jc}$ . The observation of A or B behavior will thus depend on  $E$  and the transition between the two cases corresponds to the re-attachment drop. Once the aforementioned condition reached, behavior B will be obtained: a decrease in the jet velocity will lead to a higher breakpoint position and the flames first move downstream and then re-attached when the breakpoint position reaches the upper lift position. In those cases, and for Reynolds numbers greater than the transition one ( $Re_J = Re_{Jc}$ ), a large flame base develops, thanks to the wider

mixing in this region as seen in Fig. 4.21. However, when the jet velocity is decreased, mixing in the region becomes more limited as shown in Fig. 4.21a. Moreover, based on the work by Lawn [162], it can be understood that when the  $Re_J$  is decreased, and the ratio  $U_{co}/U_J$  becomes larger, the stoichiometric line,  $Z_{st}$ , moves toward the jet, explaining why the flame base becomes narrower as visible on the shadowgraph and the direct visualization of the flame. Moreover, the jet becoming closer to laminar, turbulence and mixing are reduced, and the flame tends to move upward, close to the stoichiometric line, in favorable fuel/air mixing condition, but where the local flow velocity is sufficiently small to balance the local flame velocity [162,200]. This is summarized in Fig. 4.23, representing the jet and flame position for a decreasing jet velocity, i.e., the jet Reynolds number  $Re_J$ .

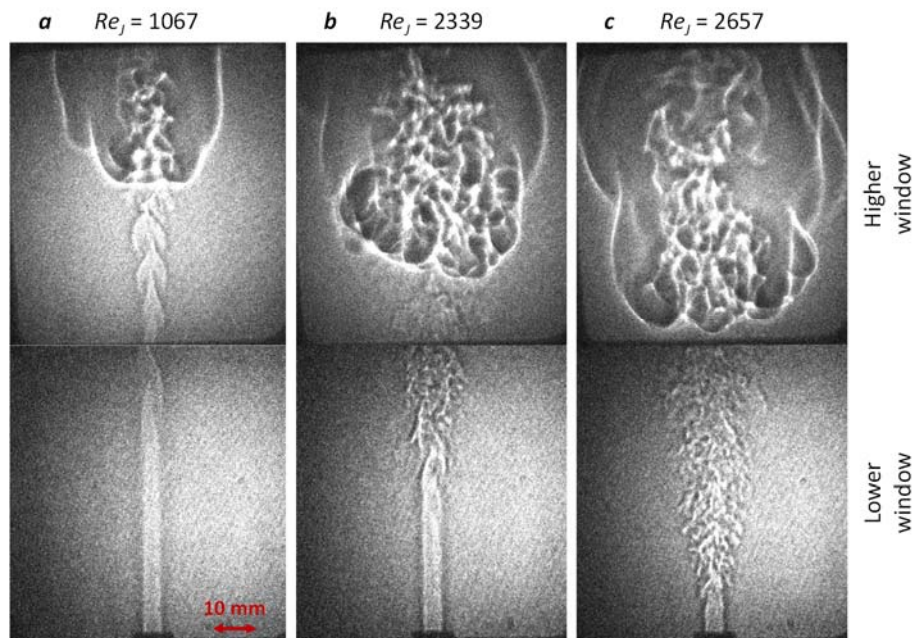


Fig. 4.21. Behavior B from shadowgraph images: (a)  $Re_J = 1067$ ; (b)  $Re_J = 2339$ ; (c)  $Re_J = 2657$ .

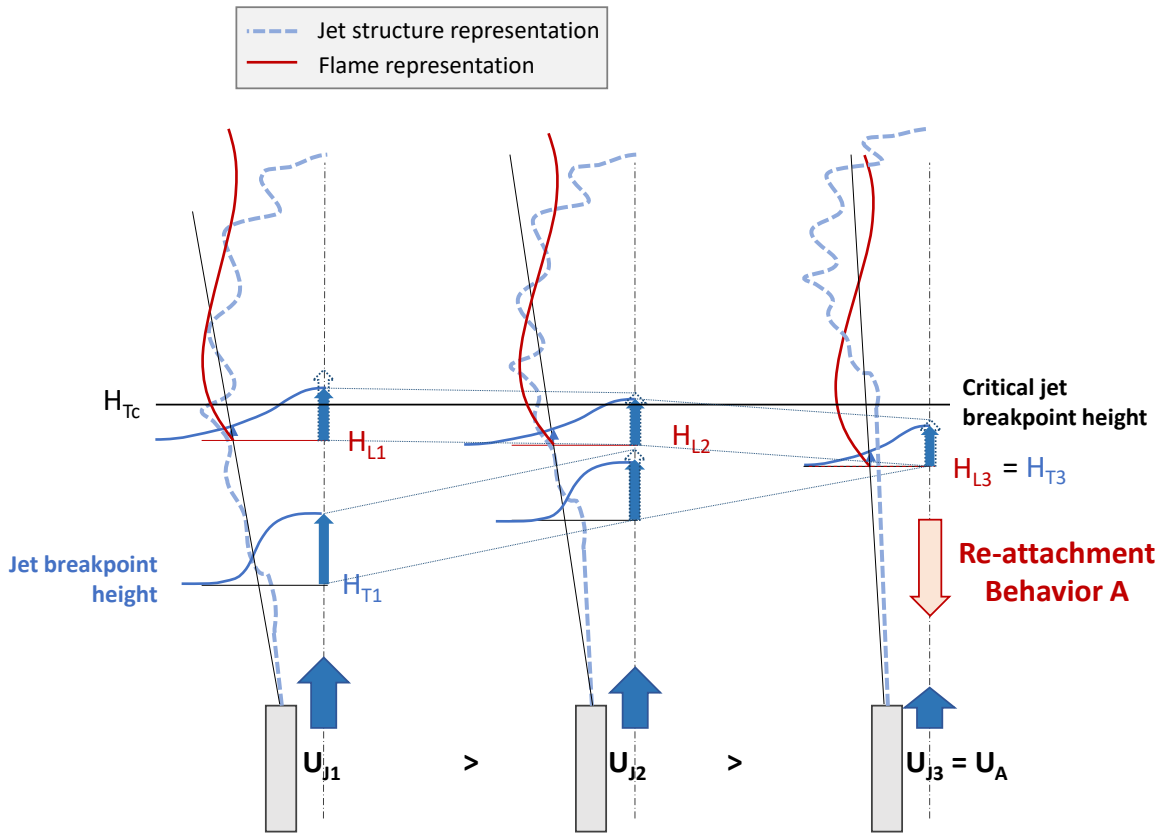


Fig. 4.22. Schematic diagram of the direct re-attachment A ( $H_L < H_{rc}$ ).



- **Comparison of the ammonia/methane case to other studies**

The behavior B, for which  $H_L/D_i$  increases in the hysteresis domain with a decrease in the jet velocity,  $U_J$ , was reported by Lee *et al.* [189] and Nada *et al.* [180] in the case of a propane jet flame diluted with  $N_2$ , as well as Terry and Lyons [200] in an ethylene jet. Similarly to what is observed in Fig. 4.20 in terms of the relationship between  $Re_J$  and  $H_L/D_i$ , in those three studies, as the  $U_J$  decreases,  $H_L$  first decreases, up to a  $Re_J$  between 2000 and 3500, roughly corresponding to the  $Re_{Jc}$  observed in the present study.  $H_L$  then reaches a minimum  $H_{Lmin}$  at  $U_J = U_{Jc}$  and finally increases as reported previously in the present work in Fig. 4.19 and Fig. 4.20. The values for  $H_{Lmin}/D_i$ , the air coflow velocity  $U_{co}$ , normalized by the jet velocity  $U_{Jc}$ ,  $U_{co}/U_{Jc}$ , and the  $Re_{Jc}$  observed in those studies are gathered in Table 4.4 and compared to the one obtained in the present study.

Table 4.4. Observations on lifted flame evolution within the hysteresis region.

	<b>Lee-Chung 1994 [189]</b>	<b>Nada 2014 [180]</b>	<b>Terry and Lyons 2006 [200]</b>	<b>Present study</b>
Jet composition	C <sub>3</sub> H <sub>8</sub> 62% / N <sub>2</sub> 38%	C <sub>3</sub> H <sub>8</sub> 60% / N <sub>2</sub> 40%	Ethylene	CH <sub>4</sub> /NH <sub>3</sub>
$Re_c$	3500	2200	3600	2000
$U_{co}/U_{Jc}$	0	0.025	0.213	0.004-0.033
$H_{Lmin}/D_i$	14	10	10	12-15

Comparing the results on propane flames diluted with nitrogen for different  $U_{co}$  by Lee *et al.* [189] and Nada *et al.* [180], it can be observed that  $H_{Lmin}/D_i$  decreases as the ratio  $U_{co}/U_{Jc}$  increases, similarly to the present study as seen in Fig. 4.20, following the trend on  $H_{Tc}$  shown in Fig. 4.18. Overall, comparing all the studies,  $H_{Lmin}/D_i$  tends to decrease with larger  $U_{co}/U_{Jc}$ . Behavior B is thus expected to appear independently of the fuel used, providing that for a given mixture,  $U_{co}$  is high enough to get  $H_L > H_{Tc}$  in the laminar-to-turbulent transition of the jet.

The addition of ammonia in a methane jet thus revealed the effect of mixing/dilution and aerodynamics coupling on the flame re-attachment. In the hysteresis region, when getting closer to the jet laminar to turbulent transition, two re-attachment behaviors could be distinguished: the common behavior A, with a lifted flame height decrease with the jet velocity decrease, or the behavior B, with an increase of the lifted flame height as represented in Fig. 4.23 and Fig. 4.22. The transition between behaviors A and B, observed under the combined effect of ammonia addition and air coflow velocity in

the present study, depends on the lifted flame position,  $H_L$ , and the structure of the jet, and more particularly the critical height,  $H_{Tc}$ , corresponding to a change in the turbulence generation, at the jet Reynolds number  $Re_{Jc}$ . This phenomenon can be observed for other fuels, providing that the burning velocity of the fuel mixture is sufficiently low, leading to a higher lifted flame position, or that the air coflow velocity is sufficiently high, leading to both higher lifted flame position and lower  $H_{Tc}$ .

### 3. Evolution of the stabilization process of the attached flame

#### 3.1. The case of methane jet flame

To better understand the flame stabilization process and the transition to lift, a study of the attached flame position, but also its thermal interaction with the burner was performed from a jet velocity of 0.05 m/s and up to the liftoff, corresponding to jet velocity between 6 m/s and 16 m/s depending on  $E$ . The air coflow velocity was kept at 0.2 m/s. The flame tip position was observed by the mean of CH\* chemiluminescence which has long been used as a marker of the reacting zone in hydrocarbons flames [201]. The radius and height of the flame tip position, respectively  $R_a$  and  $H_a$ , were obtained from the chemiluminescence images after Abel deconvolution using Matlab as presented in Fig. 4.24. The post-processing was adapted to the present configuration. Greater details on the post-processing strategy are available in Appendix 4A.

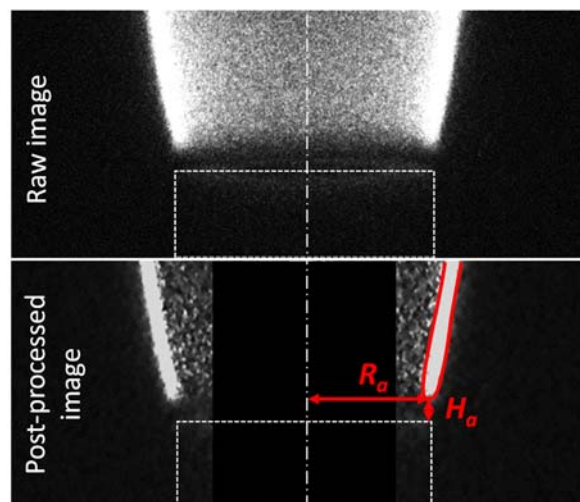


Fig. 4.24. Definition of  $H_a$  and  $R_a$  from CH\* chemiluminescence image. Original image on the left,

deconvoluted one on the right. The red contour represents the threshold value for detection.

Burner temperature measurements were performed using K-thermocouples inserted in the burner lip, as introduced in Section 1.4 and illustrated in Fig. 4.6. One thermocouple is positioned such as the hot junction is on the burner surface facing the flame tip. The temperature obtained using this thermocouple is called as burner lip temperature. A second thermocouple is introduced inside the burner lip, 6 mm under the first one and is used for heat flux calculation as described in Section 1.4. Finally, an R-thermocouple (Pt-PtRh13, 50  $\mu\text{m}$ , uncoated) was used for temperature mapping around the burner lip. Further description for the R-thermocouple is available in Appendix 4A. Raw temperature measurements are introduced in the present study, without correction, as the analysis does not rely on the temperature absolute values but rather on their evolution.

Previous studies by Lamige et al. and Min et al. [118,198] on methane flames, under both preheating and dilution conditions, showed that the flame tip position and heat transfer to the burner are highly correlated. Three regimes could be defined when increasing the jet velocity at a fixed air coflow velocity. These regimes are characteristic of this type of burner and are as follows:

- **Regime I:** For small jet velocity ( $MR = \rho_J U_J^2 / \rho_{co} U_{co}^2 < 3 - 7$ , with  $MR$  the momentum ratio of the fuel jet to the air coflow), an increase in the jet velocity leads to the motion of the stoichiometric line toward the oxidant side (expansion of the jet). Following the motion of the stoichiometric line, the flame tip moves out and down up to an extremum position when  $MR$  is around 3 – 7.
- **Regime II:** A larger jet velocity leads to air dragged in the wake of the burner lip, creating a region of mixing. The stoichiometric line tends thus to move back inward again as the mixing becomes poorer due to air recirculation apparition. In this regime, the flame moves thus in the upward-inward direction.
- **Regime III:** When the jet velocity is increased above the jet pipe flow laminar-turbulent transition, the flame motion keeps going inward due to larger air dragged toward the jet, but the height of the flame slightly decreases.

The evolution of these regimes when introducing ammonia inside the jet is detailed in the following Section 3.2, taking this previous work as a reference.

## 3.2. Effect of ammonia addition

### 3.2.1. Flame tip position evolution

The flame tip positions obtained in the present experiment are first represented in Fig. 4.25. Both the flame tip height,  $H_a$ , and the flame tip radius,  $R_a$ , are reported as a function of the jet velocity,  $U_J$ , for 4 fuel mixing configurations,  $E = 0, 0.1, 0.2$  and  $0.3$ . The experimental data from Lamige et al. [119] are included in the methane flame case. The trend observed for methane case is identical to the one observed by Lamige et al. for both  $H_a$  and  $R_a$ , with a minimum (respectively maximum) observed for the same jet velocity  $U_J \approx 0.6$  m/s, corresponding to a  $Re_J \approx 150$ . The gap between the value of  $H_a$  from previous studies and the present one can be explained by the selection of the threshold value for the detection of the flame tip. Due to the smaller signal to noise ratio for the cases with a larger content of ammonia, a higher threshold value was selected in the present experiment and conserved identical for the different mixtures investigated to allow for comparison between the different cases. The radius detection is much less sensitive to this threshold value and was less impacted by this change. The standard deviation of the post-processed position in the 300 images for each flame case, representing the flame position fluctuations, is also considered in the present work. It will be represented under the shape of a variation range in the figures. It is worth noticing that those fluctuations increase as  $E$  increases.

The same trends are observed for the different ammonia/methane mixture cases, with first a reduction of  $H_a$ , simultaneously to the rise of  $R_a$ , followed by an increase of  $H_a$  simultaneously to the decrease in  $R_a$ . The same regimes as originated from the observation of the position of the methane flame can be used to describe the present flames with ammonia addition. The maximum (minimum) of  $R_a$  ( $H_a$ ) curves, marking the transition between regime I and II, are still observed, but gradually shift for slightly larger velocities and Reynolds values, between  $U_J = 0.6$  m/s and  $U_J = 1.4$  m/s, corresponding to  $Re_J = 150$  and  $Re_J = 300$ . Moreover, the regimes II and III are gradually limited, as the liftoff occurs for slower jet velocity values. The case  $E = 0.3$  corresponds to a limit case where the attached flame range is limited to the regime I due to the liftoff occurring just after entering the region II.

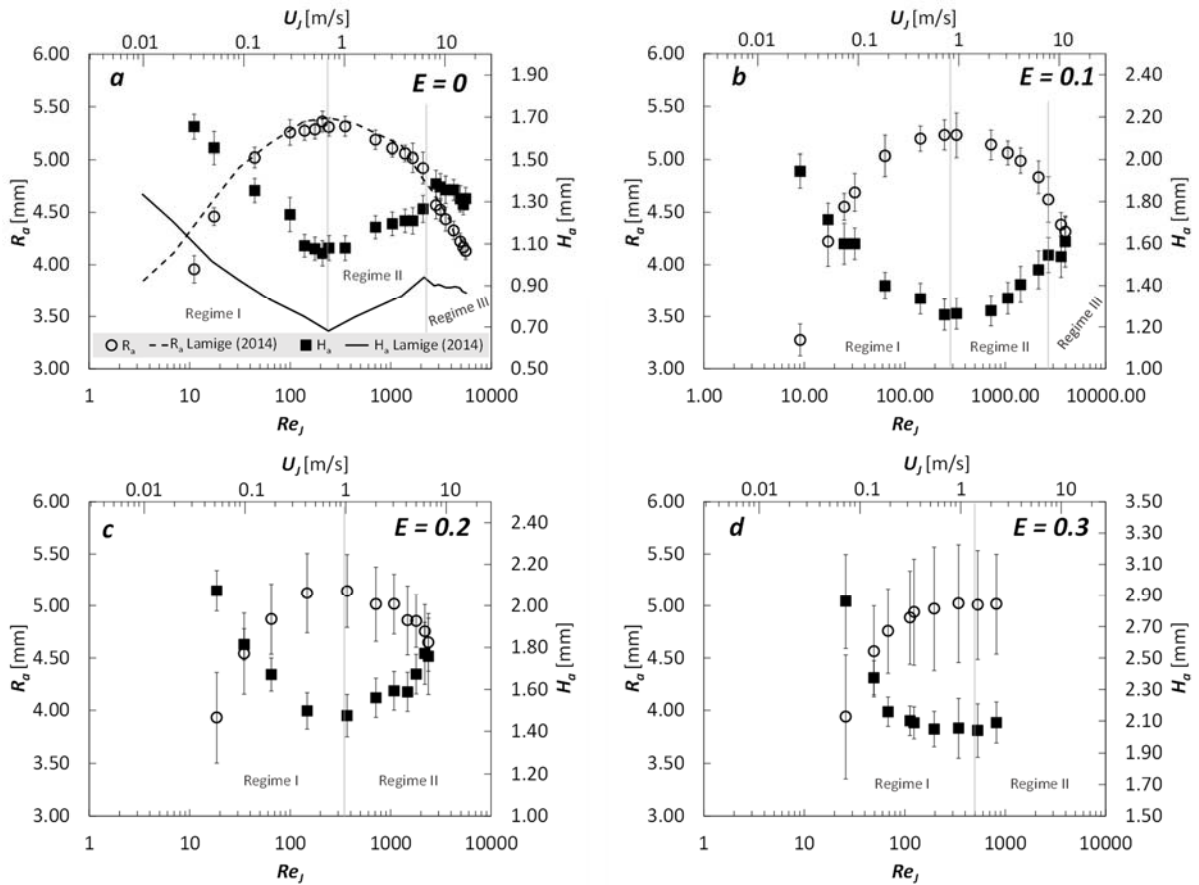


Fig. 4.25. Evolution of  $H_a$  and  $R_a$  with  $Re_j$ : (a)  $E = 0$ ; (b)  $E = 0.1$ ; (c)  $E = 0.2$ ; (d)  $E = 0.3$ .

The evolution of the flame position with ammonia addition is further investigated using Fig. 4.26, where  $R_a$  and  $H_a$  are plotted for each  $E$  as a function of the momentum ratio of the fuel on the air ( $MR$ ), which was shown to characterize well the change between regime I and II in previous work [117]. First, looking at the evolution of  $R_a$  in Fig. 4.26a, it can be observed that when ammonia is added,  $R_a$  is reduced and the flame moves toward the fuel jet. One explanation of this phenomenon is the variation of  $Z_{st}$  when introducing ammonia as presented in Table 4.5. Indeed, when ammonia is added to the mixture the stoichiometric line move toward the fuel side as  $Z_{st}$  is increased. A similar analysis was done for the dilution of the jet with inert gases in a work by Marin and Baillot [197]. In their study, the introduction of inert gases in the fuel jet, leading to a larger value of  $Z_{st}$  relative to the non-diluted case, also led to smaller  $R_a$ , with the motion of the stoichiometric line toward the jet.

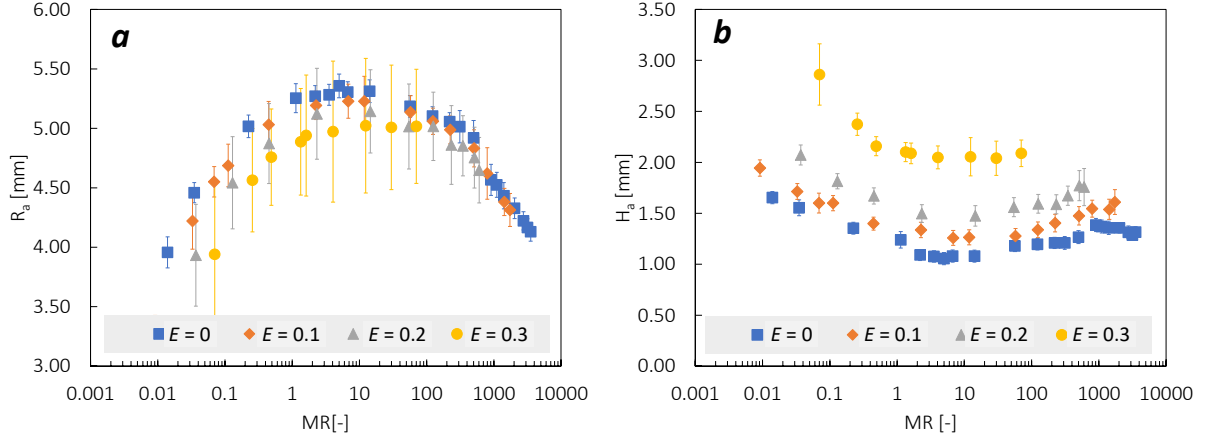


Fig. 4.26. Evolution of flame tip position with the momentum ratio,  $MR$ , and the ammonia mixing ratio,  $E$ : (a)  $R_a$ ; (b)  $H_a$ .

Table 4.5. Evolution of  $Z_{st}$  and  $S_{L0}$  with ammonia mixing ratio,  $E$ .

$E$	$Z_{st}$	$S_{L0}$ [m/s] [101]
0	0.055	0.35
0.1	0.064	0.27
0.2	0.073	0.22
0.3	0.082	0.19

The variation of  $R_a$  remains small, especially when compared to the one of  $H_a$  in Fig. 4.26b. Indeed, from Fig. 4.26b, a large increase in the flame tip height,  $H_a$ , is noticeable with an increase in ammonia. As expected, as  $S_{L0}$  decreases, the flame stabilizes upper above the burner lip in a region of lower local velocity. The change in the laminar burning velocity due to the change in the chemistry is however not the only parameter which explains this increase in  $H_a$ .

The variations of  $R_a$  and  $H_a$  relative to their value for methane case at the same jet velocity are plotted in Fig. 4.27 for  $E = 0, 0.1, 0.2$  and  $0.3$ , with  $\Delta R_a/\delta = (R_a - R_{aCH_4})/\delta$  and  $\Delta H_a/\delta = (H_a - H_{aCH_4})/\delta$ , and  $\delta$  the burner lip thickness. All the positions taken by the flames for the jet velocity range between  $U_J = 0.05$  m/s to  $U_{LO}$ , the liftoff velocity, are represented by a symbol of the same color for the same  $E$  value. As observed in Fig. 4.27, the change in the flame tip position is not constant throughout the range of jet velocity investigated, with slightly different  $\Delta R_a/\delta$  and  $\Delta H_a/\delta$  dependences on the jet aerodynamics

depending on  $E$ . Moreover, in addition to the variation in the flame velocity associated with variation of  $E$ , the variation of  $Z_{st}$  toward the jet, might also be a major contributing factor to the increase of  $H_a$ . Indeed, for a defined jet velocity and an identical flame velocity, a  $Z_{st}$  line closer to the jet will lead to the higher flame tip position for balancing the local flow velocity on this stoichiometric line.

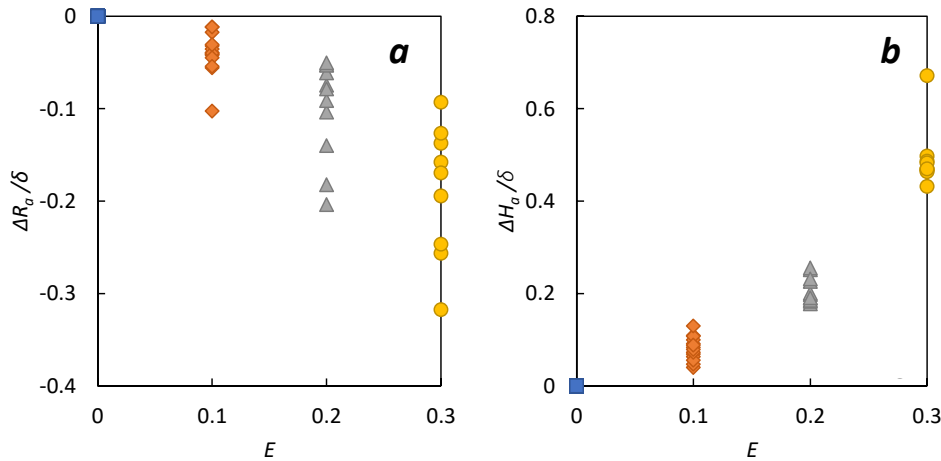


Fig. 4.27. Variation of  $R_a$  and  $H_a$  relatively to methane flame case with ammonia mixing ratio,  $E$ .

Finally, as previously seen in Fig. 4.25, the value of the maximum  $R_a$  appears for a gradually larger value of  $MR$ , above the range 3 – 7 observed in previous studies. The minimum of  $H_a$  shifts similarly as ammonia content is increased in the jet. One hypothesis to explain this phenomenon is that, due to the higher position of the flame (corresponding essentially to the lower laminar burning velocity and the  $Z_{st}$  change), the air dragged toward the jet, should be larger to modify the local concentration at the flame tip position which is higher. A slightly higher jet momentum would thus be necessary for explaining the shift. This hypothesis is further described in Fig. 4.28.

Figure 4.28 presents two cases of attached flames  $a$  and  $b$  for increasing jet velocity  $U_{J1} < U_{J2} < U_{J3}$ . Flame tip position trajectory is represented in red, and a circle represents the flame position at the jet velocity considered ( $U_{J1}$ ,  $U_{J2}$  and  $U_{J3}$ ).  $a$  is the reference case, without mixing for which  $E = 0$ .  $b$  is the case where ammonia is introduced into the jet and  $E > 0$ . The flame of the reference case  $a$  is also reported in lighter red color in  $b$ , and the corresponding stoichiometric line in dashed line, to ease the comparison. In the reference case  $a$ , when  $U_J$  is increased ( $U_J < U_{J2}$ ), flame approach its extremum position as the stoichiometric line moves with the jet expansion. This corresponds to the end of regime I. From  $U_J = U_{J2}$ , air starts to be dragged in the wake of the lip, leading the stoichiometric line and the flame to move back toward the jet when  $U_J > U_{J2}$ . When the jet is diluted, or when ammonia is

introduced,  $Z_{st,d}$ , the diluted case stoichiometric mixture fraction is larger than the one of the non-diluted case,  $Z_{st}$ , and thus stoichiometric line  $Z_{st,d}$  is closer to the jet center as presented in Fig. 4.28b. When the jet velocity is increased from  $U_{J1}$  to  $U_{J2}$ , the flame moves in the outward direction. However, at  $U_J = U_{J2}$ , the air dragged, represented by the circle and arrow, is still too small to affect the position of  $Z_{st,d}$ , and regime II is not yet reached. Regime II will only be observed when the air is dragged in sufficient amount to change the position of  $Z_{st,d}$  at the higher flame tip height. Thus, regime II will be observed at  $U_{J3} > U_{J2}$  the velocity limit corresponding to the beginning of regime II for pure methane case.

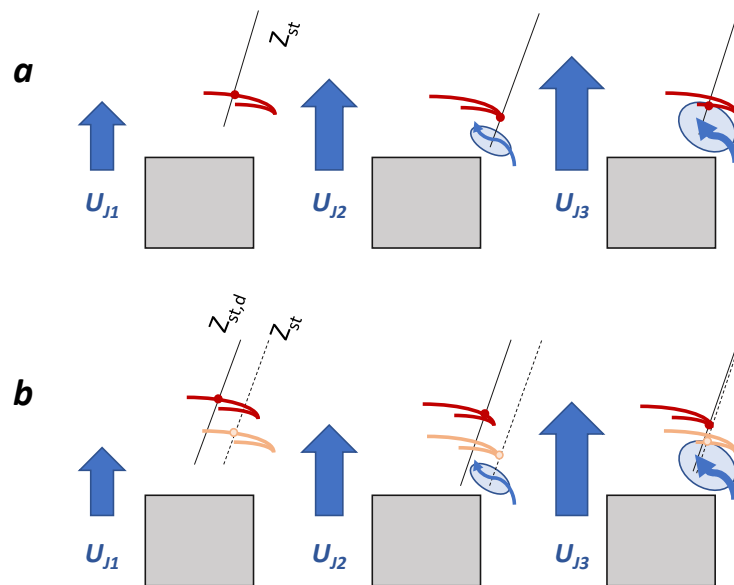


Fig. 4.28. Schematic diagram of the change in flame positioning explaining the shift observed in the flame extremum position.

To confront this hypothesis, the modification of the velocity flow field in the wake of the burner lip due to the change in the flame with  $E$  variations should be further investigated, either through velocity measurement or numerical simulation. Such measurements were not performed in the present experiment but would represent an interesting perspective to the present study.

The position of the flame just before liftoff is of particular interest to understand why the change in the stabilization regime appears. For that purpose, the evolution of this particular position with ammonia addition is summarized in Fig. 4.29. As can be seen in Fig. 4.29, the position of the attached flame just before the lift is moving downstream and toward the oxidizer region. Indeed, the flame stabilizes in a region where the local velocity is small enough and within the flammable range of stoichiometry contours. Then, due to the lower flame velocity when ammonia is introduced, flame tends to stabilize

higher above the burner. Moreover, due to the lower local flame speed, the balance with the local velocity will be broken (and liftoff will occur) for a lower jet velocity. The lower jet velocity also means less air dragged in the wake of the burner lip, and thus larger  $R_a$ .

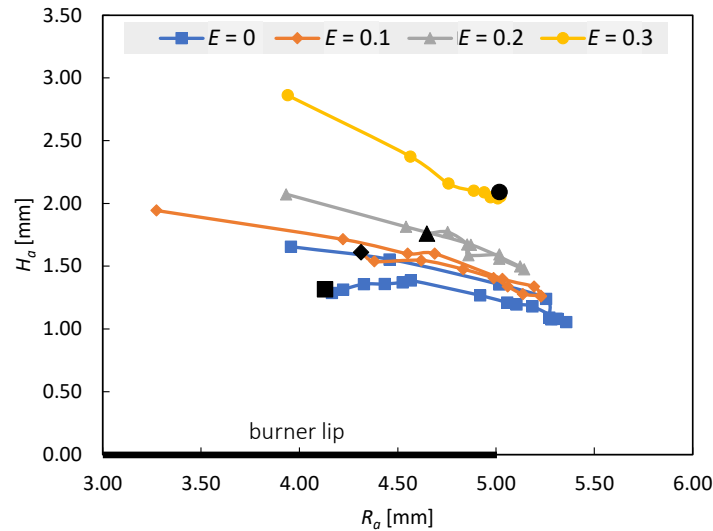


Fig. 4.29. Evolution of flame position ( $R_a$ ,  $H_a$ ) for jet velocity up to lift and  $E = 0$  (squares),  $E = 0.1$  (diamonds),  $E = 0.2$  (triangles),  $E = 0.3$  (circles). The positions just before liftoff are colored in black.

To conclude this section, the chemical and aerodynamics coupling could be examined looking at the evolution of the position of the flame tip with ammonia addition.

- $R_a$  is decreased as ammonia is added. This variation could be related to the change in stoichiometric mixture fraction  $Z_{st}$ . As  $Z_{st}$  becomes larger, the stoichiometric line becomes closer to the jet centerline.
- $H_a$  was shown to increase under the combined effects of flame speed decrease which is associated with the lower reactivity of ammonia/methane mixture as  $E$  increased, and the change in the position of the stoichiometric line.
- The regimes I, II and III are still observed with ammonia addition, however, a shift in terms of Reynolds number,  $Re_J$ , was observed for the transition between regimes I and II. This shift could be related to the higher position of the flame tip with ammonia addition.

- The evolution of the position of the flame prior to liftoff corresponds to the same effects and the gradually lower liftoff velocity.

Those explanations, however, remain limited to the chemical-aerodynamics coupling and do not take into account the thermal exchange of the flame with the burner on which it is attached. This will be developed in the following section.

### 3.2.2. Thermal interaction with the burner

The attached flame is in close relation with the burner lip. If it could be already seen that the recirculation appearing in the wake of the burner lip has some major effects on the flame stabilization process by playing on the aerodynamics of the fuel jet, the thermal interaction of the flame with the burner should be also carefully investigated. For that purpose, the temperature at the burner lip,  $T_{lip}$ , and the conductive heat flux to the burner,  $Q$ , were taken simultaneously to the flame tip position measurements using K-type thermocouples inserted in the burner lip as detailed in Section 1.4.4. Moreover, a complementary temperature mapping of the flame was taken using an R-type thermocouple.

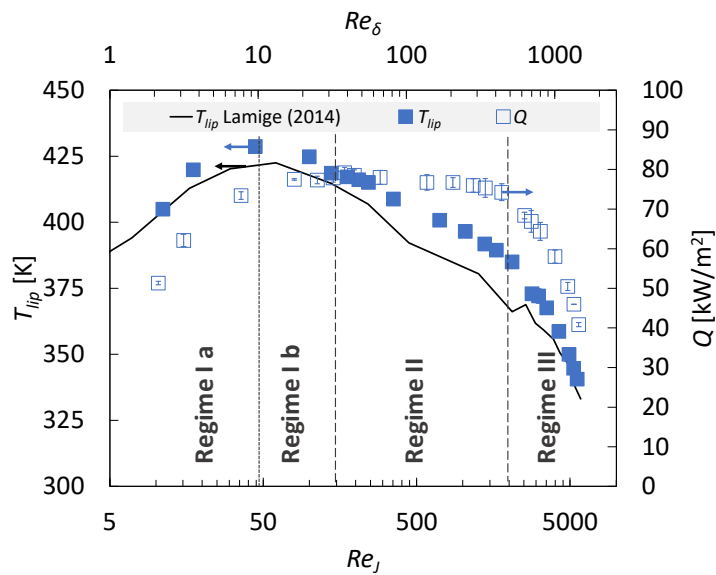


Fig. 4.30. Burner lip temperature,  $T_{lip}$ , and conductive heat flux to the burner,  $Q$ , for methane flame. Plain line represents  $T_{lip}$  results from Lamige work [117], plain squares represent  $T_{lip}$  in the present study and empty squares represent  $Q$  in the present study.

The results for the temperature at the burner lip and the conductive heat flux to the burner are presented in Fig. 4.30 for methane jet flames, with results from a previous study by Lamige et al. [117].

The trend observed in the present experiment is similar to that observed in previous studies. The burner lip temperature increases up to a maximum when the jet velocity is increased before decreasing as the jet velocity keeps rising. This maximum is related to the transition from heat transfer dominated by conduction in the extremely low-velocity case (under  $Re_\delta$  of 10 – 15) to convective transfer as the velocity is increased in the tube and air vortices appear in the wake of the lip, subdividing regime I in Ia and Ib. This transition is also noticeable from the conductive heat flux results which increase in regime Ia, stabilizes in region Ib before starting to decrease in regime II. For larger velocity and as the jet becomes turbulent, the temperature decrease becomes more important as it can be denoted when entering in the region corresponding to the regime III as previously defined. As already observed in the previous section, ammonia addition modifies the flame tip position. Moreover, due to those changes, a shift in terms of Reynolds number was observed for the transition between regimes I and II. Flame tip position is a critical parameter to understand thermal exchanges with the burner, thus ammonia addition is expected to modify them and was further examined.

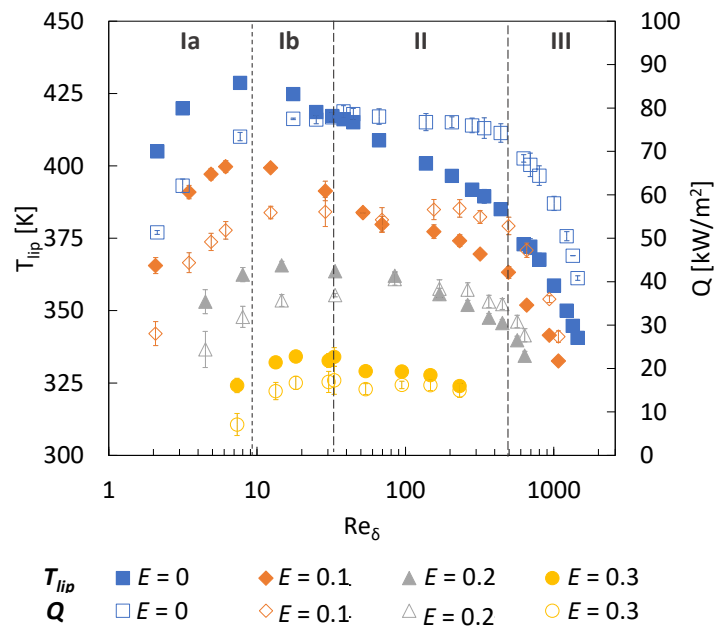


Fig. 4.31. Evolution of  $T_{lip}$  (plain symbol) and  $Q$  (empty symbol) with  $Re_\delta$  for  $E = 0$  (squares),  $E = 0.1$  (diamonds),  $E = 0.2$  (triangles) and  $E = 0.3$  circles. Regimes Ia and b, II and III obtained for methane flames are represented with dashed lines.

The effect of gradual ammonia addition on the thermal interactions with the burner is presented in Fig. 4.31, which represents both burner lip temperature,  $T_{lip}$ , variations and conductive heat flux,  $Q$ , variations for increasing  $Re_\delta$ . Variations similar to the ones in the methane case can be observed, and the distinction between regimes Ia and Ib is conserved. The transitions between the different regimes are represented by the dashed lines for the methane case in the figure. Considering then the differences with methane jet flame case, first, when ammonia is added into the mixture,  $T_{lip}$  and  $Q$  globally decrease for all the velocity conditions in the three regimes. The second noticeable point is the shift in the transition from regimes Ia to Ib, as seen comparing the curves for ammonia/methane jet flame cases to the transitions dashed line represented for methane case. This is similar to what has been observed in section 3.2.1 for the transition between regimes I and II. This phenomenon is further examined in Fig. 4.32, representing only the evolution of  $T_{lip}$  for simplification. The transition between regimes Ia and Ib is represented by a dashed line, and the shift between  $Re_\delta = 10$  and 30 is clearly noticeable.

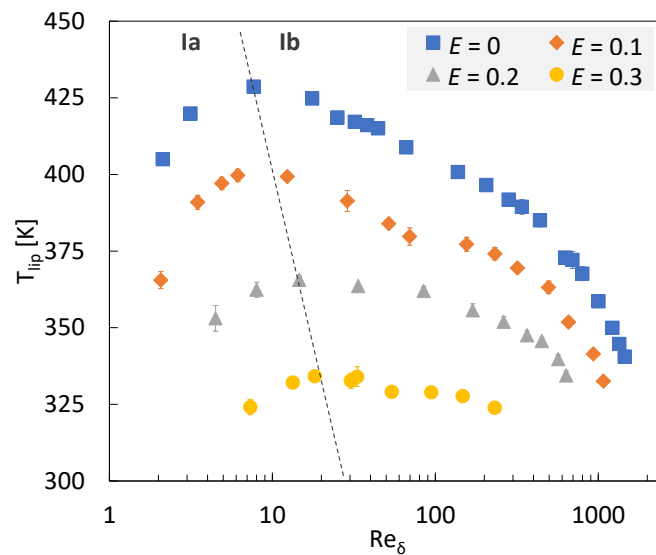


Fig. 4.32. Burner lip temperature,  $T_{lip}$ , with  $Re_\delta$  for  $E = 0$  (squares),  $E = 0.1$  (diamonds),  $E = 0.2$  (triangles),  $E = 0.3$  (circles). The dashed line represents the transition between regimes Ia and Ib.

The temperature of the burner lip is influenced by many parameters, including the flame temperature itself, but also due to the flame tip position, and the dynamic in the wake of the lip. As a first approach to understand the contribution of each of these parameters, the flame temperature is estimated by the adiabatic flame temperature of the corresponding mixture, in stoichiometric condition, and its variation with ammonia addition compared to the maximum temperature of the burner lip in Fig. 4.33. The

decrease in the adiabatic flame temperature is much smaller than the one of the burner lip and it can be expected that this contribution is not predominant.

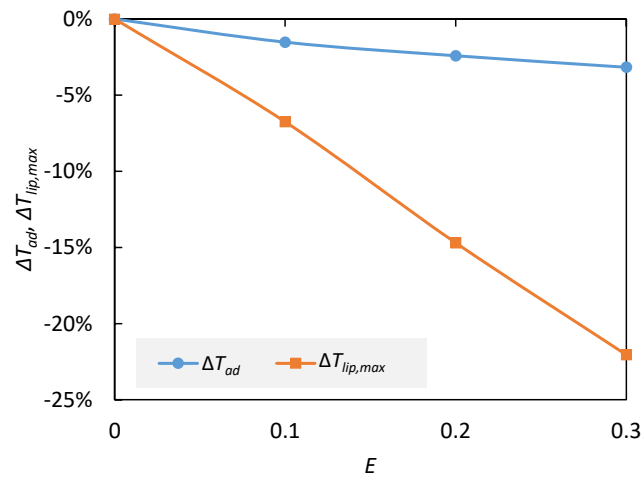


Fig. 4.33. Variation of flame adiabatic temperature and burner lip temperature with  $E$ .

The shift in the transition from regime Ia to Ib is similar to the shift from regime I to II, discussed previously. This shift was related to the change in the flame position due to larger  $E$  and this suggests the importance of the flame position and distance to the burner. The relationship of the distance between the flame tip and the thermocouple at the burner lip,  $d_a = (H_a^2 + (R_a - R_{th})^2)^{1/2}$ , with  $H_a$  and  $R_a$  the flame tip height and radius and  $R_{th}$  the distance of the thermocouple hot junction and the burner axis, with the burner lip temperature is thus examined for the different aerodynamic regimes investigated in this study. The results are proposed in Fig. 4.34. The changes between regimes I, II and III can be observed. In regimes Ia and Ib, the heat transfers are essentially conductive and the relation between the  $d_a$  and  $T_{lip}$  is clear, as expected. In regimes II and III, aerodynamically dominated, and for which convective heat transfer is dominant, the relation is more complex. In those regimes, large variations of the burner lip temperature,  $T_{lip}$ , can be observed for a small variation of  $d_a$  for each ammonia mixing ratio,  $E$ . However, a clear trend between  $T_{lip}$  and  $d_a$  cannot be seen.

The evolution of the burner lip temperature and the distance between the flame tip and the thermocouple is represented in Fig. 4.35 for increasing  $Re_j$ . From Fig. 4.35, it can be understood that the maximum temperature measured at the burner lip coincides with the minimal distance between the flame tip and the burner. The minimum distance between the flame tip and the burner is gradually shifting toward higher jet velocity, under the combined effect of chemistry and aerodynamics as

explained in section 3.2.1, which in turn affects the temperature response of the burner and leads to the shift observed.

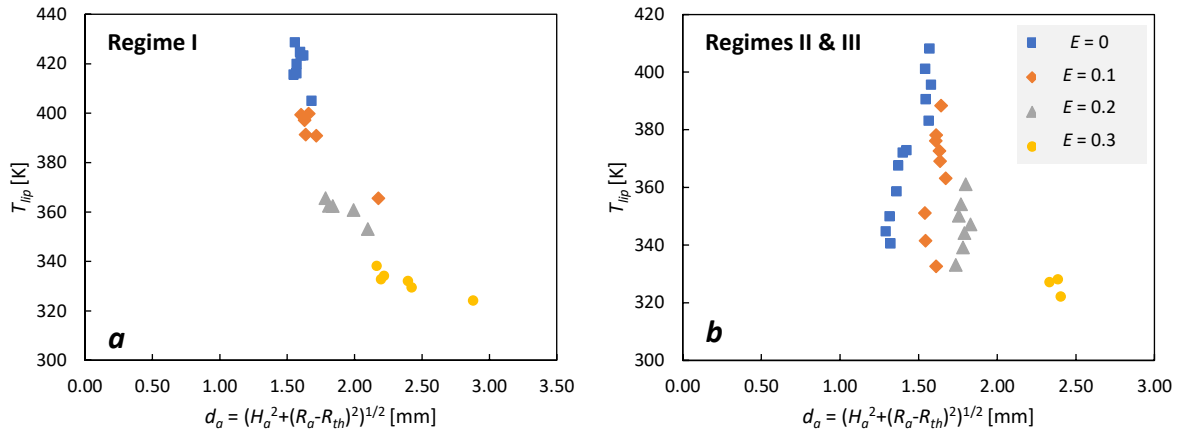


Fig. 4.34. The relative importance of  $d_a$  on  $T_{lip}$  depending on the aerodynamic regime: (a) regime I; (b) regimes II and III for  $E = 0$  (blue squares),  $E = 0.1$  (orange diamonds),  $E = 0.2$  (grey triangles) and  $E = 0.3$  (yellow circles).

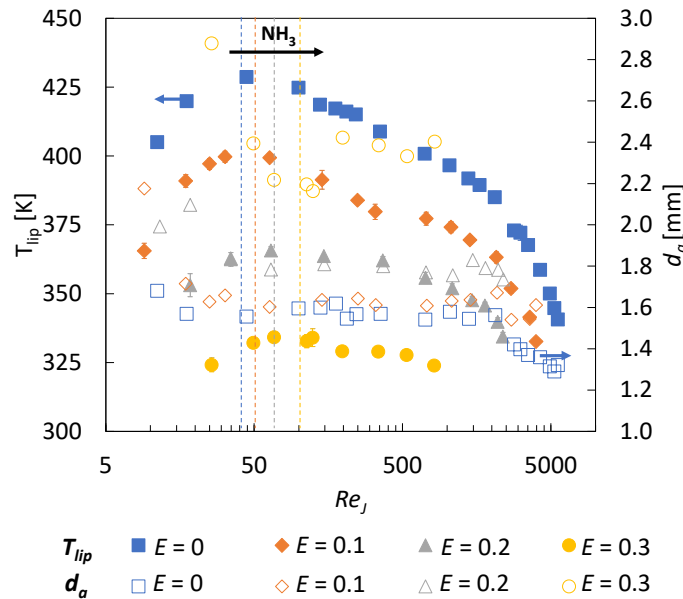


Fig. 4.35. Variation of  $T_{lip}$  (full symbol) and  $d_a$  (empty symbol) with  $Re_j$ : blue squares,  $E = 0$ ; orange diamonds,  $E = 0.1$ ; grey triangles,  $E = 0.2$ ; yellow circles,  $E = 0.3$ .

To go further in this analysis, the temperature mapping of the flame under various jet velocity conditions and fuel mixing ratio,  $E$ , was performed between a height above the burner lip,  $z$ , of 2 and 8

mm. The cases of fuel jet velocity of 0.05, 0.30, 2 and 7 m/s were investigated for  $E = 0, 0.1, 0.2$  and 0.3, corresponding to velocity in regimes Ia, Ib, II and III. The evolution of the flame temperature with the increase in ammonia mixing ratio as well as flame position can be thus clearly observed. This temperature mapping is introduced in Fig. 4.36. To ease the comparison for each case, several dashed lines are represented, they correspond to methane case observations, and comparing the temperature contour for each  $E$  with those dashed lines allows us to see the flame evolution. The red dashed line corresponds to the maximum temperature position at  $z = 2$  mm above the burner and can be used to track the radial evolution of the flame position. The blue dashed line representing the 25% contour at  $z = 2$  and 8 mm for  $E = 0$  and can be employed, for seeing the evolution of the temperature gradient in the flame when the jet velocity is increased.

The evolution of the flame position follows the observations of  $\text{CH}^*$  chemiluminescence in the different aerodynamic regimes (I, II and III) observed previously. For all the mixture observed, when the jet velocity is increased, the flames contour moves first toward the air side (regime I) before coming back toward the jet side (regime II and III). Moreover, the temperature gradient on the fuel side is increased (dashed blue lines getting closer), whereas the temperature gradient on the air side remains barely affected. This is consistent with the higher strain in this region as well as the greater heat convective heat transfer due to the larger jet velocities.

Then, looking now at the evolution of the flame with ammonia addition for the same jet velocity fuel  $U_j$ , it can be observed by comparison of the red dashed line and the normalized temperature contour that the flame is going toward the jet when adding ammonia. This shift toward the jet is also visible on the air side of the jet, looking at the difference between the lower temperature contour (25%) and the blue dashed lines. On the fuel side, however, the trend is reversed. The flame becomes narrower when  $E$  is increased. This trend corresponds to the higher attachment height,  $H_a$ , with ammonia addition. Indeed, at the same height  $z$ , when  $E$  is increased, the distance  $H_a - z$  gets smaller and the flame thus gets thinner being closer to  $H_a$  and the flame tip.

It could thus be understood that thermal interactions with the burner were modified by the introduction of ammonia in the jet. Those changes are principally triggered by the variations of the flame tip position with ammonia addition. The evolution of the aero-thermo-chemical coupling in presence could thus be clarified.

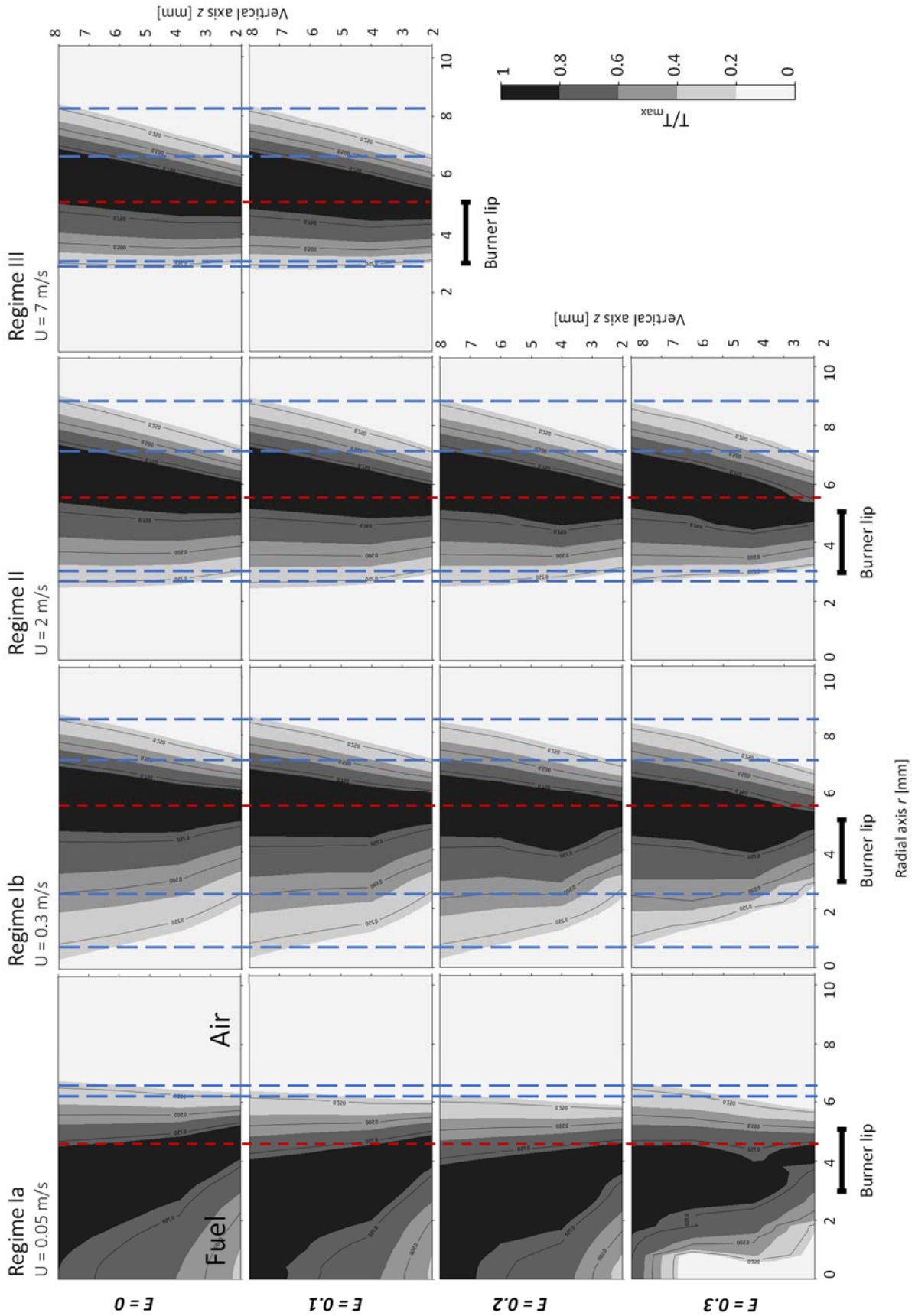


Fig. 4.36. Normalized temperature contours in the 4 different regimes. The red dashed line represents the maximum temperature position for  $z = 2$  mm and  $E = 0$ , the blue dashed line represents the edges of the contour at 25% for  $z = 2$  and 8 mm and  $E = 0$ .

## 4. Conclusions

Ammonia/methane non-premixed jet flames surrounded by an air coflow were investigated in this chapter. The evolution of the stabilization domain, particularly the liftoff and re-attachment limits, were obtained experimentally under the coupled effect of the ammonia addition in the fuel jet and the increasing air coflow velocity. The local evolution of an attached flame up to the liftoff limit was then further investigated. The attached flame position, temperature profiles and burner temperature evolution were studied to understand how the ammonia addition affects the aero-thermo-chemical mechanisms responsible for flame stabilization. The main results in this chapter are summarized in the following.

The coupled effect of ammonia addition and air coflow velocity variations on the stabilization of a non-premixed methane jet flame, developed in Section 2, led to the following conclusions:

- The stabilization domain was reduced by the addition of ammonia to the methane jet. The flame could not be stabilized for ammonia mixing ratios,  $E$ , above 0.3, value at which the jet liftoff velocity and re-attachment velocity became sensibly equal. More specifically, the introduction of ammonia in the methane jet leads to a particularly large decrease of the liftoff velocity, especially when compared to the dilution with inert gas in previous studies. This decrease is associated with the change in local flame properties due to the change in the mixture reactivity and the kinetics at stake.
- The stabilization regimes were shown to be highly dependent on the air coflow velocity, as a sudden drop of the re-attachment limit was observed when the air coflow velocity is increased. This re-attachment drop (RD) could be associated with the transition between two lifted flame behaviors in the hysteresis domain: the behavior A with decreasing lifted flame height, and the behavior B, with increasing lifted flame height.
- The transition between the two lifted flame behaviors and the RD is characterized by the critical jet breakpoint height,  $H_{Tc}$ . This height is associated with the jet aerodynamic structure and corresponds to a change in the turbulence generation within the laminar-turbulent transition. At low jet Reynolds numbers, turbulence is generated from laminar instabilities. For larger jet Reynolds numbers, turbulence is controlled by the laminar-to-turbulent transition in the pipe flow. If the lifted flame

stabilizes under  $H_{Tc}$ , it will follow behavior A, whereas if above this height, it will follow behavior B and move downstream before re-attachment.

- This phenomenon, also observed for other fuels in the literature, is due to the coupled effects of ammonia addition and larger air coflow velocity leading to both a higher liftoff height and a smaller critical jet breakpoint height. Ammonia addition leading to a decrease in the burning velocity, and thus, a major increase of the liftoff height, the consideration of this critical jet breakpoint height and its dependence on the air coflow velocity is expected to be of primary importance in the design of practical jet flame applications for ammonia blends use.

The study of the effects of ammonia addition on the local evolution of the attached flame and its interactions with the burner was developed in Section 3 and led to the following conclusions:

- The stabilization regimes of the attached flame up to liftoff corresponding to the attached flame position evolution, called in this work regimes I, II and III, as introduced by Lamige [117], were also observed for ammonia/methane non-premixed jet flame. They were nonetheless reduced, in terms of jet Reynolds number, due to the reduced stabilization domain.
- When compared to the methane non-premixed jet flame, it could be observed that the flame position moves toward the jet and downstream as ammonia is added. This phenomenon can be understood as the effect of the increase in stoichiometric fraction,  $Z_{st}$ , leading the flame toward the fuel side, where mixing is more favorable to its propagation; and the reduction of the local flame speed due to ammonia introduction, leading the flame to stabilize further downstream where the local velocity is lower.
- The transition from regimes I to II was shown to be slightly shifted, in terms of Reynolds number, as ammonia is introduced into the mixture. Indeed, as ammonia is introduced into the mixture, these transitions gradually appear for slightly higher Reynolds numbers. This phenomenon could be understood looking at the phenomenon occurring simultaneously with ammonia addition in the wake of the burner lip. The reduction of the local flame speed led to higher flame and thus higher fuel jet velocities are necessary to drag sufficient air in the wake of the burner lip and cause a change in the position of the stoichiometric line  $Z_{st}$  which is characteristic of the transition from regime I to II.

- The thermal interactions with the burner were shown to follow the same dynamics as defined by Lamige [117], but the temperature at the burner decreased drastically as ammonia was introduced in the fuel jet, under the combined effect of flame temperature decrease and higher attachment height. Moreover, similarly to the transition between regimes I and II, the transition between regimes Ia and Ib was observed for slightly larger jet Reynolds numbers. This could be associated with the evolution of the flame position with ammonia addition, moving toward the fuel jet and downstream.

As a perspective of this work, a more detailed investigation of the re-attachment behavior B, with an increase of the flame height with a decrease in the jet velocity within the hysteresis region could be considered. Simultaneous PIV and OH-PLIF measurement could be considered and would give a better insight of the changes occurring in terms of local velocity and turbulence at the flame leading edge, but are practically challenging, as the introduction of particles might greatly affect the present phenomenon. Numerical simulation of the present configuration might also be considered for that purpose. The proper modeling of the jet laminar-to-turbulent transition might however be challenging, and thus a careful comparison with the present experimental conditions should be considered.

Improvement of the study on the attached flame could be performed by considering the simultaneous measurement of the flame position and local velocity flow field, preferably PLIF and PIV. Those would allow us to go further in the analysis of the liftoff limit, particularly looking at the local strain at the attached flame position and comparing it to the results obtained in Chapter 3 of this work.

## 4A. Attached flame tip position measurements

The relative variations of the attached flame tip position up to liftoff was performed using CH\* chemiluminescence images. The CH\* chemiluminescence signal was collected using an intensified camera with a high-speed shutter (PI-MAX 2), mounted with a UV-vis lens (Hamamatsu UV lens A4869, 50mm, 3.5) and band-pass filter centered on 431 nm, with a FWHM of 5 nm. Acquisition parameters are recalled in Table 4A. 1.

Table 4A. 1. Acquisition parameters.

Camera	PI-MAX 2
ROI [pixel <sup>2</sup> ]	1024 x 1024
Exposure time [ms]	7
Gain	120
Resolution [mm/pixel]	0.042
Focal [mm]	50
Aperture	3.5
Frequency Hz	3.6
Image numbers	300

Scale and background image are taken prior to experiment in the same configuration and used in the images post-processing. The post-processing consists in the following steps:

- 1) Scaling and rotation based on the target image.
- 2) Burner position is confirmed in presence of the flame (dilatation).
- 3) Abel deconvolution is applied.
- 4) Optional filtering is applied.
- 5) High intensity region in the axis due to Abel deconvolution is masked.
- 6) Pixel value is normalized by the maximum value obtained in the image.
- 7) Attached flame tip height,  $H_a$ , is obtained by scanning the image pixel row by pixel row from the tube position. The values. If the pixel values exceed the defined intensity threshold (45% in the present study) for a minimum of 5 pixels in the row, the pixel row is defined as the row for flame tip height and  $H_a$  is calculated.
- 8) The flame tip diameter,  $D_a$ , is then obtained by scanning in this row from the axis toward the flame on each side. Flame position is then detected for a defined threshold value (40% in the present study).

This process is performed for each of the 300 images of each flame and histograms obtained for both  $H_a$  and  $D_a$ . Peak of the histogram and standard deviation are later used for the analysis. Steps 7 and 8 are represented in Fig. 4A.1.

Threshold value of 45% and 40% were selected as they enabled good determination of the flame position, even in the largest ammonia content in the fuel mixture, with lower signal intensity and smallest signal-to-noise ratio. The criteria of 5 pixel on one line was also selected based on practical consideration, particularly to avoid that a single high value pixel appearing in a row due to some noise is not considered as the flame tip.

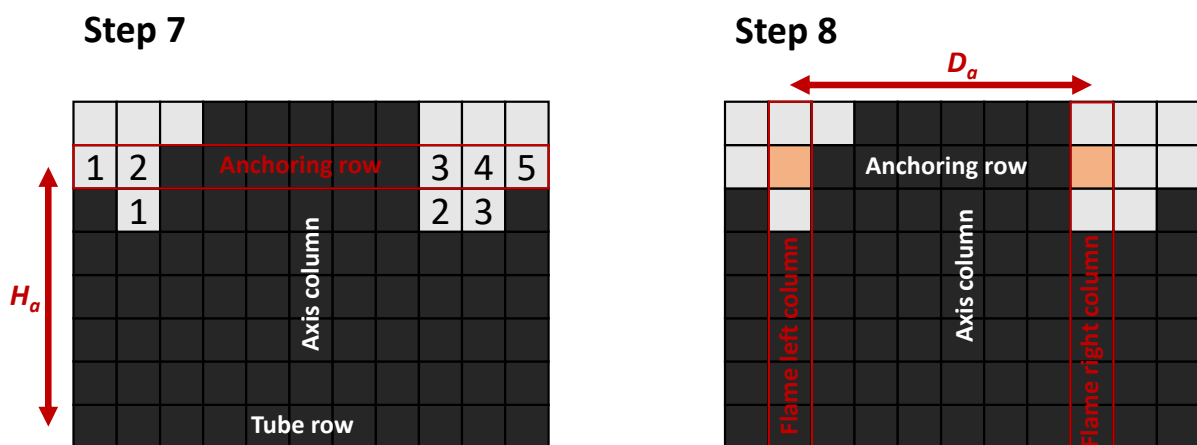


Fig. 4A.1. Representation of steps 7 and 8. Dark squares represent pixel values under 45% threshold for Step 7, 40% threshold for Step 8.

## 4B. Temperature mapping

Temperature mapping was performed for the attached flame using an R-thermocouple (Pt-Pt/Rh13%), with branches of 50  $\mu\text{m}$ . The thermocouple branches were inserted in a ceramic sleeve of 0.8 mm of diameter, for insulation and mechanical support.

The ending of the two branches and the hot junction of the thermocouple are 2 mm out of the sleeve, limiting the aerodynamic disturbances when entering the flame, similarly to what can be observed in region 1, circle in red in Fig. 4B.1. The disturbance introduced by the thermocouple sleeve can be seen in the region 2 in the same figure. Those 2 mm thus guarantee that the measurement at the hot junction is not disturbed by the sleeve.

Thermocouple positioning was managed with an automated motorized positioning system (OWIS). The thermocouple was connected to a temperature recording system (Graphtec GL900) at 10Hz. Synchronization of the positioning and recording system was performed using a LabVIEW program and an NI interface module. 50 values were taken for each position and a delay of few seconds between the end of each new motion of the positioning system and the new acquisition was set to record only when steady condition is reached.

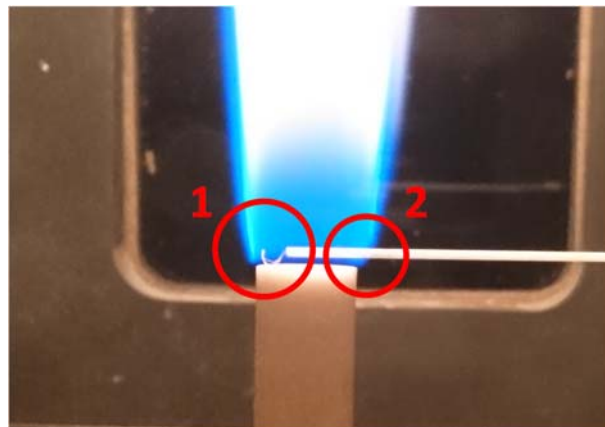


Fig. 4B.1. Photo of a complete flame crossing.

In order to check that there is no deviation of the thermocouple due to the migration of rhodium in the hot junction after several high temperature cycles, as well as no reaction of the thermocouple branches with ammonia addition in the jet, the first flame crossing done for a methane flame case was repeated after each mapping case. No deviation was observed.

Direct measurements without any correction for radiative or conductive effects on the measured temperature were considered. However, the exact temperature value is not of interest in this study. Indeed, only temperature evolution or normalized temperature mapping are considered in this study, and thus, those effects can be reasonably neglected for the present analysis.

# Chapter 5

## Conclusion

In the context of global warming, the use of ammonia as an alternative carbon-free fuel for industrial combustion systems shows promising features. However, the use of ammonia remains challenging due to two main issues: flame stabilization and NO<sub>x</sub> emissions. Several strategies can be considered to improve the flame stabilization, including the use of fuel mixing with hydrocarbons. In the present work, ammonia/methane blended fuels were considered, as this solution can be applied in an immediately effective strategy for CO<sub>2</sub> mitigation in existing facilities using natural gases.

The objective of this thesis is the investigation of fundamental flame characteristics and combustion chemistry of those blends to get a better understanding of the effect of ammonia addition on the combustion chemistry, combustion characteristics and flame stabilization. Indeed, each of those three combustion aspects are necessary for getting a unified understanding of those flames, and can be later use for efficient, low emission applications design.

The evolution of the flame chemistry and flame structure with ammonia addition was developed in Chapter 2 of this thesis and was followed by the study of the flame extinction stretch rate and OH and NO profiles in counterflow configurations applicable to chemistry validation. Chapter 3 details the effect of ammonia addition on the stabilization of a non-premixed methane jet flame. The main results of this work are recalled in the following in three sections corresponding to Chapters 2, 3, and 4. Finally, the last section is devoted to the perspectives of research in future on the basis of this work.

### 1. Ammonia/methane combustion chemistry

Ammonia/methane flame chemistry was investigated and its main characteristics were highlighted, using reaction path, flame structure, heat release, and emission analysis. NO emissions were more particularly studied, and the emission index was used to observe the impact of lower residence time on the flames NO emissions. The role of the radical diffusion on laminar burning velocity and extinction stretch rate was also investigated. The main results are as follows:

- 1.1.** Ammonia/methane flame reaction path remains overall similar to that of the two fuels taken separately and the interactions between those two oxidation paths are minor. These interactions involve indeed NO and N species interacting with the  $\text{CH}_i$  radicals and HCCO and are responsible for the formation of cyanide species HCN and CN and are more pronounced in the ammonia mixing ratio range  $E = 0.1 - 0.3$ . This range also corresponds to a higher production of  $\text{NO}_2$  and  $\text{N}_2\text{O}$ . Unburnt ammonia and NO emissions peaks for a greater value of  $E$ , close to  $E = 0.6$ .
- 1.2.** The NO formation path is dependent on the ammonia mixing ratio. Fuel-NO routes become gradually predominant for larger  $E$  and change the overall chemistry. The impact on the NH consumption is particularly important, changing from N and NO production routes, previously observed in the literature, to  $\text{N}_2\text{O}$  and  $\text{N}_2$  direct reduction and  $\text{N}_2\text{H}$ ,  $\text{N}_2\text{H}_2$  production. The C-N interactions and their impact on the  $\text{NO}_x$  formation chemistry were found to be highly dependent on the availability of NH and  $\text{CH}_3$  radicals in addition to the H, O, and OH radical pool.
- 1.3.** An artificially increased diffusion coefficient of H, O, and OH radicals in the flame led to higher laminar burning velocities. The role of these radicals diffusion is however different depending on the fuel investigated. Whereas H is a key limiting parameter in the  $\text{H}_2$  flame propagation, H and OH enhanced diffusions are, in this order, stimulating the methane flame propagation. In the case of ammonia flame, OH was found to be predominant. These observations were found to be consistent with the relative importance of the radicals in the flame chemistry and the reactions initiating the combustion by breaking an H bond from the fuel molecule. The role of radical diffusion on the extinction stretch rate was found to be lower than for the laminar burning velocity, eventually reducing the extinction stretch rate, with the broadening of the reaction zone and the loss of radicals in the burnt gas region with the reduced residence time.
- 1.4.** From the 1D freely propagating flame (FPF) observation it could be seen that short residence time leads to higher emissions in the flame. However, for longer residence time, the EINO was found to be decreasing. For counterflow premixed twin flames (PCF), it was found that for small residence time, the EINO is smaller than the one of freely propagating flame and converge to the same value for a larger residence time.

## 2. Fundamental flame characteristics and chemistry validation using counterflow flames

Extinction stretch rate and OH and NO species profiles were obtained experimentally in counterflow premixed and non-premixed flames using OH and NO-PLIF. A careful comparison of the present experimental results with simple 1D numerical simulation led to the evaluation of a selected set of mechanisms toward those criteria. The main results of this study are summarized in the following:

- 2.1. The ammonia introduction led to a large decrease in the extinction stretch rate of counterflow twin premixed flames (PCF). For all the ammonia mixing ratio investigated, the extinction stretch rate peaks between  $\phi = 0.9$  and  $0.95$ , shifting slightly on the leaner side to  $\phi = 0.9$  as ammonia mixing ratio is gradually increased. The position of these peaks on the lean side was attributed to the Lewis number less than unity of the lean mixtures.
- 2.2. The comparison of the experimental extinction stretch rate of premixed flames with the numerical simulation results highlighted the fact that none of the mechanisms selected was able to reproduce the experimental trend in all the conditions investigated. In this study, particularly large discrepancy was for lean flames. This larger discrepancy might reasonably be attributed to a lack in the methane chemistry for those flames and should be considered as a perspective of this work.
- 2.3. Ammonia-air counterflow non-premixed flame (NCF) could not be stabilized on the present burner. Slightly O<sub>2</sub>-enriched air was thus used as the oxidizer to observe the flame in conditions close to the ammonia-air non-premixed configuration. In those conditions, all the mechanisms investigated except GRI-Mech 3.0 [122] gave satisfactory estimates of the extinction stretch rate of the ammonia non-premixed flames, contrary to what was observed for premixed flames (PCF).
- 2.4. The addition of ammonia in methane non-premixed counterflow flame led to a nearly exponential decrease in the extinction stretch rate. The comparison of numerical simulations and experimental results showed that only Okafor's mechanism [63] was able to reproduce the experimental trend for methane/ammonia premixed flame in the range of ammonia mixing ratio,  $E$ , investigated. GRI-Mech 3.0 [122], Tian's [69] and UCSD [96] mechanisms could not follow the experimental trend, due to lack in nitrogen, hydrocarbons, and their interactions in each chemistry, respectively.

**2.5.** Quantitative comparison of the FWHM for OH and NO profiles from the PLIF measurement and numerical simulations suggest that further investigation in the lean chemistry is necessary for mechanisms improvement as the discrepancy is larger in this condition, as for the extinction stretch rate. All the detailed chemistries, at the exception of Tian's mechanism [69] for OH, over-predicted the apparition of both OH and NO. This over-reactivity should be considered in mechanism developments.

### 3. Stabilization mechanisms of ammonia/methane non-premixed jet flames

The evolution of the stabilization domain of a methane non-premixed jet flames with ammonia addition was studied with a special focus on the liftoff and re-attachment limits. The evolution of the lifted flame stabilization in the hysteresis domain and that of the attached flame were investigated and gave a better insight into the re-attachment and liftoff, respectively. The main results of this study are summarized in the following.

**3.1.** The stabilization domain was reduced by the addition of ammonia to the methane jet, corresponding to a significant decrease of the liftoff velocity. The flame could not be stabilized for ammonia mixing ratios,  $E$ , above 0.3, value at which the jet liftoff velocity and re-attachment velocity became sensibly equal. This drastic reduction, particularly when comparing to previous study on inert gases, was related to the change in the local flame speed due to the change in the mixture reactivity induced by ammonia addition.

**3.2.** In the present study, the stabilization regimes were shown to be highly dependent on the air coflow velocity, as a sudden drop of the re-attachment limit was observed when the air coflow velocity is increased. This re-attachment drop (RD) could be associated with the transition between two lifted flame behaviors in the hysteresis domain: the behavior A with decreasing lifted flame height, and the behavior B, with increasing lifted flame height. The transition between the two lifted flame behaviors is characterized by the critical jet breakpoint height,  $H_{Tc}$ . This height corresponds to a change in the turbulence generation within the laminar-turbulent transition; i.e., from laminar

instabilities-controlled turbulence at low jet Reynolds numbers, to laminar-to-turbulent transition in a pipe flow for larger jet Reynolds numbers. Such observations on flame behavior join previous work on other fuels, and this behavior might be observed for large dilution cases as well as high air coflow velocity cases.

- 3.3. With ammonia addition, attached flames stabilized higher and closer to the jet centerline. Indeed, the increase in stoichiometric fraction,  $Z_{st}$ , leads the flame toward the fuel side, where mixing is more favorable to its propagation; and the reduction of the local flame speed due to ammonia introduction, leading the flame to stabilize further downstream where the local velocity is lower.
- 3.4. The evolution stabilization regimes of the attached flame with the jet Reynolds number up to liftoff, called in this work regimes I, II, and III, as introduced by Lamige [117], were still observed for ammonia/methane non-premixed jet flame. They were nonetheless reduced, in terms of Reynolds number, due to the reduced stabilization domain. Moreover, the transition from regime I to II was shown to be slightly shifted to higher Reynolds number as ammonia is introduced in the mixture, compared to previous methane study [117]. The higher flame tip position with a larger ammonia mixing ratio explains this phenomenon. Indeed, for those higher flame tip position, higher fuel jet velocities are necessary to drag sufficient air in the wake of the burner lip and cause a change in the position of the stoichiometric line  $Z_{st}$ , which corresponds to the transition from regime I to II.
- 3.5. The thermal interactions with the burner were shown to follow the same dynamics as defined by Lamige [117], but the temperature at the burner decreased drastically as ammonia was introduced in the fuel jet, under the combined effect of flame temperature decrease and higher flame tip attachment height. Moreover, and similarly to the transition between regimes I and II, the transition between regimes Ia and Ib was observed for slightly larger Reynolds numbers. This could be associated with the evolution of the flame position with ammonia addition, moving toward the jet side and downstream.

## 4. Perspectives of research in future

As a perspective of this work, and regarding the evaluation of the existing detailed chemistries, other intermediate species might be considered for PLIF measurement in the premixed twin flames configuration.  $\text{NH}$  and  $\text{NH}_2$  are key radicals in ammonia and ammonia/methane combustion chemistry, and they were shown in Chapter 2 to be highly involved in NO formation, as well as the cyanides species  $\text{CN}$  and  $\text{HCN}$ , also harmful for the health and environment.  $\text{CH}$ , or  $\text{CH}_2\text{O}$ , appearing in the methane oxidation path, are also of interest. The first one appears in the branching toward cyanide formation and should be carefully monitored. It is also a good marker for the heat release peak in the flame.  $\text{CH}_2\text{O}$  is an essential intermediate in the methane oxidation path and as such an interesting candidate for chemistry validation.

A similar study for non-premixed flames might also be considered particularly to validate the present model toward the NO profiles in the flames for example and ensure that the chemistry validated for the extinction stretch rate of non-premixed flame, the Okafor's mechanism [63], is sufficiently accurate in NO predictions.

Temperature profiles are also another parameter of interest for mechanism validation which was not considered in the present study. Temperature measurements are particularly challenging in the counterflow flame configurations. Indeed, the introduction of a thermocouple highly disturbs the local flow field and generate disturbances of the flame, creating a strong bias in the measurement. Non-intrusive laser measurements might be considered. Raman spectrometry or LIF scans might reveal useful tools and later used as input for simulation if used in parallel of intermediate species measurements.

The study of the non-premixed jet flames can also be further developed. A more detailed investigation of the re-attachment behavior B, which corresponds to an increase of the flame height with a decrease in the jet velocity within the hysteresis region, could be considered. Indeed, a better insight of the changes occurring in the jet terms of local velocity and turbulence and mixing at the flame leading edge position would be interesting. Indeed, even if the general mechanism of behavior B is understood, some phenomena cannot be understood without a local study. Particularly, in the present analysis, the flame was assumed to stabilize close to stoichiometric condition (on the  $Z_{st}$  line), however previous studies suggest stabilization of the leading edge in leaner condition. Detailed local investigations, on local mixing, turbulence and velocity would enable the full characterization of the lifted flame

stabilization environment and fully understand the transition from behavior A to B. For such explorations, simultaneous PIV and OH or CH-PLIF measurement as they would allow for the instantaneous mapping of the flow field and flame position. The use of particles might however introduce some measurement bias and greater flame instability in these specific lifted flames conditions which should be carefully considered. Numerical simulations of the present configuration might also be considered for a similar purpose. The proper modeling of the jet laminar-to-turbulent transition might however be challenging, and thus a careful comparison with the present experimental conditions should be considered.

Improvement of the study on the attached flame could be performed to further analyze the liftoff limit. Comparing the local strain at the attached flame position to the extinction stretch rate results obtained in Chapter 3 would be helpful in the understanding of the liftoff phenomenon. Indeed, the large strain in the wake of the burner lip appears as a dominant parameter leading to liftoff. This study would imply velocity flow field mapping and flame position measurement. PIV measurements, combined with PLIF or chemiluminescence measurements, would be an appropriate tool for such a development. Moreover, details on mixing and air dragged in the wake of the burner lip would be of fundamental interest to explain the shift between regimes I and II and Ia and Ib, and validating the hypothesis introduced here. Here too, PIV measurement in the wake of the burner lip would be an interesting first approach to confirm the evolution of the air dragged region which appears at the transition between regimes I and II.

# References

- [1] IEA, World energy balances: overview, *World Energy Balanc.* 2018. (2018) 24. doi:10.15713/ins.mmj.3.
- [2] S. Shafiee, E. Topal, When will fossil fuel reserves be diminished?, *Energy Policy.* 37 (2009) 181–189. doi:10.1016/j.enpol.2008.08.016.
- [3] D.Y.C. Leung, G. Caramanna, M.M. Maroto-Valer, An overview of current status of carbon dioxide capture and storage technologies, *Renew. Sustain. Energy Rev.* 39 (2014) 426–443. doi:10.1016/j.rser.2014.07.093.
- [4] J.C.M.M. Pires, Negative emissions technologies: A complementary solution for climate change mitigation, *Sci. Total Environ.* 672 (2019) 502–514. doi:10.1016/j.scitotenv.2019.04.004.
- [5] X. Zhang, L. Luo, M. Skitmore, Household carbon emission research: An analytical review of measurement, influencing factors and mitigation prospects, *J. Clean. Prod.* 103 (2015) 873–883. doi:10.1016/j.jclepro.2015.04.024.
- [6] T. Jin, J. Kim, What is better for mitigating carbon emissions – Renewable energy or nuclear energy? A panel data analysis, *Renew. Sustain. Energy Rev.* 91 (2018) 464–471. doi:10.1016/j.rser.2018.04.022.
- [7] A.P. Bora, D.P. Gupta, K.S. Durbha, Sewage sludge to bio-fuel: A review on the sustainable approach of transforming sewage waste to alternative fuel, *Fuel.* 259 (2020). doi:10.1016/j.fuel.2019.116262.
- [8] V.Ş. Ediger, An integrated review and analysis of multi-energy transition from fossil fuels to renewables, *Energy Procedia.* 156 (2019) 2–6. doi:10.1016/j.egypro.2018.11.073.
- [9] A. Kibria, S.B. Akhundjanov, R. Oladi, Fossil fuel share in the energy mix and economic growth, *Int. Rev. Econ. Financ.* 59 (2019) 253–264. doi:10.1016/j.iref.2018.09.002.
- [10] J. Bartholy, R. Pongrácz, A brief review of health-related issues occurring in urban areas related to global warming of 1.5°C, *Curr. Opin. Environ. Sustain.* 30 (2018) 123–132. doi:10.1016/j.cosust.2018.05.014.
- [11] Z. Li, G. Fang, Y. Chen, W. Duan, Y. Mukanov, Agricultural water demands in Central Asia under 1.5 °C and 2.0 °C global warming, *Agric. Water Manag.* 231 (2020) 0–9. doi:10.1016/j.agwat.2020.106020.
- [12] H.C. Dai, H. Bin Zhang, W.T. Wang, The impacts of U.S. withdrawal from the Paris Agreement on the carbon emission space and mitigation cost of China, EU, and Japan under the constraints of the global carbon emission space, *Adv. Clim. Chang. Res.* 8 (2017) 226–234. doi:10.1016/j.accre.2017.09.003.
- [13] S. Arrhenius, On the Influence of Carbonic Acid in the Air upon the Temperature of the Ground Svante, *Philos. Mag. J. Sci.* 41 (1896) 237–276.
- [14] R. Právělie, Major perturbations in the Earth’s forest ecosystems. Possible implications for global warming, *Earth-Science Rev.* 185 (2018) 544–571. doi:10.1016/j.earscirev.2018.06.010.
- [15] O. Hoegh-Guldberg, D. Jacob, M. Taylor, M. Bindi, S. Brown, I. Camilloni, A. Diedhiou, D. Riyanti, K.L. Ebi, F. Engelbrecht, J. Guiot, Y. Hijoka, S. Mehrotra, A. Payne, S.I. Seneviratne,

- A. Thomas, R. Warren, G. Zhou, Impacts of 1.5°C Global Warming on Natural and Human Systems. In: Global Warming of 1.5°C. An IPCC Special Report on the impacts of global warming of 1.5°C above pre-industrial levels and related global greenhouse gas emission pathways, in the context of , 2018.
- [16] IEA, Energy technology RD budgets Overview, (2018). [www.iea.org/statistics](http://www.iea.org/statistics).
- [17] IEA, Key World Energy Statistics 2018, 2018. [https://webstore.iea.org/download/direct/2291?fileName=Key\\_World\\_2018.pdf](https://webstore.iea.org/download/direct/2291?fileName=Key_World_2018.pdf).
- [18] D. Grand, C. Le Brun, R. Vidil, F. Wagner, Electricity production by intermittent renewable sources: a synthesis of French and German studies, *Eur. Phys. J. Plus.* 131 (2016) 1–12. doi:10.1140/epjp/i2016-16329-6.
- [19] H. Ritchie, M. Roser, Fossil Fuels, (n.d.). <https://ourworldindata.org/fossil-fuels> (accessed June 15, 2020).
- [20] V. Pattabathula, J. Richardson, Introduction to ammonia production, (2016). <https://www.aiche.org/resources/publications/cep/2016/september/introduction-ammonia-production>.
- [21] P. Gilbert, S. Alexander, P. Thornley, J. Brammer, Assessing economically viable carbon reductions for the production of ammonia from biomass gasification, *J. Clean. Prod.* 64 (2014) 581–589. doi:10.1016/j.jclepro.2013.09.011.
- [22] Y. Bicer, I. Dincer, C. Zamfirescu, G. Vezina, F. Raso, Comparative life cycle assessment of various ammonia production methods, *J. Clean. Prod.* 135 (2016) 1379–1395. doi:10.1016/j.jclepro.2016.07.023.
- [23] H.A. Haugen, N.H. Eldrup, A.M. Fatnes, E. Leren, Commercial Capture and Transport of CO<sub>2</sub> from Production of Ammonia, *Energy Procedia.* 114 (2017) 6133–6140. doi:10.1016/j.egypro.2017.03.1750.
- [24] P. Arora, I. Sharma, A. Hoadley, S. Mahajani, A. Ganesh, Remote, small-scale, ‘greener’ routes of ammonia production, *J. Clean. Prod.* 199 (2018) 177–192. doi:10.1016/j.jclepro.2018.06.130.
- [25] G. Vezina, Y. Bicer, I. Dincer, C. Zamfirescu, F. Raso, Key Life Cycle Assessment Numbers for NH<sub>3</sub>, *Green and Brown Energy*, (2016). <https://nh3fuelassociation.org/2016/08/24/key-life-cycle-assessment-numbers-for-nh3-green-and-brown-energy/> (accessed January 20, 2017).
- [26] A. Sánchez, M. Martín, Optimal renewable production of ammonia from water and air, *J. Clean. Prod.* 178 (2018) 325–342. doi:10.1016/j.jclepro.2017.12.279.
- [27] D. Flórez-Orrego, F. Maréchal, S. de Oliveira Junior, Comparative exergy and economic assessment of fossil and biomass-based routes for ammonia production, *Energy Convers. Manag.* 194 (2019) 22–36. doi:10.1016/j.enconman.2019.04.072.
- [28] Y. Bicer, I. Dincer, Exergoeconomic analysis and optimization of a concentrated sunlight-driven integrated photoelectrochemical hydrogen and ammonia production system, *Int. J. Hydrogen Energy.* (2018). doi:10.1016/j.ijhydene.2018.10.074.
- [29] M. Al-Zareer, I. Dincer, M.A. Rosen, Transient analysis and evaluation of a novel pressurized multistage ammonia production system for hydrogen storage purposes, *J. Clean. Prod.* 196 (2018) 390–399. doi:10.1016/j.jclepro.2018.06.022.
- [30] R. Hawtof, S. Ghosh, E. Guarr, C. Xu, R. Mohan Sankaran, J.N. Renner, Catalyst-free, highly

- selective synthesis of ammonia from nitrogen and water by a plasma electrolytic system, *Sci. Adv.* 5 (2019) eaat5778. doi:10.1126/sciadv.aat5778.
- [31] Y. Ashida, K. Arashiba, K. Nakajima, Y. Nishibayashi, Molybdenum-catalysed ammonia production with samarium diiodide and alcohols or water, *Nature*. (n.d.). doi:10.1038/s41586-019-1134-2.
- [32] A. Valera-Medina, H. Xiao, M. Owen-Jones, W.I.F. David, P.J. Bowen, Ammonia for power, *Prog. Energy Combust. Sci.* 69 (2018) 63–102. doi:10.1016/j.pecs.2018.07.001.
- [33] NIH, Summary of AEGL Values for Ammonia, (2008). <https://www.ncbi.nlm.nih.gov/books/NBK207883/table/ttt00026/?report=objectonly> (accessed June 15, 2020).
- [34] Siemens, Green Ammonia, (2016). <https://www.siemens.com/content/dam/webassetpool/mam/tag-siemens-com/smdb/regions/united-kingdom/sustainability/siemens-green-ammonia.pdf> (accessed January 20, 2017).
- [35] IHI, Creating Value for the Future, (n.d.). <https://www.ihico.jp/csr/english/realize/future.html> (accessed March 1, 2019).
- [36] IEA, Renewable information: Overview, 2018. <https://webstore.iea.org/renewables-information-2018-overview>.
- [37] C. Philibert, Producing ammonia and fertilizers: new opportunities from renewables, (2017) 6. [https://www.iea.org/media/news/2017/Fertilizer\\_manufacturing\\_Renewables\\_01102017.pdf](https://www.iea.org/media/news/2017/Fertilizer_manufacturing_Renewables_01102017.pdf).
- [38] C. Philibert, Renewable energy for industry: From green energy to green materials and fuels, *Int. Energy Agency*. (2017) 72. doi:10.1111/j.1365-2990.2010.01130.x.
- [39] JGC Corporation, CO<sub>2</sub>-Free Ammonia Synthesis - CO<sub>2</sub>-Free Energy Carrier, (2019). <https://www.jgc.com/en/business/tech-innovation/environment/co2-free.html>.
- [40] NH<sub>3</sub> Fuel Association, Introduction to fuel ammonia, (2019). <https://nh3fuelassociation.org/introduction/>.
- [41] NASA, NASA Armstrong Fact Sheet: X-15 Hypersonic Research Program, (2014). <https://www.nasa.gov/centers/armstrong/news/FactSheets/FS-052-DFRC.html> (accessed September 20, 2002).
- [42] Z.X. Guo, C. Shang, K.F. Aguey-Zinsou, Materials challenges for hydrogen storage, *J. Eur. Ceram. Soc.* 28 (2008) 1467–1473. doi:10.1016/j.jeurceramsoc.2007.12.019.
- [43] H. Kobayashi, A. Hayakawa, K.D.K.A. Somarathne, E.C. Okafor, Science and technology of ammonia combustion, *Proc. Combust. Inst.* 37 (2019) 109–133. doi:10.1016/j.proci.2018.09.029.
- [44] J.A. Miller, C.T. Bowman, Mechanism and modeling of nitrogen chemistry in combustion, *Prog. Energy Combust. Sci.* 15 (1990) 287–338. doi:10.1016/0360-1285(90)90043-3.
- [45] W. Wittler, G. Rotzoll, K. Schügerl, Reduction of NO emissions from a coal-fired fluidized bed combustor by addition of NH<sub>3</sub> through a water-cooled injector, *Combust. Flame.* 74 (1988) 171–178. doi:10.1016/0010-2180(88)90015-6.
- [46] R.J. Martin, N.J. Brown, The importance of thermodynamics to the modeling of nitrogen combustion chemistry, *Combust. Flame.* 78 (1989) 365–376. doi:10.1016/0010-

- 2180(89)90024-2.
- [47] T. Mendiara, P. Glarborg, Ammonia chemistry in oxy-fuel combustion of methane, *Combust. Flame*. 156 (2009) 1937–1949. doi:10.1016/j.combustflame.2009.07.006.
- [48] S.J. Klippenstein, L.B. Harding, P. Glarborg, J. a. Miller, The role of NNH in NO formation and control, *Combust. Flame*. 158 (2011) 774–789. doi:10.1016/j.combustflame.2010.12.013.
- [49] N. Sullivan, A. Jensen, P. Glarborg, M.S. Day, J.F. Grcar, J.B. Bell, C.J. Pope, R.J. Kee, Ammonia conversion and NO<sub>x</sub> formation in laminar coflowing nonpremixed methane-air flames, *Combust. Flame*. 131 (2002) 285–298. doi:10.1016/S0010-2180(02)00413-3.
- [50] B. Li, Y. He, Z. Li, A.A. Konnov, Measurements of NO concentration in NH<sub>3</sub>-doped CH<sub>4</sub>+air flames using saturated laser-induced fluorescence and probe sampling, *Combust. Flame*. 160 (2013) 40–46. doi:10.1016/j.combustflame.2012.10.003.
- [51] M. Barbas, M. Costa, S. Vranckx, R.X. Fernandes, Experimental and kinetic modeling study of CO and NO formation under oxy-fuel conditions, *Combust. Flame*. 162 (2013) 1294–1303. doi:10.1016/j.combustflame.2014.10.020.
- [52] N. Lamoureux, K. Marschallek-Watroba, P. Desgroux, J.-F. Pauwels, M.D. Sylla, L. Gasnot, Measurements and modelling of nitrogen species in CH<sub>4</sub>/O<sub>2</sub>/N<sub>2</sub> flames doped with NO, NH<sub>3</sub>, or NH<sub>3</sub>+NO, *Combust. Flame*. 176 (2016) 48–59. doi:10.1016/j.combustflame.2016.10.019.
- [53] M.D. Checkel, D.S.K. Ting, W.K. Bushe, Flammability limits and burning velocities of ammonia/nitric oxide mixtures, *J. Loss Prev. Process Ind.* 8 (1995) 215–220. doi:10.1016/0950-4230(95)00027-X.
- [54] Ø. Skreiberg, P. Kilpinen, P. Glarborg, Ammonia chemistry below 1400 K under fuel-rich conditions in a flow reactor, *Combust. Flame*. 136 (2004) 501–518. doi:10.1016/j.combustflame.2003.12.008.
- [55] H. Nozari, A. Karabeyoglu, Numerical study of combustion characteristics of ammonia as a renewable fuel and establishment of reduced reaction mechanisms, *Fuel*. 159 (2015) 223–233. doi:10.1016/j.fuel.2015.06.075.
- [56] C. Duynslaegher, H. Jeanmart, J. Vandooren, Ammonia combustion at elevated pressure and temperature conditions, *Fuel*. 89 (2010) 3540–3545. doi:10.1016/j.fuel.2010.06.008.
- [57] C. Brackmann, V.A. Alekseev, B. Zhou, E. Nordström, P.E. Bengtsson, Z. Li, M. Aldén, A.A. Konnov, Structure of premixed ammonia + air flames at atmospheric pressure: Laser diagnostics and kinetic modeling, *Combust. Flame*. 163 (2016) 370–381. doi:10.1016/j.combustflame.2015.10.012.
- [58] M. Zieba, A. Brink, A. Schuster, M. Hupa, G. Scheffknecht, Ammonia chemistry in a flameless jet, *Combust. Flame*. 156 (2009) 1950–1956. doi:10.1016/j.combustflame.2009.07.002.
- [59] K.D.K.A. Somarathne, S. Colson, A. Hayakawa, H. Kobayashi, Modelling of ammonia/air non-premixed turbulent swirling flames in a gas turbine-like combustor at various pressures, *Combust. Theory Model.* 22 (2018) 973–997. doi:10.1080/13647830.2018.1468035.
- [60] O. Kurata, N. Iki, T. Inoue, T. Matsunuma, T. Tsujimura, H. Furutani, M. Kawano, K. Arai, E.C. Okafor, A. Hayakawa, H. Kobayashi, Development of a wide range-operable, rich-lean low-NO<sub>x</sub> combustor for NH<sub>3</sub> fuel gas-turbine power generation, *Proc. Combust. Inst.* 37 (2019) 4587–4595. doi:10.1016/j.proci.2018.09.012.

- [61] E.C. Okafor, K.D.K.A. Somarathne, A. Hayakawa, T. Kudo, O. Kurata, N. Iki, H. Kobayashi, Towards the development of an efficient low-NO<sub>x</sub> ammonia combustor for a micro gas turbine, *Proc. Combust. Inst.* 37 (2019) 4597–4606. doi:10.1016/j.proci.2018.07.083.
- [62] A. Hayakawa, T. Goto, R. Mimoto, T. Kudo, H. Kobayashi, NO formation/reduction mechanisms of ammonia/air premixed flames at various equivalence ratios and pressures, *Mech. Eng. J.* 2 (2015) 14-00402-14-00402. doi:10.1299/mej.14-00402.
- [63] E.C. Okafor, Y. Naito, S. Colson, A. Ichikawa, T. Kudo, A. Hayakawa, H. Kobayashi, Experimental and numerical study of the laminar burning velocity of CH<sub>4</sub>-NH<sub>3</sub>-air premixed flames, *Combust. Flame.* 187 (2018) 185–198. doi:10.1016/j.combustflame.2017.09.002.
- [64] A. Ichikawa, Y. Naito, A. Hayakawa, T. Kudo, H. Kobayashi, Burning velocity and flame structure of CH<sub>4</sub>/NH<sub>3</sub>/air turbulent premixed flames at high pressure, *Int. J. Hydrogen Energy.* 44 (2019) 6991–6999. doi:10.1016/j.ijhydene.2019.01.193.
- [65] A. Ichikawa, A. Hayakawa, Y. Kitagawa, K.D. Kunkuma Amila Somarathne, T. Kudo, H. Kobayashi, Laminar burning velocity and Markstein length of ammonia/hydrogen/air premixed flames at elevated pressures, *Int. J. Hydrogen Energy.* 40 (2015) 9570–9578. doi:10.1016/j.ijhydene.2015.04.024.
- [66] H. Xiao, Z. Wang, A. Valera-Medina, P.J. Bowen, Study on Characteristics of Co-firing Ammonia/Methane Fuels under Oxygen Enriched Combustion Conditions, *J. Therm. Sci.* 27 (2018) 270–276. doi:10.1007/s11630-018-1008-1.
- [67] H. Xiao, A. Valera-Medina, P.J. Bowen, Study on premixed combustion characteristics of co-firing ammonia/methane fuels, *Energy.* 140 (2017) 125–135. doi:10.1016/j.energy.2017.08.077.
- [68] P. Bowen, S. Dooley, M.S. Howard, H. Xiao, A. Valera-Medina, Reduced Chemical Mechanisms for Ammonia/Methane Co-firing for Gas Turbine Applications, *Energy Procedia.* 105 (2017) 1483–1488. doi:10.1016/j.egypro.2017.03.441.
- [69] Z. Tian, Y. Li, L. Zhang, P. Glarborg, F. Qi, An experimental and kinetic modeling study of premixed NH<sub>3</sub>/CH<sub>4</sub>/O<sub>2</sub>/Ar flames at low pressure, *Combust. Flame.* 156 (2009) 1413–1426. doi:10.1016/j.combustflame.2009.03.005.
- [70] J.W. Ku, S. Choi, H.K. Kim, S. Lee, O.C. Kwon, Extinction limits and structure of counterflow nonpremixed methane-ammonia/air flames, *Energy.* 165 (2018) 314–325. doi:10.1016/j.energy.2018.09.113.
- [71] N. Iki, O. Kurata, T. Matsunuma, T. Inoue, M. Suzuki, T. Tsujimura, H. Furutani, Power Generation and Flame Visualization of Micro Gas Turbine Firing Ammonia or Ammonia-Methane Mixture, in: 13th Annu. NH<sub>3</sub> Fuel Conf., 2016: pp. 1–22.
- [72] K.D.K.A. SOMARATHNE, A. HAYAKAWA, H. KOBAYASHI, Numerical investigation on the combustion characteristics of turbulent premixed ammonia/air flames stabilized by a swirl burner, *J. Fluid Sci. Technol.* 11 (2016) JFST0026–JFST0026. doi:10.1299/jfst.2016jfst0026.
- [73] C.L. Rasmussen, A.E. Rasmussen, P. Glarborg, Sensitizing effects of NO<sub>x</sub> on CH<sub>4</sub> oxidation at high pressure, *Combust. Flame.* 154 (2008) 529–545. doi:10.1016/j.combustflame.2008.01.012.
- [74] P. Glarborg, A.B. Bendtsen, J.A. Miller, Nitromethane dissociation: Implications for the CH<sub>3</sub>+NO<sub>2</sub> Reaction, *Int. J. Chem. Kinet.* 31 (1999) 591–602. doi:10.1002/(SICI)1097-4601(1999)31:9<591::AID-KIN1>3.0.CO;2-E.

- [75] J. Andersen, C.L. Rasmussen, T. Giselsson, P. Glarborg, Global combustion mechanisms for use in CFD modeling under oxy-fuel conditions, *Energy and Fuels*. 23 (2009) 1379–1389. doi:10.1021/ef8003619.
- [76] Y. Song, H. Hashemi, J.M. Christensen, C. Zou, P. Marshall, P. Glarborg, Ammonia oxidation at high pressure and intermediate temperatures, *Fuel*. 181 (2016) 358–365. doi:10.1016/j.fuel.2016.04.100.
- [77] H. Nakamura, S. Hasegawa, Combustion and ignition characteristics of ammonia/air mixtures in a micro flow reactor with a controlled temperature profile, *Proc. Combust. Inst.* 000 (2016) 1–10. doi:10.1016/j.proci.2016.06.153.
- [78] P. Glarborg, J.A. Miller, B. Ruscic, S.J. Klippenstein, Modeling nitrogen chemistry in combustion, *Prog. Energy Combust. Sci.* 67 (2018) 31–68. doi:10.1016/j.peccs.2018.01.002.
- [79] A.A. Konnov, Implementation of the NCN pathway of prompt-NO formation in the detailed reaction mechanism, *Combust. Flame*. 156 (2009) 2093–2105. doi:10.1016/j.combustflame.2009.03.016.
- [80] S.M. Burke, U. Burke, R. Mc Donagh, O. Mathieu, I. Osorio, C. Keesee, A. Morones, E.L. Petersen, W. Wang, T.A. DeVerter, M.A. Oehlschlaeger, B. Rhodes, R.K. Hanson, D.F. Davidson, B.W. Weber, C.J. Sung, J. Santner, Y. Ju, F.M. Haas, F.L. Dryer, E.N. Volkov, E.J.K. Nilsson, A.A. Konnov, M. Alrefae, F. Khaled, A. Farooq, P. Dirrenberger, P.A. Glaude, F. Battin-Leclerc, H.J. Curran, An experimental and modeling study of propene oxidation. Part 2: Ignition delay time and flame speed measurements, *Combust. Flame*. 162 (2015) 296–314. doi:10.1016/j.combustflame.2014.07.032.
- [81] P.-E. Bengtsson, A. Hosseinia, A.A. Konnov, C. Brackmann, S. El-Busaidy, J.D. Nauc ler, E.J.K. Nilsson, Experimental studies of nitromethane flames and evaluation of kinetic mechanisms, *Combust. Flame*. 190 (2017) 327–336. doi:10.1016/j.combustflame.2017.12.011.
- [82] C. Brackmann, B. Zhou, P. Samuelsson, V.A. Alekseev, A.A. Konnov, Z. Li, M. Ald n, Strategy for improved NH<sub>2</sub> detection in combustion environments using an Alexandrite laser, *Spectrochim. Acta - Part A Mol. Biomol. Spectrosc.* 184 (2017) 235–242. doi:10.1016/j.saa.2017.05.002.
- [83] C. Brackmann, E.J.K. Nilsson, J.D. Nauc ler, M. Ald n, A.A. Konnov, Formation of NO and NH in NH<sub>3</sub>-doped CH<sub>4</sub> + N<sub>2</sub> + O<sub>2</sub> flame: Experiments and modelling, *Combust. Flame*. 194 (2018) 278–284. doi:10.1016/j.combustflame.2018.05.008.
- [84] A.A. Konnov, Yet another kinetic mechanism for hydrogen combustion, *Combust. Flame*. 203 (2019) 14–22. doi:10.1016/j.combustflame.2019.01.032.
- [85] O. Mathieu, B. Giri, A.R. Agard, T.N. Adams, J.D. Mertens, E.L. Petersen, Nitromethane ignition behind reflected shock waves: Experimental and numerical study, *Fuel*. 182 (2016) 597–612. doi:10.1016/j.fuel.2016.05.060.
- [86] O. Mathieu, E.L. Petersen, Experimental and modeling study on the high-temperature oxidation of Ammonia and related NO<sub>x</sub> chemistry, *Combust. Flame*. 162 (2015) 554–570. doi:10.1016/j.combustflame.2014.08.022.
- [87] A. Hayakawa, T. Goto, R. Mimoto, Y. Arakawa, T. Kudo, H. Kobayashi, Laminar burning velocity and Markstein length of ammonia/air premixed flames at various pressures, *Fuel*. 159 (2015) 98–106. doi:10.1016/j.fuel.2015.06.070.
- [88] E.C. Okafor, Y. Naito, S. Colson, A. Ichikawa, T. Kudo, A. Hayakawa, H. Kobayashi, Measurement and modelling of the laminar burning velocity of methane-ammonia-air flames at

- high pressures using a reduced reaction mechanism, *Combust. Flame.* 204 (2019) 162–175. doi:10.1016/j.combustflame.2019.03.008.
- [89] S. Colson, A. Hayakawa, T. Kudo, H. Kobayashi, Extinction characteristics of ammonia/air counterflow premixed flames at various pressures, *J. Therm. Sci. Technol.* 11 (2016) JTST0048. doi:10.1299/jtst.2016jtst0048.
- [90] A. Kéromnès, W.K. Metcalfe, K.A. Heufer, N. Donohoe, A.K. Das, C.J. Sung, J. Herzler, C. Naumann, P. Griebel, O. Mathieu, M.C. Krejci, E.L. Petersen, W.J. Pitz, H.J. Curran, An experimental and detailed chemical kinetic modeling study of hydrogen and syngas mixture oxidation at elevated pressures, *Combust. Flame.* 160 (2013) 995–1011. doi:10.1016/j.combustflame.2013.01.001.
- [91] W.K. Metcalfe, S.M. Burke, S.S. Ahmed, H.J. Curran, A hierarchical and comparative kinetic modeling study of C1 - C2 hydrocarbon and oxygenated fuels, *Int. J. Chem. Kinet.* 45 (2013) 638–675. doi:10.1002/kin.20802.
- [92] S.M. Burke, W. Metcalfe, O. Herbinet, F. Battin-Leclerc, F.M. Haas, J. Santner, F.L. Dryer, H.J. Curran, An experimental and modeling study of propene oxidation. Part 1: Speciation measurements in jet-stirred and flow reactors, *Combust. Flame.* 161 (2014) 2765–2784. doi:10.1016/j.combustflame.2014.05.010.
- [93] U. Burke, W.K. Metcalfe, S.M. Burke, K.A. Heufer, P. Dagaut, H.J. Curran, A detailed chemical kinetic modeling, ignition delay time and jet-stirred reactor study of methanol oxidation, *Combust. Flame.* 165 (2016) 125–136. doi:10.1016/j.combustflame.2015.11.004.
- [94] C.W. Zhou, Y. Li, E. O'Connor, K.P. Somers, S. Thion, C. Keesee, O. Mathieu, E.L. Petersen, T.A. DeVerter, M.A. Oehlschlaeger, G. Kukkadapu, C.J. Sung, M. Alrefae, F. Khaled, A. Farooq, P. Dirrenberger, P.A. Glaude, F. Battin-Leclerc, J. Santner, Y. Ju, T. Held, F.M. Haas, F.L. Dryer, H.J. Curran, A comprehensive experimental and modeling study of isobutene oxidation, *Combust. Flame.* 167 (2016) 353–379. doi:10.1016/j.combustflame.2016.01.021.
- [95] Y. Li, C.W. Zhou, K.P. Somers, K. Zhang, H.J. Curran, The oxidation of 2-butene: A high pressure ignition delay, kinetic modeling study and reactivity comparison with isobutene and 1-butene, *Proc. Combust. Inst.* 36 (2017) 403–411. doi:10.1016/j.proci.2016.05.052.
- [96] University California of San Diego, Chemical-Kinetic Mechanisms for Combustion Applications, (2016). <http://web.eng.ucsd.edu/mae/groups/combustion/mechanism.html>.
- [97] Y. Jiang, A. Gruber, K. Seshadri, F. Williams, An updated short chemical-kinetic nitrogen mechanism for carbon-free combustion applications, *Int. J. Energy Res.* (2019) 1–16. doi:10.1002/er.4891.
- [98] CRECK modeling group, CRECK Modeling - Detailed reaction mechanism, (n.d.). <http://creckmodeling.chem.polimi.it/menu-kinetics/menu-kinetics-detailed-mechanisms>.
- [99] C. Lhuillier, P. Brequigny, N. Lamoureux, F. Contino, C. Mounaïm-Rousselle, Experimental investigation on laminar burning velocities of ammonia/hydrogen/air mixtures at elevated temperatures, *Fuel.* 263 (2020). doi:10.1016/j.fuel.2019.116653.
- [100] B. Mei, X. Zhang, S. Ma, M. Cui, H. Guo, Z. Cao, Y. Li, Experimental and kinetic modeling investigation on the laminar flame propagation of ammonia under oxygen enrichment and elevated pressure conditions, *Combust. Flame.* 210 (2019) 236–246. doi:10.1016/j.combustflame.2019.08.033.
- [101] X. Han, Z. Wang, M. Costa, Z. Sun, Y. He, K. Cen, Experimental and kinetic modeling study of laminar burning velocities of NH<sub>3</sub>/air, NH<sub>3</sub>/H<sub>2</sub>/air, NH<sub>3</sub>/CO/air and NH<sub>3</sub>/CH<sub>4</sub>/air

- premixed flames, *Combust. Flame*. 206 (2019) 214–226.  
doi:10.1016/j.combustflame.2019.05.003.
- [102] C. Brackmann, E.J.K. Nilsson, J.D. Nauc ler, M. Ald en, A.A. Konnov, Formation of NO and NH in NH<sub>3</sub>-doped CH<sub>4</sub> + N<sub>2</sub> + O<sub>2</sub> flame : Experiments and modelling, *Combust. Flame*. 194 (2018) 278–284. doi:10.1016/j.combustflame.2018.05.008.
- [103] J. Vandooren, J. Bian, P.J.V.A.N. Tiggelen, P.J. Van Tiggelen, Comparison of experimental and calculated structures of an ammonianitric oxide flame. Importance of the NH<sub>2</sub> + NO reaction, *Combust. Flame*. 98 (1994) 402–410. doi:10.1016/0010-2180(94)90178-3.
- [104] C.F. Ramos, R.C. Rocha, P.M.R. Oliveira, M. Costa, X. Bai, Experimental and kinetic modelling investigation on NO, CO and NH<sub>3</sub> emissions from NH<sub>3</sub> / CH<sub>4</sub> / air premixed flames, 254 (2019). doi:10.1016/j.fuel.2019.115693.
- [105] M. Woo, B.C. Choi, A.F. Ghoniem, Experimental and numerical studies on NO<sub>x</sub> emission characteristics in laminar non-premixed jet flames of ammonia-containing methane fuel with oxygen/nitrogen oxidizer, *Energy*. 114 (2016) 961–972. doi:10.1016/j.energy.2016.07.150.
- [106] F.J. Verkamp, M.C. Hardin, J.R. Williams, Ammonia combustion properties and performance in gas-turbine burners, *Symp. Combust.* 11 (1967) 985–992. doi:10.1016/S0082-0784(67)80225-X.
- [107] E. Rohde, K.R. L oblich, F. Fetting, The stabilization of turbulent ammonia-air flames on flameholders, *Combust. Flame*. 13 (1969) 327–329. doi:10.1016/0010-2180(69)90014-5.
- [108] N. Syred, J.M. Be r, Combustion in swirling flows: A review, *Combust. Flame*. 23 (1974) 143–201. doi:10.1016/0010-2180(74)90057-1.
- [109] A. Hayakawa, Y. Arakawa, R. Mimoto, K.D.K.A. Somarathne, T. Kudo, H. Kobayashi, Experimental investigation of stabilization and emission characteristics of ammonia/air premixed flames in a swirl combustor, *Int. J. Hydrogen Energy*. 42 (2017) 14010–14018. doi:10.1016/j.ijhydene.2017.01.046.
- [110] K.D.K.A. Somarathne, S. Colson, A. Hayakawa, H. Kobayashi, Modelling of ammonia/air non-premixed turbulent swirling flames in a gas turbine-like combustor at various pressures, *Combust. Theory Model.* (2018). doi:10.1080/13647830.2018.1468035.
- [111] A. Valera-medina, D.G. Pugh, P. Marsh, G. Bulat, P. Bowen, ScienceDirect Preliminary study on lean premixed combustion of ammonia-hydrogen for swirling gas turbine combustors, *Int. J. Hydrogen Energy*. 42 (2017) 24495–24503. doi:10.1016/j.ijhydene.2017.08.028.
- [112] N.A. Hussein, A. Valera-Medina, A.S. Alsaegh, Ammonia- hydrogen combustion in a swirl burner with reduction of NO<sub>x</sub> emissions, *Energy Procedia*. 158 (2019) 2305–2310. doi:10.1016/j.egypro.2019.01.265.
- [113] A. Valera-medina, M. Gutesa, H. Xiao, D. Pugh, A. Giles, B. Goktepe, R. Marsh, P. Bowen, ScienceDirect Premixed ammonia / hydrogen swirl combustion under rich fuel conditions for gas turbines operation, *Int. J. Hydrogen Energy*. 44 (2019) 8615–8626. doi:10.1016/j.ijhydene.2019.02.041.
- [114] A. Valera-medina, R. Marsh, J. Runyon, D. Pugh, P. Beasley, T. Hughes, P. Bowen, Ammonia – methane combustion in tangential swirl burners for gas turbine power generation, *Appl. Energy*. 185 (2017) 1362–1371. doi:10.1016/j.apenergy.2016.02.073.
- [115] K. Don, K. Amila, E.C. Okafor, A. Hayakawa, T. Kudo, O. Kurata, N. Iki, H. Kobayashi, Emission characteristics of turbulent non-premixed ammonia / air and methane / air swirl

- flames through a rich-lean combustor under various wall thermal boundary conditions at high pressure, 210 (2019) 247–261. doi:10.1016/j.combustflame.2019.08.037.
- [116] E.C. Okafor, K.D.K.A. Somarathne, R. Ratthan, A. Hayakawa, T. Kudo, O. Kurata, N. Iki, T. Tsujimura, H. Furutani, H. Kobayashi, Control of NO<sub>x</sub> and other emissions in micro gas turbine combustors fuelled with mixtures of methane and ammonia, *Combust. Flame*. 211 (2020) 406–416. doi:10.1016/j.combustflame.2019.10.012.
- [117] S. Lamige, Analyse de l’Influence des Conditions aux Limites Thermiques sur la Stabilisation des Flamme Non-Prémélangées, INSA de Lyon, 2014.
- [118] S. Lamige, J. Min, C. Galizzi, F. André, F. Baillet, D. Escudié, K.M. Lyons, On preheating and dilution effects in non-premixed jet flame stabilization, *Combust. Flame*. 160 (2013) 1102–1111. doi:10.1016/j.combustflame.2013.01.026.
- [119] S. Lamige, K.M. Lyons, C. Galizzi, F. André, M. Kühni, D. Escudié, Burner lip temperature and stabilization of a non-premixed jet flame, *Exp. Therm. Fluid Sci.* 56 (2014) 45–52. doi:10.1016/j.expthermflusci.2013.11.008.
- [120] CHEMKIN-PRO Release 1510, (2010).
- [121] Z. Tian, L. Zhang, Y. Li, T. Yuan, F. Qi, An experimental and kinetic modeling study of a premixed nitromethane flame at low pressure, *Proc. Combust. Inst.* 32 I (2009) 311–318. doi:10.1016/j.proci.2008.06.098.
- [122] G.P. Smith, D.M. Golden, M. Frenklach, N.W. Moriarty, B. Eiteneer, M. Goldenberg, C.T. Bowman, R.K. Hanson, S. Song, W.C. Gardiner, V. V. Lissianski, Jr., Z. Qin, GRIMEch 3.0, (2000). [http://www.me.berkeley.edu/gri\\_mech/](http://www.me.berkeley.edu/gri_mech/).
- [123] C.K. Law, *Combustion Physics*, Cambridge University Press, Cambridge, 2006. doi:10.1017/CBO9780511754517.
- [124] Chemkin, OPPDIF: A program for computing opposed flow DIFFUSION FLAMES, Chemkin Collect. Release. 3.6 (2000) 1–37.
- [125] M. Nishioka, S. Nakagawa, Y. Ishikawa, T. Takeno, NO emission characteristics of methane-air double flame, *Combust. Flame*. 98 (1994) 127–138. doi:10.1016/0010-2180(94)90203-8.
- [126] T. Takeno, M. Nishioka, Species conservation and emission indices for flames described by similarity solutions, *Combust. Flame*. 92 (1993) 465–468. doi:10.1016/0010-2180(93)90157-X.
- [127] R.P. Lindstedt, F.C. Lockwood, M.A. Selim, Detailed kinetic modelling of chemistry and temperature effects on ammonia oxidation, *Combust. Sci. Technol.* 99 (1994) 253–276. doi:10.1080/00102209408935436.
- [128] B.C. Duva, L.E. Chance, E. Toulson, Dilution effect of different combustion residuals on laminar burning velocities and burned gas Markstein lengths of premixed methane/air mixtures at elevated temperature, *Fuel*. 267 (2020) 117153. doi:10.1016/j.fuel.2020.117153.
- [129] X. Han, Z. Wang, Y. He, S. Wang, Y. Zhu, A.A. Konnov, Over-rich combustion of CH<sub>4</sub>, C<sub>2</sub>H<sub>6</sub>, and C<sub>3</sub>H<sub>8</sub> +air premixed flames investigated by the heat flux method and kinetic modeling, *Combust. Flame*. 210 (2019) 339–349. doi:10.1016/j.combustflame.2019.09.009.
- [130] A.R. Khan, M.R. Ravi, A. Ray, Experimental and chemical kinetic studies of the effect of H<sub>2</sub> enrichment on the laminar burning velocity and flame stability of various multicomponent natural gas blends, *Int. J. Hydrogen Energy*. 44 (2019) 1192–1212.

- doi:10.1016/j.ijhydene.2018.10.207.
- [131] C. Ji, D. Wang, J. Yang, S. Wang, A comprehensive study of light hydrocarbon mechanisms performance in predicting methane/hydrogen/air laminar burning velocities, *Int. J. Hydrogen Energy*. 42 (2017) 17260–17274. doi:10.1016/j.ijhydene.2017.05.203.
- [132] S. Wang, Z. Wang, Y. He, X. Han, Z. Sun, Y. Zhu, M. Costa, Laminar burning velocities of CH<sub>4</sub>/O<sub>2</sub>/N<sub>2</sub> and oxygen-enriched CH<sub>4</sub>/O<sub>2</sub>/CO<sub>2</sub> flames at elevated pressures measured using the heat flux method, *Fuel*. 259 (2020) 116152. doi:10.1016/j.fuel.2019.116152.
- [133] A.G. Shmakov, O.P. Korobeinichev, I. V. Rybitskaya, A.A. Chernov, D.A. Knyazkov, T.A. Bolshova, A.A. Konnov, Formation and consumption of NO in H<sub>2</sub> + O<sub>2</sub> + N<sub>2</sub> flames doped with NO or NH<sub>3</sub> at atmospheric pressure, *Combust. Flame*. 157 (2010) 556–565. doi:10.1016/j.combustflame.2009.10.008.
- [134] F.H.V. Coppens, J. De Ruyck, A.A. Konnov, The effects of composition on burning velocity and nitric oxide formation in laminar premixed flames of CH<sub>4</sub> + H<sub>2</sub> + O<sub>2</sub> + N<sub>2</sub>, *Combust. Flame*. 149 (2007) 409–417. doi:10.1016/j.combustflame.2007.02.004.
- [135] R.J. Kee, J.A. Miller, G.H. Evans, G. Dixon-Lewis, A computational model of the structure and extinction of strained, opposed flow, premixed methane-air flames, *Proc. Combust. Inst.* 22 (1989) 1479–1494. doi:10.1016/S0082-0784(89)80158-4.
- [136] H.K. Chelliah, C.K. Law, T. Ueda, M.D. Smooke, F.A. Williams, An experimental and theoretical investigation of the dilution, pressure and flow-field effects on the extinction condition of methane-air-nitrogen diffusion flames, *Proc. Combust. Inst.* 23 (1990) 503–511. doi:10.1016/S0082-0784(06)80297-3.
- [137] M. Matalon, On flame stretch, *Combust. Sci. Technol.* 31 (1983) 169–181. doi:http://dx.doi.org/10.1080/00102208308923638.
- [138] H. Kobayashi, M. Kitano, Dimensional Effects of Nozzle-Type Burner on Flow Fields and Extinction of Counterflow Twin Flames (in Japanese), *Trans. Japan Soc. Mech. Engrs.* 57 (1991) 363.
- [139] K. Seshadri, F.A. Williams, Laminar flow between parallel plates with injection of a reactant at high reynolds number, *Int. J. Heat Mass Transf.* 21 (1978) 251–253. doi:10.1016/0017-9310(78)90230-2.
- [140] K. Seshadri, " Counterflow Extinction of Premixed and Nonpremixed Methanol and Ethanol Flames ", *Univ. Calif. Energy Inst.* 7 (2005) 1–12.
- [141] E.M. Fisher, B.A. Williams, J.W. Fleming, Determination of the Strain in Counterflow Diffusion Flames From Flow Conditions, *Proc. East. Sect. Nof Combust. Inst.* (1997) 191–194.
- [142] H. Kobayashi, Y. Kawabata, K. Maruta, Experimental study on general correlation of turbulent burning velocity at high pressure, *Symp. Combust.* 27 (1998) 941–948. doi:10.1016/S0082-0784(98)80492-X.
- [143] Y. Ju, H. Guo, K. Maruta, F. Liu, On the extinction limit and flammability limit of non-adiabatic stretched methane–air premixed flames, *J. Fluid Mech.* 342 (1997) 315–334. doi:10.1017/S0022112097005636.
- [144] A.D. Weiss, W. Coenen, A.L. Sánchez, F.A. Williams, The acoustic response of Burke–Schumann counterflow flames, *Combust. Flame*. 192 (2018) 25–34. doi:10.1016/j.combustflame.2018.01.039.

- [145] H.G. Im, C.K. Law, J.S. Kim, F.A. Williams, to Oscillating Strain Rates, *Appl. Mech. Eng.* 2180 (1995) 21–30.
- [146] P. Papas, P.A. Monkewitz, A.G. Tomboulides, New instability modes of a diffusion flame near extinction, *Phys. Fluids*. 11 (1999) 2818–2820. doi:10.1063/1.870140.
- [147] A.C. Zambon, H.K. Chelliah, Self-sustained acoustic-wave interactions with counterflow flames, *J. Fluid Mech.* 560 (2006) 249–278. doi:10.1017/S0022112006000498.
- [148] M.P. Davis, J.W. Fleming, B.A. Williams, H.D. Ladouceur, Flow Field Considerations for Counter Flow Burners, in: *Proc. Fall Tech. Meet. East. States Sect. Combust. Inst., Raleigh NC, 1999*: pp. 200–203.
- [149] U. Niemann, K. Seshadri, F.A. Williams, Accuracies of laminar counterflow flame experiments, *Combust. Flame*. 162 (2015) 1540–1549. doi:10.1016/j.combustflame.2014.11.021.
- [150] F. Research, FtrPIV, (n.d.). <http://www.ft-r.jp/en/>.
- [151] D.F. Fairbanks, C.R. Wilke, Diffusion Coefficients in Multicomponent Gas Mixtures, *Ind. Eng. Chem.* 42 (1950) 471–475. doi:10.1021/ie50483a022.
- [152] A.W. Jasper, S.J. Klippenstein, L.B. Harding, Theoretical rate coefficients for the reaction of methyl radical with hydroperoxyl radical and for methylhydroperoxide decomposition, *Proc. Combust. Inst.* 32 I (2009) 279–286. doi:10.1016/j.proci.2008.05.036.
- [153] A.C. Eckbreth, *Laser Diagnostics for Combustion Temperature and Species*, Combustion, Gordon and Breach, Amsterdam, 1996.
- [154] B.E. Battles, R.K. Hanson, Measurements No and Oh Mole Fraction Flames : Fluorescence and Experimental, *J. Quant. Spectrosc. Radiat. Transf.* 54 (1995) 521–537.
- [155] P.H. Paul, C.D. Carter, J.A. Gray, J.L. Durant, J.W. Thoman, M.R. Furlanetto, Correlations for the NO A $2\Sigma^+$  ( $v'=0$ ) Electronic Quenching Cross-section, Sandia Rep. SAND94-8237 UC-1423. SAND94-823 (1995).
- [156] K. McManus, B. Yip, S. Candel, Emission and laser-induced fluorescence imaging methods in experimental combustion, *Exp. Therm. Fluid Sci.* 10 (1995) 486–502. doi:10.1016/0894-1777(94)00078-M.
- [157] A.F.H. van Gessel, B. Hrycak, M. Jasiński, J. Mizeraczyk, J.J.A.M. van der Mullen, P.J. Bruggeman, Temperature and NO density measurements by LIF and OES on an atmospheric pressure plasma jet, *J. Phys. D. Appl. Phys.* 46 (2013) 095201. doi:10.1088/0022-3727/46/9/095201.
- [158] K.P. Hubert, G. Herzberg, *Constants of diatomic molecules*, Van Nostrand Reinhold Company, New York, 1979.
- [159] J. Buckmaster, Edge-flames, *Prog. Energy Combust. Sci.* 28 (2002) 435–475. doi:10.1016/S0360-1285(02)00008-4.
- [160] S.H. Chung, Stabilization, propagation and instability of tribrachial triple flames, *Proc. Combust. Inst.* 31 (2007) 877–892. doi:10.1016/j.proci.2006.08.117.
- [161] K.M. Lyons, Toward an understanding of the stabilization mechanisms of lifted turbulent jet flames: Experiments, *Prog. Energy Combust. Sci.* 33 (2007) 211–231. doi:10.1016/j.peccs.2006.11.001.

- [162] C.J. Lawn, Lifted flames on fuel jets in co-flowing air, *Prog. Energy Combust. Sci.* 35 (2009) 1–30. doi:10.1016/j.peccs.2008.06.003.
- [163] A. Liñán, M. Vera, A.L. Sánchez, A. Li, M. Vera, L.S. Antonio, Ignition, Liftoff, and Extinction of Gaseous Diffusion Flames, *Annu. Rev. Fluid Mech.* 47 (2015) 293–314. doi:10.1146/annurev-fluid-010814-014711.
- [164] K.C. Smyth, J.H. Miller, R.C. Dorfman, W.G. Mallard, R.J. Santoro, Soot inception in a methane/air diffusion flame as characterized by detailed species profiles, *Combust. Flame.* 62 (1985) 157–181. doi:10.1016/0010-2180(85)90143-9.
- [165] H.C. Hottel, W.R. Hawthorne, Diffusion in laminar flame jets, *Symp. Combust. Flame Explos. Phenom.* 3 (1948) 254–266. doi:10.1016/S1062-2896(49)80034-1.
- [166] S.P. Burke, T.E.W. Schumann, Diffusion Flames, *Ind. Eng. Chem.* 20 (1928) 998–1004. doi:10.1021/ie50226a005.
- [167] W.R. Hawthorne, D.S. Weddell, H.C. Hottel, Mixing and combustion in turbulent gas jets, *Symp. Combust. Flame Explos. Phenom.* 3 (1948) 266–288. doi:10.1016/S1062-2896(49)80035-3.
- [168] S.R. Gollahalli, Ö. Savaş, R.F. Huang, J.L. Rodriguez Azara, Structure of attached and lifted gas jet flames in hysteresis region, *Proc. Combust. Inst.* 21 (1986) 1463–1471. doi:10.1016/S0082-0784(88)80379-5.
- [169] F. Takahashi, W.J. Schmoll, Lifting criteria of jet diffusion flames, *Proc. Combust. Inst.* 23 (1990) 677–683. doi:10.1016/S0082-0784(06)80316-4.
- [170] C.D. Brown, K.A. Watson, K.M. Lyons, Studies on lifted jet flames in coflow: the stabilization mechanism in the near- and far-fields, *Flow, Turbul. Combust.* 62 (1999) 249–273. doi:10.1023/A:1009925500084.
- [171] J. Min, F. Baillet, H. Guo, E. Domingues, M. Talbaut, B. Patte-Rouland, Impact of CO<sub>2</sub>, N<sub>2</sub> or Ar diluted in air on the length and lifting behavior of a laminar diffusion flame, *Proc. Combust. Inst.* 33 (2011) 1071–1078. doi:10.1016/j.proci.2010.06.100.
- [172] D.A. Scholefield, J.E. Garside, The structure and stability of diffusion flames, *Symp. Combust. Flame Explos. Phenom.* 3 (1948) 102–110. doi:10.1016/S1062-2896(49)80013-4.
- [173] H. Eickhoff, B. Lenze, W. Leuckel, Experimental investigation on the stabilization mechanism of jet diffusion flames, *Symp. Combust.* 20 (1985) 311–318. doi:10.1016/S0082-0784(85)80516-6.
- [174] G.T. Kalghatgi, Lift-off heights and visible lengths of vertical turbulent jet diffusion flames in still air, *Combust. Sci. Technol.* 41 (1983) 17–29. doi:10.1080/00102208408923819.
- [175] J. Buckmaster, Edge-flames, *J. Eng. Math.* 31 (1997) 269–284. doi:10.1023/A:1004287411382.
- [176] L. Muñoz, M.G. Mungal, Instantaneous flame-stabilization velocities in lifted-jet diffusion flames, *Combust. Flame.* 111 (1997) 16–30. doi:10.1016/S0010-2180(97)00096-5.
- [177] D. Han, M.G. Mungal, Observations on the transition from flame liftoff to flame blowout, *Proc. Combust. Inst.* 28 (2000) 537–543. doi:10.1016/S0082-0784(00)80253-2.
- [178] J.E. Broadwell, W.J.A. Dahm, M.G. Mungal, Blowout of turbulent diffusion flames, *Proc. Combust. Inst.* 20 (1984) 303–310. doi:10.1016/S0082-0784(85)80515-4.

- [179] H. Guo, J. Min, C. Galizzi, D. Escudié, F. Baillet, A numerical study on the effects of CO<sub>2</sub>/N<sub>2</sub>/Ar addition to air on liftoff of a laminar CH<sub>4</sub>/Air diffusion flame, *Combust. Sci. Technol.* 182 (2010) 1549–1563. doi:10.1080/00102202.2010.497074.
- [180] Y. Nada, K. Matsumoto, S. Noda, Liftoff heights of turbulent non-premixed flames in co-flows diluted by CO<sub>2</sub>/N<sub>2</sub>, *Combust. Flame.* 161 (2014) 2890–2903. doi:10.1016/j.combustflame.2014.05.007.
- [181] K.N. Kim, S.H. Won, S.H. Chung, Characteristics of laminar lifted flames in coflow jets with initial temperature variation, *Proc. Combust. Inst.* 31 I (2007) 947–954. doi:10.1016/j.proci.2006.08.012.
- [182] J.I. Erete, K.J. Hughes, L. Ma, M. Fairweather, M. Pourkashanian, A. Williams, Effect of CO<sub>2</sub> dilution on the structure and emissions from turbulent, non-premixed methane–air jet flames, *J. Energy Inst.* 90 (2017) 191–200. doi:10.1016/j.joei.2016.02.004.
- [183] B. Chul, S. Ho, B.C. Choi, S.H. Chung, Autoignited laminar lifted flames of methane/hydrogen mixtures in heated coflow air, *Combust. Flame.* 159 (2012) 1481–1488. doi:10.1016/j.combustflame.2011.11.016.
- [184] Y. Wu, Y. Lu, G.T. Kalghatgi, S. Sheffield, P.O. Box, C. Ch, The Effect of Hydrocarbon Fuel on the Stability of Hydrogen Jet Flames Department of Chemical and Process Engineering , University of Sheffield , Shell Global Solutions ( UK ), Cheshire Innovation Park , (n.d.).
- [185] J. Min, F. Baillet, A. Wyzgolik, E. Domingues, M. Talbaut, B. Patte-Rouland, C. Galizzi, Impact of CO<sub>2</sub>/N<sub>2</sub>/Ar addition on the internal structure and stability of nonpremixed CH<sub>4</sub>/air flames at lifting, *Combust. Sci. Technol.* 182 (2010) 1782–1804. doi:10.1080/00102202.2010.499716.
- [186] T. Leung, I. Wierzbna, The effect of co-flow stream velocity on turbulent non-premixed jet flame stability, *Proc. Combust. Inst.* 32 II (2009) 1671–1678. doi:10.1016/j.proci.2008.06.071.
- [187] B.J. Lee, S.H. Chung, Stabilization of lifted tribrachial flames in a laminar nonpremixed jet, *Combust. Flame.* 109 (1997) 163–172. doi:10.1016/S0010-2180(96)00145-9.
- [188] J. Min, F. Baillet, Experimental investigation of the flame extinction processes of nonpremixed methane flames inside an air coflow diluted with CO<sub>2</sub>, N<sub>2</sub>, or Ar, *Combust. Flame.* 159 (2012) 3502–3517. doi:10.1016/j.combustflame.2012.05.015.
- [189] B.J. Lee, J.S. Kim, S.H. Chung, Effect of dilution on the liftoff of non-premixed jet flames, *Symp. Combust.* 25 (1994) 1175–1181. doi:10.1016/S0082-0784(06)80756-3.
- [190] H. Guo, J. Min, C. Galizzi, D. Escudié, F. Baillet, A Numerical Study on the Effects of CO<sub>2</sub> / N<sub>2</sub> / Ar Addition on Liftoff of a Laminar CH<sub>4</sub> / Air Diffusion Flame, in: *Int. Colloq. Dyn. Explos. React. Syst.*, Minsk, Belarus, 2009: p. Paper 29. <http://www.icders.org/ICDERS2009/>.
- [191] Y.M. Marin Ospina, Etude de l'influence de la dilution du combustible et de l'oxydant dans le processus de décrochage de flammes-jet non-prémélangées et l'émission de polluants, INSA de Rouen, 2017.
- [192] Y. Wu, I.S. Al-Rahbi, Y. Lu, G.T. Kalghatgi, The stability of turbulent hydrogen jet flames with carbon dioxide and propane addition, *Fuel.* 86 (2007) 1840–1848. doi:10.1016/j.fuel.2006.11.032.
- [193] C.K. Law, *Transport phenomena*, in: *Combust. Phys.*, Cambridge University Press, New York, 2006: pp. 141–156.

- [194] B. Eckhardt, T.M. Schneider, How does flow in a pipe become turbulent?, *Eur. Phys. J. B.* 64 (2008) 457–462. doi:10.1140/epjb/e2008-00140-y.
- [195] B. Eckhardt, T.M. Schneider, B. Hof, J. Westerweel, Turbulence Transition in Pipe Flow, *Annu. Rev. Fluid Mech.* 39 (2007) 447–468. doi:10.1146/annurev.fluid.39.050905.110308.
- [196] H. Schlichting, *Boundary Layer Theory*, 7th ed., McGraw-Hill Book Company, New York, 1979.
- [197] M. Marin, F. Baillet, Experimental study of the lifting characteristics of the leading-edge of an attached non-premixed jet-flame: Air-side or fuel-side dilution, *Combust. Flame.* 171 (2016) 264–280. doi:10.1016/j.combustflame.2016.05.025.
- [198] J. Min, *Comportement transitionnel et stabilisation de flammes-jets non-prémélangés de méthane dans un coflow d'air dilué en CO<sub>2</sub>*, Insa de Rouen, 2011.
- [199] F. Takahashi, M. Mizomoto, S. Ikai, Transition from laminar to turbulent free jet diffusion flames, *Combust. Flame.* 48 (1982) 85–95. doi:10.1016/0010-2180(82)90117-1.
- [200] S.D. Terry, K.M. Lyons, Turbulent lifted flames in the hysteresis regime and the effects of coflow, *J. Energy Resour. Technol. Trans. ASME.* 128 (2006) 319–324. doi:10.1115/1.2358147.
- [201] E.T. Child, K. Wohl, Spectrophotometric studies of laminar flames—I the decay of radical radiation, *Symp. Combust.* 7 (1958) 215–220. doi:10.1016/S0082-0784(58)80043-0.

# Acknowledgments

I wish to express my sincere thanks to Tohoku University and INSA de Lyon, for giving me the opportunity to do this double degree program and contribute to this long history of collaboration between the two universities. From Tohoku University, I would like to thank more specifically the International Affairs Section of the Engineering School of Tohoku University, and Ms. Miyamoto, for their constant help throughout the year. From INSA de Lyon, I would like to thank FEDORA Department, Ms. Aurelie Durand and Stephanie Cauvin for their assistance.

I would also like to give a special thanks to all the members of the Reacting Flow Laboratory in Sendai and the CETHIL in Lyon. Their help and support were essential all along those 3 years of doctor course. Among them, I would like to thank Professor H. Kobayashi for the warm welcome I had in the Reacting Flow Laboratory, the useful advice and guidance for my research project and the opportunity to present my work at conferences. I would like to thank Professor D. Escudié, Professor C. Galizzi and Professor M. Kuhni, for their constant support and guidance in my research project, and for starting this new project on ammonia combustion.

In reviewing my thesis, I would like to thank Professor K. Maruta, Professor H. Nakamura and Professor A. Hayakawa for their useful comments and corrections. Also, I would like to thank Professor T. Sadegh, Dr. Okafor and Dr. Somarathne, for sharing their knowledge and experience, but also for their useful recommendations; Mr. Kudo, for his help in the laboratory, and his precious recommendations concerning experiments; M. Buathier, M. Buthod, M. Ducat, M. Durand, M. Pouchot and M. Zerbino for their patience and for sharing their technical expertise.

I also would like to thank Ms. Utria, M. Ichikawa and M. Yamaguchi who helped me through those three years, sharing their knowledge and contributing to make great experimental work; Ms. Iwaki for her kind comprehension, her help for all the laboratory administrative tasks and her cheering conversations, Ms. Dahmani, Ms. Galindo, Ms. Buttet, Ms. Marques, for their support and the joyful atmosphere they brought to the office; Ms. Kovalova for her energy and English checks; and more generally, all the members of Reacting Flow Laboratory and CETHIL that I had the opportunity to meet, for their support, but mainly for making of the laboratory much more than just a working place.

I would also like to thank my family and friends who have always been there supporting me in this project, in both the best and the toughest moments.

I would finally like to thank the Institute of Fluid Science for the financial support offered as a research assistant in the Reacting Flow Laboratory, the CETHIL for its contribution during my work in France and Tohoku University for the President Fellowship covering my tuition fees. This work was also supported by the Council for Science, Technology and Innovation (CSTI), the cross-ministerial Strategic Innovation Promotion Program (SIP) “Energy Carriers”. For their support in this international collaboration, I would also like to thank the LIA Elyt Global and the IFS Lyon Center, and more specifically Professor T. Uchimoto, as well as the Institute of Fluid Science (Collaborative Research Project), and the MEGA doctor school of Lyon (Soutien à la mobilité internationale).

# List of publications

## International journal papers

1. Sophie Colson, Akihiro Hayakawa, Taku Kudo and Hideaki Kobayashi  
Extinction characteristics of ammonia/air counterflow premixed flames at various pressures  
Journal of Thermal Science and Technology, Vol.11 (2016), JTST0048.  
<https://doi.org/10.1299/jtst.2016jtst0048>.
2. Ekenechukwu C. Okafor, Yuji Naito, Sophie Colson, Akinori Ichikawa, Taku Kudo, Akihiro Hayakawa and Hideaki Kobayashi  
Experimental and numerical study of the laminar burning velocity of CH<sub>4</sub>-NH<sub>3</sub>-air premixed flames  
Combustion and Flame, Vol.187 (2018), pp.185-198.  
[doi:10.1016/j.combustflame.2017.09.002](https://doi.org/10.1016/j.combustflame.2017.09.002).
3. K. D. Kunkuma A. Somarathne, Sophie Colson, Akihiro Hayakawa and Hideaki Kobayashi  
Modelling of ammonia/air non-premixed turbulent swirling flames in a gas turbine-like combustor at various pressures  
Combustion Theory and Modelling, Vol.22 (2018), pp.973-997.  
[doi:10.1080/13647830.2018.1468035](https://doi.org/10.1080/13647830.2018.1468035).
4. Ekenechukwu C. Okafor, Yuji Naito, Sophie Colson, Akinori Ichikawa, Taku Kudo, Akihiro Hayakawa and Hideaki Kobayashi  
Measurement and modelling of the laminar burning velocity of methane-ammonia-air flames at high pressures using a reduced reaction mechanism  
Combustion and Flame, Vol.204 (2019), pp.162-175.  
[doi:10.1016/j.combustflame.2019.03.008](https://doi.org/10.1016/j.combustflame.2019.03.008).
5. Sophie Colson, Yuta Hirano, Akihiro Hayakawa, Taku Kudo, Hideaki Kobayashi, Cédric Galizzi, Dany Escudié  
Experimental and numerical study of NH<sub>3</sub>/CH<sub>4</sub> counterflow premixed and non-premixed flames for various NH<sub>3</sub> mixing ratios  
Combustion Science and Technology, (2020), (In press, available online).  
[doi:10.1080/00102202.2020.1763326](https://doi.org/10.1080/00102202.2020.1763326).

## International conferences

1. Sophie Colson, Akihiro Hayakawa, Taku Kudo, Hideaki Kobayashi  
 Extinction characteristics of ammonia/air counterflow premixed flames at various pressures  
 The First Pacific Rim Thermal Engineering Conference, (2016), Hawaii, Paper No. 14586.  
 Journal of Thermal Science and Technology, Vol.11 (2016), JTST-0048.
  
2. Sophie Colson, Takahashi Goto, Taku Kudo, Akihiro Hayakawa, Hideaki Kobayashi  
 Extinction characteristics of counterflow twin flame for NH<sub>3</sub>/air, CH<sub>4</sub>/air and their mixtures  
 36th International Symposium on Combustion, (2016), Seoul, Poster No. 8308.
  
3. Sophie Colson, Yuta Hirano, Akihiro Hayakawa, Taku Kudo, Hideaki Kobayashi, Dany Escudié,  
 Cédric Galizzi  
 Investigation of methane-ammonia chemistry from premixed and diffusion flame structures using a  
 counterflow configuration  
 37th International Symposium on Combustion, (2018), Dublin, Poster No. 16339.
  
4. Sophie Colson, Yuta Hirano, Akihiro Hayakawa, Taku Kudo, Hideaki Kobayashi, Dany Escudié,  
 Cédric Galizzi  
 Experimental analysis and 1D modelling of counterflow ammonia-methane flames  
 9th European Combustion Meeting, (2019), Lisboa, Poster No. S1\_All\_18.

## National conferences

1. Sophie Colson, Akihiro Hayakawa, Taku Kudo, Hideaki Kobayashi  
 Extinction Analysis and Experiments of Methane/Ammonia/Air Counterflow Twin Flames  
 54th Japanese Symposium on combustion, (2016), paper No. B223.



## FOLIO ADMINISTRATIF

### THESE DE L'UNIVERSITE DE LYON OPEREE AU SEIN DE L'INSA LYON

NOM : COLSON

DATE de SOUTENANCE : 13/11/2020

Prénoms : Sophie

TITRE :

Fundamental flame characteristics and combustion chemistry for ammonia/methane blended fuels.

NATURE : Doctorat

Numéro d'ordre : 2020LYSEI103

Ecole doctorale : ED MEGA 162

Spécialité : Thermique Energétique

RESUME :

L'étude de combustibles décarbonés, tel que l'ammoniac, est essentielle dans le contexte du réchauffement climatique. Sa combustion nécessite cependant de relever plusieurs défis, notamment concernant la stabilisation des flammes et la production de NOx. Afin de pallier les problèmes de stabilisation, une solution consiste à utiliser un mélange d'ammoniac avec un autre combustible.

Cette thèse a pour objectif l'analyse des caractéristiques fondamentales de la combustion d'un mélange ammonia-méthane, encore peu étudié. Il s'agira de comprendre les mécanismes cinétiques conduisant à la formation de polluants et ceux contrôlant la stabilisation.

Dans ce but, le travail portera d'abord sur la chimie de combustion de ces mélanges, afin de clarifier leurs propriétés, notamment la structure de la flamme et les émissions engendrées. L'étude des mécanismes réactionnels, déjà validés dans un domaine limité de conditions, a montré de réelles disparités lorsque les conditions d'étude étaient élargies. Il est donc essentiel d'évaluer ces mécanismes dans des configurations diversifiées et sur une plus large base de résultats expérimentaux. Quatre mécanismes ont été sélectionnés et évalués dans une configuration à contre-courant, via l'étude du taux d'étirement à l'extinction et l'analyse des profils d'espèces OH et NO.

La stabilisation de ces flammes a ensuite été étudiée, en examinant l'influence de l'ajout d'ammoniac sur une flamme de méthane de type jet non-pré-mélangée. L'évolution des limites de suspension, de rattachement et l'étendue de la zone d'hystérésis ont notamment été examinés. La dynamique de (dé)stabilisation de la flamme attachée au brûleur, sa suspension et son rattachement ont été étudiés pour comprendre l'évolution particulière de ces régimes. Les résultats montrent une forte diminution du domaine de stabilisation avec l'ajout d'ammoniac ainsi qu'un comportement singulier de la limite de ré-attachement. Enfin, l'étude de la flamme attachée a souligné l'importance des couplages aérodynamique et chimique dans la dynamique de stabilisation du bout de flamme.

MOTS-CLÉS :

Ammoniac, Méthane, Taux d'étirement à l'extinction, OH, NO, Chimie de combustion, Stabilisation, Flamme contre-courant, Flamme jet

Laboratoire (s) de recherche :

CETHIL

Directeur de thèse:

Dany Escudié

Hideaki Kobayashi

Président de jury :

Composition du jury :

Christine Rousselle, Françoise Baillet, Frédérique Battin-Leclerc, Dany Escudié, Cédric Galizzi